Measurements of the Higgs boson decay to W^+W^- with the CMS detector

Lorenzo Viliani
of University of Florence

PhD Thesis

Abstract

The cross section for Higgs boson production in pp collisions is studied using the $\mathrm{H} \to \mathrm{W}^{+}\mathrm{W}^{-}$ decay mode, followed by leptonic decays of the W bosons, leading to an oppositely charged electron-muon pair in the final state. The measurements are performed using data collected by the CMS experiment at the LHC with pp collisions at a centre-of-mass energy of 8 TeV, corresponding to an integrated luminosity of $19.4\,\mathrm{fb}^{-1}$. The Higgs boson transverse momentum (p_{T}) is reconstructed using the lepton pair p_{T} and missing p_{T}. The differential cross section times branching fraction is measured as a function of the Higgs boson p_{T} in a fiducial phase space defined to match the experimental acceptance in terms of the lepton kinematics and event topology. The production cross section times branching fraction in the fiducial phase space is measured to be 39 ± 8 (stat) ± 9 (syst)fb. The measurements are compared to theoretical calculations based on the standard model to which they agree within experimental uncertainties.

Contents

Chapter 1.

Electroweak and QCD physics at LHC

In this chapter the Standard Model of particle physics is briefly described, in particular the main characteristics of the electroweak and strong interactions are discussed, as well as the machanism of the electroweak symmetry breaking. In addition, the phenomenology of the proton-proton interactions is described and the main features of the Monte Carlo simulation techniques are given. Eventually, an overview of the Higgs boson physics from an experimental point of view is reported.

1.1. The Standard Model of particle physics

The Standard Model of Particle Physics (SM) is the theory that describes all fundamental constituents of matter and their interactions. It is a renormalisable quantum field theory based on a $\mathrm{SU(3)_c} \otimes \mathrm{SU(2)_L} \otimes \mathrm{U(1)_Y}$ local gauge symmetry, and is capable to provide a quantitative description of three of the four interactions in nature: electromagnetism, weak interaction and strong nuclear force. The aforementioned symmetry holds only if the fermion fields are massless, in contrast with the experimental observations of massive fermions. A mechanism, known as *spontaneous symmetry breaking*, is introduced in the SM allowing the elementary particles to acquire mass. This mechanism requires the presence of a new field, known as Higgs field. During the past decades the predictions of the SM have been confirmed by experimental results with outstanding precision, and in 2012 the existence of a new boson consistent with the predicted Higgs boson was announced by the ATLAS and CMS experiments at CERN.

According to the SM, the ordinary matter is made up of spin-1/2 particles, denoted as fermions. The fermions are subdivided into two classifications of elementary particles: leptons and quarks. Both classes consist of six particles, grouped into three doublets, called generations. Additional three doublets for each class are composed of leptons and quarks antiparticles. A charged particle with electric charge $Q = -1$, either the electron e, the muon μ or the tauon τ, and a neutral particle, the corresponding neutrino, compose the following lepton generations, ordered according to an increasing mass hierarchy:

$$\begin{pmatrix} e^- \\ \nu_e \end{pmatrix}, \quad \begin{pmatrix} \mu^- \\ \nu_\mu \end{pmatrix}, \quad \begin{pmatrix} \tau^- \\ \nu_\tau \end{pmatrix} \quad . \tag{1.1}$$

Charged leptons can interact via the electromagnetic and weak force, while neutrinos, that are assumed to be massless, can interact only through the weak interaction.

Similarly, the quarks are organized in pairs composed of a particle with $Q = +2/3$, *up* (u), *charm* (c) and *top* (t) quarks, and another particle with $Q = -1/3$, *down* (d), *strange* (s) and *bottom* (b) quarks:

$$\begin{pmatrix} u \\ d \end{pmatrix}, \quad \begin{pmatrix} c \\ s \end{pmatrix}, \quad \begin{pmatrix} t \\ b \end{pmatrix} \quad . \tag{1.2}$$

As well as leptons, quarks can interact via the electromagnetic and weak forces, but also via the strong interaction, responsible of their confinement within hadrons. In fact, free quarks are not observed in nature, but they bind together forming two categories of hadrons: mesons, bound states of a quark q and an anti-quark $\bar{\mathrm{q}}$, and baryons, bound states of three quarks.

In the SM the interaction between elementary particles occurs through the exchange of spin-1 particles, known as bosons, which identify the fundamental forces. The photon γ is the mediator of the electromagnetic interaction, the $\mathrm{W}^{\pm}$ and Z bosons are the mediators of the weak interaction, while the strong force is mediated by eight gluons g. Electromagnetic and weak interactions are actually the manifestations of the same fundamental interaction, the electroweak force.

1.2. The Higgs mechanism

1.3. The strong interaction

1.4. Phenomenology of proton proton interactions

1.5. Monte Carlo simulations

1.6. Experimental results of the Higgs boson properties

Chapter 2.

The CMS experiment at the LHC

In this chapter, the main characteristics of the Large Hadron Collider (LHC particle accelerator and Compact Muon Solenoid (CMS) experiment are described.

2.1. The Large Hadron Collider

The LHC [1–4] at CERN, officially inaugurated on 21$^{\mathrm{st}}$ October 2008, is the largest and most powerful hadron collider ever built. Installed in the underground tunnel which hosted the Large Electron Positron Collider (LEP) [5–7], the leptonic accelerator in operation until 2nd November 2000, the LHC accelerator has the shape of a circle with a length of about 27 km and is located underground at a depht varying between 50 m to 175 m, straddling the Franco-Swiss border near Geneva. It is designed to collide two 7 TeV counter-circulating beams of protons resulting in a center-of-mass energy of 14 TeV, or two beams of heavy ions, in particular lead nuclei at an energy of 2.76 TeV/nucleon in the center-of-mass frame.

The transition from a leptonic collider to a hadronic collider entailed the following advantages: first, it has been possible to build a machine that having the same size of the previous one (and therefore accommodated in the same LEP tunnel, substantially reducing the cost and time of construction), could reach a higher energy in the center-of-mass frame. This is due to the much lower amount of energy loss through synchrotron radiation emitted by the accelerated particles, that is proportional to the fourth power of the ratio E/m between their energy and their mass. Secondly, the composite structure of protons compared to the elementary structure of electrons allows LHC to be able to simultaneously access a wider energy spectrum, despite the production of many low energies particles in a complex environment. This is a particularly important feature for a machine dedicated to the discovery of "new" physics.

In Fig. 2.1 a schematic description of the accelerator complex installed at CERN is shown. The acceleration is performed in several stages [4]. The protons source is a *Duoplasmatron*: the protons are obtained by removing electrons from a source of hydrogen gas and then sent to the LINAC2, a 36 m long linear accelerator which generates a pulsed beam with an energy of 50 MeV using Radio Frequency Quadrupoles (RFQ) and focusing quadrupole magnets. The beam is subsequently sent to the Proton Synchrotron Booster (PSB), a circular accelerator consisting of four superimposed synchrotron rings with a circumference of about 160 m, which increases the proton energy up to 1.4 GeV. Then, protons are injected into the Proton Synchrotron (PS), a single synchrotron ring with a circumference of about 600 m where the energy is increased to 25 GeV. The sequential combination of these two synchrotrons also allows to create a series of protons bunches interspersed by 25 ns as required for the correct operation of LHC. The final proton injection stage is the Super Proton Synchrotron (SPS), a synchrotron with a circumference of approximately 7 km where protons reach an energy value of 450 GeV. Subsequently, protons are extracted and injected into the LHC ring via two transmission lines, to generate two beams running in opposite directions in two parallel pipes and which are accelerated up to the energy of interest. In the two pipes an ultrahigh vacuum condition is maintained (about 10^{-10} Torr) to avoid the spurious proton interactions with the gas remnants. At full intensity, each proton beam consists of 2808 bunches and each bunch contains around 10^{11} protons. The beams are squeezed and collide for a length of about 130 m at four interaction points where the four main experiments (ALICE, ATLAS, CMS and LHCb) are placed:

- CMS (Compact Muon Solenoid) [8] and ATLAS (A Toroidal LHC ApparatuS) [9] are two general-purpose detectors designed to investigate the largest possible spectrum of physics. In particular, they have been devoted to the detection of particles produced by a Higgs boson decay and to look for any evidence of possible new physics. The use of two detectors chasing the same objectives but designed independently is crucial for a cross-check of any possible new discovery;
- LHCb (LHC beauty) [10] is an experiment primarily designed to study CP (combined Charge conjugation and Parity symmetry) violation in electroweak interactions and to study asymmetries between matter and antimatter through the analysis of rare decays of hadrons containing b quarks. The detector is also able to perform measurements in the forward region, at small polar angles with respect to the beam line;
- ALICE (A Large Ion Collider Experiment) [11] is an experiment studying heavy ions collisions, through the production of a new state of matter called quark-gluon plasma.

Two other smaller experiments are located along the circumference of the LHC accelerator, TOTEM and LHCf, which focus on particles emitted in the forward direction. TOTEM (TOTal Elastic and diffractive cross section Measurement) [12] measures the proton-proton interaction cross section and accurately monitors the luminosity of the LHC using detectors positioned on either side of the CMS interaction point. LHCf (LHC forward) [13] is made up of two detectors which sit along the LHC beamline, at 140 m either side of the ATLAS collision point. It makes use of neutral particles thrown forward by LHC collisions as a source to simulate the interaction with the atmosphere of very high energy cosmic rays (between 10^{17} TeV and 10^{20} TeV) in laboratory conditions.

A series of about 1200 magnetic dipoles bend the beams along the accelerator ring. They are located along the “arc” structures of the circumference. The ring, in fact, can be subdivided into octants, with eight curve regions (the “arcs”) separated by rectilinear regions. In these straight regions, instead, almost 400 focusing and defocusing quadrupoles are located, which maintain the beam stable along the orbit, and some other small multipolar magnets (sextupoles and octupoles) are used to make additional minor corrections to the beam direction. A radio frequency acceleration system, consisting of 16 superconducting

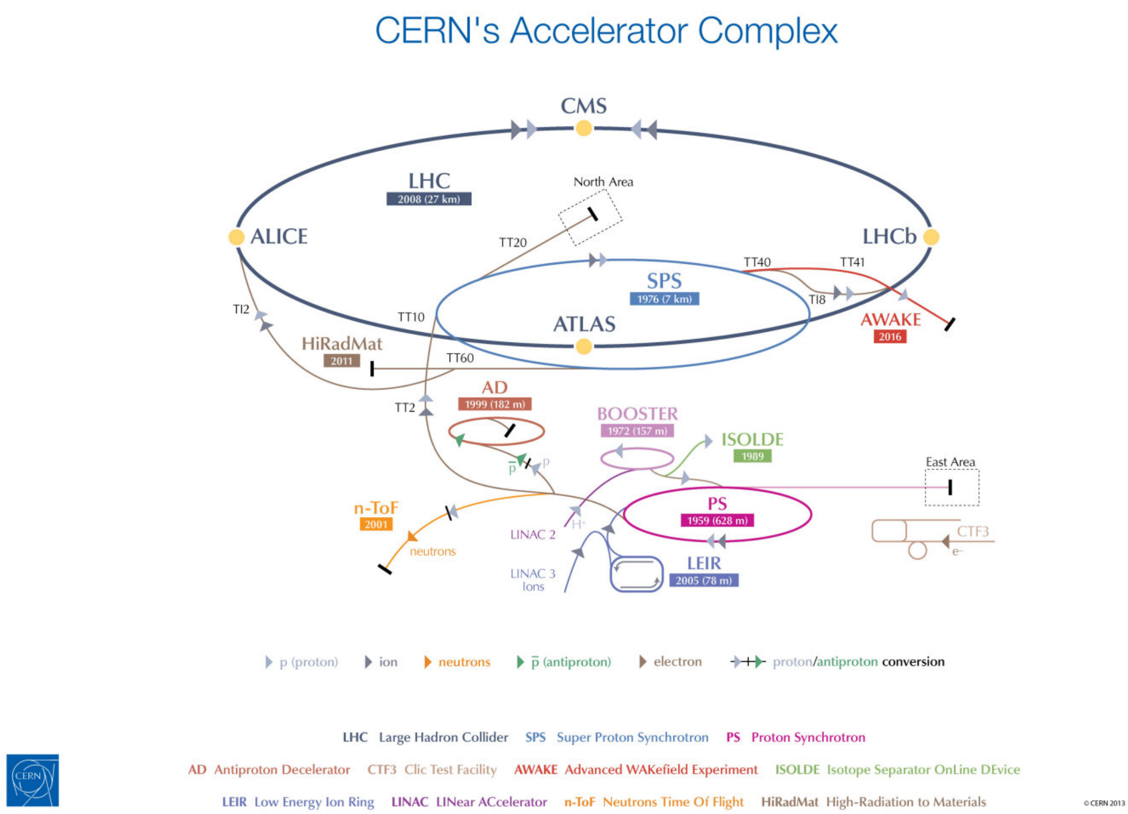

Figure 2.1.: Schematic description of the accelerator complex installed at CERN.

radio-frequency resonant cavities, is used to increase the proton energy by 0.5 MeV with each beam revolution. The 7 TeV per-beam-energy limit on the LHC is not determined by the electric field generated by the radiofrequency cavity but by the magnetic field necessary to maintain the protons in orbit, given the current technology for the superconducting magnets, which is about 5.4 T on average.

One of the most important parameters of an accelerator is the instantaneous luminosity $\mathcal{L}$, which gives a measure of the rate of events one can expect given the process cross section. In fact, for a given physics process with cross section σ, producing N events for unit of time, the instantaneous luminosity is defined by the following equation:

$$N = \sigma\mathcal{L} \quad . \tag{2.1}$$

The LHC design luminosity is $\mathcal{L} = 10^{34}\mathrm{cm}^{-2}\mathrm{s}^{-1}$, leading to around 1 billion proton interactions per second.

The instantaneous luminosity is a parameter which depends on the construction characteristics of the accelerator, and can be expressed by the following approximated formula:

$$\mathcal{L} = f \frac{n_1 n_2}{4\pi \sigma_x \sigma_y} \quad , \tag{2.2}$$

where n_1 and n_2 are the number of particles contained in the two bunches colliding at a frequency f, and σ_x and σ_y are the beam sizes in the transverse plane. At LHC, the bunches collide with $f = 40\,\mathrm{MHz}$ and the transverse size of the beam can be squeezed down to around 15 µm. Then, the integrated luminosity L is defined as the time integral of the instantaneous luminosity:

$$L = \int \mathcal{L} dt \quad . \tag{2.3}$$

The main parameters of the LHC machine are listed in Table 2.1.

The LHC started to be operative in September 2008 but, due to a faulty interconnection between two magnets which caused a helium leakage in the tunnel, the operation was stopped and restarted in March 2010. During 2010 and 2011 LHC ran successfully and provided proton proton collisions at a center-of-mass energy of 7 TeV, delivering a total integrated luminosity of about $6.1\,\mathrm{fb}^{-1}$. The encouraging results in the Higgs boson search provided by the ATLAS and CMS Collaborations led to the decision of extending the data taking period to the end of 2012, and to increase the center-of-mass energy up to 8 TeV. During 2012, LHC delivered to the experiments an integrated luminosity of $23.3\,\mathrm{fb}^{-1}$. After the first long shutdown (LS1), a two years period started in the early 2013 where the LHC operation stopped for maintenance and upgrade, the LHC started again delivering proton proton collisions on 3$^{\mathrm{rd}}$ June 2015, at the new record center-of-mass energy of 13 TeV. During the 2015 the LHC delivered an integrated luminosity of $4.2\,\mathrm{fb}^{-1}$. Nowadays, LHC is still colliding bunches of protons at $\sqrt{s} = 13\,\mathrm{TeV}$, reaching unprecedented instantaneous luminosities and delivering a total integrated luminosity of $31\,\mathrm{fb}^{-1}$. The cumulative delivered luminosity versus time for the different LHC data taking periods is shown in Fig. 2.2.

As the instantaneous luminosity increases, the probability of multiple proton proton interactions to occur in a single bunch crossing grows higher as well. In this instance, the main goal is the identification and reconstruction of a single primary collision where the physics event of interest occurs among the background of the additional proton proton interactions. Such backgrounds are due to processes occurring with very high probability, like the production of low-p_{T} jets. These additional collisions are known as pile up (PU). During the LHC current run the average number of pile up events is 23, with some event exhibiting over 45 pile up collisions.

Table 2.1.: LHC technical parameters for proton proton collisions.

Parameter	**Value**
Maximum dipole magnetic field	8.33 T
Dipole operating temperature	1.9 K
Beam energy at injection	450 GeV
Beam energy at collision (nominal)	7 TeV
Beam energy at collision (2012)	4 TeV
Beam energy at collision (2015–2016)	6.5 TeV
Maximum instantaneous luminosity (nominal)	$10^{34}\,\mathrm{cm^{-2}s^{-1}}$
Maximum instantaneous luminosity (2012)	$7.7\cdot10^{33}\,\mathrm{cm^{-2}s^{-1}}$
Maximum instantaneous luminosity (2015–2016)	$1.2\cdot10^{34}\,\mathrm{cm^{-2}s^{-1}}$
Number of bunches per proton beam (nominal)	2808
Number of bunches per proton beam (2012)	1380
Number of bunches per proton beam (2015–2016)	2220
Maximum number of protons per bunch	$1.69\cdot10^{11}$
Bunch separation in time (nominal)	25 ns
Bunch separation in time (2012)	50 ns
Bunch separation in time (2015–2016)	25 ns
Collision frequency (nominal)	40 MHz
Collision frequency (2012)	20 MHz
Collision frequency (2015–2016)	40 MHz
Energy loss per turn at 14 TeV	7 keV

2.2. The *Compact Muon Solenoid* experiment

The CMS apparatus is a general purpose detector situated in one of the four LHC interaction points[1]. The detector is designed to investigate a wide range of physics, from the search of the Higgs boson, to SM measurements and BSM physics searches. To achieve this goal, the detector is able to identify and reconstruct all the physics objects that may be produced in the proton proton collisions: electrons, muons, photons and jets. The main feature of the CMS detector is a superconducting solenoidal magnet which is capable to produce a

[1] The CMS detector is placed in a cavern 100 m underground in the area called Point 5, near the village of Cessy, in France.

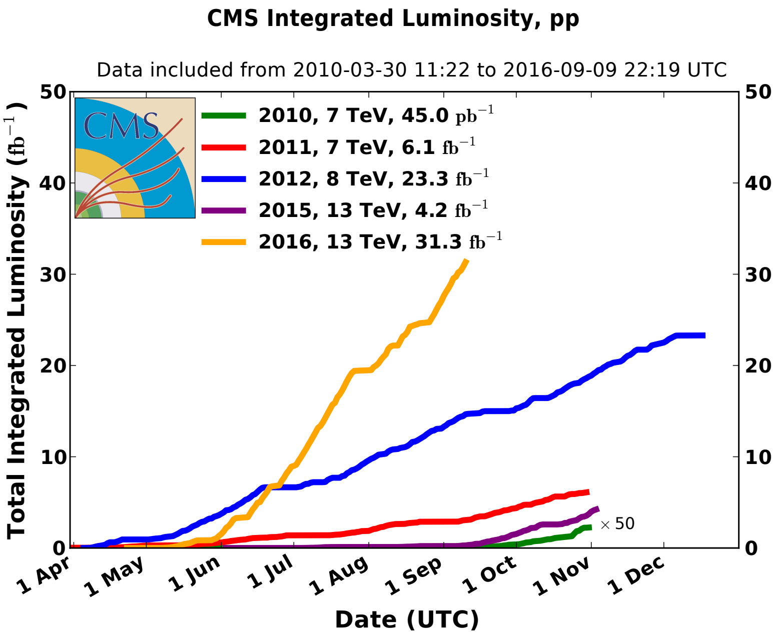

Figure 2.2.: Cumulative luminosity versus day delivered to CMS during proton proton collisions.

3.8 T magnetic field. Such a strong magnetic field is the key aspect which permits to have a compact design of the detector. The detector has a cylindrical structure, which is typical of general purpose detectors, which consists of several cylindrical detecting layers, coaxial with the beam direction (*barrel* region), closed at both ends with detecting disks (*endcap* region), in such a way to ensure the hermetic closure of the apparatus.

The coordinate system used by CMS is a right-handed Cartesian system, with the origin at the center of the detector, in the nominal beam collision point. The x-axis is chose to point radially towards the center of the LHC circumference and the y-axis is directed upwards along the vertical. The z-axis is oriented along the beam direction, according to the anticlockwise direction of the LHC ring if seen from above. The CMS cylindrical symmetry and the Lorentz invariant description of the proton proton collisions, suggest the use of a pseudo-angular reference frame, described by the triplet of coordinates (r, ϕ, η), where r is the distance from the z-axis, ϕ is the azimuthal angle, measured starting from the x-axis positive direction, and η is the pseudorapidity, defined by the following equation:

$$\eta = -\ln\left(\tan\frac{\theta}{2}\right) \quad , \tag{2.4}$$

where θ is the polar angle. The used of pseudorapidity is preferred over the polar angle because differences in pseudorapidity are Lorentz invariant under boosts along the z-axis.

In the limit of ultrarelativistic particles the pseudorapidity coincides with the rapidity y:

$$y = \frac{1}{2} \ln \left(\frac{E + p_z}{E - p_z} \right) \quad , \tag{2.5}$$

where E is the particle energy and p_z is the momentum projection along the z-axis.

The schematic view of the CMS detector, which has a length of 21.5 m, a diameter of 15 m and a weight of about 14000 tons, is shown in Fig. 2.3. From the inner region to the outer one, the various CMS sub-detectors are:

- **Silicon tracker**: it occupies the region $r < 1.2$ m and $|\eta| < 2.5$. It is composed of an inner silicon pixel vertex detector and a surrounding silicon microstrip detector, with a total active area of about 215 m^2. It is used to reconstruct charged particle tracks and vertices;

- **Electromagnetic calorimeter (ECAL)**: placed in the region 1.2 m $< r <$ 1.8 m and $|\eta| < 3$, it consists of many scintillating crystals of lead tungstate ($PbWO_4$). It is used for the measurement of the trajectory and the energy released by electrons and photons;

- **Hadronic calorimeter (HCAL)**: it is placed in the region 1.8 m $< r <$ 2.9 m and $|\eta| < 5$. It is made up of brass layers alternated with plastic scintillators and it is used to measure the direction and energy deposited by the hadrons produced in the interactions;

- **Superconducting solenoidal magnet**: it occupies the region 2.9 m $< r <$ 3.8 m and $|\eta| < 1.5$ and generates an internal uniform magnetic field with an intensity of 3.8 T, pointing along the direction of the beams. The magnetic field is necessary to bend the trajectories of charged particles, in order to allow the measurement of their momentum through the curvature observed in the tracking system. The magnetic field lines are closed by an external 21 m long iron yoke, that has a diameter of 14 m. Outside the return yoke, a residual 1.8 T magnetic field is present, pointing in the opposite direction with respect to the internal field;

- **Muon system**: the outermost system, which is placed in the region 4 m $< r <$ 7.4 m and $|\eta| < 2.4$, has the purpose of reconstructing the tracks of muons passing through it. It consists of Drift Tubes (DT) in the barrel region and Cathode Strip Chambers (CSC) in the endcaps. A complementary system of Resistive Plate Chambers (RPC) is used both in the barrel and endcaps. The muon chambers are housed inside the iron structure of the return yoke.

In Fig. 2.4 the response of the various CMS sub-detectors to the passage of different types of particles is sketched. In the following sections a brief description of each sub-detector is given.

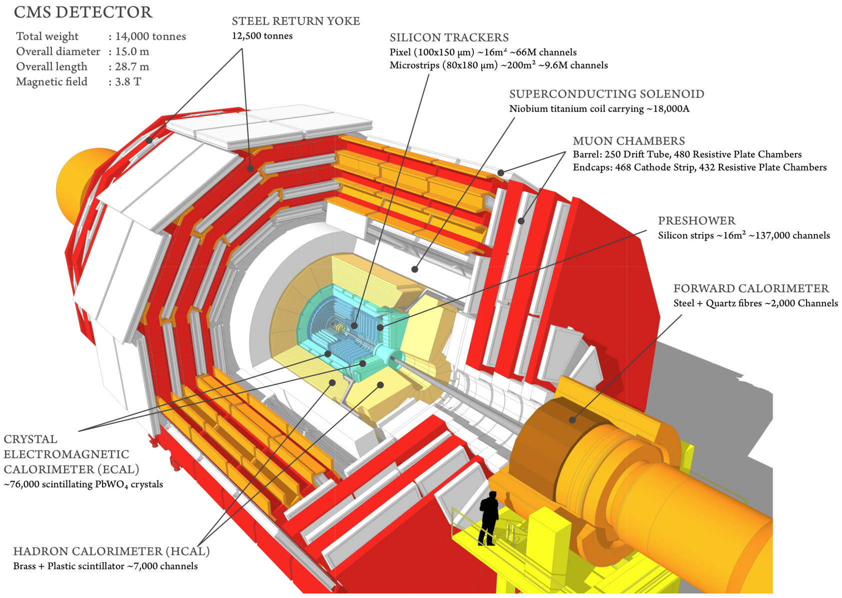

Figure 2.3.: Schematic view of the CMS detector showing its sub-detectors.

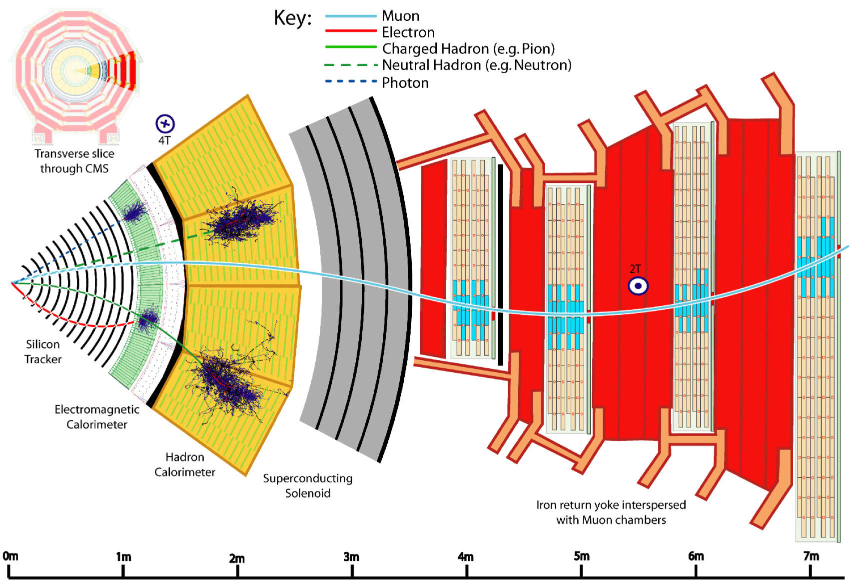

Figure 2.4.: Schematic view of a slice of the CMS detector, showing the sub-detectors response to the passage of different types of particles.

2.2.1. The solenoid

The CMS magnet [14], which contains the tracker, the electromagnetic and the hadronic calorimeters, is the biggest superconducting solenoid ever built. The solenoid can generate a magnetic field of 3.8 T in the internal bore, which has a diameter of 6 m and a length of

12.5 m. The energy stored in the magnet is about 2.7 GJ at full current. The superconductor is made of four Niobium-Titanium layers and it is cooled down to about 4 K through a liquid Helium cooling plant. In case of a quench, when the magnet loses its superconducting property, the energy is dumped to resistors within 200 ms. The magnet return yoke of the barrel is composed with three sections along the z-axis; each one is split into 4 layers (holding the muon chambers in the gaps). Most of the iron volume is saturated or nearly saturated, and the field in the yoke is about the half (1.8 T) of the field in the central volume.

2.2.2. The tracker

The silicon tracker is the detector closest to the beam collision point. Its goal is the high resolution reconstruction of the trajectories of charged particles originating from the interaction point and the identification of the position of secondary vertices produced by particles with a short mean life time (in particular hadrons containing the b quark, that decay after few hundred of µm). The events produced in the proton proton collisions can be very complex and track reconstruction is an entangled pattern recognition problem. Indeed, at the nominal instantaneous luminosity of operation, an average of about 20 pile up events overlapping to the event of interest are expected, leading to about 1000 tracks to be reconstructed every 25 ns. In order to make the pattern recognition easier, two requirements are fundamental:

- a low occupancy detector;
- a large redundancy of the measured points (*hits*) per track.

The first requirement is achieved building a detector with high granularity[2]. The redundancy of the hits is instead achieved having several detecting layers, and is necessary to reduce the ambiguity on the assignment of the hits to a given track. Nevertheless, the amount of tracker material has to be as low as possible, in order to avoid compromising the measurement of the particle trajectory. An excessive amount of material would indeed deteriorate the measurement, mainly because of the increased probability of particle multiple scattering. The outer detectors such as ECAL would be influenced by the material as well, for example because of the increased probability for a photon to convert to an electron-positron pair in the tracker material. For this reasons, the tracker layers are limited in number and thickness.

The tracker comprises a large silicon strip detector with a small silicon pixel detector inside it. In the central η region, the pixel tracker consists of three co-axial barrel layers at radii between 4.4 cm and 10.2 cm and the strip tracker consists of ten co-axial barrel layers extending outwards to a radius of 110 cm. Both sub-detectors are completed by endcaps on either side of the barrel, each consisting of two disks in the pixel tracker, and three small plus nine large disks in the strip tracker. The endcaps extend the acceptance of the tracker

[2]The granularity of a detector is defined as the angular range ($\Delta\eta \times \Delta\phi$) that each individual element is able to resolve.

up to $|\eta| < 2.5$. A three-dimensional schematic view of the tracker is shown in Fig. 2.5, while in Fig. 2.6 a pictorial representation of a slice of the tracker is displayed, showing the various layers of the sub-detectors.

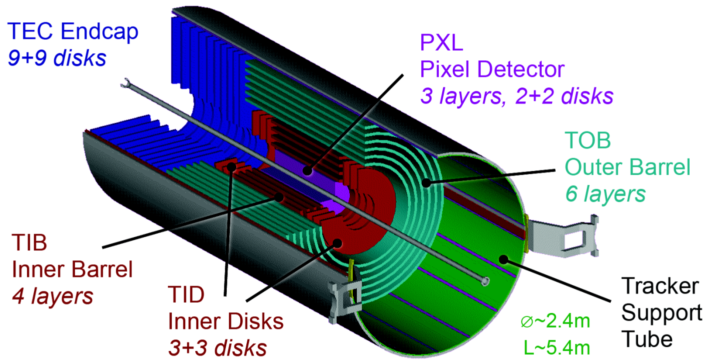

Figure 2.5.: Three-dimensional schematic view of the CMS silicon tracker.

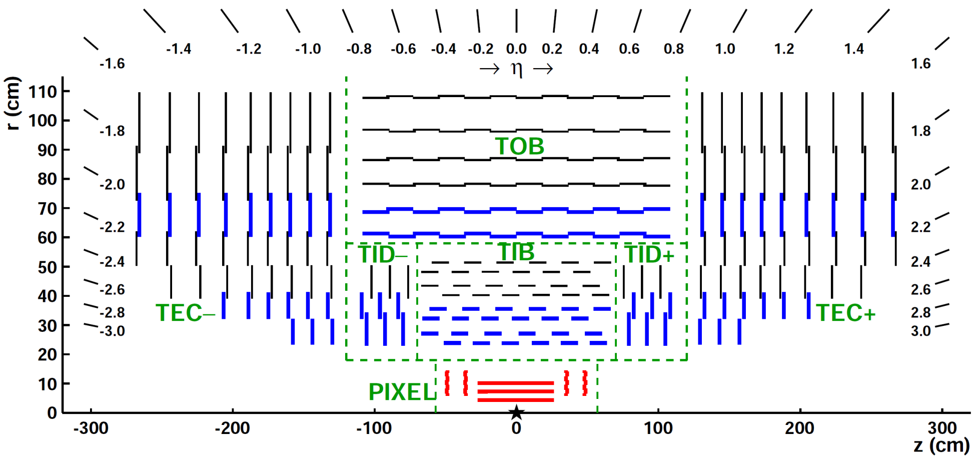

Figure 2.6.: Pictorial view of a tracker slice in the r-z plane. Pixel modules are shown in red, single-sided strip modules are depicted as black thin lines and strip stereo modules are shown as blue thick lines.

The whole tracker has a cylindrical shape with a length of 5.8 m and a diameter of 2.5 m, with the axis aligned to the beams direction. The average number of hits per track is 12-14, in order to have a high reconstruction efficiency and a low rate of fake tracks.

The material budget of the tracker as obtained from a simulation of the detector is shown in Fig. 2.7, reported both in units of radiation length t/X_0 and in units of nuclear interaction length t/λ_I, as a function of η. The region $1 < |\eta| < 2$ exhibits a larger material budget due to the presence of cables and services.

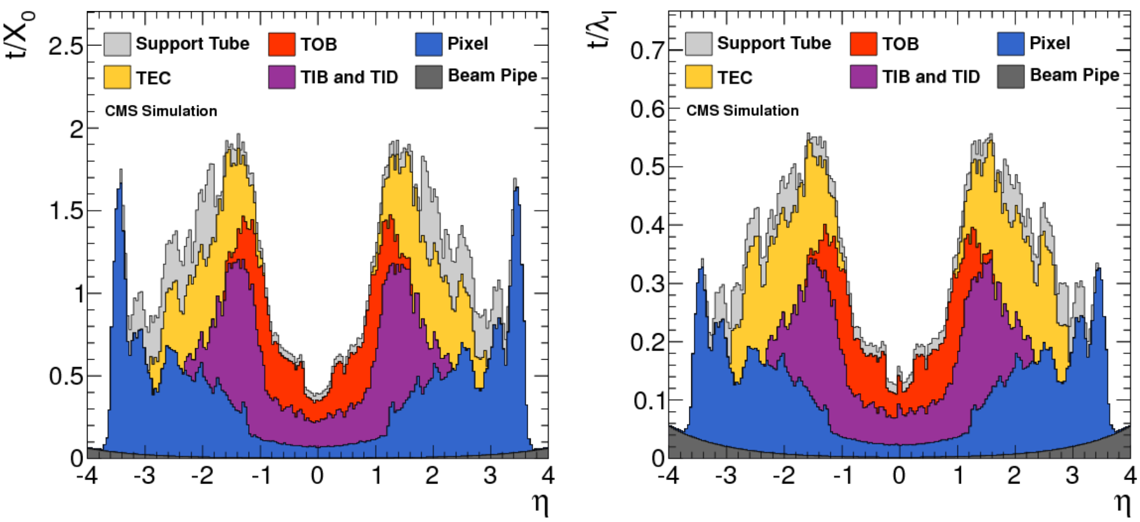

Figure 2.7.: Total thickness t of the tracker material expressed in units of X_0 (left) and λ_I (right), as a function of η. The contribution to the total material budget of each part of the detector is shown.

The pixel detector

The pixel detector, shown in Fig. 2.8, is mainly used as starting point in the CMS track reconstruction and is of fundamental importance for the reconstruction of primary and secondary vertices. The pixel detector is placed in the closest position to the collision point,

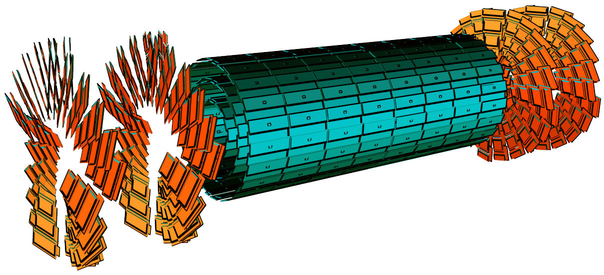

Figure 2.8.: Schematic view of the CMS pixel detector.

where the amount of radiation is larger. It is placed in the region $|\eta| < 2.5$ and consists of three cylindrical layers 53 cm long in the barrel region, located at $r = 4.4$, 7.3 and 10.2 cm, and two pairs of endcap disks with radii between 6 and 15 cm at $z = \pm 34.5$ and ± 46.5 cm, covering a total area of about 1 m^2. The detector is composed of many modules, for a total of 768 in the barrel and 672 in the endcaps. Each endcap is composed of 24 segments, each one tilted with respect to the adjacent ones adnd containing 7 modules. Each module consists of several units which contain a highly segmented silicon sensor with a thickness of 250 µm. In order to achieve an optimal vertex position resolution in both the (r, ϕ) and

z-coordinates, a design with a rectangular pixel shape with an area of $150 \times 100\,\mu\text{m}^2$ was adopted, with the $100\,\mu\text{m}$ size oriented along the (r, ϕ) direction in the barrel region, and along the z-direction in the endcap region. The achievable hit reconstruction resolution is about $10 - -15\,\mu\text{m}$ in the barrel and $15\,\mu\text{m}$ in the endcaps.

The microstrip detector

In this region of the detector the radiation flow is low enough to allow the use of a less segmented device, such as the silicon microstrip detector. The microstrip tracker is composed of 15148 silicon modules, covering a total area of about $193\,\text{m}^2$ with a total of 9.3 million strips. Two types of modules are installed: single sided modules consist of one sensor sticked onto a carbon fiber support together with the readout electronics, with the silicon strips laying along the z direction in the barrel and along the (r, ϕ) direction in the endcaps. The other type of module, referred to as stereo-module, consists of two sensors sticked together back to back and tilted of a relative angle of 100 mrad. This combination allows a three-dimensional measurement of the particle interaction point, providing the information along the z-direction. The whole microstrip tracker is 5.4 m long and extends up to $r = 1.1\,\text{m}$. As the pixel detector, the microstrip detector consists of a barrel and an endcap region and is divided into four distinct parts, as shown in Fig. 2.6. The barrel is made up of the following parts:

- TIB (*Tracker Inner Barrel*): it consists of four cylindrical coaxial layers, covering the region up to $|z| < 65\,\text{cm}$. In this region the detectors have a thickness of $300\,\mu\text{m}$ and the strips are separated by a variable pitch between 80 and $120\,\mu\text{m}$. The first two layers are composed of stereo modules while the other layers have single-sided modules. Since the strips are oriented along the z axis, the position resolution is more precise in the (r, ϕ) direction, about $23 - -34\,\mu\text{m}$, with respect to the z direction, where a resolution of about $230\,\mu\text{m}$ is obtained thanks to the stereo modules.
- TOB (*Tracker Outer Barrel*): it consists of six cylindrical coaxial layers, placed in the region $55\,\text{cm} < r < 65\,\text{cm}$ and $|z| < 110\,\text{cm}$. Stereo modules are mounted on the two inner layers. Since the density of particles passing through this region is lower with respect to the TIB, the pitch between the strips is larger ($120 - -180\,\mu\text{m}$) and the strips are longer (190 mm). The spatial resolution varies in the range $25 - 52\,\mu\text{m}$ in the (r, ϕ) direction, and is about $530\,\mu\text{m}$ in the z coordinate in the stereo modules.

The endcaps are also made up of two parts:

- TID (*Tracker Inner Disk*): it consists of six disks, three per side, placed orthogonally with respect to the beam axis, between the TIB and the TOB. The modules are positioned in a ring shape, with the strips oriented in the radial direction, and they are alternately placed on the internal and on the external side of the disk. The two innermost rings of the TID are equipped with stereo modules. The thickness of the silicon is $300\,\mu\text{m}$.
- TEC (*Tracker EndCap*): each one of the two TEC is made of nine disks which extend to the region $120\,\text{cm} < |z| < 280\,\text{cm}$. Each disk is divided into 8 slices in each of which

a number ranging from 4 to 7 modules are mounted in a ring shape, depending on the position along z. Also in this case the modules are alternately mounted on the internal and on the external side of the disk, with the strips radially oriented. On the two innermost rings and on the fifth one the stereo modules are installed to measure the z coordinate. The thickness of the sensors range between 300 and 500 µm depending on the disk.

The tracker is operated at low temperature in order to reduce those radiation damage induced effects that have a temperature dependence, such as the increase of the leakage current and the long-term increase of the depletion voltage (also called reverse annealing)[3].

The alignment of the tracker modules is very important to obtain a high spatial resolution. Deviations are caused by assembly inaccuracy, deformations due to cooling and stress from the magnetic field. Therefore, three methods are used for the tracker alignment. The geometry was determined during the assembly to an accuracy of 80 to 150 µm. An infrared laser system is used for continuous monitoring of the position of selected tracker modules. The final alignment is done with tracks from well known physics processes, e.g. cosmic muons or muon pairs from the J/Ψ, Υ or Z decays.

2.2.3. The electromagnetic calorimeter (ECAL)

The main function of an electromagnetic calorimeter is to identify electrons and photons and to measure accurately their energy. The CMS electromagnetic calorimeter (ECAL) [15, 16], shown in Fig. 2.9, is a hermetic homogeneous calorimeter with cylindrical geometry, composed of many scintillating crystals of lead tungstate ($PbWO_4$) with a truncated pyramidal shape. As the other detectors it consists of two parts, the ECAL barrel (EB), which contains 61200 crystals, and two endcaps (EE) containing 7324 crystals each one.

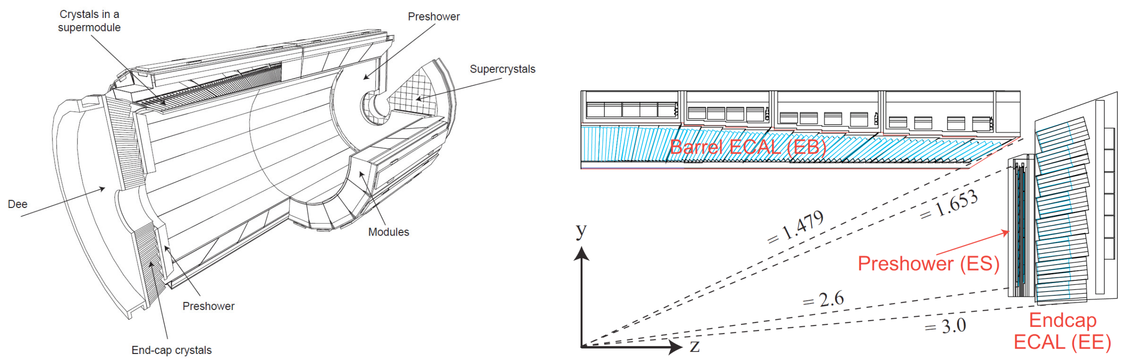

(a) $r - -z$ view of an ECAL sector. (b) ECAL three-dimensional view.

Figure 2.9.: Schematic representation of the CMS electromagnetic calorimeter.

[3]The tracker in Run 1 was operated at a temperature of +4°C, but during the Long Shutdown 1 a new cooling dry gas plant has been installed and the tracker is now operating at the lower temperature of −15°C.

The characteristics of the $PbWO_4$ crystals make them an appropriate choice for operation at LHC. The high density ($\rho = 8.3\,\mathrm{g/cm^3}$), short radiation length ($X_0 = 0.89\,\mathrm{cm}$) and small Molière radius[4] (2.2 cm) allow to build a compact and high granularity calorimeter. Another advantage of this material is the radiation hardness and the fast scintillation decay time ($\tau = 10\,\mathrm{ns}$), that permits to collect about 80% of the produced light within the 25 ns interval between two consecutive bunch crossings. The main drawbacks of this material are the low light yield ($\sim$ 10 photoelectrons/MeV) and the strong dependence on the operating temperature, that makes it necessary to keep the crystals at a stabilized temperature (18°C).

The crystals are grouped into 5×5 matrices called *towers*. The barrel has an inner radius of 129 cm, a length of 630 cm and extends in the region $|\eta| < 1.479$. The crystals in the barrel have the following dimensions: $22 \times 22\,\mathrm{mm}^2$ at the front face, $26 \times 26\,\mathrm{cm}^2$ at the rear face, and a length of 23 cm, corresponding to $25.8X_0$, and are mounted in a quasi-projective geometry, in order to have the long side tilted by 3° with respect to the direction pointing to the interaction point, both in the η and ϕ coordinates. This is done to avoid the empty spaces between adjacent crystals to be aligned with the direction pointing to the interaction point. The granularity of the EB is about 1°. Avalanche photodiodes (APDs) are used as photodetectors connected with the crystals in the barrel region.

Each endcap covers the region $1.479 < |\eta| < 3$ and is formed by two semicircular aluminium halves called *dees*. Crystals in endcaps have a length of 22 cm, a frontal area equal to $28.6 \times 28.6\,\mathrm{mm}^2$ and a rear surface of $30 \times 30\,\mathrm{mm}^2$. In the endcaps the crystals are arranged in a $\eta - -\phi$ simmetry. The photodetectors used to collect the light produced in the endcap crystals are single stage vacuum phototriodes (VPTs), because this region experiences a rather high particle flux and VPTs are more robust against radiation damages with respect to APDs. A preshower system is installed in front of the ECAL endcaps in order to separate the showers produced by a primary γ from those produced by forward emitted π^0. This detector, which covers the region $1.653 < |\eta| < 2.6$, is a sampling calorimeter consisting of two lead disks ($2X_0$ and $1X_0$ thick respectively) that initiate the electromagnetic shower from incoming photons or electrons, with silicon strip sensors after each disk, which measure the deposited energy as well as the shower transverse profile.

The energy resolution of a homogeneous calorimeter can be expressed by the sum in quadrature of three terms, as shown in the following formula:

$$\left(\frac{\sigma_E}{E}\right)^2 = \left(\frac{a}{\sqrt{E}}\right)^2 + \left(\frac{b}{E}\right)^2 + c^2 \tag{2.6}$$

The stochastic term a dominates at low energies: it includes the contribution of statistical fluctuations in the number of generated and collected photoelectrons. This term takes into account the crystal light emission, the light collection efficiency and the photodetector

[4]The Molière radius R_M characterizes the transverse development of an electromagnetic shower in a calorimeter. On average 90% of the energy deposited by a shower is contained inside a cylinder with radius R_M.

quantum efficiency[5]. The noise term b includes the contributions of pile up events and electronic noise, both due to the photodetector and preamplifier. These contributions depend on η and on the LHC operational luminosity. The constant term c, dominant at high energies, takes into account several contributions. The most relevant are the non-uniformity of the longitudinal light collection, the intercalibration errors and the leakage of energy from the rear side of the crystal. The ECAL barrel resolution for electrons was measured using test beams to be:

$$\left(\frac{\sigma_E}{E}\right)^2 = \left(\frac{2.8\%\,\mathrm{GeV}^{1/2}}{\sqrt{E}}\right)^2 + \left(\frac{12\%\,\mathrm{GeV}^{1/2}}{E}\right)^2 + (0.3\%)^2 \quad , \tag{2.7}$$

where E is the energy measured in GeV.

2.2.4. The hadron calorimeter (HCAL)

The hadron calorimeter (HCAL) [17] is used together with ECAL to make a complete calorimetric system for the jet energy and direction measurement. Moreover, thanks to its hermetic structure, it can measure the energy imbalance in the transverse plane, $E_{\mathrm{T}}^{\mathrm{miss}}$, a typical signature of non interacting particles, such as neutrinos. The HCAL is a sampling calorimeter covering the region $|\eta| < 5$. As shown in Fig. 2.10, it is divided in four sub-detectors: HB (*Barrel Hadronic Calorimeter*), located in the barrel region inside the solenoid, extending up to $|\eta| < 1.4$; HE (*Endcap Hadronic Calorimeter*), placed in the endcaps region inside the magnet, covering the region $1.3 < |\eta| < 3$ and partially overlapping with the HB coverage; HO (*Outer Hadronic Calorimeter*), also known as *tail-catcher*, placed along the inner wall of the magnetic field return yoke, just outside of the magnet; HF (*Forward Hadronic Calorimeter*), a sampling calorimeter consisting of quartz fibers sandwiched between iron absorbers, consisting of two units placed in the very forward region ($3 < |\eta| < 5$) outside the magnetic coil. The quartz fibers emit Cherenkov light with the passage of charged particles and this light is detected by radiation resistant photomultipliers. In order to maximize particle containment for a precise missing transverse energy measurement, the amount of absorber material was maximized, reducing therefore the amount of the active material. Since HCAL is mostly placed inside the magnetic coil, a non-magnetic material like brass was chosen as absorber. HB and HE are therefore made with 5 cm brass absorber layers interleaved with 3.7 mm plastic scintillators. The scintillation light is collected by wavelength shifting (WLS) fibres and read out by hybrid photodiodes (HPD). The granularity of the calorimeter is $\Delta\eta \times \Delta\phi = 0.087 \times 0.087$ for $|\eta| < 1.6$ and $\Delta\eta \times \Delta\phi \approx 0.17 \times 0.17$ for $|\eta| \geq 1.6$. HO is made of 5 rings installed in the wheel that compose the return yoke and is divided in 12 sectors, each one covering a 30° angle in ϕ. It consists of scintillating layers, with the same granularity as HB, and the solenoid coil is used as an additional absorber to increase the effective depth of the

[5]The quantum efficiency is the ratio between the number of collected electron-hole pairs (or photoelectrons) and the number of photons incident on the photodetector.

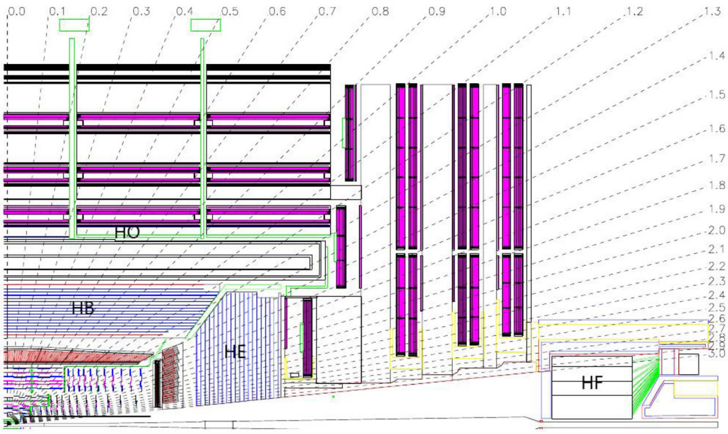

Figure 2.10.: Longitudinal view of the CMS detector showing the HCAL sub-detectors.

calorimeter in the barrel region, which is extended up to 11.8 λ_I, thus improving the energy resolution.

The energy resolution in the different regions of HCAL can be parametrized using a stochastic and a constant term, as follows:

$$
\begin{aligned}
\left(\frac{\sigma_E}{E}\right)^2 &= \left(\frac{90\%\mathrm{GeV}^{1/2}}{\sqrt{E}}\right)^2 + (4.5\%)^2 \qquad \text{in the barrel/endcap} \quad , \\
\left(\frac{\sigma_E}{E}\right)^2 &= \left(\frac{172\%\mathrm{GeV}^{1/2}}{\sqrt{E}}\right)^2 + (9\%)^2 \qquad \text{in the HF} \quad ,
\end{aligned}
\tag{2.8}
$$

where E is expressed in GeV.

2.2.5. The muon system

The CMS muon system [18] is dedicated to the identification and measure of high p_T muons, in combination with the tracker. The system is placed outside the magnetic coil, embedded in the return yoke, to fully exploit the 1.8 T return flux. As shown in Fig. 2.11, the system consists of three types of independent gaseous particle detectors:

- *Drift Tubes* (DT) are placed in the barrel region, where the occupancy is relatively low ($< 10\,\mathrm{Hz/m^2}$);
- *Cathode Strip Chambers* (CSC) are installed in the endcaps, where the occupancy is higher ($> 100\,\mathrm{Hz/m^2}$);
- *Resistive Plate Chambers* (RPC) are placed both in the barrel and endcaps.

The DT system is placed in the region of the barrel with $|\eta| < 1.2$, where the magnetic field is sufficiently weak and homogeneous. Along the longitudinal direction, the barrel

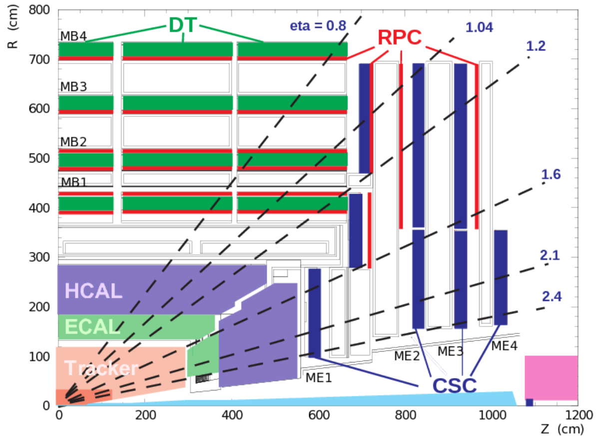

Figure 2.11.: Schematic view of a quadrant of the CMS muon system.

region is divided in 5 wheels, which are subdivided in 12 sectors covering a 30° azimuthal angle each. The wheels are composed of 4 concentric rings of chambers, called *stations*, interspersed in the layers of the iron return yoke, and each one formed by 12 DT chambers. The basic element of the DT system is a rectangular drift tube cell with a transverse size of $13 \times 42\,\mathrm{mm}^2$ and a variable length from 2 to 4 m. The chambers are filled with a gas mixture of Ar (85%) and CO_2 (15%) and are grouped in the radial direction to form detection layers. Groups of four layers form a *superlayer*. In each superlayer two chambers have anode wires parallel to the beam axis and two have perpendicular wires, thus providing two measurements of the (r, ϕ) coordinate and two measurements of the z coordinate of the track hit positions. As shown in Fig. 2.12, each chamber is made of a stainless steel anode

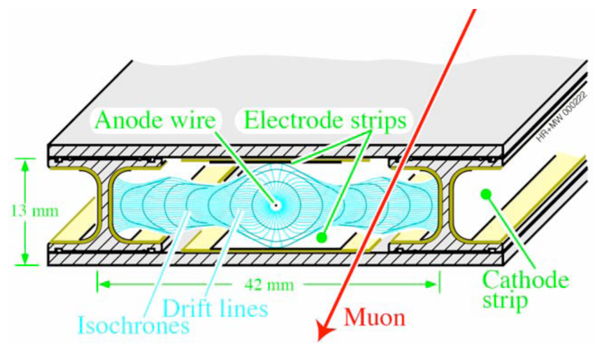

Figure 2.12.: Schematic representation of a drift tube chamber, showing the drift lines in presence of magnetic field.

wire between two parallel aluminium plates with “I” shaped spacer cathodes, isolated from the aluminium plates with polycarbonate plastic, and the hit resolution is about 100 µm in both (r, ϕ) and (r, z) directions.

In the endcaps, the high and non-uniform magnetic field and the particle rate do not allow to use drift tubes detectors to perform measurements. Therefore, a solution based on the CSC detector has been adopted. CSC are multi-wire proportional chambers with the cathodes segmented into strips oriented radially and transversely with respect to the anode wires (see Fig. 2.13), allowing a simultaneous measurement of two coordinates (r through the wires and ϕ using the strips). The CSC chambers are filled with a gas mixture of Ar (40%), CO_2 (50%) and CF_4 (10%) and provide a spatial resolution of about 80–85 µm. The drift path of the charge carriers is shorter with respect to the drift tubes, therefore these detectors can be placed in regions with higher flows of charged particles and less homogeneous magnetic fields. The CSC coverage is $0.8 < |\eta| < 2.4$.

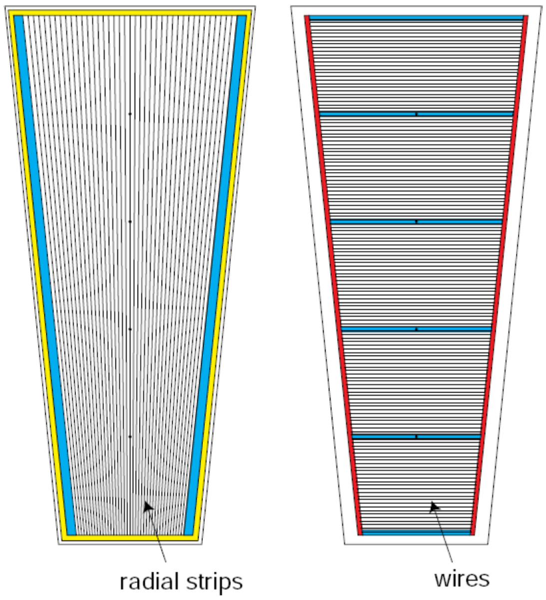

Figure 2.13.: Schematic representation of CSC cathode (left) and anode (right) panels.

RPCs are used both in barrel and endcaps, complementing DT and CSC systems, in order to ensure robustness and redundancy to the muon spectrometer. RPCs are gaseous detectors characterized by a coarse spatial resolution, but are able to perform precise time measurements, comparable with the ones provided by scintillators. These chambers are made of 4 bakelite planes, with a bulk resistivity of 10^{10}–10^{11} Ωcm. The 2 mm gap between the plates is filled with a mixture of $C_2H_2F_4$ (94.5%) and Isobutane. The central part of the chamber is equipped with insulated aluminum strips, used to collect the signal generated by crossing particles. In the barrel the strips are rectangularly segmented and run along the beam axis, whereas the endcaps are equipped with trapezoidal shaped strips. The detector operates in avalanche mode, and covers the region $|\eta| < 2.1$.

2.3. The CMS trigger system

The LHC can provide proton-proton interactions at a crossing frequency of 40 MHz and, for each bunch crossing, several collisions can occur (approximately 20 at the nominal instantaneous luminosity). Since it is impossible to store and process the large amount of data associated with the resulting large number of events, a drastic rate reduction has to be achieved. In fact the speed at which data can be written to mass storage is limited and, moreover, the vast majority of events produced is not interesting for physics analyses, because it involves low transverse momentum interactions (also called *minimum bias events*). The task of reducing this rate is accomplished by the CMS trigger system, which is the start of the physics event selection. CMS makes use of a two-stage trigger system, consisting of a *Level-1* trigger (L1) [19] and a *High Level Trigger* (HLT) [20].

Level-1 trigger runs on dedicated processors, and accesses coarse level granularity information from calorimetry and muon system. A L1 Trigger decision has to be taken for each bunch crossing within 3.2 μs. Its task is to reduce the data flow from 40 MHz to about 100 kHz.

The High Level Trigger is responsible for reducing the L1 output rate down to a maximum rate of the order of 1 kHz. The HLT code runs on a farm of commercial processors and can access the full granularity information of all the sub-detectors.

The main characteristics of the CMS trigger system are described in the following.

2.3.1. The Level-1 trigger

The L1 trigger is responsible for the identification of electrons, muons, photons, jets and missing transverse energy. It is required to have a high and carefully understood efficiency. Its output rate and speed are limited by the readout electronics and by the performances of the data acquisition (DAQ) system [20]. It consists of three main subsystems:

- L1 Calorimeter Trigger;
- L1 Muon Trigger;
- L1 Global Trigger.

The L1 Global Trigger is responsible for combining the output of L1 Calorimeter Trigger and L1 Muon Trigger and for making the decision to either retain the event or discard it. The organization of CMS L1 Trigger is schematically summarized in Fig. 2.14.

L1 Calorimeter Trigger

Controllare se stato cambiato qualcosa nel Run2

The input for the L1 Calorimeter Trigger are calorimeter towers, which are clusters of signals collected both from ECAL and HCAL. Towers are calculated by calorimeter high level readout circuits, called Trigger Primitive Generators. The Regional Calorimeter Trigger identifies electron, photon, τ and jet candidates together with their transverse energy and sends the information to the Global Calorimeter Trigger. The Global Calorimeter

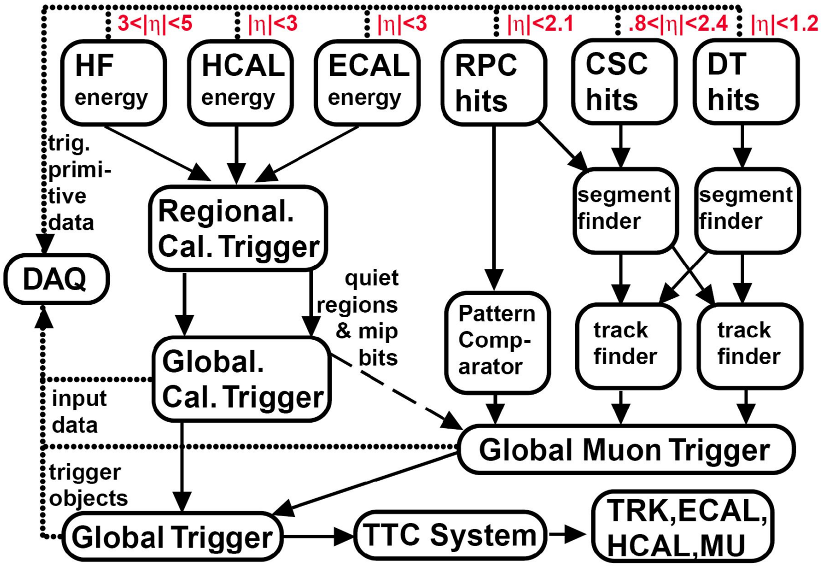

Figure 2.14.: Schematic representation of the Level-1 trigger components.

Trigger sorts the candidates according to their transverse energy and sends the first four objects to the L1 Global Trigger.

L1 Muon Trigger

Controllare se stato cambiato qualcosa nel Run2

The L1 Muon Trigger is actually a composite system istelf: information from RPC, CSC and DT specific triggers are combined in the so called L1 Global Muon Trigger.

The RPC trigger electronics builds Track Segments, gives an estimate of their p_{T} and sends these segments to the Global Muon Trigger. It also provides the CSC logic unit with information to solve hit position ambiguities in case of two or more muon tracks crossing the same CSC chamber.

The CSC trigger builds Local Charged Tracks (LCT), that is track segments made out of the cathode strips only, and assign a p_{T} value and a quality falg to the LCTs. The best three LCTs in each sector of nine CSC chambers are passed to the CSC Track Finder, that uses the full CSC information to build tracks, assigns them a p_{T} and a quality flag and sends them to the Global Muon Trigger.

DTs are equipped with Track Identifier electronics, which is able to find groups of aligned hits in the four chambers of a superlayer. Those Track Segments are sent to the DT Track Correlator that tries to combine segments from two superlayers, measuring the ϕ angle. The best two segments are sent to the DT Track Finder that builds tracks and sends them to the Global Muon Trigger.

The Global Muon Trigger sorts the RPC, CSC and DT muon tracks and tries to combine them. The final set of muons is sorted according to the quality, and the best four tracks are passed to the L1 Global Trigger.

L1 Global Trigger

Controllare se stato cambiato qualcosa nel Run2

The L1 Global Trigger is responsible for collecting objects created from the Calorimeter and Muon Triggers and for making a decision whether to retain the event or not. In case the event is accepted, the decision is sent to the Timing Trigger and Control System, that commands the readout of the remaining subsystems.

In order to take the decision, the L1 Global Trigger sorts the ranked objects produced by calorimetry and muon system and checks if at least one of the thresholds in the L1 trigger table is passed.

2.3.2. The high level trigger (HLT)

The High Level Trigger is designed to reduce the L1 output rate down to about 1000 events/s, which is the amount that will be written to mass storage. HLT code runs on commercial processors and performs reconstruction using the information from all sub-detectors. Events passing the HLT are stored on local disk or in CMS Tier 0[6].

Data read from sub-detectors are assembled by a builder unit and then assigned to a switching network that dispatches events to the processor farm. The CMS switching network has a bandwidth of 1 Tbit/s. This simple design ensures maximum flexibility to the system, the only limitation being the total bandwidth and the number of processors. The system can be easily upgraded adding new processors or replacing the existing ones with faster ones as they become available. Since the algorithms have a fully software implementation, improvements to the algorithms can be easily implemented and do not require any hardware intervention.

Event by event, the HLT code is run on a single processor, and the time available to make a decision is about 300 ms. The real time nature of this selection imposes several constraints on the resources an algorithm can use. The reliability of HLT algorithms is of capital importance, because events not selected by the HLT are lost. In order to efficiently process events, the HLT code has to be able to quickly reject not interesting events; computationally expensive algorithms must be run only on good candidates for interesting events. In order to cope with this requirement the HLT code is organized in a virtually layered structure:

[6]The Worldwide LHC Computing Grid (WLCG) is composed of four levels, or "Tiers", identified with numbers 0, 1, 2 and 3. Each Tier is made up of several computer centres and provides a specific set of services; they process, store and analyse all the data from the Large Hadron Collider (LHC). Tier 0 is the CERN Data Centre. All of the data from the LHC pass through this central hub. Tier 0 distributes the raw data and the reconstructed output to Tier 1's, and reprocesses data when the LHC is not running.

- Level 2: uses only complete muon and calorimetry information;
- Level 2.5: uses also the pixel information;
- Level 3: makes use of the full information from all the tracking detectors.

Each step reduces the number of events to be processed in the following step. The most computationally expensive tasks are executed in the Level 3; time consuming algorithms such as track reconstruction are only executed in the region of interest. Besides, since the ultimate precision is not required at a HLT level, track reconstruction is performed on a limited set of hits, and is stopped once the required resolution is achieved.

Chapter 3.

Reconstruction and identification of physics objetcs

In CMS, the physics object reconstruction and identification is based on standard algorithms developed by the collaboration and used by all the physics analyses. In this section, the techniques used for the reconstruction and identification of the physics objects of interest for $\mathrm{H} \to \mathrm{WW} \to 2\ell 2\nu$ analyses are described.

3.1. The Particle Flow technique

The Particle Flow (PF) event reconstruction technique [21] aims at the reconstruction and identification of all the stable particles in the event, i.e. electrons, muons, photons, charged and neutral hadrons, with a thorough combination of the information from all CMS sub-detectors, in order to determine their energy, direction and type. These individual particles are then used, for example, to build jets, to measure the missing transverse energy $E_{\mathrm{T}}^{\mathrm{miss}}$, to reconstruct the τ from their decay products, to quantify the charged lepton isolation and to tag b-jets.

The CMS detector is well suited for this purpose. Indeed, the presence of a large internal silicon tracker immersed in an intense solenoidal magnetic field allows the reconstruction of charged particles with high efficiency and small fake rate, and provides a high precision measurement of the particle p_{T} down to about 150 MeV, for $|\eta| \leq 2.6$. The high granularity of the ECAL calorimeter is the additional key element for the feasibility of the PF technique, allowing the reconstruction of photons and electrons with high energy resolution.

The first step of the PF technique consists in the reconstruction of the basic elements from the various sub-detectors, such as charged-particle tracks, calorimeter clusters and muon tracks. These elements, which are provided by the sub-detectors with high efficiency an low fake rate, are then connected together with a link algorithm.

The good performance of the tracking system are achieved by means of an iterative tracking strategy [22], based on the Kalman Filter algorithm [23]. The basic idea of iterative tracking is that initial iterations search for tracks that are easiest to find, e.g. high p_{T} tracks produced near the interaction region. After each iteration, hits associated to reconstructed tracks are removed from the hit collection, thereby reducing the combinatorial complexity and simplifying the subsequent iterations, which aim at finding more complicated set of tracks, e.g. low p_T or displaced tracks. The *Iteration 0*, where the majority of tracks are reconstructed, is designed to identify prompt tracks with $p_T > 0.8$ GeV that have three hits in the three layers of the pixel detector. *Iteration 1* is used to recover prompt tracks that have only two pixel hits. *Iteration 2* aims at finding low-p_T prompt tracks while *Iterations 3–5* are intended to find tracks that originate outside the collision point, i.e. tracks produced by a secondary vertex, and to recover undetected tracks in the previous iterations. Each iteration proceeds according to four steps:

- *seeding*: initial track candidates are obtained using 2 or 3 hits in the innermost layers (these proto-tracks are called seeds);
- *pattern recognition*: this step is based on Kalman Filter and searches for hits in the outer layers that could be associated to the initial track candidate, reconstructing the particle trajectory;
- *track fitting*: in this step a fit of the trajectory is performed, using its associated hits and providing an estimate of the track parameters (p_T, η, ϕ, charge, etc.);
- *selection*: finally tracks are selected based on quality requirements.

The high detection efficiency of the calorimeters is based on a specific calorimeter clustering algorithm, which is performed separately in each sub-detector. The algorithm is based on three steps: in the first step, "cluster seeds" are identified as local calorimeter cells with an energy deposit above a given threshold. Then, "topological clusters" are grown from the seeds by gathering cells with at least one side in common with a cell already in the cluster, and with an energy above a given threshold. A topological cluster usually gives rise to many "particle flow clusters" as seeds, which are identified sharing the energy of each cell among the particle flow clusters, thereby allowing the determination of the particle flow cluster energy and position.

These elements are then connected to each other using a link algorithm, which identifies blocks of elements that are topologically compatible. For example, a charged-particle track is linked to a calorimeter particle flow cluster if the extrapolated position from the track to the calorimeter is compatible with the cluster boundaries. From these blocks, PF candidates are identified according to the following order:

- Muons: a *global muon* gives rise to a *PF muon* if its combined p_T measurement is compatible within 3 standard deviation with the one provided by the sole tracker. The corresponding track is removed from the block;
- Electrons: electrons tend to give rise to short tracks, and to lose energy by Bremsstrahlung in the tracker layers on their way to the calorimeter. The link between a charged-particle track (refitted with the Gaussian-Sum Filter (GSF) [24]) and one or more ECAL clusters identifies a *PF electron*. After the identification, the corresponding tracks and clusters are removed from the block.
- Charged hadrons: the remaining tracks give rise to *PF charged hadrons*. Tracks can be linked to ECAL and HCAL clusters, and the energy is determined taking into account information from calorimeters;

- Photons and neutral hadrons: ECAL clusters not linked with tracks give rise to *PF photons*, while the remaining HCAL clusters are identified as *PF neutral hadrons*.

After the identification of all PF candidates in the event, *PF jets* are clustered as described in Sec. **??**. The last step is the reconstruction of the *PF* $\vec{p}_{\mathrm{T}}^{\mathrm{miss}}$, which is described in Sec. 3.5. The missing transverse energy, $E_{\mathrm{T}}^{\mathrm{miss}}$, is defined as the modulus of $\vec{p}_{\mathrm{T}}^{\mathrm{miss}}$.

3.2. Leptons reconstruction and identification

3.2.1. Muon reconstruction and identification

Muons produced at the collision point can go through the entire detector with a negligible energy loss, thus reaching the detector outermost part where the muon chambers are installed (see Sec. 2.2.5). Muons interact through ionization with the layers of the silicon tracker, which is able to reconstruct their tracks (*tracker track*). The muon tracks are also reconstructed using the muon system (*standalone muon track*). Based on these objects, two reconstruction approaches are used [25]: in the first method (outside-in), for each standalone muon tracks a tracker track is searched for by extrapolating the two tracks to a common surface. If a match is found, the hits associated to the two tracks are fitted together giving rise to a *Global Muon*. The second approach (inside-out) consists in considering all tracker tracks with $p_{\mathrm{T}} > 0.5$ GeV as potential muon candidates and are extrapolated to the muon system taking into account the magnetic field, the expected energy losses and the multiple scattering in the detector material. If at least one muon segment (a short track stub made of DT or CSC hits) matches the extrapolated tracks, the corresponding tracker track is identified as a *Tracker Muon*.

The matching with the muon system improves significantly the muon p_{T} resolution that can be obtained from the tracker only, especially in the region with $p_{\mathrm{T}} > 200\,\mathrm{GeV}$, as shown in Fig. 3.1.

Depending on the physics analysis, different muon definitions can be used by changing the selection on the muon identification variables, hence balancing between the muon identification efficiency and purity. The most widely used definition in physics analyses is the so-called *Tight muon selection*[1]. This selection requires the muon candidate to be reconstructed as a Global Muon and identified by the PF algorithm. The fit of the global track, which is required to include muon segments in at least two muon stations (this implies that the muon is also reconstructed as a Tracker Muon), must have a $\chi^2/d.o.f.$ less than 10 and use more than 10 inner tracker hits. The transverse impact parameter with respect to the primary vertex is required to be $|d_{xy}| < 2\,\mathrm{mm}$, significantly reducing the rate of muons from decays in flight, i.e. non prompt muons. The requirements defining the Tight Muon identification are summarized in Table 3.1.

Another selection which is optimised for low-p_{T} muons coming from in flight decays is called *Soft Muon selection*. This selection requires the muon to be reconstructed as a Tracker

[1]Small variations with respect to this baseline definition are adopted by the specific analyses.

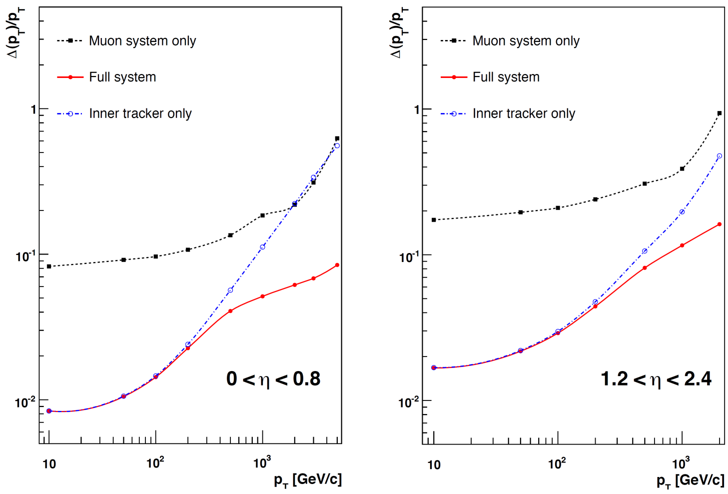

Figure 3.1.: Muon p_{T} resolution as a function of the muon p_{T} in the barrel (left) and in the endcap (right) regions. The resolution is provided for the measurement using the tracking system or the muon system only, as well as for the combination of the two methods.

Table 3.1.: Summary of the muon identification variables and the corresponding selections commonly used by physics analyses.

Observable	Cut
Is Global Muon	true
Is PF muon	true
Tracker layers with valid hits	> 5
Number of valid pixel hits	> 0
Number of valid muon hits	> 0
Number of matched muon stations	> 1
$\chi^2/d.o.f.$	< 10
$d_{xy}(PV)$	$< 0.2\,\mathrm{cm}$
$d_z(PV)$	$< 0.5\,\mathrm{cm}$

Muon with loose additional cuts on the transverse and longitudinal impact parameters. This selection is commonly used to identify muons coming from B hadron decays.

3.2.2. Muon isolation

One of the most powerful requirements to select prompt muons, as the ones produced from W or Z boson decays, and to reject muons produced by decays in flight, is the isolation.

Indeed, prompt muons are expected to be isolated in the event, differently to non prompt muons that are generally produced within jets and characterized by many nearby particles.

Muons commonly used to reconstruct the W or Z decays are thus required to pass an isolation requirement, which includes a pile up mitigation correction called "$\Delta\beta$ correction". This correction is needed to obtain a robust isolation definition that is less sensitive to the pile up contribution. Indeed, simultaneous interactions manifest themselves as a mean energy deposited over all the detector acceptance, which is not due to the particles produced in the primary events, thus spoiling the isolation measurement. The relative isolation variable, usually called *PF relative isolation*, is defined as follows:

$$I^{rel}_{\Delta\beta} = \left[\sum_{ChH} p_{\mathrm{T}} + max\left(0, \sum_{NH} p_{\mathrm{T}} + \sum_{Ph} p_{\mathrm{T}} - 0.5 \sum_{ChHPU} p_{\mathrm{T}}\right)\right] / p_{\mathrm{T}}^{\mathrm{muon}} \quad . \tag{3.1}$$

The sums in Eq. (3.1) are performed in a cone of radius $\Delta R < 0.4$ around the muon direction. The ChH subscript refers to charged hadrons, NH to neutral hadrons, Ph to photons and $ChHPU$ to charged hadrons not arising from the primary vertex.

The cut applied on the isolation variable is analysis dependent, but a common value is $I^{rel}_{\Delta\beta} < 0.15$.

A different isolation definition is called *Tracker relative isolation*, I^{rel}_{trk}, which is calculated as the scalar sum of all the p_{T} of the tracker tracks reconstructed inside a cone of radius $\Delta R < 0.3$ centred on the muon track direction.

3.2.3. Muon momentum scale and resolution

The measurement of the muon p_{T} is sensitive to the alignment of the tracker and the muon chambers, to the material composition and distribution inside the detector and to the knowledge of the magnetic field produced by the solenoid. The imperfect knowledge of the magnetic field and the effect of the material distribution introduce a relative bias in the muon p_{T} that is generally independent on the p_{T} itself, while the effect of the alignment is known to produce a bias that increases linearly with the p_{T}.

Different methods are used to estimate the muon p_{T} scale and resolution effects and to determine the corresponding uncertainties, depending on the p_{T} range. At low and intermediate p_{T} ($<$ 100 GeV), the di-muon events arising from the J/Ψ and Z resonance decays are used to correct the p_{T} scale and to measure the p_{T} resolution. In the high p_{T} regime, the muon p_{T} scale and resolution are instead measured using cosmic ray muons. One of the methods that is commonly used in the intermediate p_{T} range is the *MuScleFit* (Muon momentum Scale calibration Fit), which provides the muon p_{T} scale corrections by fitting the Z boson mass peak in data and simulation. These corrections are meant to recover the bias of the Z mass peak with respect to the η and ϕ coordinates of the muon. After applying these corrections, the relative p_{T} resolution, $\sigma(p_{\mathrm{T}})/p_{\mathrm{T}}$, is measured as a function of η and ϕ and is found to be on average of the order of 2% in the barrel and up to 6% in the endcaps, for muon p_{T} below 100 GeV.

3.2.4. Electron reconstruction and identification

The electron reconstruction is based on the combination of tracker and ECAL information. The reconstruction technique starts by measuring the energy deposits in ECAL by electrons, which form a “supercluster”. A supercluster is a group of one or more ECAL clusters associated using an algorithm that takes into account the characteristic shape of the energy deposited by electrons emitting Bremsstrahlung radiation in the tracker material. The supercluster shape is characterized by a narrow width profile in the η coordinate spread over the ϕ direction. The superclusters are matched to tracks, reconstructed in the tracker with the GSF algorithm, in order to obtain an electron candidate. An additional reconstruction method, described in details in Refs. [26, 27], is instead seeded by electron tracks reconstructed in the inner tracker layers.

Several strategies are used in CMS to identify prompt isolated electrons (characteristic of the signal processes of interest), and to separate them from background sources, mainly originating from photon conversions, jets misidentified as electrons, or electrons from semileptonic decays of b and c quarks. In order to achieve a good discrimination, several identification variables are used:

- $\Delta\eta_{\mathrm{trk,SC}}$ and $\Delta\phi_{\mathrm{trk,SC}}$: the variables measuring the spatial matching between the track and the supercluster in the η and ϕ coordinates, respectively;
- $\sigma_{i\eta,i\eta}$: a variable related to the calorimeter shower shape, measuring the width of the ECAL supercluster along the η direction computed for all the crystals in the 5×5 block of crystals centred on the highest energy crystal of the seed supercluster;
- H/E: the ratio between the energy deposited in the HCAL tower behind the ECAL seed and the supercluster seed energy;
- $|1/E - 1/p|$: the difference of the inverse of energy E measured in ECAL and the inverse of momentum p measured in the tracker;
- the number of missing hits in the back-propagation of the track to the interaction point;
- d_{xy} and d_z: the transverse and longitudinal impact parameters with respect to the primary vertex.
- a photon conversion veto ($\gamma \to \mathrm{e}^+\mathrm{e}^-$) based on the primary vertex measurement.

Different working points are provided by CMS corresponding to different selections on the previously defined variables. One of the common working points used by several physics analyses, as the $\mathrm{H} \to \mathrm{WW}$ analyses described in Secs.4, 5 and 6, is the “tight working point”, summarised in Table 3.2.

3.2.5. Electron isolation

Selected electrons are required to pass an isolation requirement that includes a pile up mitigation correction based on the electron effective catchment area, which is different in different η ranges. The isolation variable is given by the following formula:

Table 3.2.: Electron identification selections corresponding to the tight working point.

Variable	Selection	
	$\lvert\eta_{\mathrm{SC}}\rvert \leq 1.479$	$1.479 < \lvert\eta_{\mathrm{SC}}\rvert \leq 2.5$
$\sigma_{i\eta,i\eta}$	0.01	0.028
$\lvert\Delta\eta_{\mathrm{trk,SC}}\rvert$	0.009	0.007
$\lvert\Delta\phi_{\mathrm{trk,SC}}\rvert$	0.03	0.09
H/E	0.06	0.06
$\lvert 1/E - 1/p\rvert$	0.012	0.010
$\lvert d_{xy}\rvert$	0.011 cm	0.035 cm
$\lvert d_z\rvert$	0.047 cm	0.42 cm
missing inner hits	≤ 2	≤ 1
conversion veto	yes	yes

$$I^{rel}_{EA\ corrected} = \left[\sum_{ChH} p_{\mathrm{T}} + max\left(0, \sum_{Ph} p_{\mathrm{T}} + \sum_{NH} p_{\mathrm{T}} - \rho EA\right)\right] / p_{\mathrm{T}}^{\mathrm{electron}} \tag{3.2}$$

where ChH refers to charged hadrons, Ph to photons, NH to neutral hadrons, ρ is the energy density due to pile up events, E is the energy and A is an effective area. The sums are performed inside a cone of radius $\Delta R < 0.4$ around the electron direction. The cut applied on this variable for the tight working point is $I^{rel}_{EA\ corrected} < 0.04$.

3.2.6. Electron momentum scale and resolution

The electron momentum is estimated using a combination of the tracker and ECAL measurements. Before making the combination of the two measurements, the ECAL energy response is calibrated. Before doing the clustering, the energy response in individual crystals is calibrated and a correction factor is applied to take into account effects as energy leakage or changes in the crystal transparency induced by radiation [2]. Then the supercluster energy is also corrected using an MVA technique, selecting $Z \rightarrow e^+e^-$ events in data and comparing to simulation. A detailed description of the techniques used to estimate the electron scale and resolution and the associated uncertainties is given in Ref. [27].

[2] The continuous monitoring of the crystals transparency is achieved by a laser-monitoring system.

3.2.7. Lepton identification and isolation efficiency

The efficiency related to the identification and isolation selections applied to muons and electrons are generally estimated both in data and simulation and the simulated events are corrected for the observed differences by means of a scale factor (SF), defined as the ratio of the efficiency measured in data and simulation, i.e. $SF = \varepsilon_{\text{data}}/\varepsilon_{\text{MC}}$.

The identification and isolation efficiencies are measured using a Tag and Probe technique. The Tag and Probe technique is a method to estimate the efficiency of a selection on data. In can be applied whenever one has two objects in one event, by using one of the two, the *tag*, to identify the process of interest, and using the second, the *probe*, to actually measure the efficiency of the selection being studied. Concerning the electron and muon case, the Tag and Probe method uses a known mass resonance (e.g. J/Ψ, Z) to select particles of the desired type, and probe the efficiency of a particular selection criterion on these particles. In general the *tag* is an object that passes a set of very tight selection criteria designed to isolate the required particle type. Tags are often referred to as a "golden" electrons or muons and the fake rate for passing tag selection criteria should be very small. A generic set of the desired particle type (i.e. with potentially very loose selection criteria) known as *probe* is selected by pairing these objects with tags such that the invariant mass of the combination is consistent with the mass of the resonance. Combinatoric backgrounds may be eliminated through any of a variety of background subtraction methods such as fitting, or sideband subtraction. The definition of the probe objects depend on the specifics of the selection criterion being examined. The simple expression to get the efficiency ε as a function of p_{T} and η is given below:

$$\varepsilon(p_{\text{T}}, \eta) = \frac{N^{\text{probe}}_{\text{pass}}}{N^{\text{probe}}_{\text{pass}} + N^{\text{probe}}_{\text{fail}}} \tag{3.3}$$

For the estimation of the electron or muon identification efficiency, the tag is chosen to be a well identified and isolated electron or muon, while the probe is chosen as an electron identified with loose selections. The invariant mass of the tag-probe pair is required to be within a Z boson mass window (the effect of changing the Z mass window is included as a systematic uncertainty). After that, the probe is required to pass the identification selections discussed before for electrons and muons, and the efficiency is computed both in data and simulation. A scale factor is then calculated by taking the ratio of the two efficiencies and applied to reweight simulated events.

There are two methods to measure the efficiencies: the counting method consists in simply computing the ratio of probe events that pass the selections and total number of probe events, as shown in Eq. (3.3). This method can be used when the tag requirement selects a very pure set of events, with a small background contribution. The other approach is the fitting method, which is used when the background contamination is not negligible. In this latter case, which represents the commonly used method for estimating the lepton identification and isolation efficiencies, the invariant mass distribution of the tag-probe pair for signal and background is fitted choosing proper functions. The signal plus background fit is performed simultaneously in two categories, corresponding to events in which the probe lepton pass or fail the identification requirements, and separately in bins of η and p_T.

A similar approach is used to estimate the lepton isolation efficiency, requiring the probe lepton to pass the isolation requirements instead of the identification ones and calculating the corresponding scale factor.

The identification and isolation efficiency and the scale factor are shown in Fig. 3.2 corresponding to the selections described in Sec. 3.2.4, for events of interest for a typical physics analysis of the $\mathrm{H} \to \mathrm{WW} \to 2\ell 2\nu$ channel (in particular the analyses described in Sec. 5 and 6).

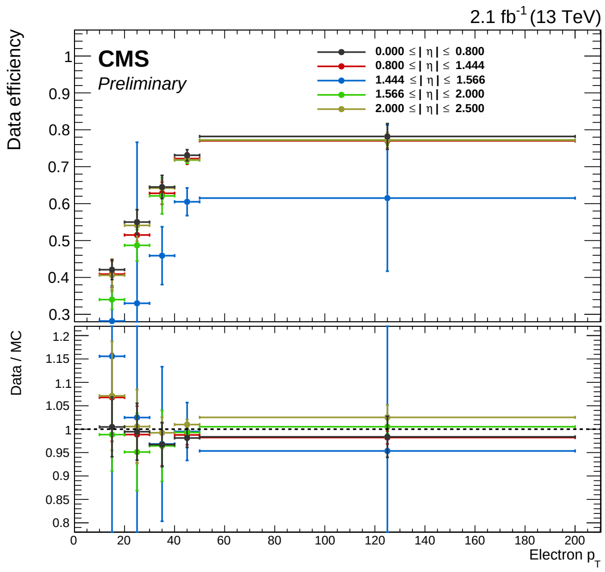

Figure 3.2.: Typical electron identification and isolation efficiencies in data (top panel) and data/simulation scale factor (bottom panel), as a function of the electron p_T and for different η bins.

3.2.8. Lepton trigger efficiency

Analyses that involves leptons in the final state generally select the interesting events using lepton triggers. For instance, the $\mathrm{H} \to \mathrm{WW} \to 2\ell 2\nu$ channel is characterized by the presence of two leptons in the final state, thereby both single lepton and double lepton triggers are used. The lepton triggers at the HLT level are characterized by p_T thresholds, above which the trigger efficiency is very high (plateau region). Nevertheless, the trigger efficiency as a function of the lepton p_T is not a step function, but is characterized by a steep increase of the efficiency around the p_T threshold (turn-on region). The simulated samples thus need to be corrected in order to properly take into account the trigger efficiency. This can be achieved in two ways: including the HLT trigger in the event simulation or calculating the trigger efficiency in data and then applying it on top of simulated events. Several analyses, such as those related to the $\mathrm{H} \to \mathrm{WW} \to 2\ell 2\nu$ channel, opt for the second approach.

The trigger efficiency for single and double lepton triggers is calculated in bins of η and p_{T} using a Tag and Probe technique similar to the one described in Sec. 3.2.7, separately for muons and electrons. Since the triggered events arise from a mixture of two different triggers, the combined efficiency has to be computed and applied to simulated samples as an event weight. In the following, the approach used in the $\mathrm{H} \to \mathrm{WW} \to 2\ell 2\nu$ analyses is described.

The event efficiency $\varepsilon_{\mathrm{ev}}$ for an event with two leptons to pass the single lepton trigger is given by the following formula:

$$\varepsilon_{\mathrm{ev}} = 1 - (1 - \varepsilon_{S,\ell 1}) \cdot (1 - \varepsilon_{S,\ell 2}) \quad , \tag{3.4}$$

where $\varepsilon_{S,\ell 1}$ and $\varepsilon_{S,\ell 2}$ are the efficiencies for the leading and subleading lepton to pass the single lepton trigger. In other words, the dilepton event passes the single lepton trigger if either one of the two leptons passes the single lepton trigger, excluding the cases for which both leptons pass the trigger.

For double lepton triggers the efficiency is calculated separately for each leg of the trigger. In the calculation of the efficiencies, the two trigger legs are considered independent, given that the correlations are very small. The combined efficiency is then used as a kinematics-dependent weight to be applied on top of simulated events. The event efficiency can be written as:

$$\varepsilon_{\mathrm{ev}} = \varepsilon^{\mathrm{lead}}_{D,\ell 1} \cdot \varepsilon^{\mathrm{trail}}_{D,\ell 2} + (1 - \varepsilon^{\mathrm{lead}}_{D,\ell 1} \cdot \varepsilon^{\mathrm{trail}}_{D,\ell 2}) \cdot \varepsilon^{\mathrm{trail}}_{D,\ell 1} \cdot \varepsilon^{\mathrm{lead}}_{D,\ell 2} \quad , \tag{3.5}$$

where $\varepsilon^{\mathrm{lead}(trail)}_{D,\ell 1}$ is the efficiency of the first lepton to pass the leading (trailing) leg of the double lepton trigger, and $\varepsilon^{\mathrm{lead}(trail)}_{D,\ell 2}$ is the efficiency of the second lepton to pass the leading (trailing) leg of the double lepton trigger. The final event efficiency applied to reweight the events in simulation is given by the boolean OR of the event efficiencies corresponding to the single and double lepton triggers, which, using Eqs. (3.4) and (3.5), can be written as:

$$\begin{aligned} \varepsilon_{\mathrm{ev}} = {} & 1 - (1 - \varepsilon_{S,\ell 1}) \cdot (1 - \varepsilon_{S,\ell 2}) + \\ & + (1 - \varepsilon_{S,\ell 1}) \cdot (1 - \varepsilon_{S,\ell 2}) \cdot \\ & \cdot [\varepsilon^{\mathrm{lead}}_{D,\ell 1} \cdot \varepsilon^{\mathrm{trail}}_{D,\ell 2} + (1 - \varepsilon^{\mathrm{lead}}_{D,\ell 1} \cdot \varepsilon^{\mathrm{trail}}_{D,\ell 2}) \cdot \varepsilon^{\mathrm{trail}}_{D,\ell 1} \cdot \varepsilon^{\mathrm{lead}}_{D,\ell 2}] \quad . \end{aligned} \tag{3.6}$$

3.3. Jets reconstruction and identification

Jets are the experimental signature of quarks and gluons produced in high energy physics processes. They arise from the hadronization of partons, which forms collimated sprays of particles, and play a predominant role in hadron colliders like the LHC, where the production cross section is very large. In this section, the jet reconstruction techniques used in CMS are described.

3.3.1. Jet reconstruction in CMS

The majority of physics analyses involving jets in the final state make use of particle flow jets. The PF jets are reconstructed using the technique described in Sec. 3.1, clustering all particles reconstructed with the PF algorithm, without any distinction of type and energy threshold. This method allows a remarkable improvement in the jet momentum and spatial resolutions with respect to the calorimeter jets, which are instead reconstructed using solely the information from the calorimeters, as the use of the tracker information provides a better p_{T} resolution for the charged particles constituting the jets[3].

Jets are defined through sequential, iterative clustering algorithms that combine the four-momenta of input particles until certain conditions are satisfied and jets are formed [28]. Several algorithms are available for jet clustering, characterized by different features. From a theoretical point of view, an ideal jet clustering algorithm should fulfil the following requirements [29]:

- *Infrared safety*: infrared singularities should not appear in the perturbative calculations and the solutions of the algorithm should be insensitive to soft radiation in the event;
- *Collinear safety*: collinear singularities should not appear in the perturbative calculations and jets should be insensitive to collinear radiation in the event;
- *Invariance under boosts*: the solutions of the algorithm should be the same independently of boosts in the longitudinal direction. This is particularly important for pp colliders, where the centre-of-mass of the individual proton proton collisions is typically boosted along the beam direction;
- *Order independence*: the algorithm should find the same jets at parton, particle and detector level;
- *Straightforward implementation*: the algorithm should be straightforward to implement in perturbative calculations.

The ideal algorithm should also follow some experimental attributes. Among them, the performance of the algorithm should be as independent as possible of the detector that provides the data, the algorithm should not amplify the inevitable effects of resolution smearing and angle bias and should not be strongly affected by pile up and high beam luminosities. Furthermore, the algorithm should be easy to implement, efficient to identify all possible jet candidates and should keep at an acceptable level the necessary computing resources.

Two main classes of jet clustering algorithms can be defined. The first one consists in the "cone" recombination, where jets are reconstructed associating together particles

[3] On average, the typical jet energy fractions carried by charged particles, photons and neutral particles are 65%, 25% and 10%, respectively.

whose trajectories lie within a cone of radius ΔR in the η–ϕ plane. The second class of algorithms uses the sequential recombination scheme, that iteratively recombine the closest pair of particles according to some distance measure. The standard algorithms used by CMS are the SISCone, which is a "cone" recombination algorithm, and the k_t, anti-k_t and *Cambridge Aachen* (CA) algorithms, which instead belong to the sequential recombination class. All the analyses presented in Secs. 4, 5 and 6 make use of the sequential recombination scheme, in particular of the anti-k_t algorithm with $R = 0.4$, which is briefly described in the following.

The k_t, anti-k_t and CA algorithms are infrared and collinear safe algorithms characterized by the introduction of two definitions of distance: d_{ij}, the distance the two objects i and j, and d_{iB}, the distance between the object i and the beam. These distances are defined by the following equations:

$$\begin{aligned} d_{ij} &= min\left(k_{ti}^{2p}, k_{tj}^{2p}\right)\frac{\Delta_{ij}^2}{R^2} \quad , \\ d_{iB} &= k_{ti}^{2p} \quad , \end{aligned} \tag{3.7}$$

where $\Delta_{ij} = (y_i - y_j)^2 + (\phi_i - \phi_j)^2$ and $k_t i$, y_i and ϕ_i are the transverse momentum, rapidity and azimuthal angle of the particle i, respectively. In these formulas, R represents the radial parameter and p is a parameter that is 1 for k_t, 0 for CA and -1 for anti-k_t algorithm. The algorithm proceeds as follows:

- the distances d_{ij} are calculated for all pair of particle i, j and the distances d_{iB} are calculated for each particle i, according to Eq. (3.7);
- the smallest distance, which could be either of type d_{ij} or d_{iB}, is identified;
- if the smallest distance is a d_{ij}, the particles i and j are combined into a single new particle summing their four-momenta and the algorithm restarts from the first step;
- otherwise, if it is a d_{iB}, i is declared to be a final state jet and the algorithm returns to the first step;
- the procedure is repeated until no particles are left.

The physical difference between the three algorithms is the momentum weighting. For the k_t algorithm, the weighting proportional to k_t^2 implies that jets are reconstructed starting from particles with low transverse momentum. Moreover this algorithm produces jets with irregular borders, thereby complicating the correction for effects such as pile up. For the CA algorithm there is no transverse momentum weighting, and the particles are merged following just an angular approach, based on the distance Δ_{ij}. Also this algorithm leads to jets with irregular borders. Finally, the anti-k_t algorithm, uses a weighting proportional to $1/k_t^2$, favouring the merging of high transverse momentum particles. In this case the jets grow around the particles with highest transverse momenta and the jets have a circular shape.

Jets reconstructed with different algorithms starting from the same set of simulated particles are shown in Fig. 3.3.

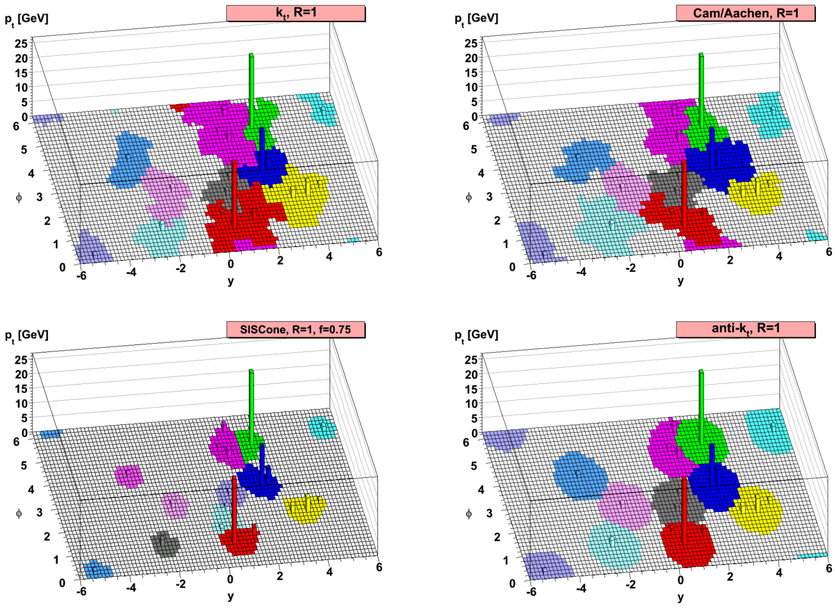

Figure 3.3.: Jets reconstructed with different algorithms starting from the same set of simulated particles. The jets reconstructed with the sequential recombination algorithms described in the text are shown, as well as with the SISCone algorithm.

3.3.2. Jet energy correction

The purpose of jet energy correction is to relate, on average, the jet energy measured in the detector to the true energy of the corresponding final state particle or parton jet. The latter is obtained in simulation by clustering, with the same algorithm used for jets in the detector, all the stable particles, i.e. with $c\tau > 1\,\mathrm{cm}$, produced in the event excluding neutrinos. This mismatch is mainly ascribable to the non uniform and linear response of the CMS calorimeters, to the electronics noise and to pile up. For this reason, CMS has developed a sequential procedure to calculate and apply the *jet energy corrections* (JEC) [30].

The correction is applied as a multiplicative factor $\mathcal{C}$ to each component of the raw jet four-momentum p_μ^{raw} (components are indexed by μ in the following):

$$p_\mu^{\mathrm{cor}} = \mathcal{C} \cdot p_\mu^{\mathrm{raw}} \quad , \tag{3.8}$$

where p_μ^{cor} is the corrected jet four-momentum. The correction factor is composed of the offset correction C_{offset}, the MC calibration factor C_{MC}, and the residual calibrations C_{rel} and C_{abs} for the relative and absolute energy scales, respectively. The offset correction removes the extra energy due to noise and pile up, and the MC correction removes the bulk of the non-uniformity in η and the non-linearity in p_{T}. Finally, the residual corrections account for the small differences between data and simulation. The various components are applied in sequence as described by the equation below:

$$\mathcal{C} = C_{\text{offset}}(p_{\text{T}}^{\text{raw}}) \cdot C_{\text{MC}}(p'_{\text{T}}, \eta) \cdot C_{\text{rel}}(\eta) \cdot C_{\text{abs}}(p''_{\text{T}}) \quad , \tag{3.9}$$

where p'_{T} is the jet p_{T} after applying the offset correction and p''_{T} is the jet p_{T} after applying all previous corrections. Each component is briefly described in the following sections.

Offset correction

The offset correction purpose is to estimate and subtract, on average, the energy contribution that is not associated with the hard scattering in the event. The energy excess includes contributions from electronics noise and pile up. The approach followed for the estimation of the offset correction is known as *Jet Area Method*. For each event, an average p_{T}-density per unit area, ρ, is estimated, characterizing the soft jet activity. This p_{T}-density represents the combination of the underlying event, the electronics noise and the pile up effects. The two latter components contaminate the hard jet energy measurement and need to be corrected for with the offset correction. The key element for this approach is the jet area A_j. A very large number of infinitely soft four-momentum vectors (soft enough not to change the properties of the true jets) are artificially added in the event and clustered by the jet algorithm together with the true jet components. The extent of the region in the η–ϕ space occupied by the soft particles clustered in each jet defines the active jet area. The p_{T}-density ρ is calculated with the k_t algorithm with a distance parameter $R = 0.6$. The quantity ρ is estimated event by event as the median of the distribution of the variable $p_{\text{T}j}/A_j$, where j runs over all jets in the event, and is not sensitive to the presence of hard jets in the event. At the detector level, the measured density ρ is the convolution of the true particle-level activity (underlying event, pile-up) with the detector response to the various particle types. The event-by-event and jet-by-jet offset correction can thus be defined as:

$$C_{\text{offset}}(p_{\text{T}}^{\text{raw}}, A_j, \rho) = 1 - \frac{(\rho - \langle \rho_{\text{UE}} \rangle) \cdot A_j}{p_{\text{T}}^{\text{raw}}} \quad . \tag{3.10}$$

In the formula above, $\langle \rho_{\text{UE}} \rangle$ represents the average p_{T}-density component due to the underlying event and electronics noise, and is measured in events with exactly one reconstructed primary vertex, i.e. no pile up.

An additional pile up subtraction method that is used in CMS is called *Charged Hadron Subtraction*. This method makes use of PF jets and exploits the excellent CMS tracking capabilities to identify and remove charged hadrons inside jets, which are known to originate from pile up vertices. This is a particle-by-particle method that is applied to jets before calculating the offset correction.

MC calibration correction

The MC calibration is based on the simulation and corrects the energy of the reconstructed jets such that it is equal on average to the energy of the generated jets. In order to evaluate this correction, simulated QCD events are generated and then processed through the CMS detector simulation, based on the GEANT4 software. The jet reconstruction in simulation is identical to the one applied to the data. Each reconstructed jet is spatially matched, in the η–ϕ space, to a generated jet by requiring $\Delta R < 0.25$. In each bin of the generated jet transverse momentum $p_{\mathrm{T}}^{\mathrm{gen}}$, the response variable $\mathcal{R} = p_{\mathrm{T}}^{\mathrm{reco}}/p_{\mathrm{T}}^{\mathrm{gen}}$ and the reconstructed jet transverse momentum $p_{\mathrm{T}}^{\mathrm{reco}}$, are saved. The average correction in each bin is therefore defined as:

$$C_{\mathrm{MC}}(p_{\mathrm{T}}^{\mathrm{reco}}) = \frac{1}{\langle R \rangle} \quad , \tag{3.11}$$

and is expressed as a function of the average reconstructed jet p_{T}, $\langle p_{\mathrm{T}}^{\mathrm{reco}} \rangle$.

Relative jet energy scale

The goal of the relative jet energy scale correction is to make the jet response flat versus η. This is achieved by employing a Tag and Probe technique, selecting di-jet events in data. The size of this residual correction is of the order of 2–3% in the central η region, while it goes up to about 10% in the forward region.

Absolute jet energy scale

The goal of the absolute jet energy scale correction is to make the jet response at versus p_{T}. The absolute jet energy response is measured in the reference region $|\eta| < 1.3$ with the *Missing Transverse Energy Projection Fraction* (MPF) method [31], using $\gamma +$jets and Z+jets events. The method is used to estimate the absolute jet energy correction and is based on the fact that $\gamma +$jets and Z+jets events have no intrinsic $E_{\mathrm{T}}^{\mathrm{miss}}$ and that, at parton level, the γ and Z boson are perfectly balanced by the hadronic recoil in the transverse plane.

Jet energy uncertainties

The uncertainties in the jet energy estimation arise from several different sources. Generally these can be categorized as follows:

- physics modelling in MC such as showering, underlying event, etc.;
- MC modelling of true detector response and properties;
- potential biases in the methodologies used to estimate the corrections.

The sources are combined in different groups: absolute scale, relative scale, pile up, jet flavor and time stability. In Fig. 3.4 the effect of each group of uncertainties is shown together with the total uncertainty obtained summing all sources in quadrature, both as a function of η and p_{T}. The pile up uncertainty dominates for low values of the jet p_{T} while the relative and absolute uncertainties are more important in the high p_{T} region.

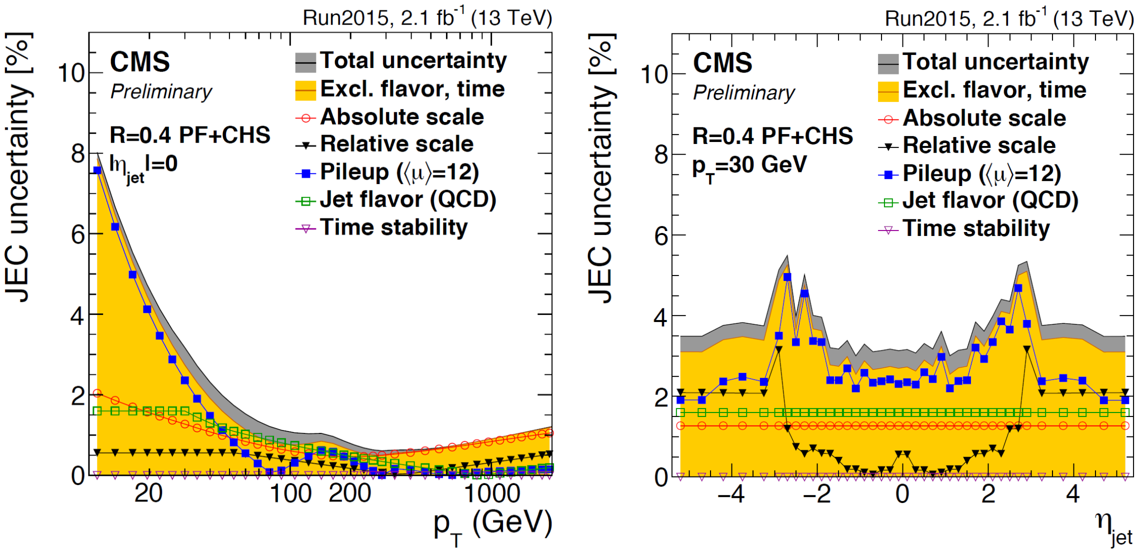

Figure 3.4.: JEC uncertainties as a function of p_{T} (left) for jets reconstructed with $\eta = 0$ and as a function of η (right) for jets with $p_{\mathrm{T}} = 30$ GeV. All jets are reconstructed with the PF technique and using the anti-k_t algorithm with $R = 0.4$, after applying the CHS correction. Results are based on 2.1 fb^{-1} of data collected at 13 TeV.

Jet energy resolution

Measurements show that the jet energy resolution (JER) in data is worse than in the simulation, therefore the simulated jets need to undergo a smearing procedure in order to have a better description of the data.

Reconstructed jets in simulated events are corrected for the jet energy resolution using a two step procedure. In the first step, the reconstructed jet p_{T} is scaled for the observed p_{T} difference between reconstructed and generated jets. This method only works for reconstructed jets that are well matched to generated jets, where the matching is based on ΔR and Δp_{T} requirements. For reconstructed jets that do not fulfil the matching requirements, a gaussian smearing of the p_{T} distribution is applied in order to obtain the desired resolution.

jet identification?

3.4. Jet b tagging

Jets that arise from bottom quark hadronization (b-jets) are present in many physics processes, such as the decay of top quarks. The ability to accurately identify b-jets is crucial to reduce the otherwise overwhelming background from these processes to channels involving jets from gluons (g) and light-flavour quarks (u, d, s), and from c-quark fragmentation.

Algorithms for b jet identification (also known as b tagging algorithms) exploit the long life time of b hadrons present in jets originating from the hadronization of b quarks. This long life time results in a decay of the b hadron that is displaced with respect to the primary interaction vertex. This displacement of a few millimetres results in the presence of displaced tracks from which a secondary vertex may be reconstructed. In addition, b hadrons have a probability of around 20% to decay to a muon or electron. Hence, also the presence of these charged leptons can be exploited for b jet identification techniques and for measuring their performance with the collision data.

A variety of reconstructed physics objects, as tracks, vertices and identified leptons, can be used to build observables that discriminate between b and light-quark jets. Several b tagging algorithms have been developed by CMS, each one based on different input information. A common feature of all the algorithms is that each one yields a single discriminator value for each jet, which measures the likelihood that the jet has been produced by the hadronization of a b quark. The minimum thresholds on these discriminators define loose ("L"), medium ("M"), and tight ("T") operating points with a misidentification probability for light-parton jets close to 10%, 1%, and 0.1%, respectively, at an average jet p_{T} of about 80 GeV. The misidentification probability, also known as mistag rate, is defined as the probability to wrongly identify a light-parton jet as a b-jet.

Some of the algorithms make use of the track impact parameters (IP) with respect to the primary vertex, defined as the distance between the primary vertex and the track at their point of closest approach, to distinguish the decay products of a b hadron from prompt tracks. The impact parameter has the same sign as the scalar product of the vector pointing from the primary vertex to the point of closest approach with the jet direction. Tracks originating from the decay of particles travelling along the jet axis will tend to have positive IP values. In contrast, the impact parameters of prompt tracks can have positive or negative IP values. The impact parameter significance, defined as the ratio of the IP to its estimated uncertainty, is used as an observable.

The *Track Counting* (TC) algorithm sorts tracks inside a jet by decreasing values of the IP significance. Although the ranking tends to bias the values for the first track to high positive IP significances, the probability to have several tracks with high positive values is low for light-parton jets. Therefore the two different versions of the algorithm use the IP significance of the second and third ranked track as the discriminator value. These two versions of the algorithm are called *Track Counting High Efficiency* (TCHE) and *Track Counting High Purity* (TCHP), respectively.

A general extension of the TC algorithm, i.e. the *Jet Probability* (JP), combines the IP information of several tracks inside the jet, using an estimate of the likelihood that all tracks associated to the jet come from the primary vertex as a discriminating variable. A variant of the JP algorithm also exists in which the four tracks with the highest impact parameter significance get a higher weight in the jet probability calculation. This algorithm is referred to as *Jet B-Probability* (JBP).

A different approach consists in using the secondary vertices and the related kinematic variables, together with displaced tracks information, to discriminate between b and non-b jets. This algorithm is known as *Combined Secondary Vertex* (CSV)[4]. The magnitude and direction of the vector connecting the primary and secondary vertices are used as a discriminating variables and quality requirements are imposed to secondary vertex candidates. In addition, the usage of displaced tracks information allows to increase the efficiency for events where no secondary vertex is found. Several variables related to secondary vertices and displaced tracks are used to build likelihood ratios that have a good discriminating power.

Two algorithms for reconstructing secondary vertices are exploited. For the first algorithm, the tracks associated to jets and fulfilling some quality requirements are used in the adaptive vertex reconstruction (AVR) algorithm [32]. The AVR is the algorithm used for CMS analyses during the 8 TeV data taking. In contrast with this method, the Inclusive Vertex Finder (IVF) algorithm is not seeded from tracks associated to reconstructed jets, but instead makes use of all the tracks in the event, with appropriate selections, to reconstruct the secondary vertices. The latter is the default algorithm used to reconstruct secondary vertices for CMS analyses using 13 TeV data.

A new b jet identification algorithm has been recently developed, combining the discriminators provided by the JP and CSV algorithms with a Boosted Decision Tree (BDT) technique. This combined multivariate algorithm (cMVA) is found to slightly improve the b jet identification efficiency.

The performance of these algorithms is determined using simulated $\mathrm{t\bar{t}}$ events, selecting events with at least one jet with $p_{\mathrm{T}} > 30$ GeV. This is shown in Fig. 3.5, where the b jet identification efficiency versus the misidentification probability is reported for the various algorithms. This figure serves as an illustration as the b tagging performance depend on the p_{T} and η distribution of the jets, and need to be checked for each analysis phase space.

3.5. Missing transverse energy

In hadron colliders the longitudinal momentum (along the beam axis) carried by the incoming partons is not known, preventing the possibility to measure the total missing energy. Nevertheless, the initial transverse momentum carried by the incoming partons is expected to be zero, thereby, for the conservation of the momentum components, also the net momentum of all the particles in the final state of collisions must be zero. The missing transverse momentum ($\vec{p}_{\mathrm{T}}^{\,\mathrm{miss}}$) is the momentum imbalance in the transverse plane of all the visible particles in the event, and its modulus is the missing transverse energy ($E_{\mathrm{T}}^{\mathrm{miss}}$). The $\vec{p}_{\mathrm{T}}^{\,\mathrm{miss}}$ vector is defined as the negative vectorial sum of transverse momenta of all reconstructed PF objects, as shown in the following equation:

[4]An improved version of this algorithm, CSVv2, has been developed for Run 2 analyses.

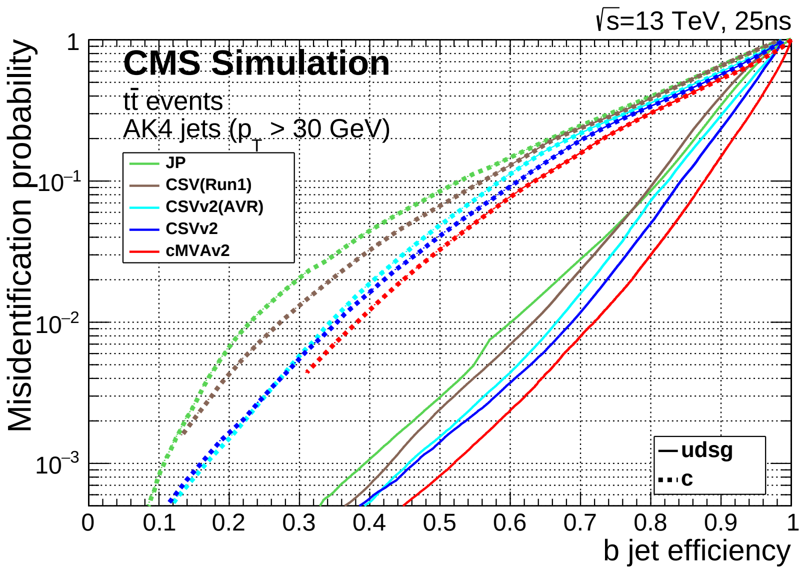

Figure 3.5.: Performance of the b jet identification efficiency algorithms demonstrating the probability for non-b jets to be misidentified as b jet as a function of the efficiency to correctly identify b jets. The curves are obtained on simulated $\mathrm{t\bar{t}}$ events using anti-k_t jets clustered with $R = 0.4$ and requiring $p_\mathrm{T} > 30$ GeV.

$$\vec{p}_\mathrm{T}^{\,\mathrm{miss}} = - \sum_{\mathrm{PF\,obj}} \vec{p}_\mathrm{T}^{\,\mathrm{PF\,obj}} \quad , \tag{3.12}$$

where the sum extends over all the PF objects. A $E_\mathrm{T}^\mathrm{miss}$ value different from zero is a potential signature of the presence of particles in the event that have not interacted with the detector, such as neutrinos or beyond the SM particles predicted by some models, but can also be ascribable to detector inefficiencies.

In addition to imperfect resolution of all detectable and reconstructed physics objects, the $E_\mathrm{T}^\mathrm{miss}$ measurement is also sensitive to overlapping detector signals from additional pile up interactions (both in-time and out-of-time pile up **definire in-time e out-of-time PU la prima volta che parlo di PU**), particle misidentification, as well as detector malfunctions [33, 34]. The bias on the $E_\mathrm{T}^\mathrm{miss}$ measurement is reduced by correcting the p_T of the jets with the jet energy corrections described in 3.3.2, and propagating the correction to the $E_\mathrm{T}^\mathrm{miss}$ according to:

$$\vec{p}_\mathrm{T}^{\,\mathrm{miss\,Type-I}} = \vec{p}_\mathrm{T}^{\,\mathrm{miss}} - \sum_{\mathrm{jets}} \left(\vec{p}_\mathrm{T,jet}^{\,\mathrm{JEC}} - \vec{p}_\mathrm{T,jet} \right) \quad , \tag{3.13}$$

where the superscript JEC refers to corrected jets. This correction, called “Type-I” correction, uses the JEC for all jets with $p_{\mathrm{T}} > 15\,\mathrm{GeV}$ that have less than 90% of their energy deposited in ECAL. Furthermore, if a muon is found inside a jet, its four-momentum is subtracted from the jet four-momentum before the correction, and added back to the corrected object.

Anomalous high-$E_{\mathrm{T}}^{\mathrm{miss}}$ events can be due to various phenomena. In the ECAL, spurious deposits may appear due to particles striking sensors in the ECAL photodetectors, or from real showers with non-collision origins such as those caused by beam halo particles[5]. ECAL dead cells can cause real energy to have been missed, again leading to a spurious imbalance. In the HCAL, spurious energy can arise due to noise in the hybrid photodiode and readout electronics, as well as direct particle interactions with the light guides and photomultiplier tubes of the forward calorimeter. The spurious $E_{\mathrm{T}}^{\mathrm{miss}}$ produced by these effects is estimated using dedicated algorithms, and a cleaning procedure is applied to data in order to remove the affected events.

3.5.1. $E_{\mathrm{T}}^{\mathrm{miss}}$ scale and resolution measurement

The performance (scale and resolution) of $E_{\mathrm{T}}^{\mathrm{miss}}$ can be studied in events with an identified Z boson or an isolated photon. Momenta of leptons and photons can be reconstructed with good resolutions, around 1–6%, while momenta of jets are reconstructed with less precision, with typical resolutions of 5–15%. As a consequence, the $E_{\mathrm{T}}^{\mathrm{miss}}$ resolution in Z or γ+jets events is dominated by hadronic activity in the event.

The comparison of the momenta of the vector boson with respect to the hadronic recoil system is used to measure the $E_{\mathrm{T}}^{\mathrm{miss}}$ performance. In Fig. 3.6 the vector boson momentum in the transverse plane is shown as $\vec{q}_{\mathrm{T}}$, and transverse momentum of the hadronic recoil, defined as the vectorial sum of the transverse momenta of all particles except the vector boson (or its decay products, in the case of Z bosons), is shown as $\vec{u}_{\mathrm{T}}$. Momentum conservation in the transverse plane dictates that $\vec{q}_{\mathrm{T}} + \vec{u}_{\mathrm{T}} + \vec{p}_{\mathrm{T}}^{\mathrm{miss}} = 0$.

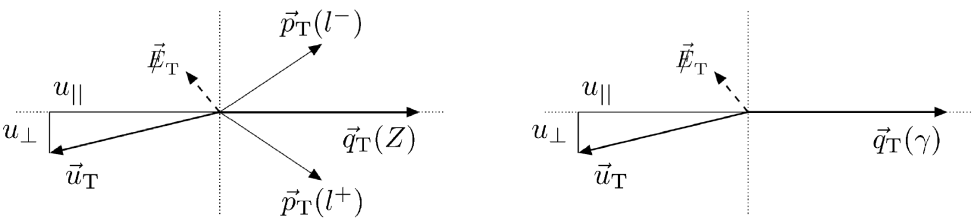

Figure 3.6.: Illustration of the Z$\rightarrow$ $\ell^+\ell^-$ (left) and photon (right) event kinematics in the transverse plane.

[5]These background, also known as *Machine-Induced Background*, originates mainly from interactions of the beam protons with the final set of collimators before the CMS experiment and from proton gas interactions.

The $E_{\mathrm{T}}^{\mathrm{miss}}$ characteristics are evaluated using two components of $\vec{u}_{\mathrm{T}}$, one parallel $(u_{\parallel})$ and one perpendicular $(u_{\perp})$ to the axis defined by $\vec{q}_{\mathrm{T}}$. The distributions of these variables are parametrized using a convolution of a Breit-Wigner and a Gaussian distribution, i.e. a Voigtian distribution, which is found to provide a good description of the observables and is used to measure the resolution in $u_{\parallel}$ and $u_{\perp}$, $\sigma(u_{\parallel})$ and $\sigma(u_{\perp})$, respectively. These resolutions are closely related to the $E_{\mathrm{T}}^{\mathrm{miss}}$ resolution. The resolutions $\sigma(u_{\parallel})$ and $\sigma(u_{\perp})$ obtained using recent 13 TeV data are shown in Fig. 3.7.

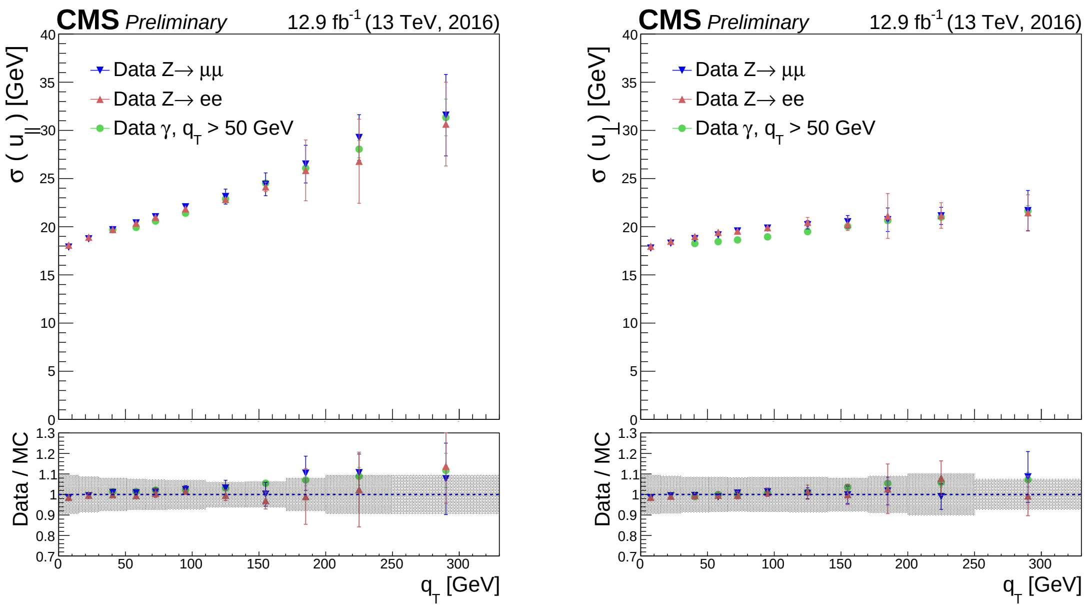

Figure 3.7.: Resolutions $\sigma(u_{\parallel})$ (left) and $\sigma(u_{\perp})$ (right) for Z→ $\mu^{+}\mu^{-}$, Z→ $e^{+}e^{-}$ and γ events as a function of the vector boson p_{T}. The upper panels show the resolution measured in data and the bottom panels the data to simulation ratio.

Chapter 4.

Measurement of the Higgs boson transverse momentum at 8 TeV using $\mathbf{H \to WW \to 2\ell 2\nu}$ decays

4.1. Introduction

The Higgs boson production at hadron colliders is characterized by the Higgs boson transverse momentum, $p_{\mathrm{T}}^{\mathrm{H}}$, and its pseudorapidity, η. The η distribution is essentially driven by the PDF of the partons in the colliding hadrons, and it is only mildly sensitive to radiative corrections. The $p_{\mathrm{T}}^{\mathrm{H}}$ distribution is instead sensitive to QCD radiative corrections. Considering the ggH production mode, at LO in perturbation theory, $\mathcal{O}(\alpha_s^2)$, the Higgs boson is always produced with $p_{\mathrm{T}}^{\mathrm{H}}$ equal to zero. Indeed in order to have p_{T} different from zero, the Higgs boson has to recoil at least against one parton. Higher order corrections to the ggH process are numerically large and are known at NLO including full top quark mass dependence [35, 36], and at NNLO using the so-called large-m_{t} approximation [37–39], in which the top quark mass is assumed to be very large and the fermionic loop is replaced by an effective vertex of interaction. Starting from the NLO, the Higgs boson can be produced recoiling against other final state partons, resulting in a finite $p_{\mathrm{T}}^{\mathrm{H}}$. For this reason the LO process for Higgs production at $p_{\mathrm{T}} \neq 0$ is at $\mathcal{O}(\alpha_s^3)$, and the counting of perturbative orders differs between inclusive Higgs boson production and $p_{\mathrm{T}}^{\mathrm{H}}$ distribution. Also, NNLO QCD corrections in the $p_{\mathrm{T}}^{\mathrm{H}}$ observable have recently been shown [40].

When $p_{\mathrm{T}}^{\mathrm{H}} \sim m_{\mathrm{H}}$ the QCD radiative corrections to $p_{\mathrm{T}}^{\mathrm{H}}$ differential cross section are theoretically evaluated using fixed-order calculations. When $p_{\mathrm{T}}^{\mathrm{H}} \ll m_{\mathrm{H}}$ the perturbative expansion does not converge due to the presence of large logarithmic terms of the form $\alpha_s^n \ln^{2n} m_{\mathrm{H}}^2/p_{\mathrm{T}}^2$, leading to a divergence of $d\sigma/dp_{\mathrm{T}}$ in the limit of $p_{\mathrm{T}} \to 0$. For computing the $p_{\mathrm{T}}^{\mathrm{H}}$ spectrum in this region, soft-gluon resummation techniques are used [41, 42], and matched to the fixed-order calculation in the $p_{\mathrm{T}}^{\mathrm{H}} \sim m_{\mathrm{H}}$ region. For the $p_{\mathrm{T}}^{\mathrm{H}}$ differential cross section the large-m_{t} calculation is a crude approximation, since it is known that the top quark mass has a non-negligible effect on the shape of the spectrum. Moreover the inclusion of the bottom quark contribution in the fermionic loop can significantly modify the $p_{\mathrm{T}}^{\mathrm{H}}$ shape [43], as shown in Fig. 4.1. Hence, a precise experimental measurement of the $p_{\mathrm{T}}^{\mathrm{H}}$ spectrum is important to test the existing SM calculations.

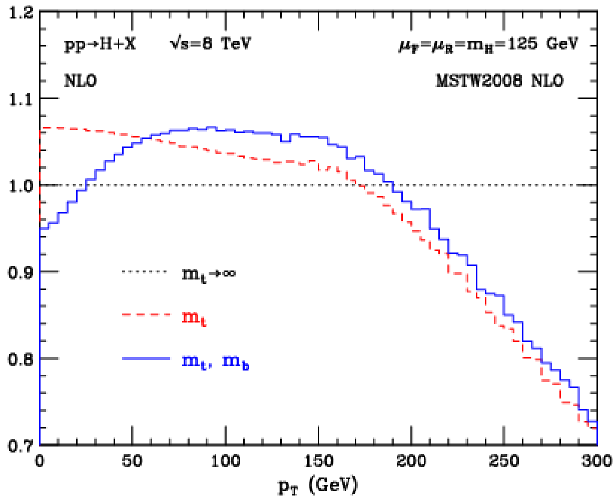

Figure 4.1.: Distribution of $p_{\mathrm{T}}^{\mathrm{H}}$ computed at NLO (α_s^4) and divided by the calculation obtained in the large-m_{t} approximation. The red dashed line corresponds to the calculation including the top quark mass while the blue line refers to the calculation including also the bottom quark effects.

Possible extensions of the SM predict a modification of the Higgs boson couplings to gluons and to the top quark. Many of these models actually predict the existence of new states that interact with the SM Higgs boson, but are beyond the direct production reach at the actual LHC energies. The effect of these new states could however show up as a deviation of the Higgs boson couplings with respect to the SM expectation. The modification of the couplings, as shown in Refs. [44, 45], can change the kinematics of the Higgs boson production and the effect can be particularly sizeable in the tail of the $p_{\mathrm{T}}^{\mathrm{H}}$ distribution. Other models, such as Composite Higgs [46], predict the existence of top-partners, which are heavy resonances with the same quantum numbers as the top quark, that can interact with the Higgs boson in the ggH fermionic loop, changing the $p_{\mathrm{T}}^{\mathrm{H}}$ shape with respect to what the SM predicts [47]. The measurement of the $p_{\mathrm{T}}^{\mathrm{H}}$ spectrum is thus a useful tool for indirect searches of new particles predicted by theories beyond the SM.

Measurements of the fiducial cross sections and of several differential distributions, using the $\sqrt{s} = 8\,\mathrm{TeV}$ LHC data, have been reported by ATLAS [48–50] and CMS [51, 52] for the $\mathrm{H} \to \mathrm{ZZ} \to 4\ell$ ($\ell = \mathrm{e}, \mu$) and $\mathrm{H} \to \gamma\gamma$ decay channels. In this chapter a measurement of the fiducial cross section times branching fraction ($\sigma \times \mathcal{B}$) and p_{T} spectrum for Higgs boson production in $\mathrm{H} \to \mathrm{WW} \to \mathrm{e}^{\pm}\mu^{\mp}\nu\nu$ decays, based on $\sqrt{s} = 8\,\mathrm{TeV}$ LHC data, is reported.

The analysis is performed looking at different flavour leptons in the final state in order to suppress the sizeable contribution of backgrounds containing a same-flavour lepton pair originating from Z boson decay.

Although the $\mathrm{H} \to \mathrm{WW} \to 2\ell 2\nu$ channel has lower resolution in the $p_{\mathrm{T}}^{\mathrm{H}}$ measurement compared to the $\mathrm{H} \to \gamma\gamma$ and $\mathrm{H} \to \mathrm{ZZ} \to 4\ell$ channels because of neutrinos in the final state, the channel has a significantly larger $\sigma \times \mathcal{B}$, exceeding those for $\mathrm{H} \to \gamma\gamma$ by a factor of 10 and $\mathrm{H} \to \mathrm{ZZ} \to 4\ell$ by a factor of 85 for a Higgs boson mass of 125 GeV [53], and is characterized by good signal sensitivity. Such sensitivity allowed the observation of a Higgs boson at the level of 4.3 (5.8 expected) standard deviations for a mass hypothesis of 125.6 GeV using the full LHC data set at 7 and 8 TeV [54].

The measurement is performed in a fiducial phase space defined by kinematic requirements on the leptons that closely match the experimental event selection.

The effect of the limited detector resolution, as well as the selection efficiency with respect to the fiducial phase space are corrected to particle level with an unfolding procedure [55], as explained in Sec. 4.7.

4.2. Data sets, triggers and MC samples

4.2.1. Data sets and triggers

The data set used for the analysis corresponds to $19.4\,\mathrm{fb}^{-1}$ of proton-proton collisions at $\sqrt{s} = 8\,\mathrm{TeV}$, collected by the CMS detector during 2012. Only data corresponding to good data taking quality are considered.

Events are required to fire one of the unprescaled single-electron, single-muon or muon-electron triggers. Due the rather high LHC instantaneous luminosity the single-lepton triggers must have high HLT p_{T} thresholds, otherwise the rate of these triggers would be too large to be sustained. The double-lepton triggers allow to lower down the p_{T} thresholds while keeping a sustainable trigger rate, thus maintaining a good sensitivity to the Higgs boson signal, for which the lepton p_{T} can be rather small. A brief overview of the HLT p_{T} criteria on the leptons is given in Table 4.1. While the HLT lepton p_{T} thresholds of 17 and 8 GeV for the double lepton triggers accommodate the offline lepton p_{T} selection of 20 and 10 GeV, the higher p_{T} thresholds in the single lepton triggers help partially recovering double lepton trigger inefficiencies as a high p_{T} lepton is on average expected due to the kinematic of the Higgs decay.

Table 4.1.: Highest transverse momentum thresholds applied in the lepton triggers at the HLT level. Double set of thresholds indicates the thresholds for each leg of the double lepton triggers.

Trigger Path	8 TeV
Single-Electron	$p_{\mathrm{T}} > 27$ GeV
Single-Muon	$p_{\mathrm{T}} > 24$ GeV
Muon-Electron	$p_{\mathrm{T}} > 17$ and 8 GeV
Electron-Muon	$p_{\mathrm{T}} > 17$ and 8 GeV

The trigger is not simulated in MC samples but the combined trigger efficiency is estimated from data and applied as a weight to all simulated events, as described in Sec. 3.2.8.

4.2.2. Monte Carlo samples

Several Monte Carlo event generators are used to simulate the signal and background processes:

- The first version of the POWHEG program [56–60] (POWHEG V1) provides event samples for the $H \to WW$ signal for the gluon fusion (ggH) and VBF production mechanisms, as well as $t\bar{t}$ and tW processes [61], with NLO accuracy.
- The $qq \to W^+W^-$, Drell-Yan, ZZ, WZ, Wγ, Wγ^*, tri-bosons and W+jets processes are generated using the MADGRAPH 5.1.3 [62] event generator.
- The gg$\to$ W^+W^- process is generated using the GG2WW 3.1 generator [63] and its cross section is scaled to the approximate NLO prediction [64, 65].
- The VH process is simulated using PYTHIA 6.426 [66].

For leading-order generators samples, the CTEQ6L [67] set of parton distribution functions (PDF) is used, while CT10 [68] is used for next-to-leading order (NLO) ones. Cross section calculations at next-to-next-to-leading order (NNLO) are used for the $H \to WW$ process [69]. The $H \to WW$ process simulation is reweighted so that the p_T^H spectrum and inclusive production cross section closely match the SM calculations that have NNLO+NNLL pQCD accuracy in the description of the Higgs boson inclusive production, in accordance with the LHC Higgs Cross Section Working Group recommendations [53]. The reweighting of the p_T^H spectrum is achieved by tuning the POWHEG generator, as described in detail in Ref. [70]. Cross sections computed with NLO pQCD accuracy are used for the background processes [53]. The contribution of the $t\bar{t}$H production mechanism is checked to be negligible in each bin of p_T^H (below 1%) and is not included among the different production mechanisms. In Fig. 4.2 the relative fraction of the four production mechanisms is shown for each p_T^H bin.

For all processes, the detector response is simulated using a detailed description of the CMS detector, based on the GEANT4 package [71].

Minimum bias events are superimposed on the simulated events to emulate the additional proton-proton interactions per bunch crossing. The pile up multiplicity in simulated events has been generated poissonianly sampling from a distribution similar to the one expected from data. The simulated events are reweighted to correct for observed differences between data and simulation in the number of pile up events, as shown in Fig. 4.3.

For the comparison of the measured unfolded spectrum with the theoretical predictions, two additional MC generators are used for simulating the SM Higgs boson production in the ggH process: HRES 2.3 [42, 43] and the second version of the POWHEG generator (POWHEG V2) [72]. HRES is a partonic level MC generator that computes the SM Higgs boson cross section at NNLO accuracy in pQCD and performs the NNLL resummation of soft-gluon effects at small p_T. The central predictions of HRES are obtained including the exact top and bottom quark mass contribution to the gluon fusion loop, fixing the renormalization and factorization scale central values at a Higgs boson mass of 125 GeV. The cross section normalization is scaled, to take into account electroweak corrections, by a factor of 1.05 and the effects of threshold resummation by a factor of 1.06 [73, 74]. The upper and lower bounds of the uncertainties are obtained by scaling up and down both the

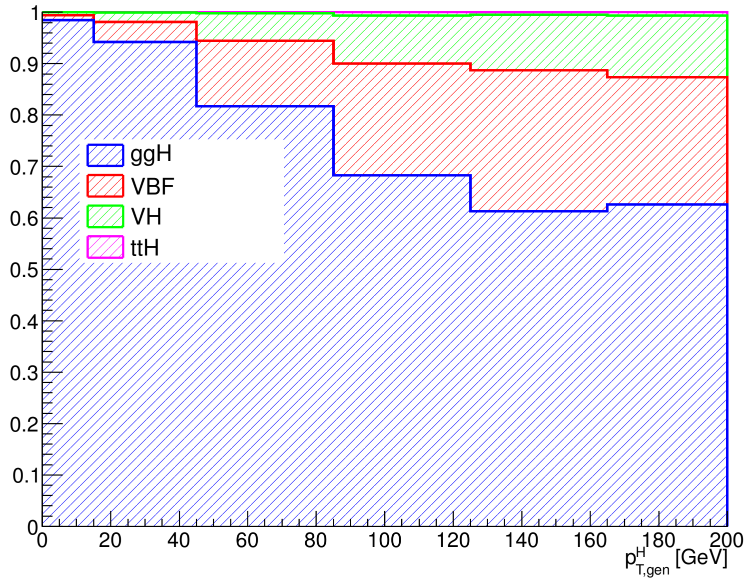

Figure 4.2.: Relative fraction of ggH, VBF, VH and ttH in each bin of the Higgs boson transverse momentum.

1377 renormalization and the factorization scales by a factor of two. The POWHEG V2 generator
1378 is a matrix element based generator that provides a NLO description of the ggH process
1379 in association with zero jets, taking into account the finite mass of the bottom and top
1380 quarks. The POWHEG prediction is tuned using the POWHEG damping factor *hdump* of
1381 104.17 GeV, in order to match the $p_{\mathrm{T}}^{\mathrm{H}}$ spectrum predicted by HRES in the full phase space.
1382 This factor reduces the emission of additional jets in the high p_{T} regime, and enhances the
1383 contribution from the Sudakov form factor in the limit of low p_{T}. The POWHEG generator
1384 is interfaced to the JHUGEN generator version 5.2.5 [75–77] for the decay of the Higgs
1385 boson to a W boson pair and interfaced with PYTHIA 8 [78] for the simulation of parton
1386 shower and hadronization effects.

1387 4.3. Analysis Strategy

1388 The analysis presented here is based on that used in the previously published $\mathrm{H} \to \mathrm{WW} \to 2\ell 2\nu$
1389 measurements by CMS [54], modified to be inclusive in the number of jets. This modifica-
1390 tion significantly reduces the uncertainties related to the modelling of the number of jets
1391 produced in association with the Higgs boson.

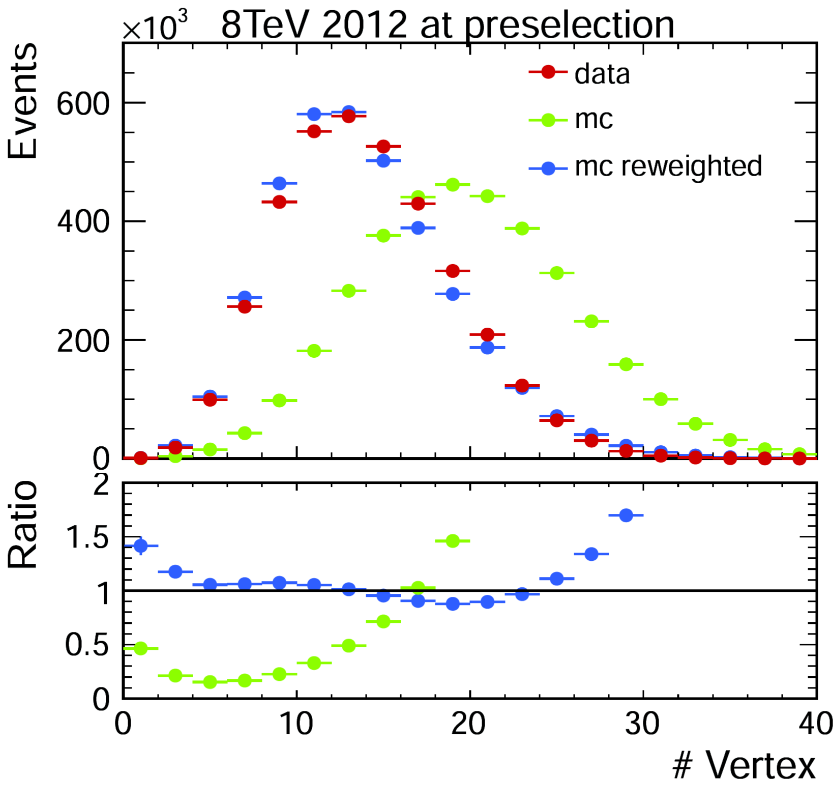

Figure 4.3.: Distribution of the number of vertices in data and in simulation, before and after applying the pile-up reweighting.

4.3.1. Event reconstruction and selections

Electrons and muons used in the analysis are reconstructed using the PF technique as described in Sec. 3.2. In particular, muon candidates are required to be identified both as Tracker Muons and Global Muons.

Jets are reconstructed using the standard PF algorithm and using the anti-k_t clustering algorithm with $\mathrm{R} = 0.5$, as described in Sec. 3.3. If not specified otherwise, jets considered for jet counting are the ones with $p_{\mathrm{T}} > 30$ GeV.

In addition to the standard CMS PF $E_{\mathrm{T}}^{\mathrm{miss}}$, in this analysis a *projected* $E_{\mathrm{T}}^{\mathrm{miss}}$ variable is also used. The *projected* $E_{\mathrm{T}}^{\mathrm{miss}}$ is defined as the component of $\vec{p}_{\mathrm{T}}^{\mathrm{miss}}$ transverse to the nearest lepton if the lepton is situated within the azimuthal angular window of $\pm\pi/2$ from the $\vec{p}_{\mathrm{T}}^{\mathrm{miss}}$ direction, or the $E_{\mathrm{T}}^{\mathrm{miss}}$ itself otherwise. Since the $E_{\mathrm{T}}^{\mathrm{miss}}$ resolution is degraded by pileup, the minimum of two projected $E_{\mathrm{T}}^{\mathrm{miss}}$ variables is used: one constructed from all identified particles (full projected $E_{\mathrm{T}}^{\mathrm{miss}}$), and another constructed from the charged particles only (track projected $E_{\mathrm{T}}^{\mathrm{miss}}$).

Background events from $\mathrm{t\bar{t}}$ and tW production are rejected applying a soft-muon veto and b tagging veto. The soft-muon algorithm is designed to identify muons from b quark decays. Events containing a muon satisfying the following requirements are rejected by the soft-muon veto:

- reconstructed as TrackerMuon;
- number of hits in the Silicon Tracker greater than 10;
- transverse impact parameter less than 0.2 cm;
- relative isolation greater than 0.1 for muons with $p_{\mathrm{T}} > 20$ GeV.

The b tagging veto rejects events that contain jets identified as b-jets using two different algorithms for high and low p_{T} jets (see Sec. 3.4). For jets with p_{T} between 10 and 30 GeV, the TCHE algorithm is applied. Low-p_{T} jets passing the TCHE discriminant threshold of 2.1 are tagged as b-jets. For jets with $p_{\mathrm{T}} > 30$ GeV, a better performing algorithm, JP, is used. Jets are identified as b-jets by the JP algorithm if the discriminating variable has a value above 1.4. In the following, a b tagged jet is defined as a jet, within $|\eta| < 2.4$ (b-tagging requires the tracker information), and with a value of the discriminating variable above the mentioned thresholds for the two algorithms.

The event selection consists of several steps. The first step is to select WW-like events applying a selection that consists of the following set of cuts:

1. **Lepton preselection**:
   - two opposite charge and different flavour (eμ) isolated leptons reconstructed in the event;
   - $|\eta| < 2.5$ for electrons and $|\eta| < 2.4$ for muons;
   - $p_{\mathrm{T}} > 20$ GeV for the leading lepton. For the trailing lepton, the transverse momentum is required to be larger than 10 GeV.
2. **Extra lepton veto**: the event is required to have two and only two leptons with opposite charge passing the lepton selection.
3. **$\boldsymbol{E_{\mathrm{T}}^{\mathrm{miss}}}$ preselection**: particle flow $E_{\mathrm{T}}^{\mathrm{miss}}$ is required to be greater than 20 GeV.
4. **projected $\boldsymbol{E_{\mathrm{T}}^{\mathrm{miss}}}$ selection**: minimum projected $E_{\mathrm{T}}^{\mathrm{miss}}$ required to be larger than 20 GeV.
5. **Di-lepton mass cut**: $m_{\ell\ell} > 12$ GeV in order to reject low mass resonances and QCD backgrounds.
6. **Di-lepton $\boldsymbol{p_{\mathrm{T}}}$ cut**: $p_{\mathrm{T}}^{\ell\ell} > 30$ GeV to reduce the contribution of W+jets and DY to $\tau\tau$ backgrounds.
7. **Transverse mass**: $m_{\mathrm{T}} > 60$ GeV to reject DY to $\tau\tau$ events.

The requirement of different flavour leptons in the final state is important in order to suppress the sizeable contribution of backgrounds containing a same flavour lepton pair originating from Z boson decay.

Events surviving these requirements are dominantly those where a top quark-antiquark pair is produced and both W bosons, which are part of the top quark decay chain, decay leptonically (dileptonic $\mathrm{t\bar{t}}$). Two different selections are used depending on the number of jets in the event. This is done to suppress the top quark background both in the low p_T^H region, where 0-jets events have the largest contribution, and for higher p_T^H values where also larger jet multiplicity events are important. The selection for 0-jets events relies on the soft-muon veto and on a soft jet (with $p_T < 30\,\text{GeV}$) b tagging veto. The latter requirement exploits the TCHE algorithm to reject soft jets that are likely to come from b quarks hadronization.

For events with a jet multiplicity greater or equal than one, a different selection is applied. In this case we exploit the good b tagging performances of the JP tagger to reject all the jets with $p_T > 30\,\text{GeV}$ that are likely to come from b quarks hadronization. The analysis selection requires to have no events containing b-tagged jets with $p_T > 30\,\text{GeV}$.

A cut-flow plot is reported in Fig. 4.4, showing the effect of each selection using signal and background simulations. In the first bin, labelled as “No cut”, no selection is applied and the bin content corresponds to the total expected number of events with a luminosity of 19.4 fb^{-1}. All the events in this bin have at least two leptons with a loose transverse momentum cut of 8 GeV. In the following bin the lepton cuts are applied, including the requirement to have two opposite sign and different flavour leptons and the extra lepton veto. Then all the other selections are progressively reported, showing the effect of each cut on the background and signal yields. For each selection the expected signal over background

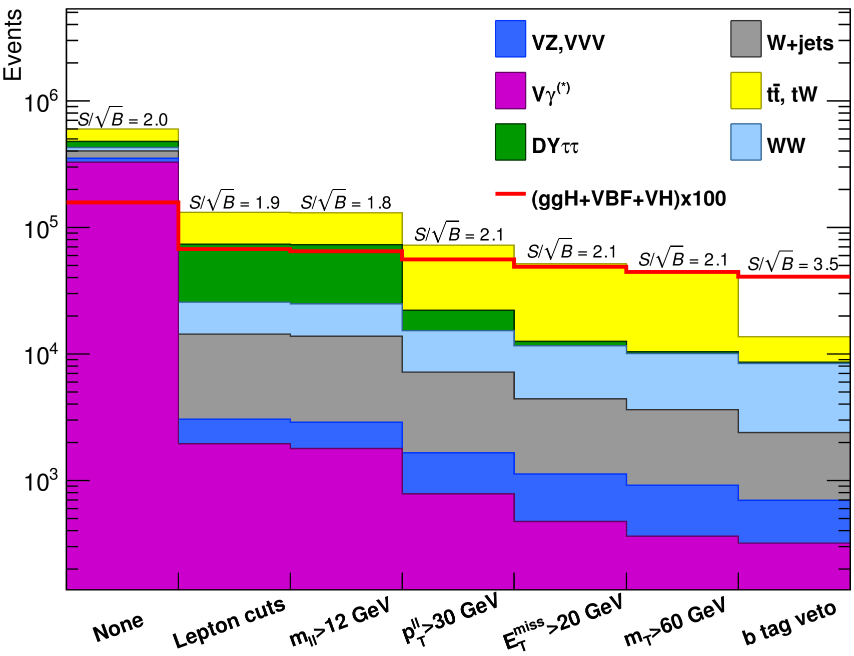

Figure 4.4.: Effect of selection cuts on simulated samples. The signal (red line) is multiplied by 100 and superimposed on stacked backgrounds. In each bin, corresponding to a different selection, is reported the expected number of events in MC at a luminosity of 19.46 fb^{-1}.

ratio is also shown, which, after the full selection requirements, reaches a maximum value of about 3%.

4.3.2. Simulation efficiencies and scale factors

The efficiencies for the identification and isolation of the electrons and muons are measured in data and simulation selecting a pure sample of leptons coming from the $Z \to \ell\ell$ decay, and using the Tag and Probe technique described in Sec. 3.2.7. The efficiencies for data and simulation are used as scale factors to correct the simulated events to precisely model the data.

The trigger efficiency is measured in data and applied to simulation as explained in Sec. 3.2.8.

The efficiency of b tagging algorithms is not well simulated by MC generators and discrepancies can occur with respect to the data. For this reason is important to measure the b tagging efficiency and the misidentification probability for the given algorithms both in data and simulation, and to correct the simulated events using scale factors. This affects not only the top quark background estimation, but also the other backgrounds and the signal. As an example, if a light-parton jet in a signal event was misidentified as a b-jet, this event would be rejected by the b-jet veto.

In this analysis, the b tagging efficiency and the misidentification probability are measured both in data and simulation, selecting a control sample enriched in b-jets, and using a Tag and Probe technique similar to the one described in Sec. 3.2.7. Below is described the method used to estimate the efficiency of the JP b tagging algorithm, but it is extendible to any other algorithm.

The control sample is defined selecting the events that pass the selections listed in Sec. 4.3.1, and have at least two jets with p_T greater than 30 GeV. If the leading jet has a JP discriminator values above the threshold of 0.5, it is considered a *tag*, and the sub-leading jet is the *probe*. In order to avoid any bias that could arise from the probe being always the sub-leading jet, the pair is tested also in reverse order, i.e. sub-leading jet is tested against the *tag* selection, and in case it passes, then the leading jet is used as *probe* forming an independent *tag-probe* pair. If the *probe* jet has a discriminator value above the threshold used in the analysis, i.e. > 1.4, then the *tag-probe* pair is called a *tag-pass-probe* pair. Otherwise it is identified as a *tag-fail-probe* pair.

If the *tag* selection was sufficient to suppress any non top quark event, one could estimate the efficiency by dividing the number of *tag-probe* pairs in which the *probe* passes the analysis JP requirement by the total number of *tag-probe* pairs. However this is not the case, since the contamination due to other background sources is not negligible. In order to estimate the efficiency in the presence of background, a variable that discriminates between true b-jets and other jets in a $t\bar{t}$ sample is needed. This variable is the p_T of the *probe* jet. For real b-jets this variable has a peak around 60 GeV, while it has a broad distribution for other types of jets.

The efficiencies are estimated performing a χ^2 simultaneous fit of the *probe* p_T spectrum in two different categories: one containing events with a *tag-pass-probe* pair and the other containing events with a *tag-fail-probe* pair. The normalisations in the two categories are linked by the following formulas:

$$\begin{aligned} N_{\mathrm{TPP}} &= N_{\mathrm{s}}\varepsilon_{\mathrm{s}} + N_{\mathrm{b}}\varepsilon_{\mathrm{b}} \\ N_{\mathrm{TFP}} &= N_{\mathrm{s}}(1-\varepsilon_{\mathrm{s}}) + N_{\mathrm{b}}(1-\varepsilon_{\mathrm{b}}) \quad , \end{aligned} \tag{4.1}$$

where:

- N_{TPP} is the number of *tag-pass-probe* pairs;
- N_{TFP} is the number of *tag-fail-probe* pairs;
- N_{s} is the number of *tag-probe* pairs in which the *probe* is a b-jet;
- N_{b} is the number of *tag-probe* pairs in which the *probe* is not a b-jet;
- ε_{s} is the efficiency to identify a b-jet, i.e. the b tagging efficiency;
- ε_{b} is the probability to misidentify a non b-jet as a b-jet, i.e. the misidentification probability[1].

The p_{T} shapes of the *probe* jet used in the fit are taken from simulation, where the real flavour of the jet is known, both for the *tag-pass-probe* and *tag-fail-probe* categories. To check the consistency of the fitting procedure, a closure test fitting the simulation itself has been performed. The result of the fit on MC simulation is shown in Fig. 4.9. The relevant efficiencies are:

$$\begin{aligned} \varepsilon_{\mathrm{s}}^{\mathrm{MC}} &= 0.766 \pm 0.007 \\ \varepsilon_{\mathrm{b}}^{\mathrm{MC}} &= 0.208 \pm 0.015 \quad . \end{aligned} \tag{4.2}$$

These values are consistent with the true value of the b tagging efficiency in simulation. The true value is computed by selecting jets that are matched within a cone of $\Delta R < 0.5$ with a generator level b quark, and counting the fraction of those that have a JP discriminator above threshold of 1.4. This check also assures that the *tag-probe* method does not introduce any bias within the simulation statistic accuracy.

In order to assess the robustness of the fit, 5000 toy simulated samples have been generated with a statistics equivalent to the one expected in data and the same fit is performed. All the 5000 fit succeeded, and the pull distributions for ε_{s} and ε_{b} parameters are shown in Fig. 4.10. The distributions represent the *pull* of the efficiencies measured in the fit, where the pull variable for each toy i is defined as:

$$pull(\varepsilon_{\mathrm{s(b)}}) = \frac{\varepsilon_{\mathrm{s(b)}}^{\mathrm{true}} - \varepsilon_{\mathrm{s(b)}}^{i}}{\sigma(\varepsilon_{\mathrm{s(b)}}^{i})} \quad , \tag{4.3}$$

[1] In these naming convention, the subscript "s" stays for "signal", since the b-jets represent the signal in this method. Similarly, the "b" subscript stays for "background", identifying the cases where the *probe* is not a b-jet

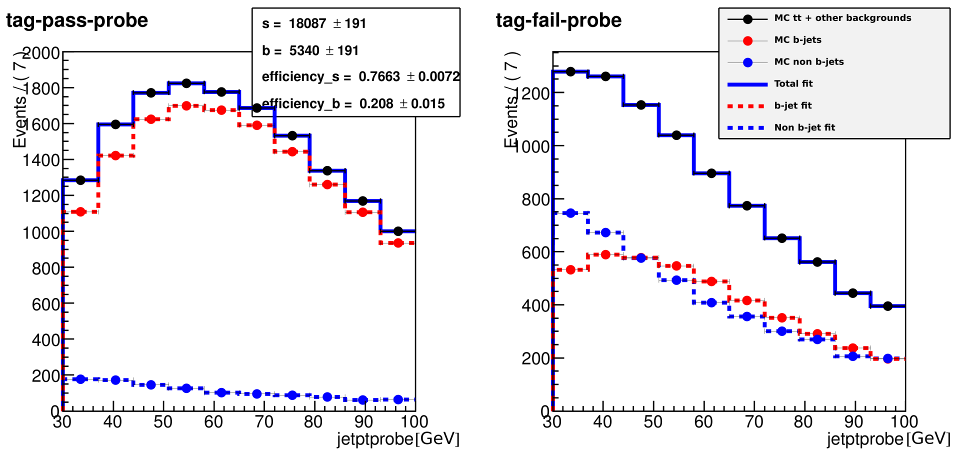

Figure 4.5.: Simultaneous fit of the *tag-pass-probe* and *tag-fail-probe* pairs in the MC.

where $\sigma(\varepsilon^i_{\mathrm{s(b)}})$ is the uncertainty on the efficiency extracted from the fit. The pull distributions are centred on zero and have σ close to one, as expected.

Before running the fit on data, the shapes used in the fit have been validated. To do so, a very pure phase space enriched in b jets has been defined by selecting events containing exactly two jets with a JP discriminator greater than 1.5 and no additional b-tagged jets, rejecting also events containing jets with p_{T} smaller than 30 GeV. On this very pure sample, data have been compared against the shape used to fit the true b-jets in the *tag-pass-probe* distribution. The result is shown in Fig. 4.12 and shows good agreement within uncertainties.

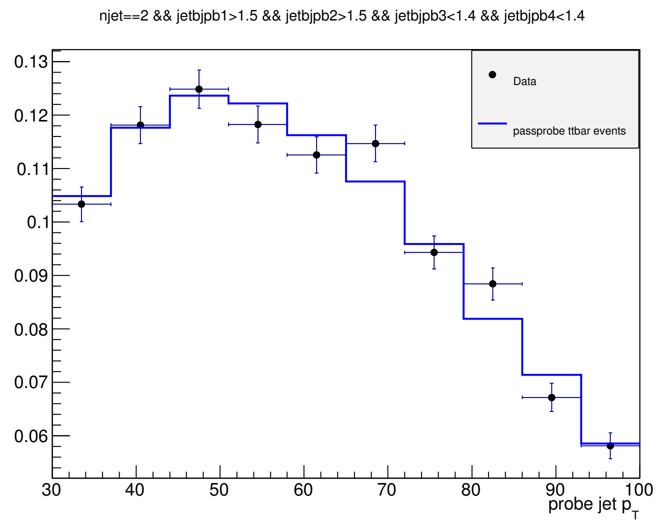

Figure 4.6.: Shape comparison for the p_{T} spectrum of the *probe* jet in data and simulation in a very pure phase space enriched in b-jets.

Finally the fit has been performed on data, as shown in Fig. 4.13, providing the following efficiencies:

$$\begin{aligned} \varepsilon_{\mathrm{s}}^{\mathrm{Data}} &= 0.77 \pm 0.02 \\ \varepsilon_{\mathrm{b}}^{\mathrm{Data}} &= 0.12 \pm 0.05 \end{aligned} \tag{4.4}$$

Further studies have been performed to assess the effect of the relative uncertainty on the $\mathrm{t\bar{t}}$ and tW event fractions. The same procedure described above has been applied to different simulation templates obtained varying the $\mathrm{t\bar{t}}$ and tW fractions within theoretical uncertainties, and the effect on the parameters extracted with the fit procedure is found to be well below the fit uncertainties.

The ratio of the efficiency measured in data and simulation represents a per-jet scale factor that can be used to reweight the simulated events. The weights to be applied event-by-event depend on the particular jet configuration in the events itself. For the signal region (SR), in which a b tagging veto is required, the event weight to be applied is given by:

$$w_{SR} = \prod_{N_{\mathrm{b-jets}}} \left(\frac{1 - \varepsilon_{\mathrm{s}}^{\mathrm{Data}}}{1 - \varepsilon_{\mathrm{s}}^{\mathrm{MC}}} \right) \prod_{N_{\mathrm{non\ b-jets}}} \left(\frac{1 - \varepsilon_{\mathrm{b}}^{\mathrm{Data}}}{1 - \varepsilon_{\mathrm{b}}^{\mathrm{MC}}} \right) \quad , \tag{4.5}$$

where $N_{\mathrm{b-jets}}$ and $N_{\mathrm{non\ b-jets}}$ are the number of true b-jets and the number of non b-jets in the simulated event, respectively. This weight is valid if the a b tagging veto is applied. If instead the b tagging veto is reverted, also the event weight has to be modified. This is done, for example, when one wants to define a $\mathrm{t\bar{t}}$ enriched control region ($CR_{\mathrm{t\bar{t}}}$) for the purpose of measuring the contribution of this background in a phase space orthogonal to the signal region. One simple way to define this control region is to require the leading jet

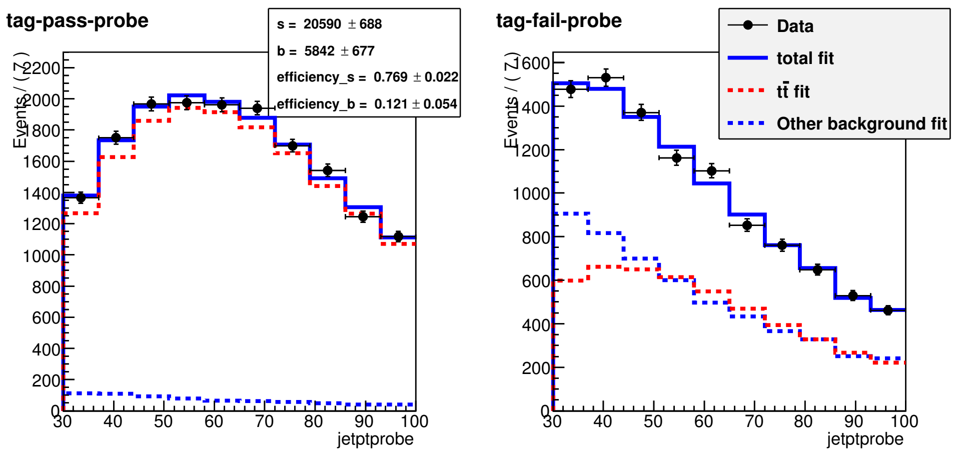

Figure 4.7.: Simultaneous fit of the *tag-pass-probe* and *tag-fail-probe* pairs in data.

in the event to be b-tagged. Therefore, the simulated events falling in this category must be reweighted using the following weight:

$$w_{CR_{\mathrm{t\bar{t}}}} = \begin{cases} \varepsilon_{\mathrm{s}}^{\mathrm{Data}}/\varepsilon_{\mathrm{s}}^{\mathrm{MC}}, & \text{if the leading jet is a b-jet} \\ \varepsilon_{\mathrm{b}}^{\mathrm{Data}}/\varepsilon_{\mathrm{b}}^{\mathrm{MC}}, & \text{if the leading jet is not a b-jet} \end{cases} \tag{4.6}$$

4.3.3. Fiducial phase space

The Higgs boson transverse momentum is measured in a fiducial phase space, whose definition is chosen in order to minimize the dependence of the measurements on the underlying model of the Higgs boson production and decay properties.

The exact requirements are determined by considering the two following correlated quantities: the reconstruction efficiency for signal events originating from within the fiducial phase space (fiducial signal efficiency $\varepsilon_{\mathrm{fid}}$), and the ratio of the number of reconstructed signal events that are from outside the fiducial phase space ("out-of-fiducial" signal events) to the number from within the fiducial phase space. The requirement of having a small fraction of out-of-fiducial signal events, while at the same time preserving a high value of the fiducial signal efficiency ϵ_{fid}, leads to fiducial requirements at the generator level on the low-resolution variables, $E_{\mathrm{T}}^{\mathrm{miss}}$ and m_{T}, that are looser with respect to those applied in the reconstructed event selection.

The fiducial phase space used for the cross section measurements is defined at the particle level by the requirements given in Table 4.2. The leptons are defined as Born-level leptons, i.e. before the emission of final-state radiation (FSR), and are required not to originate from leptonic τ decays. The effect of including FSR is found to modify ϵ_{fid} at most of about 5%. For the VH signal process, the two leptons are required to originate from the $\mathrm{H} \to \mathrm{WW} \to 2\ell 2\nu$ decays in order to avoid including leptons coming from the associated W or Z boson.

Table 4.2.: Summary of requirements used in the definition of the fiducial phase space.

Physics quantity	**Requirement**
Leading lepton p_{T}	$p_{\mathrm{T}} > 20\,\mathrm{GeV}$
Subleading lepton p_{T}	$p_{\mathrm{T}} > 10\,\mathrm{GeV}$
Pseudorapidity of electrons and muons	$\lvert\eta\rvert < 2.5$
Invariant mass of the two charged leptons	$m_{\ell\ell} > 12\,\mathrm{GeV}$
Charged lepton pair p_{T}	$p_{\mathrm{T}}^{\ell\ell} > 30\,\mathrm{GeV}$
Invariant mass of the leptonic system in the transverse plane	$m_{\mathrm{T}}^{\ell\ell\nu\nu} > 50\,\mathrm{GeV}$
$E_{\mathrm{T}}^{\mathrm{miss}}$	$E_{\mathrm{T}}^{\mathrm{miss}} > 0$

A detailed description of the fiducial region definition and its optimization is given in appendix A.

4.3.4. Binning of the $p_{\mathrm{T}}^{\mathrm{H}}$ distribution

Experimentally, the Higgs boson transverse momentum is reconstructed as the vector sum of the lepton momenta in the transverse plane and $E_{\mathrm{T}}^{\mathrm{miss}}$.

$$\vec{p}_{\mathrm{T}}^{\;\mathrm{H}} = \vec{p}_{\mathrm{T}}^{\;\ell\ell} + \vec{p}_{\mathrm{T}}^{\;\mathrm{miss}} \tag{4.7}$$

Compared to other differential analyses of the Higgs cross section, such as those in the ZZ and $\gamma\gamma$ decay channels, this analysis has to cope with the limited resolution due to the $E_{\mathrm{T}}^{\mathrm{miss}}$ entering the transverse momentum measurement. The effect of the limited $E_{\mathrm{T}}^{\mathrm{miss}}$ resolution has two main implications on the analysis strategy: the first one is that the choice of the binning in the $p_{\mathrm{T}}^{\mathrm{H}}$ spectrum needs to take into account the detector resolution; the second implication is that migrations of events across bins are significant and an unfolding procedure needs to be applied to correct for selection efficiencies and bin migration effects.

Given these aspects, the criterion that is used to define the $p_{\mathrm{T}}^{\mathrm{H}}$ bin size is devised to keep under control the bin migrations due to the finite resolution. For any given bin i, the purity P_i of the signal sample is defined as the number events that are generated and also reconstructed in that bin, i.e. $N_i^{\mathrm{GEN|RECO}}$, divided by the number of events reconstructed in the same bin, N_i^{RECO}:

$$P_i = \frac{N_i^{\mathrm{GEN|RECO}}}{N_i^{\mathrm{RECO}}} \quad . \tag{4.8}$$

The bin width is chosen in such a way as to make the smallest bins able to ensure a purity of about 60%, based on a ggH simulated sample. Following this prescription, the whole $p_{\mathrm{T}}^{\mathrm{H}}$ range is dividedin the following six bins: [0–15] GeV, [15–45] GeV, [45–85] GeV, [85–125] GeV, [125–165] GeV, [165–∞] GeV.

The fiducial signal efficiency $\varepsilon_{\mathrm{fid}}$ and the fraction of out-of-fiducial signal events, $f_{\mathrm{out-of-fid}}$, are different in each $p_{\mathrm{T}}^{\mathrm{H}}$ bin and depend on the definition of the fiducial phase space. In Fig. 4.8 the $\varepsilon_{\mathrm{fid}}$ and $f_{\mathrm{out-of-fid}}$ parameters are shown in each $p_{\mathrm{T}}^{\mathrm{H}}$ bin for different definitions of the fiducial phase space. In particular, they have been evaluated adding the requirements reported in Table 4.2 in sequence, starting from a fiducial phase space defined just by the lepton p_{T} and η selections, together with the different flavour requirement, and adding each time an additional selection until the full fiducial phase space in obtained. In this way, the effect of every single selection (or group of selections) on $\varepsilon_{\mathrm{fid}}$ and $f_{\mathrm{out-of-fid}}$ can be assessed. Since the variables related to leptons are measured with good resolution, the effect of including the related selections in the fiducial phase space is to increase $\varepsilon_{\mathrm{fid}}$ keeping $f_{\mathrm{out-of-fid}}$ constant. Instead, the effect of including low-resolution variables, such ad m_{T}, is to increase both $\varepsilon_{\mathrm{fid}}$ and $f_{\mathrm{out-of-fid}}$. Nevertheless, the $f_{\mathrm{out-of-fid}}$ parameter is different from zero even if only lepton cuts are taken into account. This is ascribable to two different aspects: the first one is that in the fiducial definition electrons and muons are required not to originate from τ decays; the second one is instead related to the VH production mechanism, i.e. to the fact that leptons coming from the associated boson are not included.

The overall values integrating over p_T^H are $\varepsilon_{fid} = 0.362 \pm 0.005$ and $f_{out-of-fid} = 0.126 \pm 0.004$ respectively, where only statistical uncertainties are taken into account.

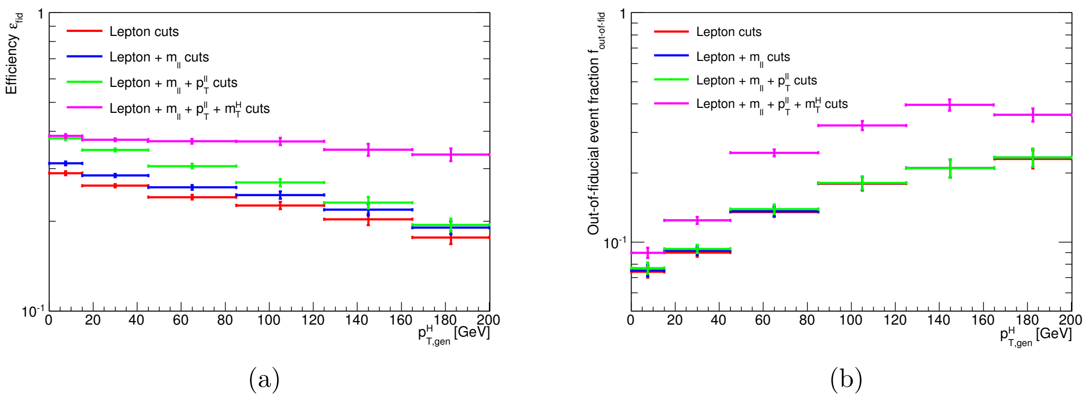

Figure 4.8.: Fiducial signal efficiency ε_{fid} and fraction of out-of-fiducial signal events $f_{out-of-fid}$ in each bin of the generator level p_T^H.

If a 4π acceptance is defined, requiring just that the Higgs decays to WW and then to $2\ell 2\nu$, the efficiency becomes $\epsilon = 0.0396 \pm 0.0003$ and the fake rate is zero.

4.4. Background estimation

4.4.1. Top quark background

In this analysis the top quark background is divided into two different categories depending on the number of jets in the event. In the two categories different selections are applied, especially concerning the b-tagging requirements.

The general strategy for determining the residual top events in the signal region is to first measure the top tagging efficiencies from an orthogonal region of phase space in data. The orthogonal phase space is defined inverting the b-veto requirement of the signal region, in such a way to have a control region enriched in top quark events. Then, using this efficiency, the number of events with the associated uncertainty is propagated from the control region to the signal region. The number of surviving top events in the signal region would then be:

$$N_{bveto}^{\text{signal}} = N_{btag}^{\text{control}} \cdot \frac{1 - \epsilon_{\text{top}}}{\epsilon_{\text{top}}} \tag{4.9}$$

where $N_{\text{btag}}^{\text{control}}$ is the number of events in the control region and ϵ_{top} is the efficiency as measured in data.

The methods to estimate the top background contribution in the two jet categories are different and are explained below.

0-jets category

Most of the top background, composed of $\mathrm{t\bar{t}}$ and tW processes, is rejected in the 0-jet bin by the jet veto. The top-tagging efficiency in the zero jet bin, $\epsilon_{\text{tag}}^{0-jet}$, is the probability for a top event to fail one of either the b-tagging veto or the soft muon veto, and is defined as:

$$\epsilon_{\text{tag}} = \frac{N_{\text{tag}}^{\text{control}}}{N^{\text{control}}} \quad , \tag{4.10}$$

where N^{control} is the number of events in the top control phase space defined requiring one b-tagged jet with $p_{\mathrm{T}} > 30\,\mathrm{GeV}$, and $N_{\text{tag}}^{\text{control}}$ is the subset of those events that pass either the soft muon tagging or the low-p_{T} b jet tagging. The purity of this control sample, as estimated from simulation, is about 97%. The remaining 3% background contribution is estimated from simulation and subtracted from the numerator and denominator of Eq. (4.11). The efficiency $\epsilon_{\text{top}}^{0-jet}$ can then be estimated using the following formula:

$$\epsilon_{\text{top}}^{0-jet} = f_{\mathrm{t\bar{t}}} \cdot \epsilon_{2b} + f_{\mathrm{tW}} \cdot (x \cdot \epsilon_{2b} + (1-x) \cdot \epsilon_{\text{tag}}) \quad , \tag{4.11}$$

$$\epsilon_{2b} = 1 - (1 - \epsilon_{\text{tag}})^2 \quad , \tag{4.12}$$

where $f_{\mathrm{t\bar{t}}}$ and f_{tW} are the $\mathrm{t\bar{t}}$ and tW fractions respectively, x is the fraction of tW events containing 2 b jets, and ϵ_{2b} is the efficiency for a top event with 0 counted jets, i.e. two soft b jets, to pass the top veto. For the ratio of $\mathrm{t\bar{t}}$ and tW cross-sections an uncertainty of 17% is assumed. The fraction $f_{\mathrm{t\bar{t}}}$ is estimated using MC simulation of the $\mathrm{t\bar{t}}$ and tW processes at NLO accuracy.

Using this procedure a data/simulation scale factor of 0.98 ± 0.17 is found, and is applied to correct the MC simulation in order to match the data.

Category with more than 0 jets

The strategy for the estimation of the top background in events with at least one jet with p_{T} greater than 30 GeV is the following. First of all the efficiency for tagging a b jet is measured both in data and simulation and the values are used to correct the simulation for different b-tagging efficiencies in data and simulation. This evaluation is performed in a control region, called CtrlTP, containing at least two jets, using a Tag&Probe technique. The procedure to extract these scale factors is presented in Sec. 4.4.1. Then a larger statistics control region, CtrlDD, is defined by requiring at least one b-tagged jet and we use the simulation, corrected for the previously computed b-tagging efficiency scale factor, to derive the factor that connects the number of events in CtrlDD to the number of events in the signal region. This second step is explained in detail in Sec. 4.4.1.

Tag&Probe

The Tag&Probe technique is a method to estimate the efficiency of a selection on data. In can be applied whenever one has two objects in one event, by using one of the two, the *tag*, to identify the process of interest, and using the second, the *probe*, to actually measure the efficiency of the selection being studied. In our case we want to measure the b-tagging efficiency, so what we need is a sample with two b-jets per event. The easiest way to construct such a sample is to select $\mathrm{t\bar{t}}$ events.

The CrtlTP control region is defined selecting the events which pass the lepton preselection cuts listed in Sec. 4.3.1, and have at least two jets with p_{T} greater than 30 GeV. One of the two leading jets is required to have a *JetBProbability* score higher than 0.5. From events in this control region we built *tag-probe* pairs as follows. For each event the two leading jets are considered. If the leading jet passes the *JetBProbability* cut of 0.5, that is considered a *tag*, and the sub-leading jet is the *probe*. In order to avoid any bias that could arise from the probe being always the second jet, the pair is tested also in reverse order, meaning that the sub-leading jet is tested against the *tag* selection, and in case it passes, then the leading jet is used as *probe* in an independent *tag-probe* pair. This means that from each event passing the CrtlTP cuts one can build up to two *tag-probe* pairs.

If the *tag* selection were sufficient to suppress any non top events, one could estimate the efficiency by dividing the number of *tag-probe* pairs in which the *probe* passes the analysis cut *JetBProbability* >1.4 (*tag-pass-probe*) by the total number of *tag-probe* pairs. However this is not the case. In order to estimate the efficiency in the presence of background a variable that discriminates between true b-jets and other jets in a $t\bar{t}$ sample is chosen. The variable is the p_{T} of the *probe* jet. For real b-jets this variable has a peak around 60 GeV, while it does not peak for other jets. The idea is to fit simultaneously the p_{T} spectrum for *probe* jets in *tag-pass-probe* and *tag-fail-probe* pairs, linking together the normalizations of the two samples as follows:

$$N_{TPP} = N_s \epsilon_s + N_b \epsilon_b \tag{4.13}$$

$$N_{TFP} = N_s(1 - \epsilon_s) + N_b(1 - \epsilon_b) \tag{4.14}$$

where N_{TPP} is the number of *tag-pass-probe* pairs, N_{TFP} is the number of *tag-fail-probe* pairs, N_{s} is the number of *tag-probe* pairs in which the probe is a b-jet, N_{b} is the number of *tag-probe* pairs in which the probe is a not b-jet, ϵ_{s} is the b-tagging efficiency, ϵ_{b} is the probability of identifying as b-jet a non-b-jets, i.e. the mistag rate.

A χ^2 simultaneous fit of the *probe* p_{T} spectrum for *tag-pass-probe* and *tag-fail-probe* pairs is performed, deriving the shapes for true b-jets and non-b-jets from the simulation, and extracting N_{s}, N_{b}, ϵ_{s} and ϵ_{b} from the fit. The result of the fit on simulation is shown in Fig. 4.9. The relevant efficiencies are:

$$\epsilon_s^{MC} = 0.7663 \pm 0.0072 \tag{4.15}$$

$$\epsilon_b^{MC} = 0.208 \pm 0.015 \tag{4.16}$$

We have checked that these values are consistent with the true value for the b-tagging efficiency. The true value is computed by selecting jets that are matched within a cone of $\Delta R < 0.5$ with a generator level b-quark, and counting the faction of those that pass the *JetBProbability* cut of 1.4. This means that the *tag-probe* method does not introduce biases within the simulation statistic accuracy.

In order to assess the robustness of the fit, 5000 toy MC samples have been generated with a statistics equivalent to the one expected in data and the same fit is performed. All the 5000 fit succeeded, and the pull distributions for ϵ_{s} and ϵ_{b} parameters are shown in Fig. 4.10. The plots show the pull of the efficiencies measured in the fit, where the pull variable for each toy i is defined as:

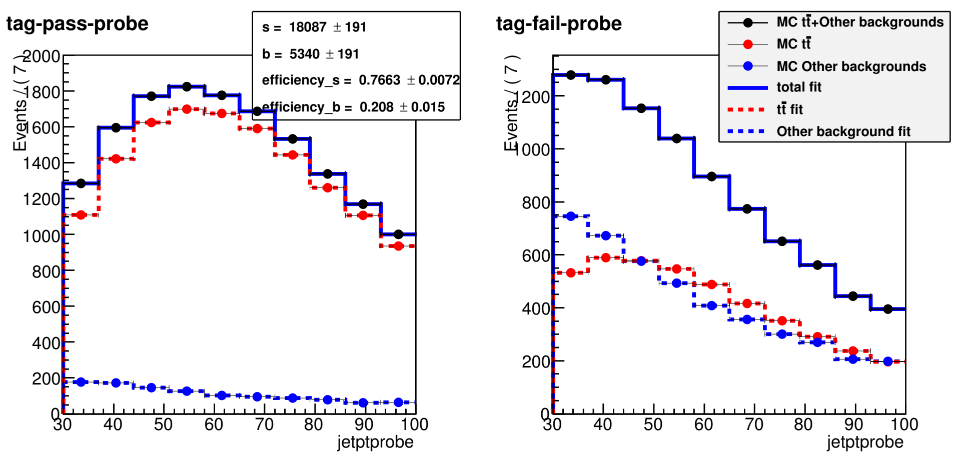

Figure 4.9.: Simultaneous fit of the *tag-pass-probe* and *tag-fail-probe* pairs in the MC.

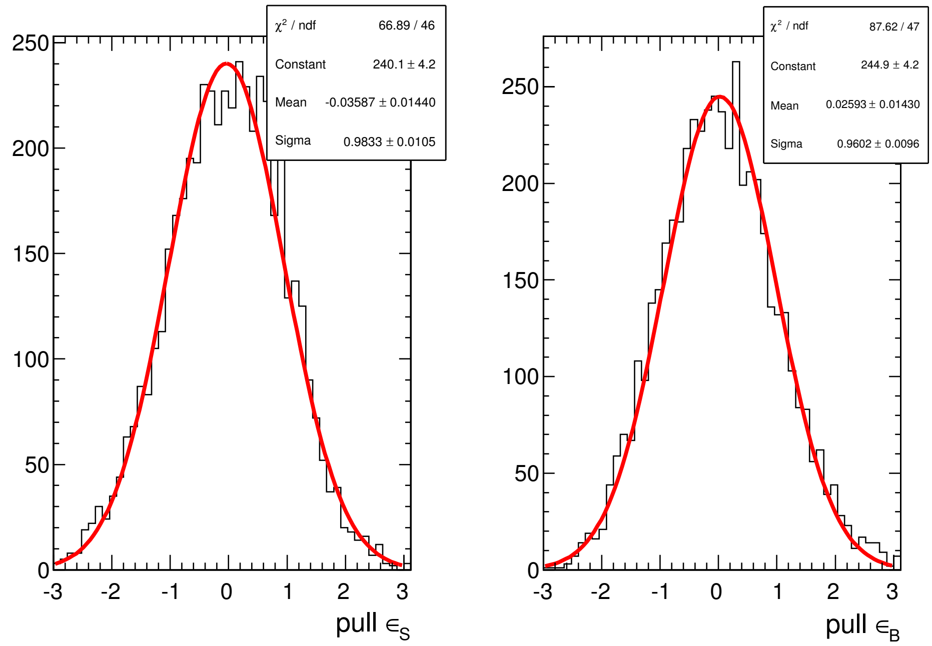

Figure 4.10.: Pulls of the ϵ_s and ϵ_b parameters in 5000 toy MC.

$$pull(\epsilon_{\mathrm{s(b)}}) = \frac{\epsilon^{\mathrm{true}}_{\mathrm{s(b)}} - \epsilon^{i}_{\mathrm{s(b)}}}{\sigma(\epsilon^{i}_{\mathrm{s(b)}})} \tag{4.17}$$

The pulls are centered on 0 and have σ close to 1, as expected.
An example fit for one of the toys is shown in Fig. 4.11

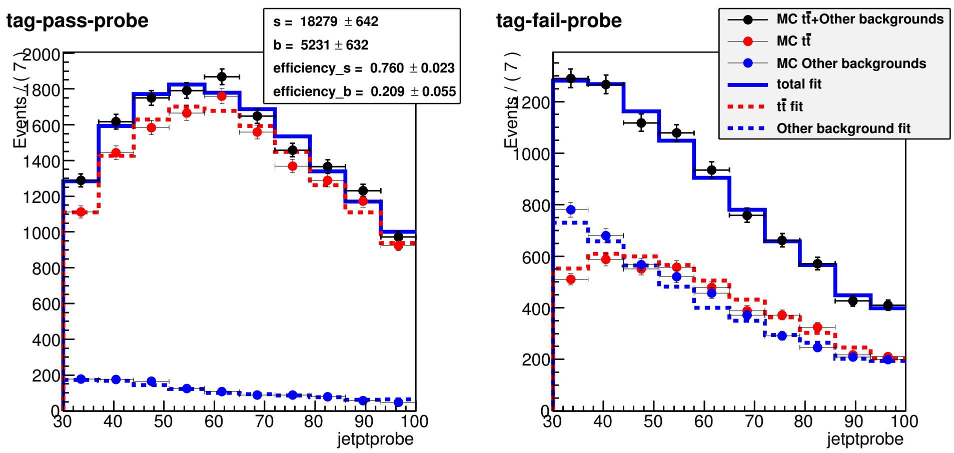

Figure 4.11.: Fit of a toy MC sample.

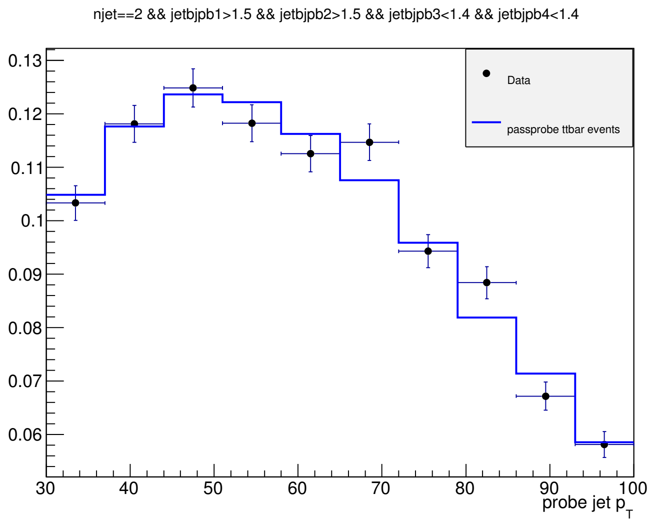

Figure 4.12.: Shape comparison for the *probe* p_T spectrum in data and in MC in a very pure $t\bar{t}$ sample.

Before running the fit on data, the shapes used in the fit have been validated. To do so, a purer top enriched phase space has been defined by requiring exactly two jets with *JetBProbability* score higher than 1.5 and no additional b-tagged jets, rejecting also jets with p_T smaller than 30 GeV. On this purer sample we have compared data against the shape used to fit the true b-jets in the *tag-pass-probe* distribution. The result is shown in Fig. 4.12 and shows good agreement.

Finally the fit has been performed on data, as shown in Fig. 4.13, providing the following efficiencies:

$$\epsilon_s^{Data} = 0.769 \pm 0.022 \tag{4.18}$$

$$\epsilon_b^{Data} = 0.121 \pm 0.054 \tag{4.19}$$

Further studies have been performed to assess the effect of the relative uncertainty on the $t\bar{t}$ and tW event fractions. The same procedure described above has been applied to different simulation templates obtained varying the $t\bar{t}$ and tW fractions within theoretical uncertainties, and the effect on the parameters extracted with the fit procedure is found to be well below the fit uncertainties.

Data driven estimation

In addition to the b-tagging efficiency, the other ingredient to estimate the $t\bar{t}$ background is the process cross section. The idea is to measure the cross section in a $t\bar{t}$ enriched control region, that is called CtrlDD. CtrlDD is defined according to the lepton preselection cuts defined in Sec. 4.3.1, and requiring in addition at least one jet with *JetBProbability* score higher than 1.4.

From the simulation we derive the factor α that connects CrtlDD to the signal region, calculating the ratio of $t\bar{t}$ events in the two regions:

$$\alpha = \frac{N^{SIG}_{t\bar{t}\ MC}}{N^{CtrlDD}_{t\bar{t}\ MC}} \quad . \tag{4.20}$$

The number of events in the CtrlDD region in data is counted, subtracting the expected number of events from non-$t\bar{t}$ backgrounds, and obtaining $N^{CtrlDD}_{t\bar{t}\ Data}$. Finally the number of expected $t\bar{t}$ events in the signal region ($N^{SIG}_{t\bar{t}\ Data}$) is obtained as:

$$N^{SIG}_{t\bar{t}\ Data} = \alpha N^{CtrlDD}_{t\bar{t}\ Data}. \tag{4.21}$$

In evaluating α and its error the b-tagging efficiencies determined in Sec. 4.4.1 are used. For each event an efficiency scale factor and a mistag rate scale factor are derived, depending on whether the event falls in the signal or CtrlDD region.

$$SF_{SIG} = \left(\frac{1-\epsilon_s^{Data}}{1-\epsilon_s^{MC}}\right)^{min(2,n_{b-jets})} \left(\frac{1-\epsilon_b^{Data}}{1-\epsilon_b^{MC}}\right)^{n_{non-b-jets}} \tag{4.22}$$

$$SF_{CtrlDD} = \left(\frac{\epsilon_s^{Data}}{\epsilon_s^{MC}}\right)^{(jet1==b-jet)} \left(\frac{\epsilon_b^{Data}}{\epsilon_b^{MC}}\right)^{(jet1==non-b-jets)} \tag{4.23}$$

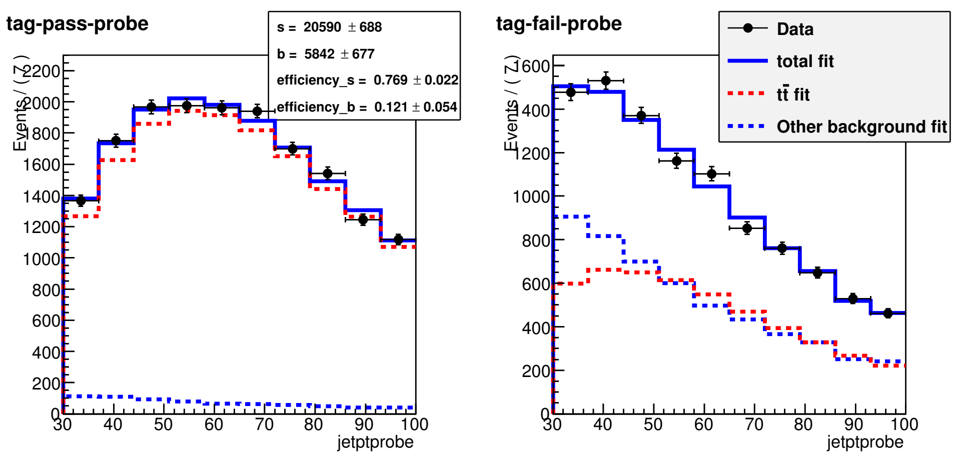

Figure 4.13.: Simultaneous fit of the *tag-pass-probe* and *tag-fail-probe* pairs in data.

where n_{b-jets} is the number of true b-jets in the event and $n_{non-b-jets}$ is the number of non-b-jets in the event. The writing $jet1 == b - jet$ ($jet1 == non - b - jets$) is a boolean flag that is true when the leading jet, the one used for the CtrlDD selection, is (not) a true b-jet.

Since the efficiency and mistag rate that have been measured on data are close to the one in the simulation, it was decided to assume a scale factor of 1 for both b-tagging efficiency and mis-tag rate. This means that the central values of the scale factors defined in Eq. 4.22 and Eq. 4.23 is 1, but these numbers have an error that is derived assuming an uncertainty on ϵ_s^{Data} and ϵ_b^{Data} that covers both the statistical error from the fit of the two quantities and the difference with respect to the simulation. This results in an up and a down variation of the scale factors in the signal and CtrlDD regions, that is used to derive an error on α.

A data driven estimation of the top quark background with the method described above is performed in each of the $p_{\mathrm{T}}^{\mathrm{H}}$ bins independently. The reason to make this estimation in $p_{\mathrm{T}}^{\mathrm{H}}$ bins, rather than inclusively is explained in Fig. 4.14, where the $p_{\mathrm{T}}^{\mathrm{H}}$ distribution is shown in the CtrlDD region normalized to the cross section measured by a specific CMS analysis [79]. As shown in the ratio plot, an overall normalization factor would not be able to accommodate for the variations of the data/simulation ratio from bin to bin.

The α factors for each bin and the number of events in signal, CtrlDD regions in MC as well as in data are listed in Tab. 4.3.

A comparison of the $m_{\ell\ell}$ distribution in the six $p_{\mathrm{T}}^{\mathrm{H}}$ bins used in the analysis in CtrlDD after the data driven correction is shown in Fig. 4.15

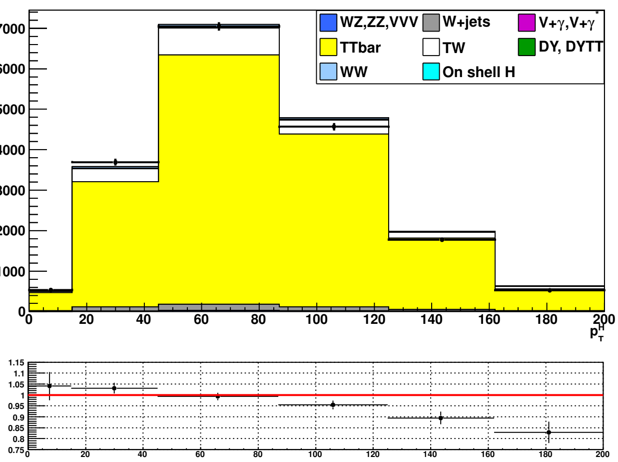

Figure 4.14.: $p_{\mathrm{T}}^{\mathrm{H}}$ distribution in the CtrlDD control region.

$p_{\mathrm{T}}^{\mathrm{H}}$ [GeV]	N_{CTRL}^{DATA}	N_{CTRL}^{TOP}	N_{SIG}^{TOP}	α	$\Delta\alpha$
[0–15]	406.71	358.78	117.83	0.328	0.075
[15–45]	2930.14	2703.44	859.08	0.318	0.071
[45–85]	5481.02	5207.48	1506.05	0.289	0.065
[85–125]	4126.35	4032.56	861.22	0.214	0.052
[125–165]	1612.64	1654.27	304.69	0.184	0.055
[165–∞]	647.50	760.37	201.70	0.265	0.147

Table 4.3.: Data driven scale factors related to the top quark background estimation.

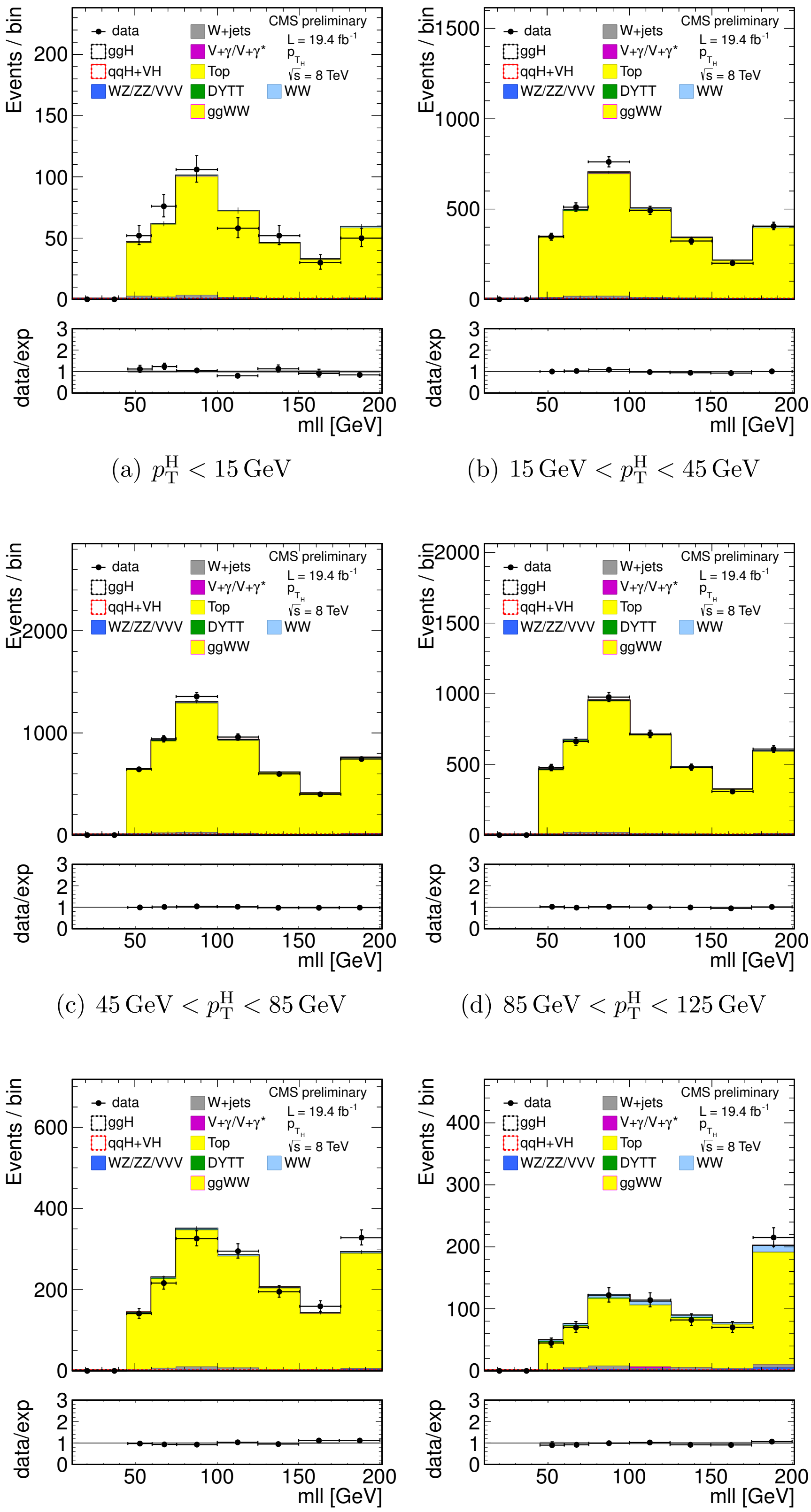

(a) $p_T^H < 15$ GeV

(b) $15\,\mathrm{GeV} < p_T^H < 45$ GeV

(c) $45\,\mathrm{GeV} < p_T^H < 85$ GeV

(d) $85\,\mathrm{GeV} < p_T^H < 125$ GeV

(e) $125\,\mathrm{GeV} < p_T^H < 165$ GeV

(f) $p_T^H > 165$ GeV

Figure 4.15.: $m_{\ell\ell}$ distributions in the CtrlDD region for the different p_T^H bins.

4.4.2. WW background

For what the qq $\rightarrow$ W$^+$W$^-$ background shape is concerned, the prediction from the simulation is used. This background is divided into six different parts, corresponding to the six $p_{\mathrm{T}}^{\mathrm{H}}$ bins defined in the analysis. The normalization of the qq $\rightarrow$ W$^+$W$^-$ background is left free to float in each bin, in such a way to adjust it in order to match the data during the fit procedure. In this way the shape difference between the $p_{\mathrm{T}}^{\mathrm{WW}}$ theory prediction and the distribution provided by the simulation, which is obtained with the MADGRAPH generator, is minimized.
In figure 4.16 a comparison is shown between the $p_{\mathrm{T}}^{\mathrm{WW}}$ spectra of two different qq $\rightarrow$ W$^+$W$^-$ samples: one obtained with the MADGRAPH generator and the other after applying to the same distribution a reweighting in order to match the theoretical prediction at NLO+NNLL precision.

A shape discrepancy can be clearly observed and the effect becomes larger at high values of $p_{\mathrm{T}}^{\mathrm{H}}$. In order to assess the effect of this discrepancy on the shapes of the variables used for the signal extraction, $m_{\ell\ell}$ and m_{T}, the shapes have been checked in all $p_{\mathrm{T}}^{\mathrm{H}}$ bins, comparing different MC samples. The MADGRAPH sample used for the nominal shape is compared to the MADGRAPH sample with NLO+NNLL reweighting, a POWHEG sample with NLO accuracy and an aMC@NLO sample. The results of this comparison are shown in figures 4.17 and 4.18. The shape discrepancy among the different models is included as an additional systematic uncertainty.

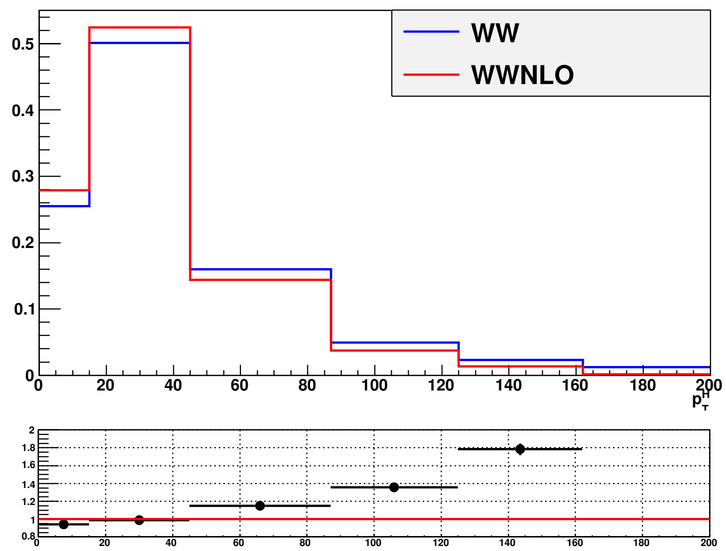

Figure 4.16.: Comparison between the $p_{\mathrm{T}}^{\mathrm{WW}}$ distributions obtained with two different MC generators: the blue line corresponds to the MADGRAPH generator and the red line refers to he same sample in which a reweighting has been applied in order to match the theoretical prediction at NLO+NNLL precision.

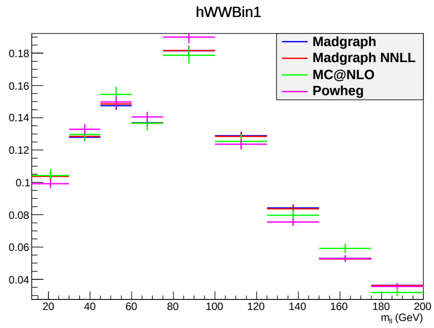

(a) $0 < p_{\mathrm{T}}^{\mathrm{H}} < 15\,\mathrm{GeV}$

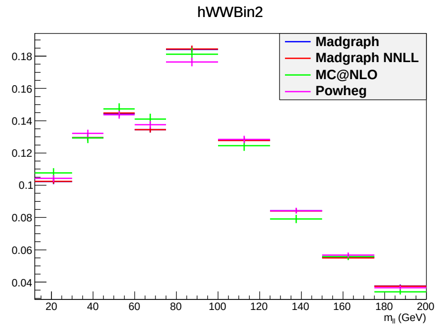

(b) $15 < p_{\mathrm{T}}^{\mathrm{H}} < 45\,\mathrm{GeV}$

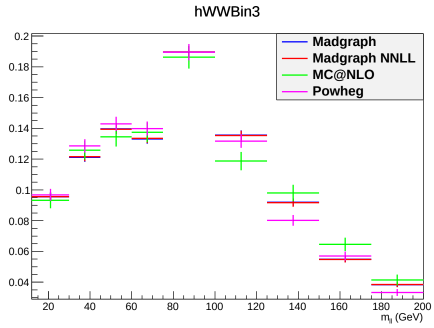

(c) $45 < p_{\mathrm{T}}^{\mathrm{H}} < 85\,\mathrm{GeV}$

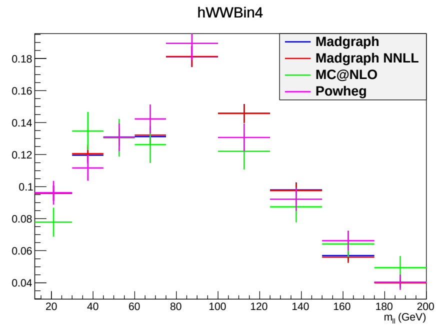

(d) $85 < p_{\mathrm{T}}^{\mathrm{H}} < 125\,\mathrm{GeV}$

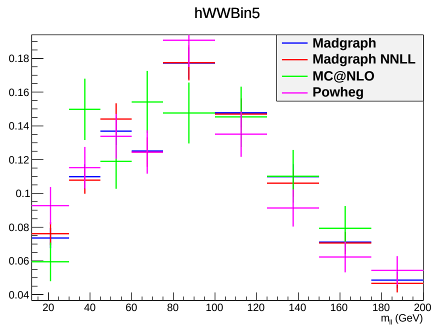

(e) $125 < p_{\mathrm{T}}^{\mathrm{H}} < 165\,\mathrm{GeV}$

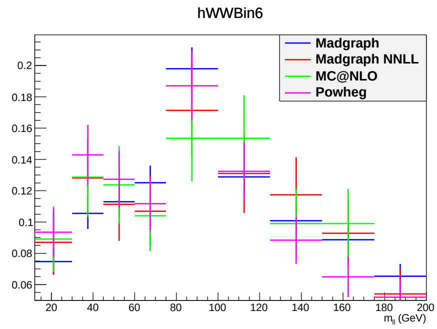

(f) $p_{\mathrm{T}}^{\mathrm{H}} > 165\,\mathrm{GeV}$

Figure 4.17.: Comparison between the default WW background sample and other theoretical models for the $m_{\ell\ell}$ distributions in every $p_{\mathrm{T}}^{\mathrm{H}}$ bin.

The gluon-induced WW process, i.e. $\mathrm{gg} \to \mathrm{W}^+\mathrm{W}^-$, has a sub-dominant contribution with respect to the quark-induced process, being the cross section ratio between the two of about 5%. The $m_{\ell\ell}$ and m_{T} shapes for this background are taken from simulation while the cross section is scaled to the approximate NLO calculation [64, 65].

The agreement of the $m_{\ell\ell}$ and m_{T} shapes between simulation and data for this background was checked in a signal-free control, defined selecting events with values of $m_{\ell\ell}$

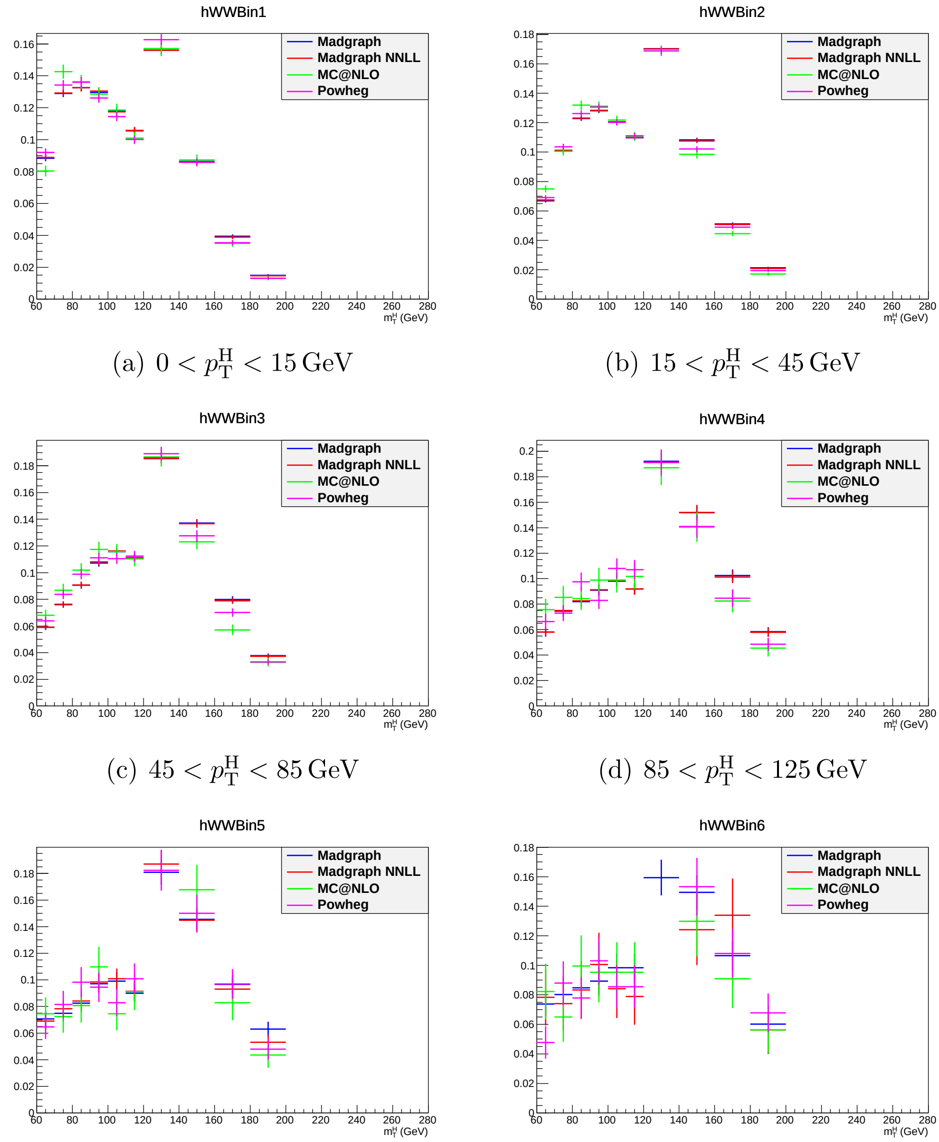

(a) $0 < p_T^H < 15\,\mathrm{GeV}$ (b) $15 < p_T^H < 45\,\mathrm{GeV}$

(c) $45 < p_T^H < 85\,\mathrm{GeV}$ (d) $85 < p_T^H < 125\,\mathrm{GeV}$

(e) $125 < p_T^H < 165\,\mathrm{GeV}$ (f) $p_T^H > 165\,\mathrm{GeV}$

Figure 4.18.: Comparison between the default WW background sample and other theoretical models for the m_T distributions in every p_T^H bin.

greater than 70 GeV. A comparison of the $m_{\ell\ell}$ and m_T shapes in data and simulation is shown in Fig. 4.19 for events containing zero and one jets, inclusive in p_T^H.

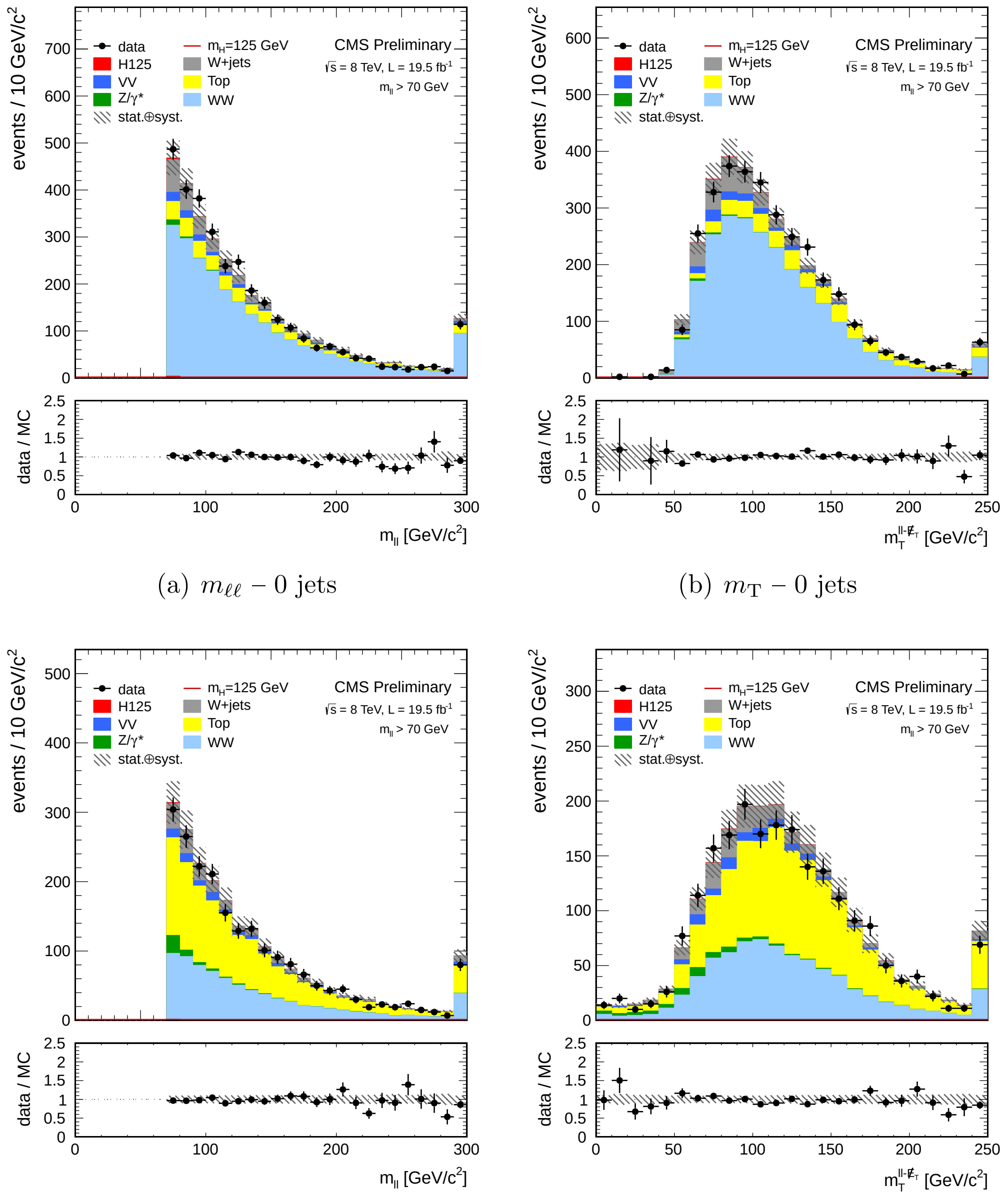

(a) $m_{\ell\ell}$ – 0 jets (b) m_{T} – 0 jets

(c) $m_{\ell\ell}$ – 1 jet (d) m_{T} – 1 jet

Figure 4.19.: Comparison of the $m_{\ell\ell}$ and m_{T} shapes in data and simulation for events with zero and 1 jets, inclusive in $p_{\mathrm{T}}^{\mathrm{H}}$. The events are required to pass the analysis requirements and, in order to define a signal-free control region, to have $m_{\ell\ell} > 70\,\mathrm{GeV}$.

4.4.3. Other backgrounds

W+jets background

Events in which W bosons are produced in association with jets, as well as multi-jet events, constitute a background for this analysis, because one or more jets can be misidentified as leptons. The rate at which jets are misidentified as leptons may be not accurately described in simulation, hence a data driven method is used to estimate this background.

The idea is to estimate the background containing one or two fake leptons selecting events with relaxed lepton quality criteria, i.e. looser with respect to the selections used at the analysis level, and computing the efficiencies for real and fake leptons to pass the tight lepton quality requirements of the analysis. A data-driven approach is pursued to estimate this background. A set of loosely selected lepton-like objects, referred to as the "fakeable object' or "denominator" from here on, is defined in a data set of events dominated by dijet production. To measure the fake rate we count how many fakeable objects pass the full lepton selection of the analysis, parameterized as a function of the phase space of the fakeable lepton, therefore it is extracted in bins of η and p_{T}. The ratio of the fully identified lepton, referred as "numerator", to the fakeable objects is taken as the probability for a fakeable object to fake a lepton:

$$Fake\ Rate = \frac{\#of\ fully\ reconstructed\ leptons}{\#of\ fakeable\ objects} \tag{4.24}$$

It is then used to extrapolate from the loose leptons sample to a sample of leptons satisfying the full selection.

The definition of the denominator is of large impact in the systematic uncertainties related to this method. For the 2012 data taking period a summary of the selections used for the numerator and the denominator of Eq. (4.24) is shown below for electrons and muons respectively. For electrons the denominator is defined by the following requirements:

- $\sigma_{\mathrm{i}\eta\mathrm{i}\eta} < 0.01(0.03)$ for barrel (endcap);
- $|\Delta\phi_{\mathrm{in}}| < 0.15(0.10)$ for barrel (endcap);
- $|\Delta\eta_{\mathrm{in}}| < 0.007(0.009)$ for barrel (endcap);
- $H/E < 0.12(0.10)$ for barrel (endcap);
- electron conversion rejection;
- $|d_0| < 0.02\,\mathrm{cm}$;
- $\frac{\sum_{\mathrm{trk}} E_{\mathrm{T}}}{p_{\mathrm{T}}^{\mathrm{ele}}} < 0.2$;
- $\frac{\sum_{\mathrm{ECAL}} E_{\mathrm{T}}}{p_{\mathrm{T}}^{\mathrm{ele}}} < 0.2$;
- $\frac{\sum_{\mathrm{HCAL}} E_{\mathrm{T}}}{p_{\mathrm{T}}^{\mathrm{ele}}} < 0.2$.

For muons the selection are loosened with respect to the tight analysis selection requiring that:

- $|d_0| < 0.02\,\mathrm{cm}$;
- MVA isolation output > -0.6.

The dijet enriched data set used for the fake rate measurement, which is selected using single lepton triggers with low p_{T} thresholds, it is not a pure sample containing just fake leptons, but may still contain prompt leptons coming from the W and Z boson decays. To reject muons from the W decay, the events are required to have $E_{\mathrm{T}}^{\mathrm{miss}} < 20\,\mathrm{GeV}$ and a W transverse mass below 20 GeV as well. Muons from the Z decay are instead remove requiring $m_{\mu\mu} > 20\,\mathrm{GeV}$ and $m_{\mu\mu} \notin [76, 106]\,\mathrm{GeV}$. For electrons the Z mass peak veto is enlarged to $m_{\mathrm{ee}} \notin [60, 120]\,\mathrm{GeV}$. Finally both electrons and muons are required to be isolated from the leading jet in the event, i.e. $\Delta\phi(\ell, j) > 1$. The residual prompt lepton contamination from EW processes such as W/Z+jets production, which can bias the fake rate measurement, is estimated using simulation and subtracted from both the numerator and denominator. The contamination from EW processes is different for the numerator and denominator and is particularly important for relatively high lepton p_{T} values.

In addition to the fake rate, also a prompt lepton rate is evaluated, defined as the probability of a prompt lepton passing the loose requirements to also pass the tight analysis selections. The prompt rate is also measured in data, defining a control region enriched in $\mathrm{Z} \to \ell\ell$ events, selecting dilepton events with an invariant mass of the two leptons in the Z peak mass region.

Both the fake and prompt rate are used to reweight the data samples used in the analysis in order to obtain directly from data the contribution of the fake lepton background. The method to apply those rates is explained below in the simple case of just one lepton in the data sample, i.e. data selected by single lepton triggers, but can be straightforwardly generalized to situations with more than one lepton. Suppose that the total number of leptons passing the loose requirements, N_ℓ, is made up of N_p prompt and N_f fake leptons. N_p and N_f cannot be directly measured but one can measure the number of events where no leptons, N_{t0}, or one lepton, N_{t1}, pass the tight analysis requirement. These numbers are related by the following equations:

$$\begin{aligned} N_\ell = N_p + N_f &= N_{t0} + N_{t1} \\ N_{t0} &= (1-p)N_p + (1-f)N_f \\ N_{t1} &= pN_p + fN_f \end{aligned} \tag{4.25}$$

where p and f are the prompt and fake rates respectively. Equation (4.25) can be inverted to obtain the number of prompt and fake leptons:

$$\begin{aligned} N_p &= \frac{1}{p-f}\left[(1-f)N_{t1} - fN_{t0}\right] \\ N_f &= \frac{1}{p-f}\left[pN_{t0} - (1-p)N_{t1}\right] \end{aligned} \tag{4.26}$$

The number of fake events passing the tight analysis requirement is $N_{\text{fake}} = fN_f$. The fake background contribution is estimated directly from data, applying the kinematics-dependent weights (f and p are estimated in bins of p_{T} and η) defined in Eq.(4.26).

The prompt and fake rate estimations after the removal of the EW contribution are shown in Tables 4.4 and 4.5 separately for electrons and muons.

Table 4.4.: Measured prompt rate for electrons and muons in bins of η, p_{T}. Only the statistical uncertainties are shown.

Electron prompt rate			
p_{T} range [GeV]	$0 < \eta \leq 1.4442$	$1.4442 < \eta \leq 1.566$	$1.566 < \eta$
$10 < p_{\mathrm{T}} \leq 15$	0.5738 ± 0.0045	0.5366 ± 0.0204	0.2947 ± 0.0047
$15 < p_{\mathrm{T}} \leq 20$	0.7091 ± 0.0020	0.5484 ± 0.0185	0.4477 ± 0.0034
$20 < p_{\mathrm{T}} \leq 25$	0.7175 ± 0.0013	0.6297 ± 0.0067	0.6200 ± 0.0001
$25 < p_{\mathrm{T}} \leq 50$	0.9219 ± 0.0002	0.8404 ± 0.0007	0.8509 ± 0.0001
$p_{\mathrm{T}} > 50$	0.9693 ± 0.0002	0.9398 ± 0.0021	0.9385 ± 0.0005

Muon prompt rate		
p_{T} range [GeV]	$0 < \eta \leq 1.5$	$1.5 < \eta \leq 2.5$
$10 < p_{\mathrm{T}} \leq 15$	0.7119 ± 0.0003	0.7582 ± 0.0006
$15 < p_{\mathrm{T}} \leq 20$	0.8049 ± 0.0018	0.8495 ± 0.0001
$20 < p_{\mathrm{T}} \leq 25$	0.9027 ± 0.0008	0.8948 ± 0.0012
$25 < p_{\mathrm{T}} \leq 50$	0.9741 ± 0.0001	0.9627 ± 0.0002
$p_{\mathrm{T}} > 50$	0.9900 ± 0.0001	0.9875 ± 0.0003

The region obtained by reversing the opposite sign lepton requirement in the analysis selection is enriched with W+jets events where one of the jets is misidentified as a lepton. The fake rate procedure can be applied to this same-sign control region to perform a closure test of the method. The results of the closure test on same-sign events gives good agreement with the expectations.

The systematic uncertainty on the prompt and fake rate estimation is evaluated by varying the jet thresholds in the dijet control sample, and an uncertainty on the background normalization is added according to the agreement with data in the same-sign control region. The systematic uncertainty amounts to about 36% of the fake background yield.

Drell-Yan to $\tau\tau$ background

The low $E_{\mathrm{T}}^{\mathrm{miss}}$ threshold in the eμ final state requires the consideration of the contribution from $Z/\gamma^* \to \tau^+\tau^-$, that estimated from data. This is accomplished by selecting $Z/\gamma^* \to$

Table 4.5.: Measured electrons and muons fake rates in bins of η and p_{T}, after the EWK correction. Only statistical uncertainties are shown.

electron fake rate				
p_{T} range [GeV]	$0 < \eta \leq 1$	$1 < \eta \leq 1.479$	$1.479 < \eta \leq 2$	$2 < \eta \leq 2.5$
$10 < p_{\mathrm{T}} \leq 15$	0.045 ± 0.005	0.033 ± 0.004	0.008 ± 0.002	0.021 ± 0.005
$15 < p_{\mathrm{T}} \leq 20$	0.044 ± 0.003	0.049 ± 0.003	0.017 ± 0.001	0.017 ± 0.002
$20 < p_{\mathrm{T}} \leq 25$	0.041 ± 0.002	0.064 ± 0.003	0.025 ± 0.002	0.025 ± 0.002
$25 < p_{\mathrm{T}} \leq 30$	0.059 ± 0.003	0.101 ± 0.005	0.041 ± 0.003	0.043 ± 0.003
$30 < p_{\mathrm{T}} \leq 35$	0.084 ± 0.006	0.111 ± 0.009	0.058 ± 0.006	0.066 ± 0.005
muon fake rate				
p_{T} range [GeV]	$0 < \eta \leq 1$	$1 < \eta \leq 1.479$	$1.479 < \eta \leq 2$	$2 < \eta \leq 2.5$
$10 < p_{\mathrm{T}} \leq 15$	0.131 ± 0.002	0.154 ± 0.004	0.194 ± 0.005	0.241 ± 0.009
$15 < p_{\mathrm{T}} \leq 20$	0.143 ± 0.007	0.191 ± 0.012	0.235 ± 0.016	0.308 ± 0.027
$20 < p_{\mathrm{T}} \leq 25$	0.198 ± 0.005	0.239 ± 0.009	0.221 ± 0.011	0.271 ± 0.021
$25 < p_{\mathrm{T}} \leq 30$	0.182 ± 0.011	0.228 ± 0.018	0.195 ± 0.022	0.287 ± 0.045
$30 < p_{\mathrm{T}} \leq 35$	0.170 ± 0.021	0.244 ± 0.036	0.195 ± 0.041	0.289 ± 0.111

$\mu^+\mu^-$events in data and replacing both muons with a simulated $\tau \to \ell\nu_\tau\bar{\nu}_\ell$ decay [54], thus obtaining a "hybrid" event. The Z boson four-momentum is reconstructed in data from the four-momenta of the daughter muons. Then a simulation step allows the replacement of the muon objects with τ leptons, in such a way to preserve the Z boson momentum direction is preserved in its rest frame. The $Z/\gamma^* \to \tau^+\tau^-$decay is simulated with the TAUOLA package [80] to correctly describe the τ-polarization effects.

After replacing muons from $Z/\gamma^* \to \mu^+\mu^-$decays with simulated τ decays, the set of pseudo-$Z/\gamma^* \to \tau^+\tau^-$events undergoes the reconstruction step. Good agreement in kinematic distributions for this sample and a MC based $Z/\gamma^* \to \tau^+\tau^-$sample is found. The global normalization of pseudo-$Z/\gamma^* \to \tau^+\tau^-$events is checked in the low m_{T} spectrum where a rather pure $Z/\gamma^* \to \tau^+\tau^-$sample is expected.

This method allows to avoid the simulation of very large MC samples that would be needed for an accurate description of this process.

ZZ, WZ and Wγ backgrounds

The WZ and ZZ backgrounds are partially estimated from data when the two selected leptons come from the same Z boson. If the leptons come from different bosons the contribution is expected to be small. The WZ component is largely rejected by requiring only two high p_{T} isolated leptons in the event.

The $W\gamma^{(*)}$ background, where the photon decays to an electron-positron pair, is expected to be very small, thanks to the stringent photon conversion requirements. This background also includes events where a real photon is produced in association with the W boson. These events constitute a background for this analysis because the photon can interact with the tracker material converting to an electron-positron pair.

Since the WZ simulated sample has a generation level cut on the di-lepton invariant mass ($m_{\ell\ell} > 12$ GeV) and the cross-section raises quickly with the lowering of this threshold, a dedicated MADGRAPH sample has been produced with lower momentum cuts on two of the three leptons ($p_{\mathrm{T}} > 5$ GeV) and no cut on the third one. The surviving contribution estimated with this sample is still very small, and since the uncertainty on the cross-section for the covered phase space is large, a conservative 100% uncertainty has been given to it. A k-factor for $W\gamma^*$ of 1.5 ± 0.5 based on a dedicated measurement of tri-lepton decays, $W\gamma^* \to e\mu\mu$ and $W\gamma^* \to \mu\mu\mu$, is applied [54]. The contribution of $W\gamma^{(*)}$ is also constrained by a closure test with same sign leptons on data, which reveals a good compatibility of the data with the expected background.

4.5. Systematic uncertainties

Systematic uncertainties play an important role in this analysis where no strong mass peak is expected due to the presence of undetected neutrinos in the final state. One of the most important sources of systematic uncertainty is the normalization of the backgrounds that are estimated on data control samples whenever is possible.

A summary of the main sources of systematic uncertainty and the corresponding estimate is reported in Table 4.6. A detailed description of each source of systematic uncertainty is discussed in the following sections.

4.5.1. Background normalization uncertainties

The signal extraction is performed subtracting the estimated backgrounds to the event counts in data. This uncertainty depends on the background:

- **$\mathrm{t\bar{t}}$ and tW backgrounds:** The efficiency on jets b-tagging is estimated using the Tag&Probe technique in data and simulation control regions, as explained in 4.4.1. A per-jet scale factor, which takes into account the possibly different efficiency of the anti b-tagging selection in data and simulation, is computed by means of the efficiency measured with the Tag&Probe method. The Tag&Probe method has been used also to measure the mistag rates in data and simulation, which are the probability to b-tag a jet that is not produced by the hadronization of a b quark. These factors are used to reweigh the Top MC samples as explained in 4.4.1. The uncertainties provided by the Tag&Probe fit are then propagated to the factor α that is used in the top data driven estimation 4.4.1. These uncertainties are embedded in a systematic error that affects the shape of the Top background in each $p_{\mathrm{T}}^{\mathrm{H}}$ bin.

Table 4.6.: Main sources of systematic uncertainties and their estimate. The first category reports the uncertainties in the normalization of background contributions. The experimental and theoretical uncertainties refer to the effect on signal yields. A range is specified if the uncertainty varies across the p_T^H bins.

Uncertainties in backgrounds contributions	
Source	Uncertainty
$t\bar{t}$, tW	20–50%
W+ jets	40%
WZ, ZZ	4%
$W\gamma^{(*)}$	30%
Effect of the experimental uncertainties on the signal and background yields	
Source	Uncertainty
Integrated luminosity	2.6%
Trigger efficiency	1–2%
Lepton reconstruction and identification	3–4%
Lepton energy scale	2–4%
E_T^{miss} modelling	2%
Jet energy scale	10%
Pileup multiplicity	2%
b mistag modelling	3%
Effect of the theoretical uncertainties on signal yield	
Source	Uncertainty
b jet veto scale factor	1–2%
PDF	1%
WW background shape	1%

Provided that the simulated samples include both $t\bar{t}$ and tW processes, a systematic uncertainty related to the $tW/t\bar{t}$ fraction has been included. In fact, a relative variation of the contribution of these two processes could modify the shape of the MC sample, and is thus included as a shape uncertainty affecting the top quark background shape in each p_T^H bin in a correlated way.

- **W+jets background:** It is estimated with data control sample as described in Sec.4.4.3. With $19.4\,\mathrm{fb}^{-1}$ at 8 TeV, the uncertainty receives similar contributions from statistics and systematic error (mainly jet composition differences between the fake rate estimation sample and the application sample), the total error being about 40%, dominated by the closure test of the method on a same-sign control region.

- **WZ,ZZ,W$\boldsymbol{\gamma^{(*)}}$ backgrounds:** those backgrounds, which are expected to give a small contribution, are estimated from simulation. Uncertainties on the cross sections reported in [81, 82] are 4% for WZ and 2.5% for ZZ. A 30% uncertainty is assigned to the $W\gamma$ [83] yield and another 30% on $W\gamma^{(*)}$ contribution according to the uncertainty on the normalization study (see Sec. 4.4.3).

4.5.2. Experimental uncertainties

The following experimental systematic sources have been taken into account:

- **Luminosity:** Using the online luminosity monitoring CMS reached an uncertainty on the luminosity of 2.6% at 8 TeV.
- **Trigger efficiency.** The uncertainties for both electrons and muons are at 1-2% level, which is added together to the lepton efficiency uncertainty.
- **Lepton reconstruction and identification efficiency:** The lepton reconstruction and identification efficiencies are measured with the Tag&Probe method in data. To correct for the difference in the lepton identification efficiencies between data and MC, a scale factor is applied to MC. The uncertainties resulting from this procedure on the lepton efficiencies are 4% for electrons and 3% for muons.
- **Muon momentum and electron energy scale:** The momentum scale of leptons have relatively large uncertainties due to different detector effects. For electrons a scale uncertainty of 2% for the barrel, and 4% for the endcaps respectively, is assigned. For muons, a momentum scale uncertainty of 1.5%, independent of its pseudorapidity, is assigned.
- **$\boldsymbol{E_{\mathrm{T}}^{\mathrm{miss}}}$ modeling:** The $E_{\mathrm{T}}^{\mathrm{miss}}$ measurement is affected by the possible mis-measurement of individual particles addressed above, as well as the additional contributions from the pile-up interactions. The effect of the missing transverse momentum resolution on the event selection is studied by applying a Gaussian smearing of 10% on the x- and y-components of the missing transverse momentum. All correlated variables, like the transverse mass, are recalculated.
- **Jet energy scale (JES) uncertainties:** It affects both the jet multiplicity and the jet kinematic variables, such as m_{jj}. We estimate this uncertainty applying variations of the official jet uncertainties on the JES (which depend on η and p_{T} of the jet [84]) and compute the variation of the selection efficiency.
- **b jets mistag modeling:** A fraction of signal events is rejected because erroneously identified as b jets by the b-tagging algorithms. The mistag rate, as measured with the Tag&Probe technique described in Sec. 4.4.1, comes with an uncertainty due to different modeling of the b-tagging performance in data and simulation.
- **Pileup multiplicity:** Some of the variables used in the analysis are affected by the average number of pileup interactions. The simulated events have been reweighted according the instantaneous luminosity measured on data. The error in the average

number of pileup interactions measured in data and the simulation of the modeling and physics aspects of the pileup simulation gives an uncertainty of 5% on the distribution used in the reweighting procedure. This uncertainty is propagated through all the analysis, and the estimated uncertainty on the efficiency is 2%.

4.5.3. Theoretical uncertainties

- **QCD scale uncertainties:** The uncertainties on the total cross sections due to the choice of the renormalization and factorization scale are assigned to MC-driven backgrounds. For the signal processes these uncertainties are separated in two categories: those affecting the selection efficiency and those affecting the jet bin fractions. The effect of renormalization and factorization scale on the selection efficiency is of the order of 2% for all processes. Although this analysis is inclusive in number of jets, the effect of the QCD scale variation on the jet bin migrations has to be taken into account because of the b-tagging veto efficiency. The efficiency of this selection depends on jet multiplicity and the effect of the QCD scale variation has been evaluated using the Stewart-Tackman method, as explained in 4.5.3.
- **PDFs uncertainties:** The utilization of different PDF sets can affect both the normalization and the shapes of the signal contributions. The uncertainty related due to the variations in the choice of PDFs is considered following the PDF4LHC [85, 86] prescription, using CT10, NNPDF2.1 [87] and MSTW2008 [88] PDF sets.
- **WW:** Due to the fact that the WW shape is entirely taken from simulation, the analysis is strongly relying on theoretical models and can thus be strongly affected by their uncertainties. Especially higher order QCD radiative effects have an influence on the generated WW shape. To study this impact, the shapes of the distributions produced with the MadGraph generator (which is the generator for the MC simulation used in the analysis) are compared to the ones produced with mc@nlo. The comparison is performed separately in each bin of p_T^H and the uncertainty includes shape differences originating from the renormalization and factorization scale choice. A comparison of the $m_{\ell\ell}$ and m_T shapes for the WW background using different MC generators is reported in section 4.4.2.

Jet multiplicity uncertainty

The jet bin uncertainty on the ggH production mode has been evaluated using the Stewart-Tackman method, following the recipe proposed in Refs. [53, 89]. Three independent nuisance parameters have to be associated with the inclusive ggH production cross sections $\sigma_{\geq 0}$, $\sigma_{\geq 1}$ and $\sigma_{\geq 2}$, which corresponds to the cross sections with ≥ 0 jets, ≥ 1 jet and ≥ 2 jets respectively. According to the agreement on the treatment of uncertainties in the combination of ATLAS and CMS results [90], these nuisance parameters are labelled as *QCDscale_ggH*, *QCDscale_ggH1in* and *QCDscale_ggH2in*. However, in case the analysis is split in exclusive jet multiplicity bins, the jet bin uncertainties can be evaluated taking into account the correct correlations among the three nuisances following the Stewart-Tackman prescription. Even though this analysis is inclusive in number of jets, the jet binning uncertainties must be included due to the presence of the b-jet veto, that introduces a dependency of the selection efficiency on the number of jets in the event. The veto efficiency has been evaluated in all the $p_{\mathrm{T}}^{\mathrm{H}}$ bins defined in the analysis and as a function of jets multiplicity. The results are shown in Figs. 4.20(a) and 4.20(b). The drop of the veto efficiency at high values of $p_{\mathrm{T}}^{\mathrm{H}}$ is due to the correlation with jets multiplicity.

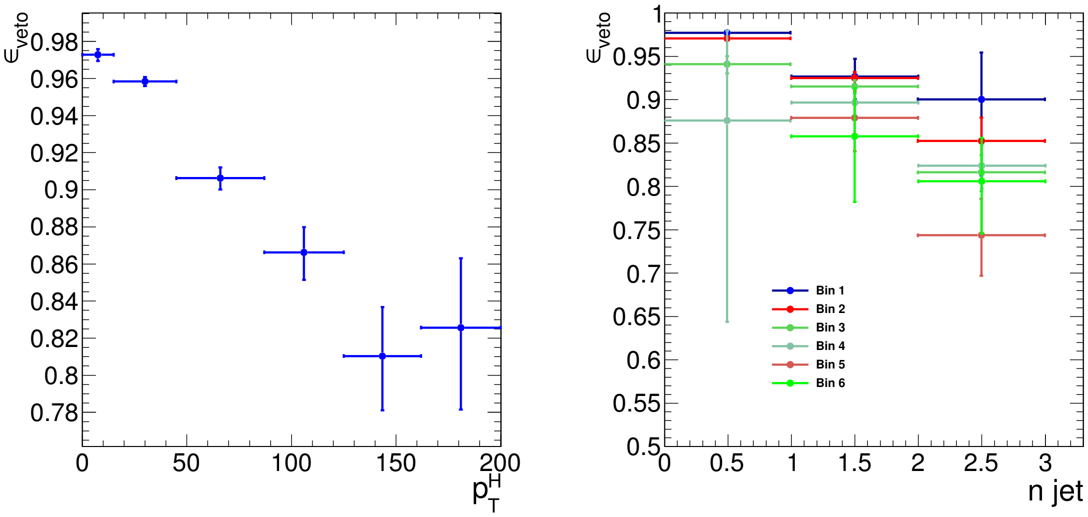

(a) (b)

Figure 4.20.: (a) Efficiency of the b-tagging veto in different bins of $p_{\mathrm{T}}^{\mathrm{H}}$. (b) Efficiency of the b-tagging veto in different bins of $p_{\mathrm{T}}^{\mathrm{H}}$, as a function of number of jets.

The first step of this procedure is to take the inclusive ggH cross section, σ_{ggH}, and to convert the relative QCD up/down scale uncertainties, ϵ_+ and ϵ_-, to a log-normal uncertainty, i.e. $\kappa = \sqrt{\exp(\epsilon_+) \cdot \exp(\epsilon_-)}$. The exclusive cross sections, σ_0, σ_1 and σ_2, can be calculated starting from σ_{ggH} and using the selection efficiencies for the three jet bins. For every exclusive cross section the corresponding relative uncertainty is computed varying the renormalization (μ_R) and factorization (μ_F) scales independently of a factor 2 and 1/2, and taking the cross section value corresponding to half of the maximum variation. The inclusive cross sections are then obtained summing the exclusive cross sections and propagating the uncertainties, i.e. $\sigma_{\geq 0} = \sigma_0 + \sigma_1 + \sigma_2$, $\sigma_{\geq 1} = \sigma_1 + \sigma_2$, $\sigma_{\geq 2} = \sigma_2$.

The three nuisance parameters, including all the proper correlations among the jet bins, are defined according to Table 4.7, where the f_n constants represent the exclusive theoretical n jet bin fractions, i.e. $f_0 = \sigma_0/\sigma_{\geq 0}$, $f_1 = \sigma_1/\sigma_{\geq 0}$, $f_2 = \sigma_2/\sigma_{\geq 0}$.

Table 4.7.: Numerical calculation for the systematic uncertainties of jet binning.

Nuisance parameter	0-jet bin	1-jet bin	2-jet bin
QCDscale_ggH	$\Delta^0_{\geq 0} = (\kappa_{\geq 0})^{\frac{1}{f_0}}$		
QCDscale_ggH1in	$\Delta^0_{\geq 1} = (\kappa_{\geq 1})^{-\frac{f_1+f_2}{f_0}}$	$\Delta^1_{\geq 1} = (\kappa_{\geq 1})^{\frac{f_1+f_2}{f_1}}$	
QCDscale_ggH2in		$\Delta^1_{\geq 2} = (\kappa_{\geq 2})^{-\frac{f_2}{f_1}}$	$\Delta^2_{\geq 2} = (\kappa_{\geq 2})$

The nuisance parameters reported in table 4.7 have then been calculated for each p_T^H bin embedding the b-jet veto efficiency and using the following formulas:

$$QCDscale\_ggH = \frac{\Delta^0_{\geq 0} \cdot f_0 \cdot \varepsilon_0 + \Delta^0_{\geq 1} \cdot f_1 \cdot \varepsilon_1}{\Delta^0_{\geq 0} \cdot f_0 \cdot \varepsilon_0 + \Delta^0_{\geq 1} \cdot f_1 \cdot \varepsilon_0} \quad , \tag{4.27}$$

$$QCDscale\_ggH1in = \frac{\Delta^1_{\geq 1} \cdot f_1 \cdot \varepsilon_1 + \Delta^1_{\geq 2} \cdot f_2 \cdot \varepsilon_2}{\Delta^1_{\geq 1} \cdot f_1 \cdot \varepsilon_1 + \Delta^1_{\geq 2} \cdot f_2 \cdot \varepsilon_1} \quad , \tag{4.28}$$

$$QCDscale\_ggH2in = 1 \quad , \tag{4.29}$$

where ε_0, ε_1 and ε_2 are the selection efficiencies for the three jet categories. These nuisance parameters are expected to be equal to one in case the efficiency is independent on the number of jets, i.e if $\varepsilon_0 = \varepsilon_1 = \varepsilon_2$.
The numerical values obtained following this procedure are reported in Table 4.8 for each p_T^H bin.

4.5.4. Statistics uncertainty of the simulated samples

Due to the large range of weights used to correct the simulated distributions in order to match those in data, the effective size of the MC samples are sometimes smaller than the actual number of events in the sample. The statistical uncertainties of the event yields estimated from MC samples are included as nuisance parameters in the fit and have a small impact on the final result.

Table 4.8.: Values of the jet binning nuisance parameters for different $p_{\mathrm{T}}^{\mathrm{H}}$ bins.

Nuisance parameter	$p_{\mathrm{T}}^{\mathrm{H}}$ bin [GeV]					
	[0-15]	[15-45]	[45-85]	[85-125]	[125-165]	[165-∞]
QCDscale_ggH	0.998	0.993	0.989	1.000	1.000	1.000
QCDscale_ggH1in	0.997	0.993	0.984	0.975	0.946	0.974

4.5.5. Treatment of systematic uncertainties in the shape analysis

One can distinguish between normalization uncertainties, where a systematic effect is changing the normalization of a given process assuming the shape is not affected, and shape uncertainties where the actual change in the shape of the distribution is taken into account. The normalization uncertainties enter the shape analysis as a constant normalization factor, whereas for shape uncertainties the nominal and the $+1\sigma$ and -1σ shapes enter the analysis in form of three histograms with the same normalization.

For the W+jets background, the shape differences for different jet p_{T} thresholds in the di-jet control sample are considered separately for electron and muon fakes, while the other sources of systematics are taken as normalization uncertainties as in the cut-based analysis.

Effects from experimental uncertainties are studied by applying a scaling and smearing of certain variables of the physics objects, followed by a subsequent recalculation of all the correlated variables. This is done for simulation, to account for possible systematic mis-measurements of the data. All experimental sources from Section 4.5.2 but luminosity are treated both as normalization and shape uncertainties. For background with a data-driven normalization estimation, only the shape uncertainty is considered.

To account for statistical uncertainties, for each distribution going into the shape analysis, the $+1\sigma$ and -1σ shapes were obtained by adding/subtracting the statistical error in each bin and renormalizing it to the nominal distribution. In addition to this procedure a constant normalization uncertainty due to the finite statistics of the MC sample used to extract the shape is assigned.

4.6. Signal extraction

According to the "blinding" policy of the CMS Collaboration, the strategy of the analysis has been scrutinized and approved by a selected committee of internal reviewers before looking at the data in the signal region. This approach prevents the analysts from being biased by the data in the developing phase of the analysis. Below are shown the results after having looked at the data.

4.6.1. Fitting procedure

The signal, including ggH, VBF, and VH production mechanisms, is extracted in each bin of p_T^H by performing a binned maximum likelihood fit simultaneously in all p_T^H bins to a two-dimensional template for signals and backgrounds in the $m_{\ell\ell}$–m_T plane. The variables used for the two-dimensional template are chosen for their power to discriminate signal and background contributions. This is shown in Fig. 4.21, where the two-dimensional MC distributions are shown for the signal and background processes in the 0-jets category.

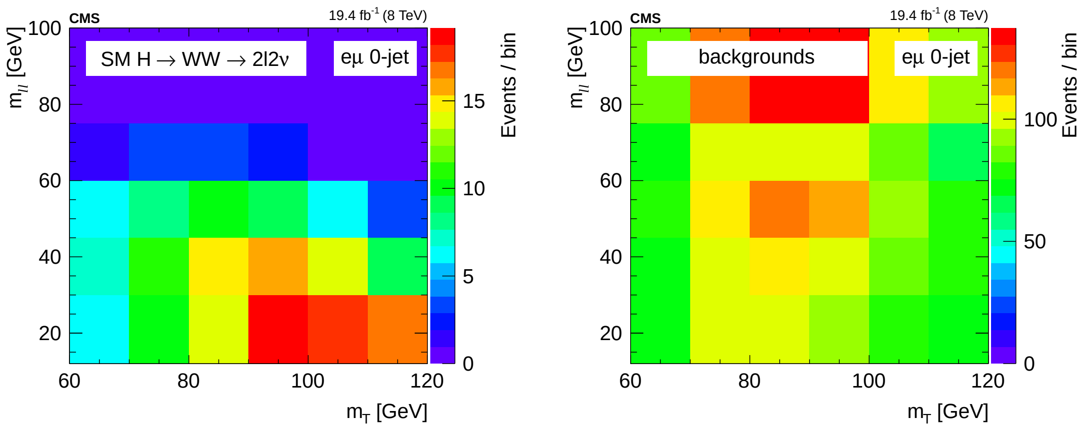

(a) (b)

Figure 4.21.: Two-dimensional $m_{\ell\ell}$–m_T distribution for signal (a) and background (b) processes in the 0-jets category.

Six different signal strength parameters are extracted from the fit, one for each p_T^H bin. The relative contributions of the different Higgs production mechanisms in the signal template are taken to be the same as in the SM. The systematic uncertainty sources are considered as nuisance parameters in the fit.

The binning of the $m_{\ell\ell}$ and m_T templates is chosen to be:

- $m_{\ell\ell}$: $[12, 30, 45, 60, 75, 100, 125, 150, 175, 200]$
- m_T: $[60, 70, 80, 90, 100, 110, 120, 140, 160, 180, 200, 220, 240, 280]$

To avoid a dependence of the results on the variables used for the template fit, $m_{\ell\ell}$ and m_T need to be uncorrelated with respect to p_T^H. This as been verified and the correlation between the discriminating variables and p_T^H is shown in Fig. 4.22 and Fig. 4.23 for ggH and VBF production modes respectively.

The relative contribution for different production mechanisms in the input signal template is taken to be the same as the SM. The signal strength μ in each bin, i.e. the ratio between the measured cross section and the SM one, $\mu = \sigma/\sigma_{SM}$, is allowed to float between -10 and +10, thus allowing negative values. This is mainly intended to allow the error bars to float below 0.

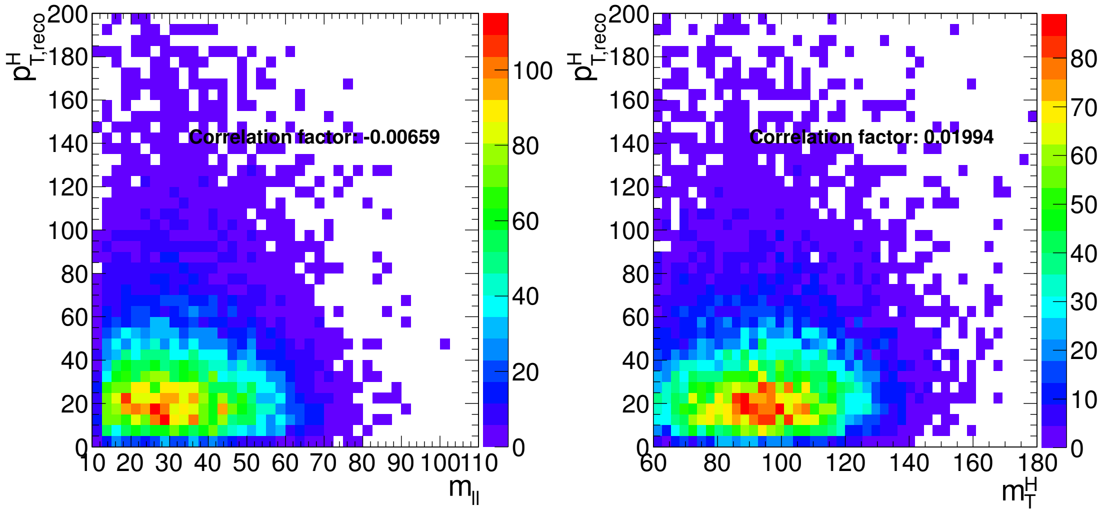

(a) (b)

Figure 4.22.: Correlation between p_T^H and $m_{\ell\ell}$ (a) and between p_T^H and m_T (b) after the full selection for the ggH production mode.

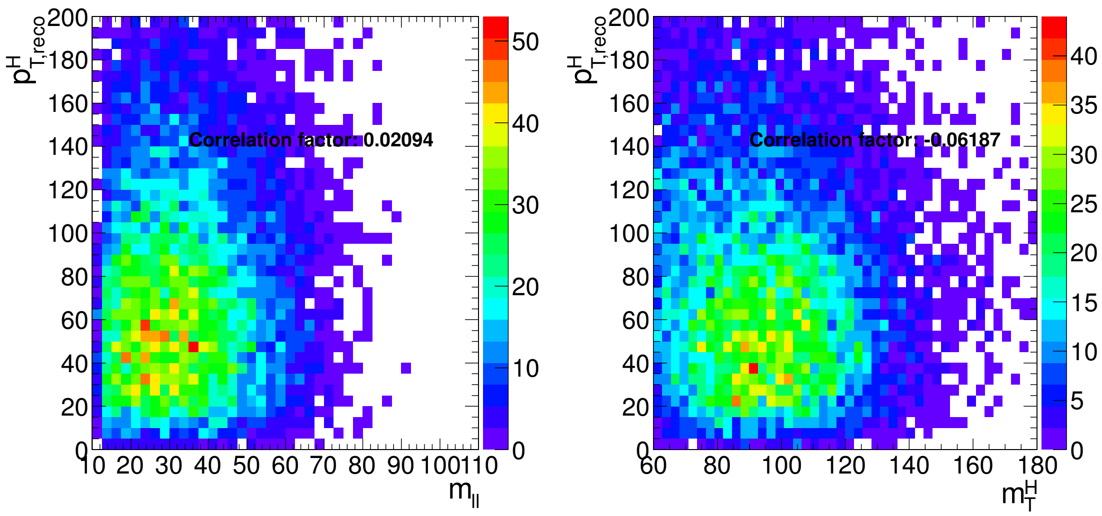

(a) (b)

Figure 4.23.: Correlation between p_T^H and $m_{\ell\ell}$ (a) and between p_T^H and m_T (b) after the full selection for the VBF production mode.

Because of detector resolution effects, some of the reconstructed $H \to WW$ signal events might originate from outside the fiducial phase space. These out-of-fiducial signal events cannot be precisely handled by the unfolding procedure and must be subtracted from the measured spectrum. The p_T^H distribution of the out-of-fiducial signal events is taken from simulation, and each bin is multiplied by the corresponding measured signal strength before performing the subtraction.

At the end, the number of events in each bin i of the measured spectrum is:

$$N_i = \mu_i(s_i - f_i) \quad , \tag{4.30}$$

where s_i and f_i are respectively the number of signal and fake events expected from simulation and μ_i is the measured signal strength.

The fit makes use of the binned maximum likelihood approach.The likelihood function, $\mathcal{L}$, restricted to the p_T^H bin j, can be written as: CHECK!!

$$\mathcal{L}(data|\mu_j,\theta) = \prod_{i=0}^{N_{\text{bins}}} \frac{(\mu_j s_i(\theta) + b_i(\theta))^{n_i}}{n_i!} e^{-\mu_j s_i(\theta) - b_i(\theta)} \cdot p(\tilde{\theta}|\theta) \quad , \tag{4.31}$$

where *data* corresponds to the experimental observation and μ_j is the signal strength in the bin j, i.e. the parameter of interest of the fit, which multiplies the signal yield. The index i runs over the bins of the $m_{\ell\ell}$-m_T two-dimensional histogram corresponding the p_T^H bin j, s_i and b_i are the expected number of signal and background events respectively in bin i, and n_i is the total number of observed events in bin i. The set of parameters θ represents the full suite of nuisance parameters used to incorporate the systematic uncertainties. Each nuisance parameter is constrained in the fit including the prior distributions functions $p(\tilde{\theta}|\theta)$ in the likelihood, where $\tilde{\theta}$ is the set of default values for the θ parameters. For the major part of the nuisance parameters a log-normal prior distribution is used, with a standard deviation corresponding to the given systematic uncertainty. For some nuisance parameters, as the ones related to the statistical uncertainty coming from the background measurement in data control regions, a Gamma distribution is instead recommended. A log-uniform distribution is used for the uncertainty related to the normalization of background contributions that are left unconstrained in the fit, such as the WW background process. Finally, some of the experimental uncertainties, related to the shape of signal and background processes, are modelled by means of additional histograms as explained in Sec. 4.5.5. The nuisance parameters correlations across different p_T^H bins are taken into account. Moreover the nuisance parameters can also be correlated (or anti-correlated) between signal and different background processes. As an example, the uncertainty related to the integrated luminosity measurement is fully correlated for all the signal and background processes.

Before running the fit on the data, the same procedure has been applied to the so called *Asimov data set*[2], which provides a simple method to estimate the signal sensitivity before looking at the data [91].

[2] In a parallel reality imagined by the science fiction writer I. Asimov, politics was run in a peculiar way: instead of mobilizing millions of people to cast their vote to deliberate on something, an algorithm was used to select an individual "average" person, and then this person was asked to take the decision on that matter.

4.6.2. Signal and background yields

A comparison of data and background prediction is shown in Fig. 4.24, where the $m_{\ell\ell}$ distribution is shown for the six p_T^H bins. Distributions correspond to the m_T window of [60, 110] GeV, in order to emphasize the signal contribution [54]. The m_T distributions are shown in Fig. 4.25 and correspond to the $m_{\ell\ell}$ window of [12, 75] GeV.

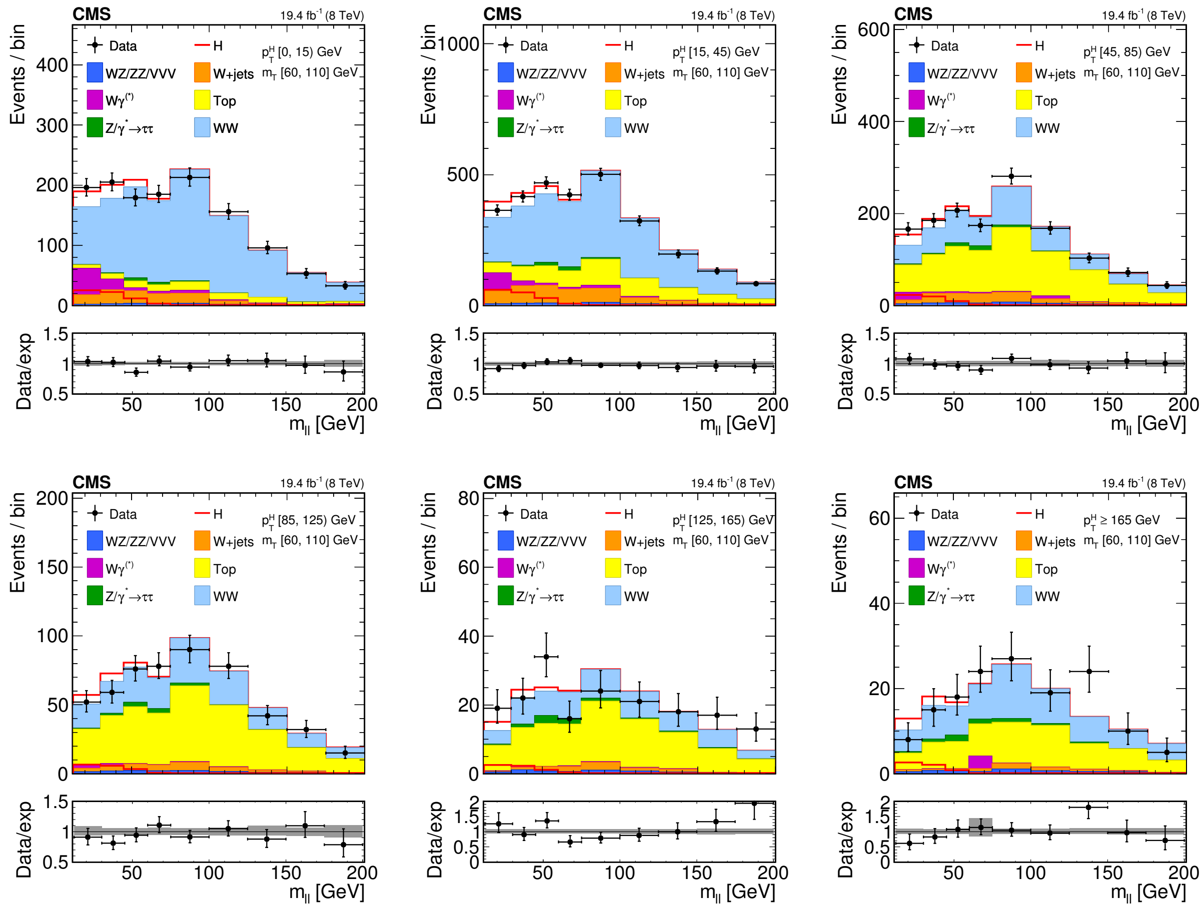

Figure 4.24.: Distributions of the $m_{\ell\ell}$ variable in each of the six p_T^H bins. Background normalizations correspond to the values obtained from the fit. Signal normalization is fixed to the SM expectation. The distributions are shown in an m_T window of [60,110] GeV in order to emphasize the Higgs boson (H) signal. The signal contribution is shown both stacked on top of the background and superimposed to it. Ratios of the expected and observed event yields in individual bins are shown in the panels below the plots. The uncertainty band shown in the ratio plot corresponds to the envelope of systematic uncertainties after performing the fit to the data.

The signal and background yields after the analysis selection are reported in Table 4.9.

The spectrum shown in Fig. 4.26 is obtained after having performed the fit and after the subtraction of the out-of-fiducial signal events, but before undergoing the unfolding pro-

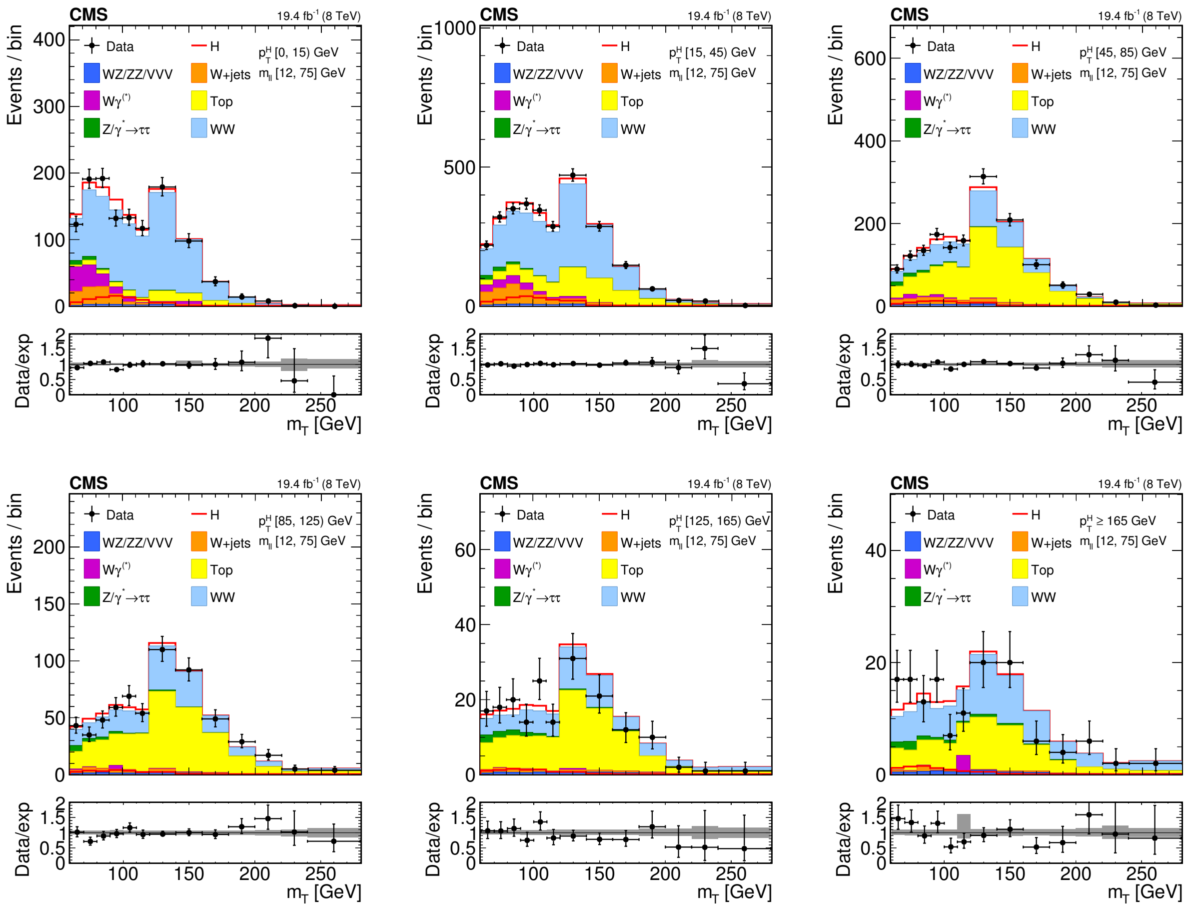

Figure 4.25.: Distributions of the m_{T} variable in each of the six $p_{\mathrm{T}}^{\mathrm{H}}$ bins. Background normalizations correspond to the values obtained from the fit. Signal normalization is fixed to the SM expectation. The distributions are shown in an $m_{\ell\ell}$ window of [12,75] GeV in order to emphasize the Higgs boson (H) signal. The signal contribution is shown both stacked on top of the background and superimposed to it. Ratios of the expected and observed event yields in individual bins are shown in the panels below the plots. The uncertainty band shown in the ratio plot corresponds to the envelope of systematic uncertainties after performing the fit to the data.

Table 4.9.: Signal prediction, background estimates and observed number of events in data are shown in each p_T^H bin for the signal after applying the analysis selection requirements. The total uncertainty on the number of events is reported. For signal processes, the yield related to the ggH are shown, separated with respect to the contribution of the other production mechanisms (XH=VBF+VH). The WW process includes both quark and gluon induced contribution, while the Top process takes into account both $t\bar{t}$ and tW.

$\mathbf{p_T^H}$ **[GeV]**	**0-15**	**15-45**	**45-85**	**85-125**	**125-165**	**165-∞**
ggH	73 ± 3	175 ± 5	59 ± 3	15 ± 2	5.1 ± 1.5	4.9 ± 1.4
XH=VBF+VH	4 ± 2	15 ± 4	16 ± 4	8 ± 2	3.8 ± 1.1	3.0 ± 0.8
Out-of-fiducial	9.2 ± 0.5	19.9 ± 0.7	11.4 ± 0.6	4.4 ± 0.3	1.6 ± 0.2	2.4 ± 0.2
Data	2182	5305	3042	1263	431	343
Total background	2124 ± 128	5170 ± 321	2947 ± 293	1266 ± 175	420 ± 80	336 ± 74
WW	1616 ± 107	3172 ± 249	865 ± 217	421 ± 120	125 ± 60	161 ± 54
Top	184 ± 38	1199 ± 165	1741 ± 192	735 ± 125	243 ± 51	139 ± 49
W+jets	134 ± 5	455 ± 10	174 ± 6	48 ± 4	14 ± 3	9 ± 3
WZ+ZZ+VVV	34 ± 4	107 ± 10	71 ± 7	29 ± 5	14 ± 3	13 ± 4
$Z/\gamma^* \to \tau^+\tau^-$	23 ± 3	67 ± 5	47 ± 4	22 ± 3	12 ± 2	10 ± 2
$W\gamma^{(*)}$	132 ± 49	170 ± 58	48 ± 30	12 ± 9	3 ± 3	5 ± 10

cedure. The theoretical distribution after the detector simulation and event reconstruction is also shown for comparison.

In order to assess the robustness of the fit, several toy MC samples have been produced, with a statistical accuracy corresponding to the one expected in data. The distribution of the signal strengths extracted in each bin using the toy MC samples and the their pull distributions are shown in Fig. 4.27.

4.7. Unfolding

To facilitate comparisons with theoretical predictions or other experimental results, the signal extracted performing the fit has to be corrected for detector resolution and efficiency effects and for the efficiency of the selection defined in the analysis. An unfolding procedure is used relying on the RooUnfold package [92], which provides the tools to run various unfolding algorithms.

The basic principle behind the unfolding procedure in this analysis is to use MC signal samples to make the "true" distribution of the variable of interest, which is obtained using simulated events before particle interaction with the detector, and the same distribution obtained using events reconstructed after the full Geant4 simulation of the CMS detector and event reconstruction. These two distributions are used to calculate the detector response matrix M:

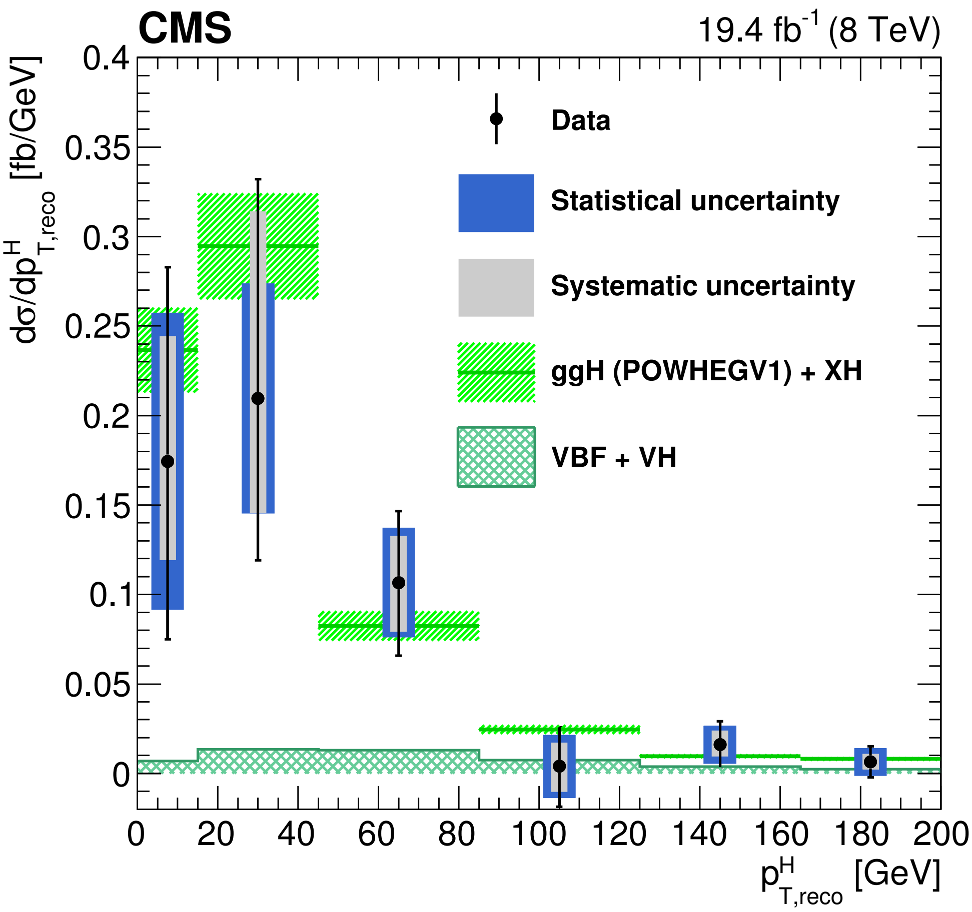

Figure 4.26.: Differential Higgs boson production cross section as a function of the reconstructed p_T^H, before applying the unfolding procedure. Data values after the background subtraction are shown together with the statistical and the systematic uncertainties, determined propagating the sources of uncertainty through the fit procedure. The line and dashed area represent the SM theoretical estimates in which the acceptance of the dominant ggH contribution is modelled by Powheg V1. The sub-dominant component of the signal is denoted as XH=VBF+VH, and is shown with the cross filled area separately.

$$R_i^{\mathrm{MC}} = \sum_{j=1}^{n} M_{ij} T_j^{\mathrm{MC}} \quad , \tag{4.32}$$

where R^{MC} and T^{MC} are two n-dimensional vectors representing the distribution before and after event processing through CMS simulation and reconstruction. The dimension n of the two vectors corresponds to the number of bins in the distributions, equal to six in this analysis. The response matrix M includes all the effects related to the detector and

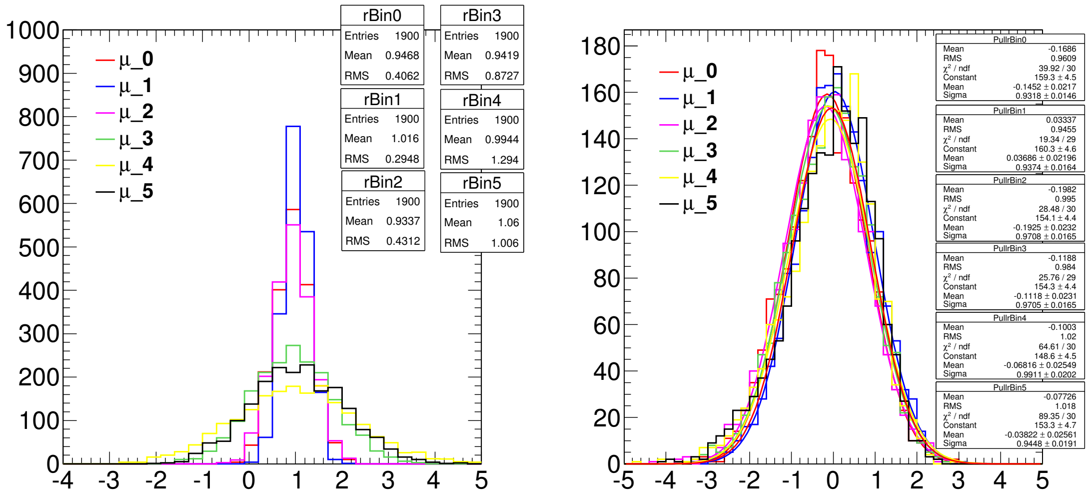

(a) (b)

Figure 4.27.: Signal strength distribution as extracted from the fit of toy MC samples (a). Distribution of the pull of the signal strength parameters (b).

analysis selection that affect the R^{MC} distribution. The goal of the unfolding procedure is to obtain the T^{truth} distribution starting from the measured R^{observed} distribution by inverting the matrix M. To avoid the large variance and strong negative correlation between the neighbouring bins [55], the unfolding procedure in this analysis relies on the singular value decomposition [93] method based on the Tikhonov regularization function. Since the response matrix is in general limited by the statistical uncertainties of simulated samples and given the finite data statistical accuracy, a simple inversion could lead to large fluctuations between bins in the unfolded result. In particular, if the off-diagonal elements of the response matrix are sizeable, the unfolded distribution has large variance and strong negative correlations between the neighbouring bins [55]. Several unfolding methods with regularization are available in literature, such as a method based on the Bayes' theorem, which overcome the unfolding instability using an iterative procedure [94]. One possible solution is the utilization of regularization methods. Such methods introduce a regularization function that controls the smoothness of the distribution and depends generally on one regularization parameter, which can be controlled to achieve the desired degree of smoothness. The choice of the regularization parameter is particularly critical, and it should represent an optimal trade-off between taming the fluctuations in the unfolded result, and biasing the unfolded distribution towards the one used to build the response matrix. The main feature of this method is the use of the singular value decomposition of the response matrix, including an additional term to suppress the oscillatory component of the solution, i.e. the regularization term, which represents some *a priori* knowledge of the final solution. The regularization parameter is chosen to obtain results that are robust against numerical instabilities and statistical fluctuations, following the prescription described in Ref. [93]. Maybe I should add an appendix describing the SVD method in details

The response matrix is built as a two-dimensional histogram, with the generator-level $p_{\mathrm{T}}^{\mathrm{H}}$ on the y axis and the same variable after the reconstruction on the x axis, using the same binning for both distributions. The resulting detector response matrix, including all signal sources and normalized by row, is shown in Fig. 4.28(a). The value of the diagonal bins corresponds to the stability S. The same matrix, normalized by column, is shown in Fig. 4.28(b). In this case the diagonal bins correspond to the purity P. The S and P parameters, defined in Sec. 4.3, provide an estimate of the $p_{\mathrm{T}}^{\mathrm{H}}$ resolution and migration effects. The main source of bin migrations effects in the response matrix is the limited resolution in the measurement of $E_{\mathrm{T}}^{\mathrm{miss}}$.

The resulting detector response matrix, which includes the effects of all signal sources and is represented by normalizing each row to unity is shown in Fig. 4.28(a). This representation shows the stability S in the diagonal bins, where S is defined as the ratio of the number of events generated and reconstructed in a given bin, and the number of events generated in that bin. In addition, a deconvolution matrix is constructed by normalizing each column to unity and is shown in Fig. 4.28(b). This latter representation shows the purity P in the diagonal bins, where P is defined as the ratio of the number of events generated and reconstructed in a given bin, and the number of events reconstructed in that bin. The S and P parameters provide an estimate of the $p_{\mathrm{T}}^{\mathrm{H}}$ resolution and of migration effects. The response matrix built including all signal sources is shown in Fig. 4.28. In order to point out either the purity or the stability in diagonal bins, each column or row of the matrix was respectively normalized to unity. The matrix obtained in the first case is what is actually called detector response matrix, while in the other case the matrix is usually referred to as detector deconvolution matrix.

Several closure tests are performed in order to validate the unfolding procedure. To estimate the uncertainty in the unfolding procedure due to the particular model adopted for building the response matrix, two independent gluon fusion samples are used, corresponding to two different generators: POWHEG V1 and JHUGEN generators, both interfaced to PYTHIA 6.4. The JHUGEN generator sample is used to build the response matrix while the POWHEG V1 sample is used for the measured and the MC distributions at generator level. The result of this test shows good agreement between the unfolded and the distribution from MC simulation.

In order to further prove the choice of the regularization parameter, a large number of simulated pseudo-experiments has been generated to verify that the coverage of the unfolded uncertainties obtained with this procedure is as expected. From each pseudo-experiment the reconstructed $p_{\mathrm{T}}^{\mathrm{H}}$ spectrum is obtained and then unfolded using the procedure described above, including only the statistical uncertainties. The coverage is calculated for each $p_{\mathrm{T}}^{\mathrm{H}}$ bin, counting the number of pseudo-experiments for which the statistical uncertainty covers the true value. The confidence intervals are calculated using the Clopper-Pearson approach, and the results are shown in Table 4.10 for different values of the regularization parameter: starting from $k_{\mathrm{reg}} = 2$ (stronger regularization) up to $k_{\mathrm{reg}} = 5$ (weaker regularization). The criterion for choosing the best k_{reg} value is to increase the regularization as much as possible

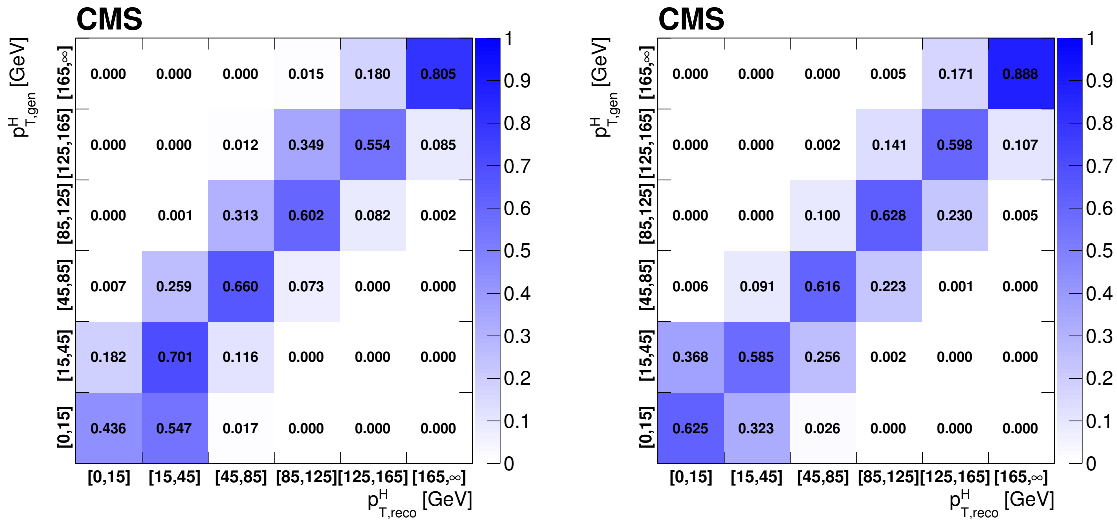

(a) Response matrix (b) Deconvolution matrix

Figure 4.28.: Response matrix (a) and deconvolution matrix (b) including all signal processes. The matrices are normalized either by row (a) or by column (b) in order to show the purity or stability respectively in diagonal bins.

Table 4.10.: Coverage interval for each bin and for different values of the regularization parameter, obtained using pseudo-experiments.

p_T^H bin [GeV]	Coverage			
	$k_{reg} = 2$	$k_{reg} = 3$	$k_{reg} = 4$	$k_{reg} = 5$
0–15	$0.654^{+0.015}_{-0.016}$	$0.704^{+0.015}_{-0.015}$	$0.727^{+0.014}_{-0.015}$	$0.755^{+0.014}_{-0.014}$
15–45	$0.701^{+0.015}_{-0.015}$	$0.665^{+0.015}_{-0.016}$	$0.683^{+0.015}_{-0.015}$	$0.733^{+0.014}_{-0.015}$
45-85	$0.717^{+0.014}_{-0.015}$	$0.706^{+0.015}_{-0.015}$	$0.709^{+0.015}_{-0.015}$	$0.716^{+0.014}_{-0.015}$
85–125	$0.634^{+0.016}_{-0.016}$	$0.681^{+0.015}_{-0.015}$	$0.714^{+0.015}_{-0.015}$	$0.739^{+0.014}_{-0.015}$
125–165	$0.599^{+0.015}_{-0.016}$	$0.650^{+0.015}_{-0.016}$	$0.700^{+0.015}_{-0.015}$	$0.751^{+0.014}_{-0.014}$
165–∞	$0.632^{+0.016}_{-0.016}$	$0.674^{+0.015}_{-0.015}$	$0.701^{+0.015}_{-0.015}$	$0.722^{+0.014}_{-0.015}$

without introducing a bias, i.e. until a 68% coverage is fulfilled. This criterion leads to the same result as the prescription described in Ref. [93], strengthening the choice of $k_{reg} = 3$.

4.7.1. Treatment of systematic uncertainties

An important aspect of this analysis is the treatment of the systematic uncertainties and the error propagation through the unfolding procedure. The sources of uncertainty are divided into three categories, depending on whether the uncertainty affects only the signal yield (type A), both the signal yield and the response matrix (type B), or only the response matrix (type C). These three classes propagate differently through the unfolding procedure.

Type A uncertainties are extracted directly from the fit in the form of a covariance matrix, which is passed to the unfolding tool as the covariance matrix of the measured distribution. The nuisance parameters belonging to this category are the background shape and normalization uncertainties. To extract the effect of type A uncertainties a dedicated fit is performed, fixing to constant all the nuisance parameters in the model, but type A nuisance parameters. The correlation matrix among the six signal strengths corresponding to the six p_T^H bins, including all type A uncertainties, is shown in Fig. 4.29. The correlation cor(i,j) of bins i and j is defined as:

$$\mathrm{cor}(i,j) = \frac{\mathrm{cov}(i,j)}{s_i s_j} \quad , \tag{4.33}$$

where $\mathrm{cov}(i,j)$ is the covariance of bins i and j, and (s_i, s_j) are the standard deviations of bins i and j, respectively.

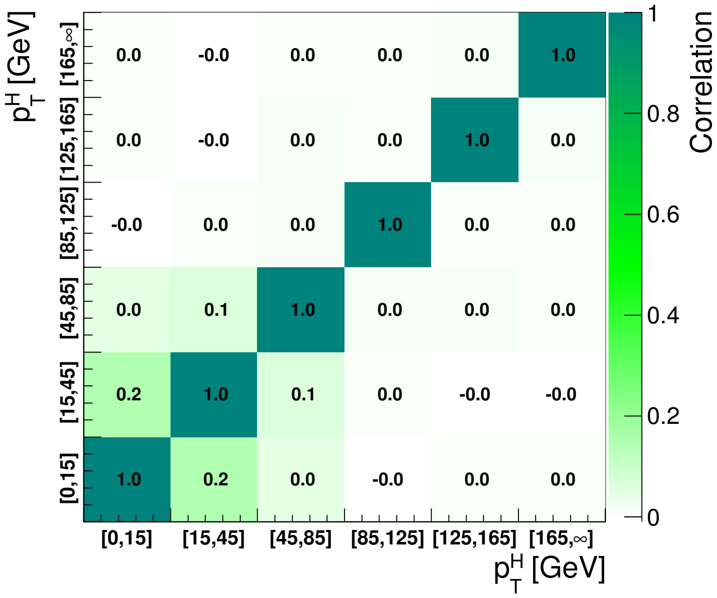

Figure 4.29.: Correlations among the signal strengths corresponding to the six p_T^H bins including all type A uncertainties.

The nuisance parameters falling in the type B class are:

- the b veto scale factor. It affects the signal and background templates by varying the number of events with jets that enter the selection. It also affects the response matrix because the reconstructed spectrum is harder or softer depending on the number of jets, which in turn depends on the veto.

- the lepton efficiency scale factor. It affects the signal and background template shape and normalization. It affects the response matrix by varying the reconstructed spectrum;
- the $E_{\mathrm{T}}^{\mathrm{miss}}$ scale and resolution, which have an effect similar to the above;
- lepton scale and resolution. The effect is similar to the above;
- jet energy scale. It affects the signal and background template shape and normalization. It also affects the response matrix because, by varying the fraction of events with jets, the b veto can reject more or fewer events, thus making the reconstructed spectrum harder or softer.

The effect of each type B uncertainty is evaluated separately, since each one changes the response matrix in a different way. In order to evaluate their effect on the signal strengths parameters, two additional fits are performed, each time fixing the nuisance parameter value to ± 1 standard deviation with respect to its nominal value. The results of the fits are then compared to the results of the full fit obtained by floating all the nuisance parameters, thus determining the relative uncertainty on the signal strengths due to each nuisance parameter, as shown in Tab. 4.11. Using these uncertainties, the measured spectra for each type B source are built. The effects are propagated through the unfolding by building the corresponding variations of the response matrix and unfolding the measured spectra with the appropriate matrix.

Type C uncertainties are related to the underlying assumption on the Higgs boson production mechanism used to extract the fiducial cross sections. These are evaluated using alternative response matrices that are obtained by varying the relative fraction of the VBF and ggH components within the experimental uncertainty, as given by the CMS combined measurement [95]. Three different response matrices are built, corresponding to the nominal, scaled up, and scaled down VBF/ggH ratio. The nominal matrix assumes the SM VBF/ggH ratio, while up- and down-scaled matrices are constructed by varying the SM signal strengths within the experimental constraints for VBF and ggH in such a way as to obtain the maximal variation of the VBF/ggH ratio allowed by the experimental constraints. These three matrices are used to unfold the reconstructed spectrum with the nominal VBF/ggH fraction, and obtain an uncertainty on the unfolded spectrum.

4.8. Results

In order to unfold the spectrum, the procedure described in section 4.7 has been pursued. The statistical plus type A systematic uncertainties are propagated by the unfolding procedure into the final spectrum, taking into account the signal strengths covariance matrix. The type B systematic uncertainty has been propagated using the following procedure: for each $p_{\mathrm{T}}^{\mathrm{H}}$ bin, we compute the upper bound of the systematic band computing

Table 4.11.: Effect of all the Type B uncertainties on the signal strengths of each bin. In the table are reported the signal strength variations corresponding to an up or down scaling of each nuisance.

Type B uncertainty	Effect on signal strength ($+1\sigma/-1\sigma$ [%])					
	[0–15]	[15–45]	[45–85]	[85–125]	[125–165]	[165–∞]
b veto	-10.1/-8.8	7.3/12.2	-6.3/3.1	-14.4/-4.8	-5.4/14.5	-7.9/17.8
lepton efficiency	-14.7/-3.9	4.5/15.1	-5.7/2.5	-13.2/-5.3	-0.2/7.6	-0.1/6.8
E_T^{miss} resolution	-12.5/0.0	15.4/-0.0	-12.8/-0.0	8.7/0.0	-20.9/-0.0	10.5/0.0
E_T^{miss} scale	-14.4/-6.8	-0.0/17.7	-6.1/-7.1	9.6/-20.9	2.3/32.4	2.5/2.6
lepton resolution	-12.5/-0.0	11.2/0.0	-2.4/0.0	-13.4/-0.0	9.9/0.0	-4.6/-0.0
electron momentum scale	-2.7/-13.1	15.9/9.9	10.8/-16.8	16.2/-33.1	30.9/-14.4	12.6/-10.9
muon momentum scale	-7.0/-10.7	11.8/8.9	1.1/-8.7	-0.7/-14.4	14.5/-4.6	8.0/-1.6
jet energy scale	-10.9/-10.1	9.0/9.0	-3.0/-2.9	-10.3/-8.9	0.3/3.4	5.2/3.1

Table 4.12.: Differential cross section in each p_T^H bin, together with the total uncertainty and the separate components of the various sources of uncertainty.

p_T^H [GeV]	$d\sigma/dp_T^H$ [fb/GeV]	Total uncertainty [fb/GeV]	Statistical uncertainty [fb/GeV]	Type A uncertainty [fb/GeV]	Type B uncertainty [fb/GeV]	Type C uncertainty [fb/GeV]
0-15	0.615	+0.370/-0.307	±0.246	±0.179	+0.211/-0.038	+0.0782/-0.0608
15-45	0.561	+0.210/-0.157	±0.120	±0.093	+0.146/-0.041	+0.0395/-0.0327
45-85	0.215	+0.084/-0.078	±0.059	±0.037	+0.047/-0.034	+0.0089/-0.0084
85-125	0.071	+0.038/-0.038	±0.029	±0.017	+0.018/-0.017	+0.0018/-0.0022
125-165	0.027	+0.020/-0.019	±0.016	±0.009	+0.007/-0.007	+0.0003/-0.0006
165-∞	0.028	+0.027/-0.027	±0.023	±0.012	+0.008/-0.007	+0.0002/-0.0006

the square sum of all the signal strength variations that deviate in the up direction with respect to the bin central value, whether or not this variation corresponds to the up or down shift of the systematic uncertainty. The same is done for the lower bound of the systematic band. If both the up and down shifts of a given nuisance parameter lead to a same direction variation of the signal strength, only the larger variation is considered.

The unfolded p_T^H spectrum is shown in Fig. 4.30. Statistical, systematic, and theoretical uncertainties are shown as separate error bands in the plot. The unfolded spectrum is compared with the SM-based theoretical predictions where the ggH contribution is modelled using the HRes and Powheg V2 programs. The comparison shows good agreement between data and theoretical predictions within the uncertainties. The measured values for the differential cross section in each bin of p_T^H are reported together with the total uncertainty in Table 4.12.

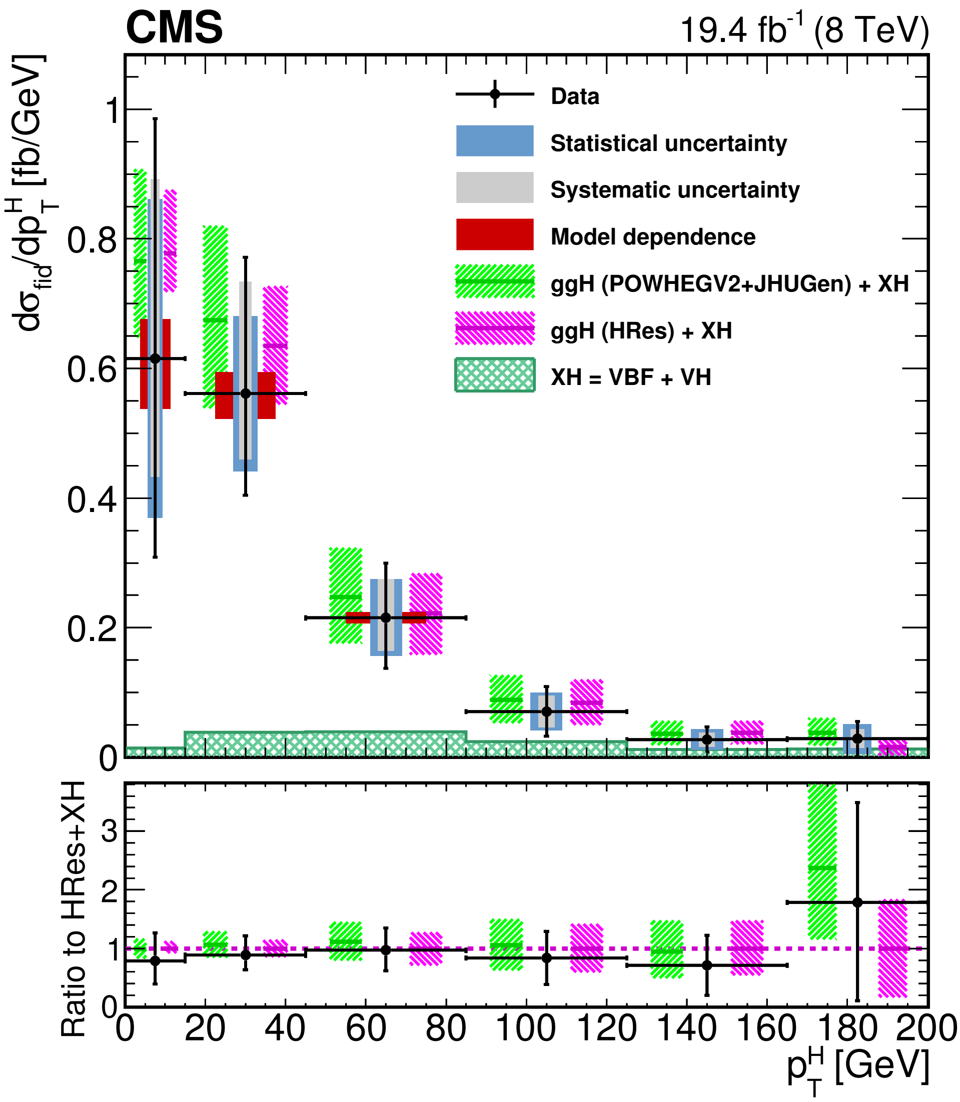

Figure 4.30.: Higgs boson production cross section as a function of $p_{\mathrm{T}}^{\mathrm{H}}$, after applying the unfolding procedure. Data points are shown, together with statistical and systematic uncertainties. The vertical bars on the data points correspond to the sum in quadrature of the statistical and systematic uncertainties. The model dependence uncertainty is also shown. The pink (and back-slashed filling) and green (and slashed filling) lines and areas represent the SM theoretical estimates in which the acceptance of the dominant ggH contribution is modelled by HRes and Powheg V2, respectively. The subdominant component of the signal is denoted as XH=VBF+VH and it is shown with the cross filled area separately. The bottom panel shows the ratio of data and Powheg V2 theoretical estimate to the HRes theoretical prediction.

Figure 4.31 shows the correlation matrix for the six bins of the differential spectrum. The correlation of of bins is defined as in Eq. (4.33).

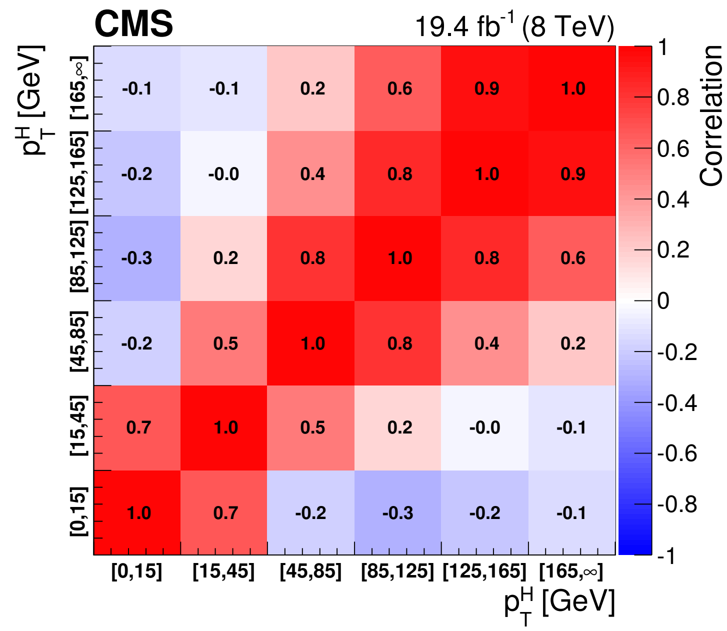

Figure 4.31.: Correlation matrix among the $p_{\mathrm{T}}^{\mathrm{H}}$ bins of the differential spectrum.

To measure the inclusive cross section in the fiducial phase space, the differential measured spectrum is integrated over $p_{\mathrm{T}}^{\mathrm{H}}$. In order to compute the contributions of the bin uncertainties of the differential spectrum to the inclusive uncertainty, error propagation is performed taking into account the covariance matrix of the six signal strengths. For the extrapolation of this result to the fiducial phase space, the unfolding procedure is not needed, and the inclusive measurement has only to be corrected for the fiducial phase space selection efficiency ϵ_{fid}. Dividing the measured number of events by the integrated luminosity and correcting for the overall selection efficiency, which is estimated in simulation to be $\epsilon_{\mathrm{fid}} = 36.2\%$, the inclusive fiducial $\sigma \times \mathcal{B}$, σ_{fid}, is computed to be:

$$\sigma_{\mathrm{fid}} = 39 \pm 8 \text{ (stat)} \pm 9 \text{ (syst) fb} \quad , \tag{4.34}$$

in agreement within the uncertainties with the theoretical estimate of 48 ± 8 fb, computed integrating the spectrum obtained with the Powheg V2 program for the ggH process and including the XH contribution.

Chapter 5.

Search for the SM Higgs boson in the H → WW channel with the first 13 TeV LHC data

5.1. Introduction

In this chapter, the first search for the SM Higgs boson decaying to a W boson pair at 13 TeV is presented, using a total integrated luminosity of 2.3 fb^{-1}, collected during the 2015 proton proton data taking period of the LHC.

Final states in which the two W bosons decay leptonically are studied. Therefore, events with a pair of oppositely-charged leptons, exactly one electron and one muon, a substantial amount of missing transverse energy, $E_{\mathrm{T}}^{\mathrm{miss}}$, due to the presence of neutrinos in the final state, and either zero or one jet are selected. This signature is common to other processes, which enter the analysis as backgrounds. The main background comes from WW production, irreducible background that shares the same final states and can only be separated by the use of certain kinematic properties. Another important background is W+jets, where a jet can mimick a leptonic signature. Background coming from top quark events, i.e. $\mathrm{t\bar{t}}$ and single top production, is also important, followed by other processes such as Drell-Yan, WZ, and other EWK production. The analysis strategy follows the one used during Run 1 in the same channel, described in Chapter 4, with a few different aspects that are described in the next sections.

With respect to 8 TeV, the ggH production cross section at 13 TeV is expected to increase of a factor of 2, thus raising the number of expected signal events. In addition, the cross section for the background processes is increasing as well. The WW production cross section increases of a factor of 1.8 and and the $\mathrm{t\bar{t}}$ cross section of a factor of 3.5, due to the enhancement of the gluon PDFs at higher center of mass energies.

5.2. Data and simulated samples

Data recorded in proton proton collisions at 13 TeV during 2015 was used in the analysis, with a total integrated luminosity of 2.3 fb^{-1}. Single and double lepton triggers are used similarly to the same analysis at 8 TeV. The HLT paths and descriptions of the triggers used in this analysis are described in Tables 5.1 and 5.2 for electrons and muons respectively.

Table 5.1.: HLT paths related to Electrons

HLT Path	Description
HLT_Ele23_WPLoose_Gsf_v*	Single Electron trigger. Best trigger to be used for 2015 data. In HWW, we are using "Trigger safe" Id. Turn on is at around Ele p_T = 30 GeV
HLT_Ele17_Ele12_CaloIdL_TrackIdL_IsoVL_DZ_v*	Double Electron Trigger. Best trigger to cover the turn on region from single electron trigger. "DZ" filter is also present. Its efficiency is also calculated separately.
HLT_Ele12_CaloIdL_TrackIdL_IsoVL_v*	This electron leg of HLT_Mu17_TrkIsoVVL_Ele12_CaloIdL_TrackIdL_IsoVL_v* same as Ele12 leg of double electron trigger.
HLT_Ele17_CaloIdL_TrackIdL_IsoVL_v*	This electron leg of HLT_Mu8_TrkIsoVVL_Ele17_CaloIdL_TrackIdL_IsoVL_v* same as Ele17 leg of double electron trigger.

The trigger efficiencies are measured in data and applied on simulated events as described in Sec. 4.2.1.

Concerning the simulated samples, several different Monte Carlo (MC) generators were used. In the simulation, 'lepton' includes also τ. Higgs signal samples have been simulated in all channels with POWHEG V2 [57, 70, 96], designed to describe the full NLO properties of these processes. In particular, for Higgs produced via gluon fusion [59], and vector-boson-fusion (VBF) [60], the decay of the Higgs boson into two W boson and subsequently into leptons was done using JHUGEN v5.2.5 [97]. For associated production with a vector boson (W^+H, W^-H, ZH) [98], including gluon fusion produced ZH (ggZH), the Higgs decay was done via PYTHIA 8.1 [78]. Alternative signal samples were produced with AMC@NLO [62], or with POWHEG V2 but decayed via PYTHIA 8.1 for gluon fusion and VBF assuming a Higgs boson mass of 125 GeV. In the following, the mass of the SM Higgs boson is assumed to be 125 GeV.

The WW production, irreducible background for the analysis, was simulated in different ways. POWHEG V2 [99] was used for $q\bar{q}$ produced WW in different decays. The cross section used for normalizing WW processes produced via $q\bar{q}$ was computed at next-to-next-to-leading order (NNLO) [100]. In order to control the top quark background processes, the analysis is performed with events that have no more than one high-p_T jet. The veto on high-p_T jets enhances the importance of logarithms of the jet p_T, spoiling the convergence of fixed-order calculations of the qq→WW process and requiring the use of dedicated resummation techniques for an accurate prediction of differential distributions [101, 102]. The p_T of the jets produced in association with the WW system is strongly correlated with its transverse momentum, p_T^{WW}, especially in the case where only one jet is produced. The

Table 5.2.: Muon trigger's elements description

HLT path	
HLT_IsoMu18_v*	single muon trigger
HLT_IsoTrMu20_v*	single muon trigger with tracker isolation
HLT_Mu17_TrkIsoVVL	leg for the HLT_Mu17_TrkIsoVVL_Mu8_TrkIsoVVL_DZ_v*, HLT_Mu17_TrkIsoVVL_TkMu8_TrkIsoVVL_DZ_v* and HLT_Mu17_TrkIsoVVL_Ele12_CaloIdL_TrackIdL_IsoVL_v* double lepton triggers
HLT_Mu8_TrkIsoVVL	leg for the HLT_Mu17_TrkIsoVVL_Mu8_TrkIsoVVL_DZ_v* and HLT_Mu8_TrkIsoVVL_Ele17_CaloIdL_TrackIdL_IsoVL_v* double lepton triggers
HLT_TkMu8_TrkIsoVVL	leg for the HLT_Mu17_TrkIsoVVL_TkMu8_TrkIsoVVL_DZ_v* double muon trigger
$DZ_{\mu\mu}$	efficiency of DZ cut in the HLT_Mu17_TrkIsoVVL_Mu8_TrkIsoVVL_DZ_v* and HLT_Mu17_TrkIsoVVL_TkMu8_TrkIsoVVL_DZ_v* double muon triggers, it is around 95%

simulated qq→WW events are reweighted to reproduce the $p_{\mathrm{T}}^{\mathrm{WW}}$ distribution from the p_{T}-resummed calculation.

Gluon fusion produced WW was generated, with and without Higgs diagrams, using MCFM v7.0 [103]. A $\mathrm{t\bar{t}}$ sample dilepton sample was also generated using POWHEG V2. The WW and $\mathrm{t\bar{t}}$ samples produced specifically for this analysis are presented in Table 5.3. Other background samples are used, a list of the most relevant ones is presented in Table 5.4.

Table 5.3.: Simulated samples for $\mathrm{t\bar{t}}$ and WW production. The $gg \rightarrow$WW $\rightarrow 2\ell 2\nu$ (H diagr.) sample includes both ggH production, the ggWW component and the interference.

Process	$\sigma \times \mathcal{B}$ [pb]
$\mathrm{t\bar{t}} \rightarrow \mathrm{WW}\ b\bar{b} \rightarrow 2\ell 2\nu b\bar{b}$	87.31
$\mathrm{q\bar{q}} \rightarrow \mathrm{WW} \rightarrow 2\ell 2\nu$	12.178
$gg \rightarrow \mathrm{WW} \rightarrow 2\ell 2\nu$	0.5905
$gg \rightarrow \mathrm{WW} \rightarrow 2\ell 2\nu$ (H diagr.)	0.9544

All processes are generated using the NNPDF2.3 [104, 105] parton distribution functions (PDF) for NLO generators, while the LO version of the same PDF is used for LO generators. All the event generators are interfaced to PYTHIA 8.1 [78] for the showering of partons

Table 5.4.: Simulated samples for other backgrounds used in the analysis.

Process	$\sigma \times \mathcal{B}$ [pb]
Single top	71.7
Drell-Yan ($10\,\mathrm{GeV} < m_{\ell\ell} < 50\,\mathrm{GeV}$)	20471.0
Drell-Yan ($m_{\ell\ell} > 50\,\mathrm{GeV}$)	6025.26
WZ$\rightarrow 2\ell 2$q	5.5950
ZZ$\rightarrow 2\ell 2$q	3.2210
WWZ	0.1651
WZZ	0.05565
ZZZ	0.01398

and hadronization, as well as including a simulation of the underlying event (UE) and multiple interaction (MPI) based on the CUETP8M1 tune [106]. To estimate the systematic uncertainties related to the choice of UE and MPI tune, the signal processes and the WW events are also generated with two alternative tunes which are representative of the errors on the tuning parameters. The showering and hadronization systematic uncertainty is estimated by interfacing the same MC samples with the HERWIG ++ 2.7 parton shower [107, 108]. For all processes, the detector response is simulated using a detailed description of the CMS detector, based on the GEANT4 package [71].

The simulated samples are generated with distributions for the number of pileup interactions that are meant to roughly cover, though not exactly match, the conditions expected for the different data-taking periods. In order to factorize these effects, the number of true pileup interactions from the simulation truth is reweighted to match the data. The re-weighting is propagated automatically to both the in-time pile up and the out-of-time one. In Fig. 5.1, the effect of this reweighting on a sample enriched in Drell-Yan events is shown. Before the reweighting the simulation is presented in the open red histogram; after the reweighting, it is represented by the solid green histogram that matched well the data. In order to select this sample, events with two leptons with $p_{\mathrm{T}} > 20\,\mathrm{GeV}$, opposite sign, and same flavour, are selected only if $|m_{\ell\ell} - m_{\mathrm{Z}}| < 15\,\mathrm{GeV}$.

The average number of pileup is approximately 11.5.

Different sources and calculations are used to obtain the cross sections for the different processes at 13 TeV. For Higgs signal, the cross sections used are the ones reported by the LHC Higgs Cross Section Working Group [109], computed at NNLO and NNLL QCD and NLO EW for gluon fusion, and at NNLO QCD and NLO EW for the rest of the production modes. The branching fractions are the ones reported in Ref. [53].

The cross section used for normalizing $\mathrm{q}\bar{\mathrm{q}}$ produced WW processes was computed at next-to-next-to-leading order (NNLO) [100]. The leading-order (LO) cross section for ggWW is obtained directly from MCFM. For gluon fusion, the difference between LO and NNLO cross sections is significantly big. A scale factor of 1.4 is theoretically calculated [110].

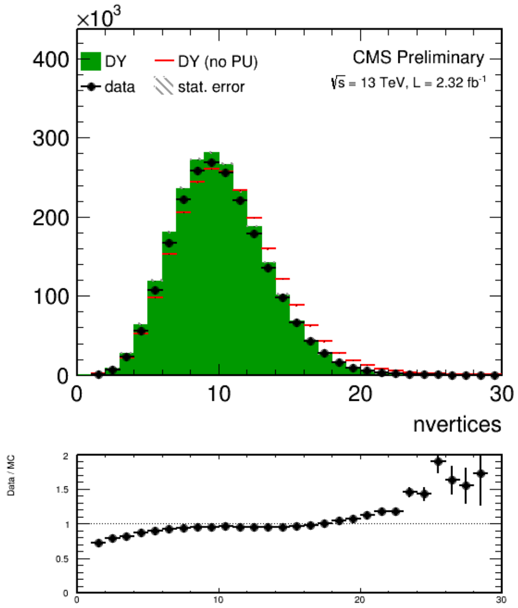

Figure 5.1.: Distributions of the number of vertices in a Drell-Yan enriched sample in data, together with the simulation before (red) and after (solid green) the pileup reweighting.

For the LO simulation of the interference between gg→WW and gluon fusion produced H→WW a k-factor of 1.87 is applied. This k-factor is obtained as the average between LO to NNLO ggH scale factor and LO to NLO ggWW scale factor.

The cross sections of the different single top processes are estimated by the LHC Top Working group [111] at NLO. The $t\bar{t}$ cross section is also provided by the LHC Top Working group [112], and it is computed at NNLO, with NNLL soft gluon resummation.

Drell-Yan (DY) production of Z/γ^* is generated using aMC@NLO [62]. Other multi-boson processes, such as WZ,ZZ, and VVV (V=W/Z), are generated with aMC@NLO and normalized to the cross section obtained at NLO in generation.

All processes are generated using the NNPDF2.3 [104, 105] parton distribution functions (PDF) for NLO generators, while the LO version of the same PDF is used for LO generators. All the event generators are interfaced to PYTHIA 8.1 for the showering of partons and hadronization, as well as including a simulation of the underlying event (UE) and multiple interaction (MPI) based on the CUET8PM1 tune [106].

5.3. Analysis strategy

5.3.1. Event reconstruction

Regarding the electrons, muons, jets and $E_{\mathrm{T}}^{\mathrm{miss}}$ definition and reconstruction, the standard CMS recommendations described in Chapter 2 are used. The specific selections used in this analysis are briefly summarised below.

Muons are identified according to the CMS recommendations for the medium working point, with the addition of some extra cuts, as defined by the following selections:

- identified by the standard medium muon selection described in Sec. **??**; Not yet defined :)
- $p_{\mathrm{T}} > 10\,\mathrm{GeV}$;
- $|\eta < 2.4|$;
- $|d_{xy}| < 0.01\,\mathrm{cm}$ for $p_{\mathrm{T}} < 20\,\mathrm{GeV}$ and $|d_{xy}| < 0.02\,\mathrm{cm}$ for $p_{\mathrm{T}} > 20\,\mathrm{GeV}$, d_{xy} being the transverse impact parameter with respect to the primary vertex;
- $|d_z| < 0.1\,\mathrm{cm}$, where d_z is the longitudinal distance of the muon track in the tracker extrapolated along the beam direction.

For the muon isolation, the CMS recommended particle flow isolation based on the tight working point is used, corresponding to a requirement on the isolation variable of $ISO_{\mathrm{tight}} < 0.15$. In addition a tracker relative isolation is also applied.

For the electron identification, the tight working point is used. In addition some additional cuts to make the selection "trigger-safe" are included. This is done because the electron triggers already include some identification and isolation requirements that are based on the raw detector information, while the offline selections make use of particle flow requirements. The "trigger-safe" selections are defined to make the the offline identification and isolation requirements tighter with respect to the online triggers.

The simulated events are corrected for the lepton trigger, identification and isolation efficiencies measured in data using the same techniques described in Sec. 4.3.1.

Jets are defined clustering the particle flow objects using the anti-k_t algorithm with a distance parameter of 0.4. The CHS pileup mitigation technique is used. The L1, L2, L3 and L2L3 jet energy correction described in Sec. **??** are applied. The reject jets coming from calorimeter or readout electronics noise, the loose working point for PF jet identification is used.

The b-tagging algorithm for this analysis is chosen comparing the performances of different algorithms using simulations for signal and background contributions in the phase space defined by the analysis kinematic requirements. More precisely, two MC samples are used, one corresponding the the $\mathrm{H} \to \mathrm{WW} \to 2\ell 2\nu$ signal produced via the ggH production mode and another corresponding to the $\mathrm{t\bar{t}}$ process. In fact, the first sample is enriched in light jets, i.e. originating by the hadronization of light quarks like u,d,c and s quarks, while the second sample is enriched in b jets, coming from the top quark decay. The b-veto efficiency, $\epsilon_{\mathrm{bveto}}$, is computed separately for the two samples and for the various b tagging algorithms. To compare the b tagging performance $\epsilon_{\mathrm{bveto}}$ is computed for different working points, i.e. different selections on the specific b tagging discriminator, and the results are reported in the form of a ROC curve. The ROC curves corresponding to events with 0, 1 and ≥ 2 jets are shown in Fig. 5.2. Events considered for this study are the ones passing the WW baseline selection.

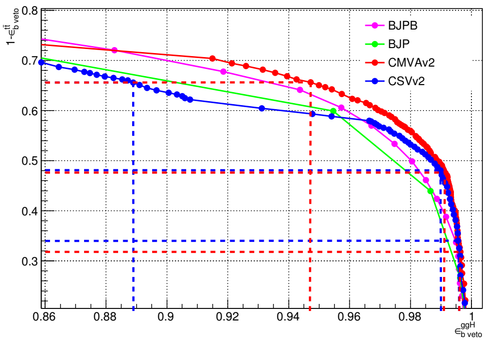

(a) $N_{\mathrm{jets}} = 0$

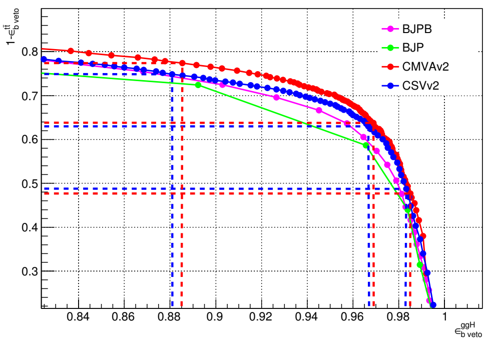

(b) $N_{\mathrm{jets}} = 1$

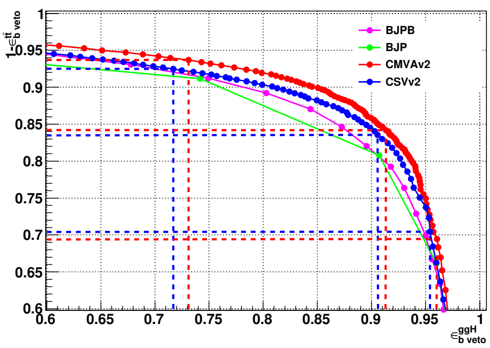

(c) $N_{\mathrm{jets}} \geq 2$

Figure 5.2.: ROC curve for the b veto efficiency on signal and background events. The blue and red lines point out the signal efficiency and the background rejection corresponding to the three working points considered for the CSVv2 and the cMVAv2 algorithms respectively.

The ROC curves show that the cMVAv2 algorithm has the best performance for the analysis phase space among the algorithms taken into account. For both the CSVv2 and cMVAv2 algorithms, three working points are defined corresponding to the mistag rates[1] of 10% for the loose, 1% for the medium and 0.1% for the tight working point. The distribution of the cMVAv2 discriminator associated to the leading jet both for the ggH and the $t\bar{t}$ MC sample is shown in figure 5.3.

[1]The mistag rate is defined as the probability for a light jet to be identified as a b-jet by the b tagging algorithms.

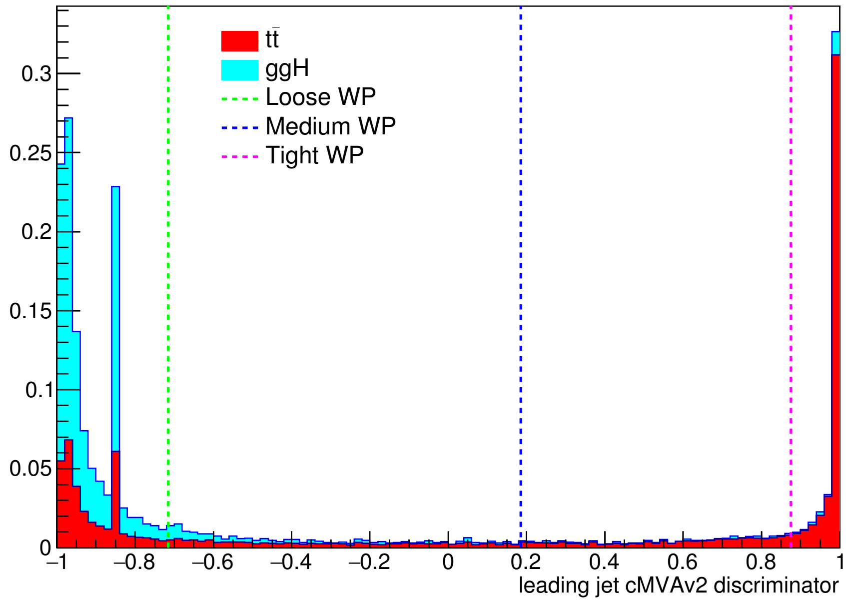

Figure 5.3.: cMVAv2 discriminator associated to the leading jet (with $p_T > 30$ GeV) both for the ggH and the $t\bar{t}$ processes. The two processes are normalized to unity and stacked. The vertical dashed lines show the discriminator value corresponding to the three working points.

In order to determine the best working point for this analysis a preliminary significance assessment is performed, using a complete analysis procedure in which only statistical effects are taken into account (no systematics are included). The significance assessment was performed using a two dimensional discriminating variable consisting of the dilepton invariant mass versus the transverse mass. The assessment was performed with the following leptonic selection:

- two leptons, an electron and a muon with opposite charge, with leading lepton p_T greater than 20 GeV and sub-leading lepton p_T greater than 13 GeV;
- no other lepton (electron or muon) with p_T greated than 10 GeV;
- $m_{\ell\ell}$ greater than 12 GeV;
- PF type 1 corrected MET greater than 20 GeV;
- $p_T^{\ell\ell}$ greater than 30 GeV.

In addition to this global selection, two categories were identified:

- 0 jets: no jets above 30 GeV, jets between 20 GeV and 30 GeV are b-vetoed with the cMVAv2 WP under study;
- 1 jet: exactly 1 jet above 30 GeV, no b-tagged jets above 30 GeV according to the cMVAv2 WP under study.

Table 5.5.: Significance corresponding to the three working points and for different jet categories using a shape analysis.

Jet category	Loose WP (-0.715)	Medium WP (0.185)	Tight WP (0.875)
0 jets	2.022	2.043	2.036
1 jet	1.439	1.404	1.305
$0+1$ jets	2.481	2.479	2.420

The two categories were eventually combined together and the significance assessment was repeated for the three working points. With these selection we find the significance values listed in Table 5.5 for the three working points.

The working point providing the best significance in the combined $0+1$ jets category is found to be the loose one.

To correct for a possible different b tagging efficiency in data and simulation, the simulated events are reweighted using scale factors computed in bins of the jet η and p_{T}. These scale factors and the corresponding uncertainties are centrally calculated for each working point, in such a way to be employable by all the CMS analyses. The prescription to reweight the simulated events is the following. First of all one has to compute the b tagging efficiency using the MC samples, $\varepsilon_{\mathrm{MC}}(p_{\mathrm{T}}, \eta, f)$, for the chosen working point in bins of jet p_{T} and η. The efficiency has to be computed for different flavours f of the jets, b, c and light (u,d,s), using the jet matching information[2] which is available in all the MC samples. An MC-based event weight is then calculated computing the probability P_{MC} of a given b tagging configuration to occur, e.g.:

$$P_{\mathrm{MC}} = \prod_{i\ \in\ b-tagged-jets} \varepsilon_{\mathrm{MC}_i} \prod_{j\ \in\ non-b-tagged-jets} (1 - \varepsilon_{\mathrm{MC}_j}) \tag{5.1}$$

Afterwards, a similar probability is computed using data:

$$P_{\mathrm{DATA}} = \prod_{i\ \in\ b-tagged-jets} SF_i \varepsilon_{\mathrm{MC}_i} \prod_{j\ \in\ non-b-tagged-jets} (1 - SF_j \varepsilon_{\mathrm{MC}_j}) \quad , \tag{5.2}$$

where SF_i is the provided scale factor value for the relevant jet flavour, p_{T} and η. Products in Eqs. 5.1 and 5.2 run over all jets. The event weight is finally given by the ration $P_{\mathrm{DATA}}/P_{\mathrm{MC}}$.

The b tagging efficiencies to be fed into Eq. 5.1 and Eq. 5.2 are derived using $\mathrm{t\bar{t}}$ simulated events and applying basic leptonic selections. These efficiencies are shown in Fig. 5.4 for

[2]There are a couple of techniques developed by the CMS Collaboration to assess the flavour of a reconstructed jet in simulation. The technique used here makes use of the flavour of the hadrons clustered into a jet.

light (a), c-jets (b) and b-jets (c), in bins of η and p_{T}. The uncertainties associated to the efficiencies are representative of the statistics of the simulated $\mathrm{t\bar{t}}$ sample, and are computed according to a binomial distribution.

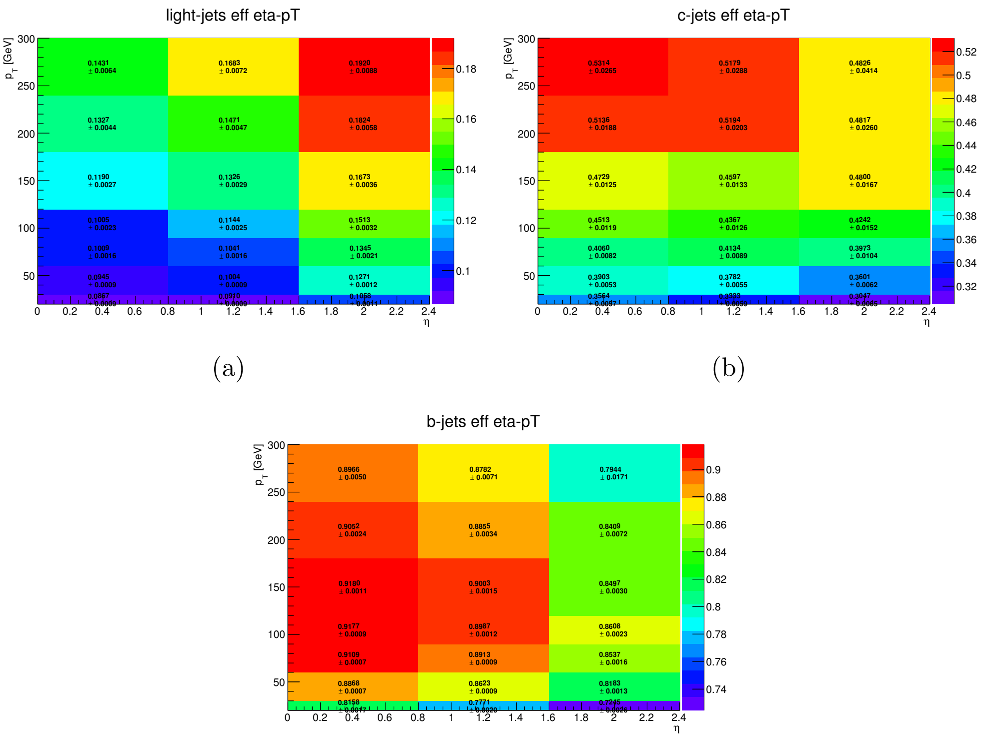

(a) (b)

(c)

Figure 5.4.: B tagging efficiencies for light jets (a), c-jets (b) and b jets (c), as a function of η and p_{T}.

The effect of the event reweighting is to correct the shape of the b tagging discriminator in simulation, moving events from the b tag region (discriminator greater than > -0.715) to the b veto region (discriminator < -0.715) and viceversa. A data/simulation comparison of the b tagging discriminator for the leading and subleading jets is performed to check the agreement after the application of the event weights. In order to evaluate the data/simulation agreement for b-jets, the data and simulation are compared in a top enriched control region, defined by the following requirements:

- two leptons, an electron and a muon with opposite charge, with leading lepton p_{T} greater than 20 GeV and sub-leading lepton p_{T} greater than 15 GeV;
- no other lepton (electron or muon) with p_{T} greater than 10 GeV;
- lepton invariant mass greater than 50 GeV;
- at least two jets with p_{T} greater than 30 GeV;

- at least one of the two leading jets with cMVAv2 btagging score greater than -0.715 (i.e. the loose working point).

In order to evaluate the agreement for light jets, a second control region is defined, populated by Z+light jet events, defined as follows:

- two leptons, two electrons or two muons with opposite charge, with leading lepton p_{T} greater than 20 GeV and sub-leading lepton p_{T} greater than 15 GeV.
- no other lepton (electron or muon) with p_{T} greater than 10 GeV.
- lepton invariant mass greater between 80 GeV and 110 GeV.
- at least two jets with p_{T} greater than 30 GeV.
- at least one jet above 30 GeV.
- no jets above 20 GeV with a TCHE score above 2.1.

Although a Z+jets sample is dominated by light flavor jets, a b-veto on an alternative algorithm (TCHE) is applied to reduce the contamination from b-jets, especially above the cMVAv2 cut. This helps mitigating possible data/simulation discrepancies in the modeling of the heavy/light flavour ratio. The comparison between data and simulation after the event reweighting is shown in Figs. 5.5 and 5.6 for the b-jets and light jets enriched control regions, respectively.

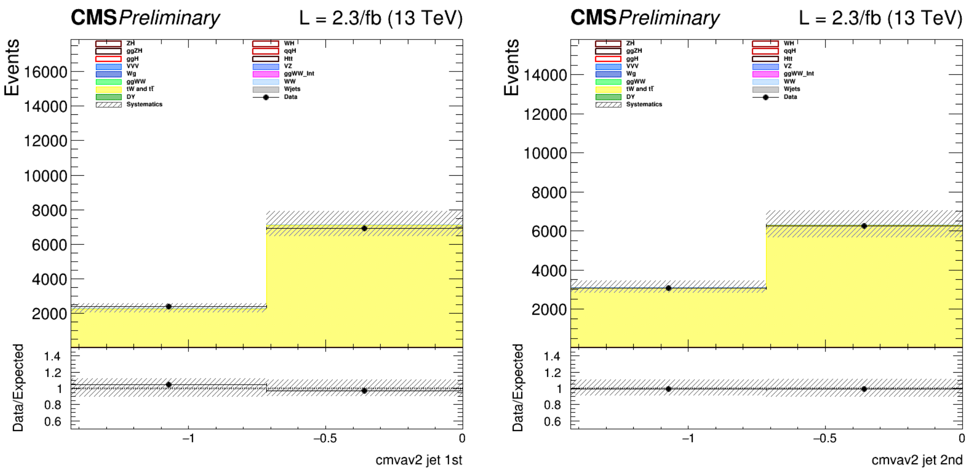

(a) (b)

Figure 5.5.: B tagging cMVAv2 discriminator for the leading (a) and the subleading (b) jet in the b-jets enriched control region.

5.3.2. Event selection and background rejection

Since the ggH production mechanism, which is the main production mode for a Higgs mass of around 125 GeV, is characterized by the emission of few jets arising from initial

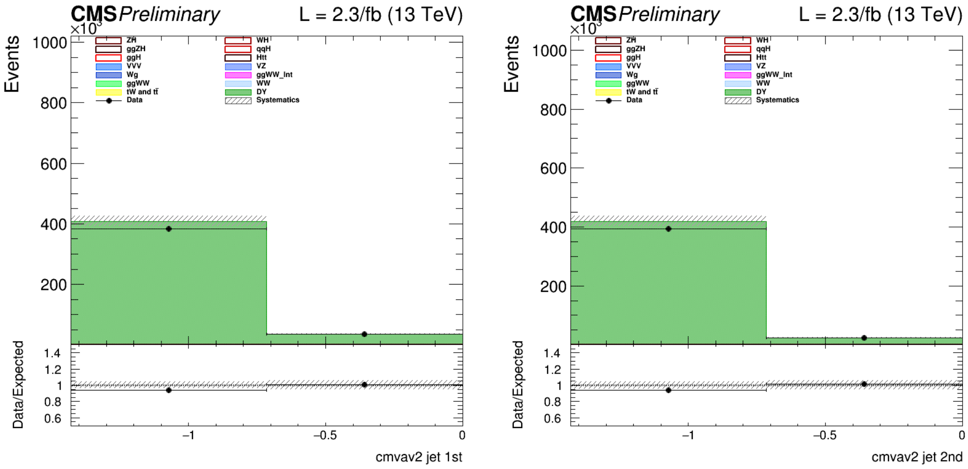

(a) (b)

Figure 5.6.: B tagging cMVAv2 discriminator for the leading (a) and the subleading (b) jet in the light jets enriched control region.

or final state radiation, this analysis is limited to events with no jets or one jet. Due to the large DY background in di-electrons and di-muons events, only the $e\mu$ final state is studied in this early Run 2 data analysis, including the indirect contribution from τ leptons decaying to electron or muons. Exactly one electron and one muon are required to be reconstructed in the event with opposite charges and a minimum p_{T} of 10 (13) GeV for the muon (electron). One of the two leptons should also have a p_{T} greater than 20 GeV and both leptons are required to be well identified and isolated to reject fake leptons and leptons coming from QCD sources. To suppress background processes with three or more leptons in the final state, such as ZZ, WZ, Zγ, Wγ, or tri-boson production, no additional identified and isolated lepton with $p_{\mathrm{T}} > 10$ GeV should be reconstructed. The low $m_{\ell\ell}$ region dominated by QCD production of leptons is not considered in the analysis and $m_{\ell\ell}$ is requested to be higher than 12 GeV. To suppress the background arising from DY events decaying to a τ lepton pair which subsequently decays to an $e\mu$ final state and suppress processes without genuine $E_{\mathrm{T}}^{\mathrm{miss}}$, a minimal $E_{\mathrm{T}}^{\mathrm{miss}}$ of 20 GeV is required. The DY background is further reduced by requesting $p_{\mathrm{T}}^{\ell\ell} > 30$ GeV. Finally the contribution from leptonic decays of single top and $\mathrm{t\bar{t}}$ production is reduced by requesting that no jets with $p_{\mathrm{T}} > 20$ GeV are identified by the b tagging algorithm as originating from a b quark in the event.

The requirements described above define the WW baseline selection. After those requirements the data sample is dominated by events arising from the non-resonant WW production and $\mathrm{t\bar{t}}$ production. To further reduce the effect of these backgrounds on the signal sensitivity, the events are categorized depending on the jet multiplicity, counting jets with $p_{\mathrm{T}} > 30$ GeV. Events with zero associated jets mainly arise from the WW production, while WW and $\mathrm{t\bar{t}}$ productions have a similar contribution in the category with one jet.

Higher jet multiplicity categories, which are sensitive to other Higgs production mechanisms, such as VBF, are not included in this analysis, given the very low expected yield for other production modes with the analysed integrated luminosity.

Distributions of some variables of interest for the 0 and 1 jet categories separately, but merging the eμ and μe final states together, are shown in Figs. 5.7, 5.8 and 5.9 after applying the WW baseline selections, with the addition of a cut on $m_{\ell\ell}$ to remove the Higgs signal contribution ($m_{\ell\ell} > 80\,\mathrm{GeV}$), and a cut on m_T to be orthogonal to the $\mathrm{Z}\gamma^* \to \tau\tau$ background control region ($m_\mathrm{T} > 60\,\mathrm{GeV}$).

The W+jets background, where one jet can be misidentified as a lepton, is a subdominant background in the phase space defined by the analysis kinematic requirements. The 0 ad 1 jets categories are further split according to the lepton flavour to eμ and μe, where the first lepton refers to the leading one. In this way an improvement of about 10% in terms of the signal significance can be achieved, exploiting the different W+jets background contribution in the two categories. Indeed the probability for a jet to be misidentified as an electron or a muon is not the same.

5.3.3. Signal extraction

To extract the Higgs boson signal contribution in the four previously mentioned categories, a similar approach to the one used in the Run 1 analysis [54] is pursued. The analysis is based on two-dimensional templates of $m_{\ell\ell}$ versus m_T to discriminate signal and background contributions. The $m_{\ell\ell}$ template is defined using 5 bins from $m_{\ell\ell} = 10\,\mathrm{GeV}$ up to $m_{\ell\ell} = 110\,\mathrm{GeV}$, while for the m_T template 7 bins are defined in the range $60\,\mathrm{GeV} < m_\mathrm{T} < 200\,\mathrm{GeV}$. The phase space with $m_\mathrm{T} < 60\,\mathrm{GeV}$ is used as an orthogonal control region to extract the normalization of the DY background. A binned maximum likelihood fit to the signal and background two-dimensional templates is performed to extract the signal strength in the four categories.

Distributions of the $m_{\ell\ell}$ and m_T variables after the WW level selection are shown in Fig. 5.10 for the 0 and 1 jet categories separately, but merging the eμ and μe final states together.

The statistical methodology used to interpret the data and to combine the results from the independent 0-jet and 1-jet categories in the eμ and μe final states has been developed by the ATLAS and CMS collaborations in the context of the LHC Higgs Combination Group [95, 113]. The number of events in each category and in each bin of two-dimensional template is modelled as a Poisson random variable, with a mean value given by the sum of the contributions from all the processes under consideration. Systematic uncertainties are represented by individual nuisance parameters with log-normal distributions. The uncertainties affect the overall normalization of the signal and backgrounds as well as the shape of the predictions across the distribution of the observables. Correlation between systematic uncertainties in different categories are taken into account.

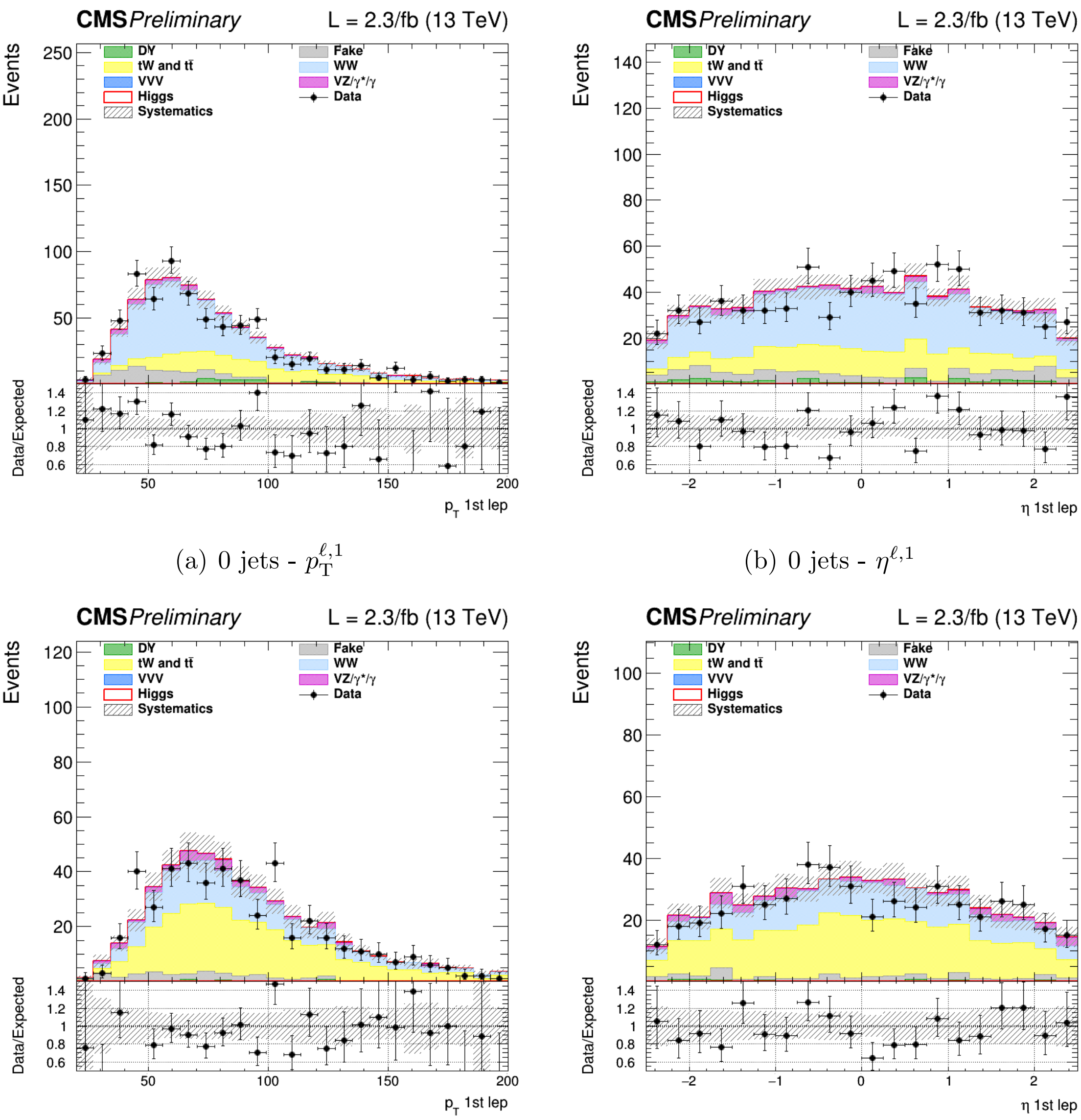

(a) 0 jets - $p_{\mathrm{T}}^{\ell,1}$

(b) 0 jets - $\eta^{\ell,1}$

(c) 1 jet - $p_{\mathrm{T}}^{\ell,1}$

(d) 1 jet - $\eta^{\ell,1}$

Figure 5.7.: Distributions of p_{T} (left) and η (right) of the leading lepton for events with 0 jet (upper row) and 1 jet (lower row), for the main backgrounds (stacked histograms), and for a SM Higgs boson signal with $m_{\mathrm{H}} = 125\,\mathrm{GeV}$ (superimposed and stacked red histogram) at the WW selection level. The last bin of the histograms includes overflows. The simulation of the WW background is normalized to data.

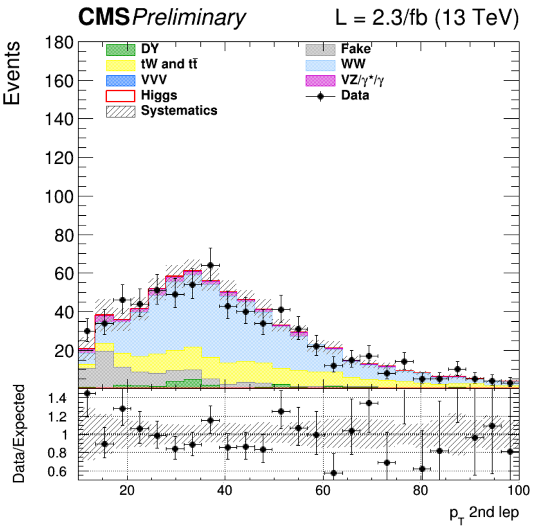

(a) 0 jets - $p_{\mathrm{T}}^{\ell,2}$

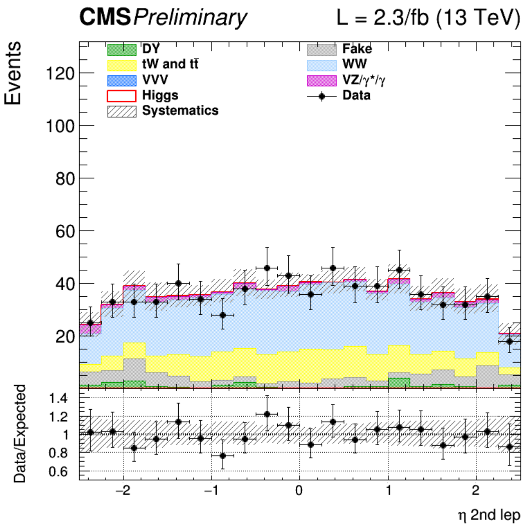

(b) 0 jets - $\eta^{\ell,2}$

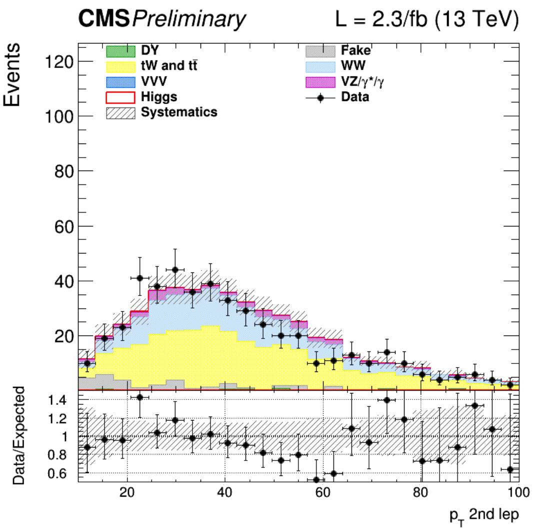

(c) 1 jet - $p_{\mathrm{T}}^{\ell,2}$

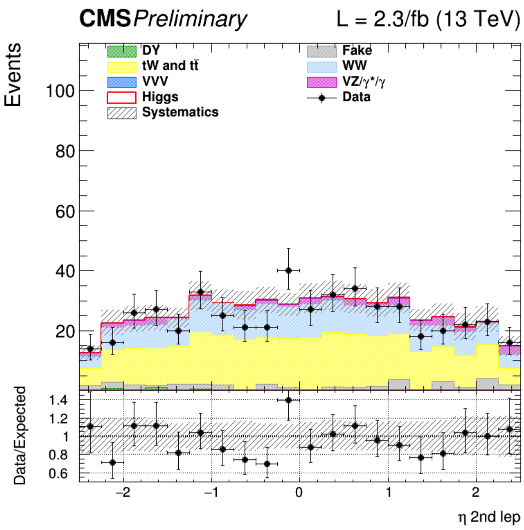

(d) 1 jet - $\eta^{\ell,2}$

Figure 5.8.: Distributions of p_{T} (left) and η (right) of the subleading lepton for events with 0 jets (upper row) and 1 jet (lower row), for the main backgrounds (stacked histograms), and for a SM Higgs boson signal with $m_{\mathrm{H}} = 125\,\mathrm{GeV}$ (superimposed and stacked red histogram) at the WW selection level. The last bin of the histograms includes overflows. The simulation of the WW background is normalized to data.

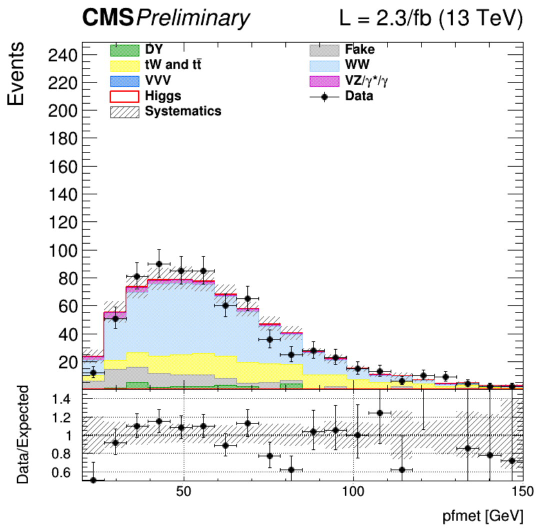

(a) 0 jets - $E_{\mathrm{T}}^{\mathrm{miss}}$

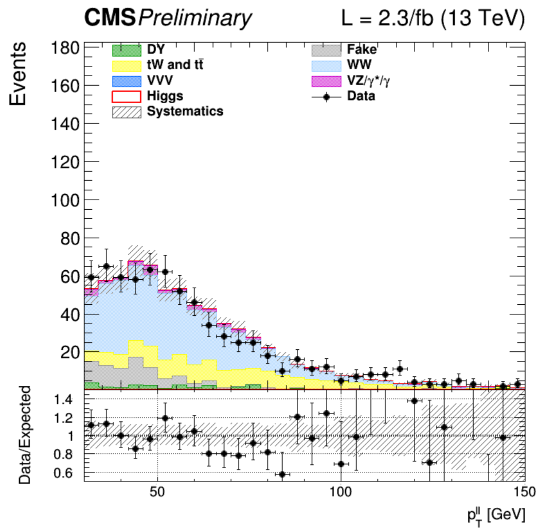

(b) 0 jets - $p_{\mathrm{T}}^{\ell\ell}$

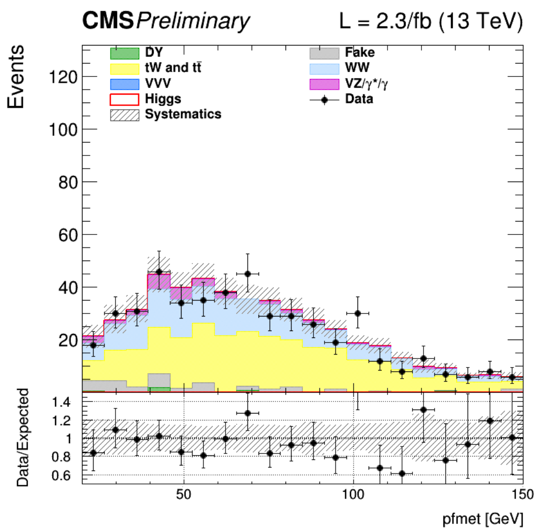

(c) 1 jet - $E_{\mathrm{T}}^{\mathrm{miss}}$

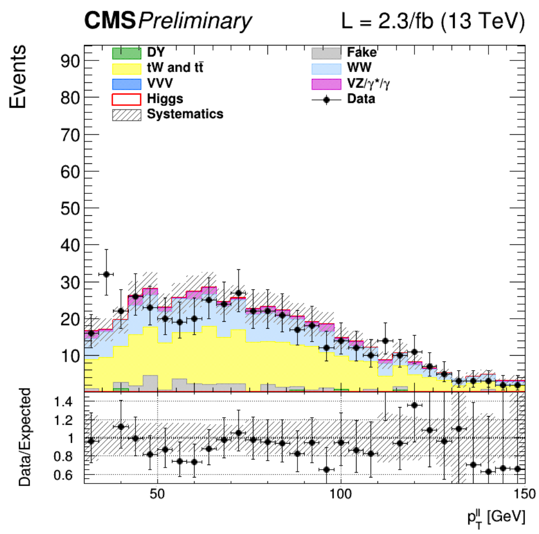

(d) 1 jet - $p_{\mathrm{T}}^{\ell\ell}$

Figure 5.9.: Distributions of $E_{\mathrm{T}}^{\mathrm{miss}}$ (left) and $p_{\mathrm{T}}^{\ell\ell}$ (right) for events with 0 jets (upper row) and 1 jet (lower row), for the main backgrounds (stacked histograms), and for a SM Higgs boson signal with $m_{\mathrm{H}} = 125\,\mathrm{GeV}$ (superimposed and stacked red histogram) at the WW selection level. The last bin of the histograms includes overflows. The simulation of the WW background is normalized to data.

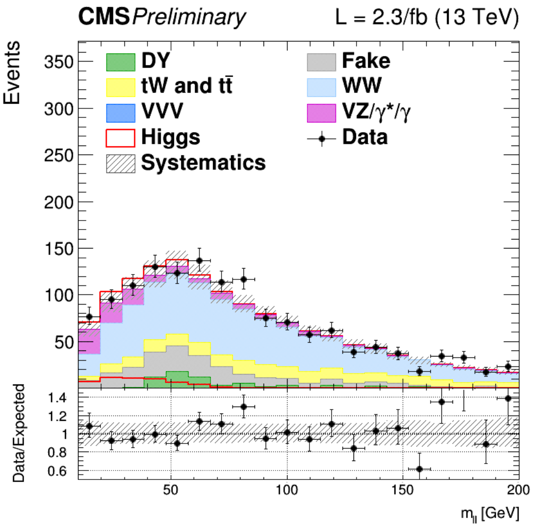

(a) 0 jets - $m_{\ell\ell}$

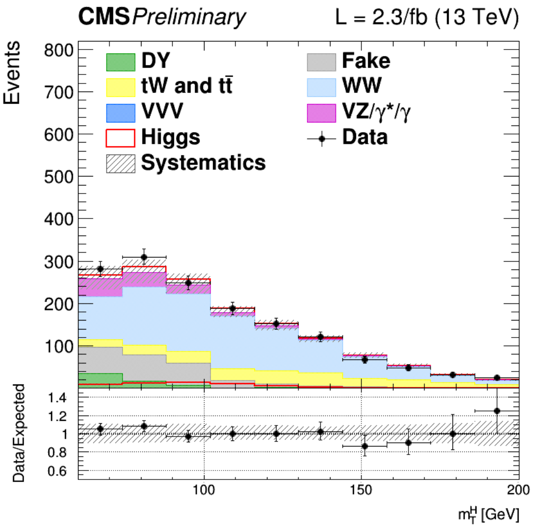

(b) 0 jets - m_{T}

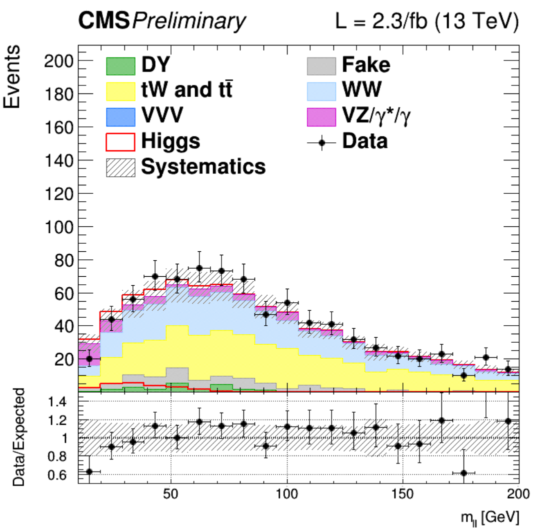

(c) 1 jet - $m_{\ell\ell}$

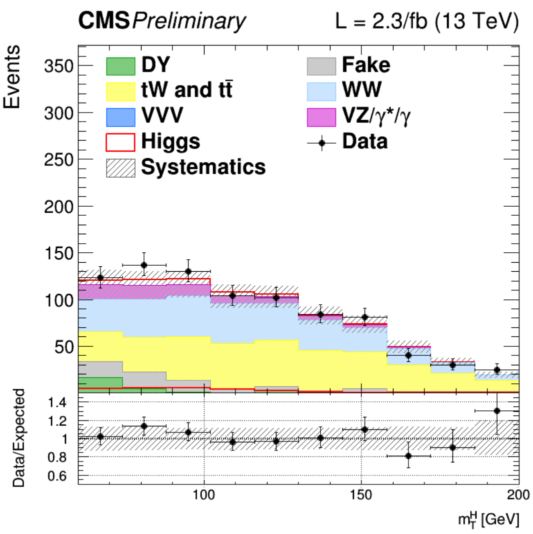

(d) 1 jet - m_{T}

Figure 5.10.: Distributions of $m_{\ell\ell}$ (left) and m_{T} (right) for events with 0 jets (upper row) and 1 jet (lower row), for the main backgrounds (stacked histograms), and for a SM Higgs boson signal with $m_{\mathrm{H}} = 125\,\mathrm{GeV}$ (superimposed and stacked red histogram) at the WW selection level. The last bin of the histograms includes overflows. The simulation of the WW background is normalized to data.

5.4. Background estimation

The main background processes affecting the analysis signature, non-resonant WW production and top quark processes, are estimated using data. Backgrounds arising from an experimental misidentification of the objects, such as W+jets (also called "Fake"), are estimated using data as well. The other minor backgrounds are generally estimated directly from simulation as described in the following subsections.

5.4.1. WW background

The quark-induced WW background is simulated with NLO accuracy in perturbative QCD, and the transverse momentum of the diboson system is reweighted to match the NNLO+NNLL accuracy from theoretical calculations [101, 102]. However, given the large uncertainties on the jet multiplicity distribution associated to this process, the normalization of this background is measured from data separately for the 0 and 1 jet categories. The normalization k-factors are extracted directly from the fit together with the signal strengths, leaving the WW normalization free to float separately in the two jet multiplicity categories. An orthogonal control region for the WW background normalization estimation is not needed in this case, owing to the different $m_{\ell\ell}$-m_{T} shape for signal and background.

The gluon-induced WW production is sub-dominant with respect to the quark-induced production, and its shape and normalization is fully taken from simulation, scaling the cross section to the theoretical prediction with NLO accuracy [110].

5.4.2. Top quark background

As explained in Sec. 5.3, the production of top quark pairs represents one of the dominant backgrounds in this analysis given its large cross section and a similar final state compared to the signal. A b-jet veto, based on the *cMVAv2* b tagging algorithm, is used to suppress this background and a reweighting procedure is applied on top of the simulated events to correct for different b tagging efficiency in data and simulation.

The top quark background normalization is measured using data, defining a b-jets enriched control region by inverting the b-jet veto. More precisely, the b-jets enriched control region for the 0-jet category is defined with the same WW baseline selection but requiring at least one jet with $20 < p_{\mathrm{T}} < 30\,\mathrm{GeV}$ to be identified as a b jet and no other jets with $p_{\mathrm{T}} > 30\,\mathrm{GeV}$. For the 1-jet category, the b-jets enriched region is defined requiring exactly one jet with $p_{\mathrm{T}} > 30\,\mathrm{GeV}$ identified as a b-jet. To reduce other backgrounds in these two regions, the dilepton mass has to be greater than 50 GeV. Distributions of the $m_{\ell\ell}$ and m_{T} variables in the b-jets enriched control regions after applying the data driven estimation are shown in Figure 6.5, for the 0 and 1 jet categories separately.

The top quark background normalization is constrained during the fit procedure separately in the two jet categories, by means of the control regions defined above, which are treated in the fit as two additional categories.

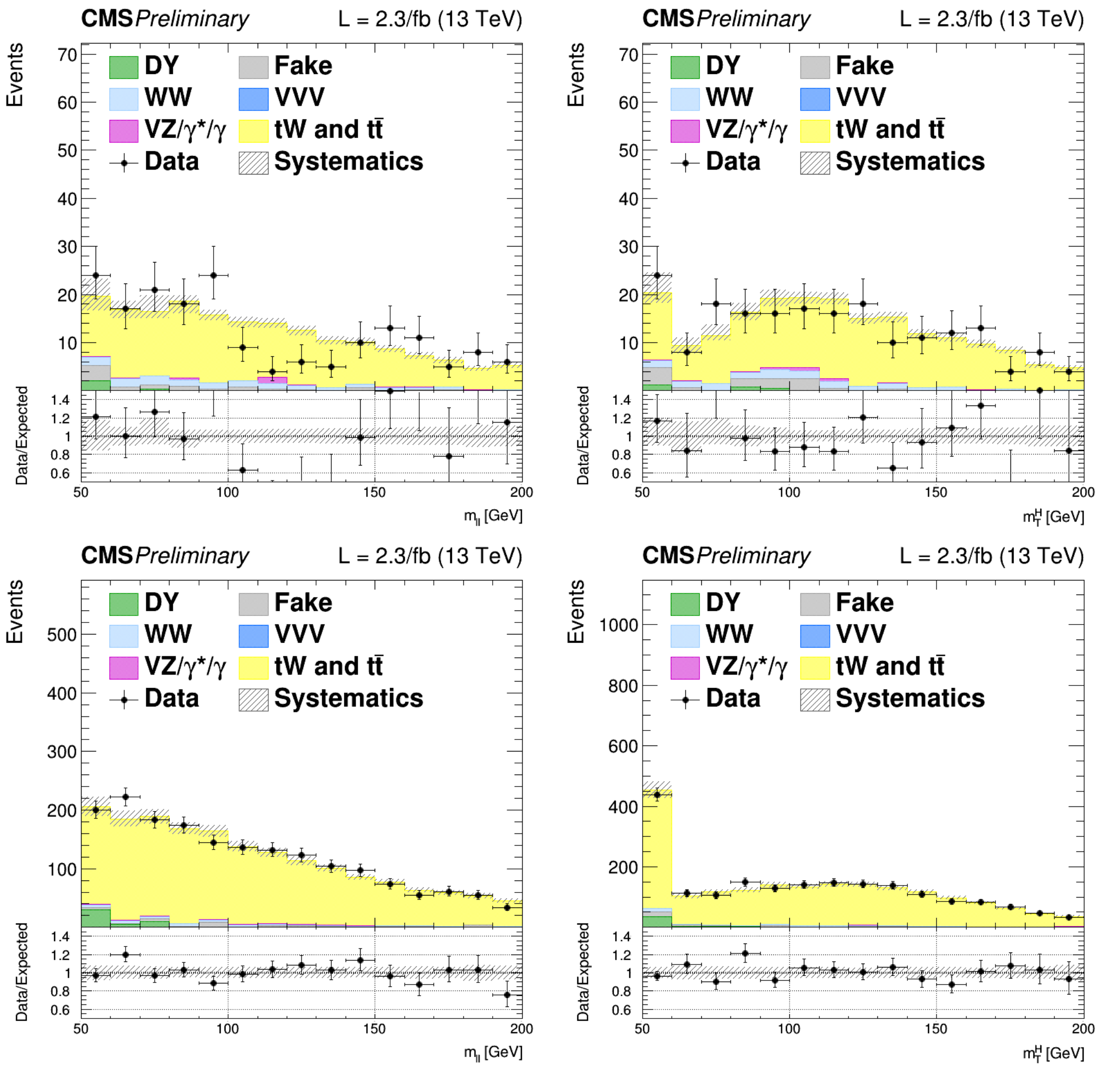

Figure 5.11.: Distributions of $m_{\ell\ell}$ (left) and m_{T} (right) for events with 0 jet (top) and 1 jet (bottom) in top enriched phase space. Scale factors estimated from data are applied. The first (last) bin includes underflows (overflows).

5.4.3. Jet-induced (or Fake) background

One of the primary source belonging to this category arises from the misidentification of leptons in W+jets processes in the 0 jet category. Also, semileptonic $\mathrm{t\bar{t}}$ decays contribute especially for higher jet multiplicities. Multijet production and hadronic $\mathrm{t\bar{t}}$ decays are also taken into account, but have a much smaller contribution.

This background is fully estimated using data, with the technique described in Sec. 4.4.3. To check the agreement of the background estimated in this way with data, a control sample enriched in jet-induced events is defined. The events in the control sample are selected applying the WW baseline requirements but requesting an eμ pair with same charge, which significantly suppresses the WW and $\mathrm{t\bar{t}}$ processes. The $m_{\ell\ell}$ distributions in this control region for the 0 and 1 jet categories are shown in Fig. 5.12. From the crosscheck in this control region, a global normalization factor of 0.8 is derived and applied to the jet-induced background.

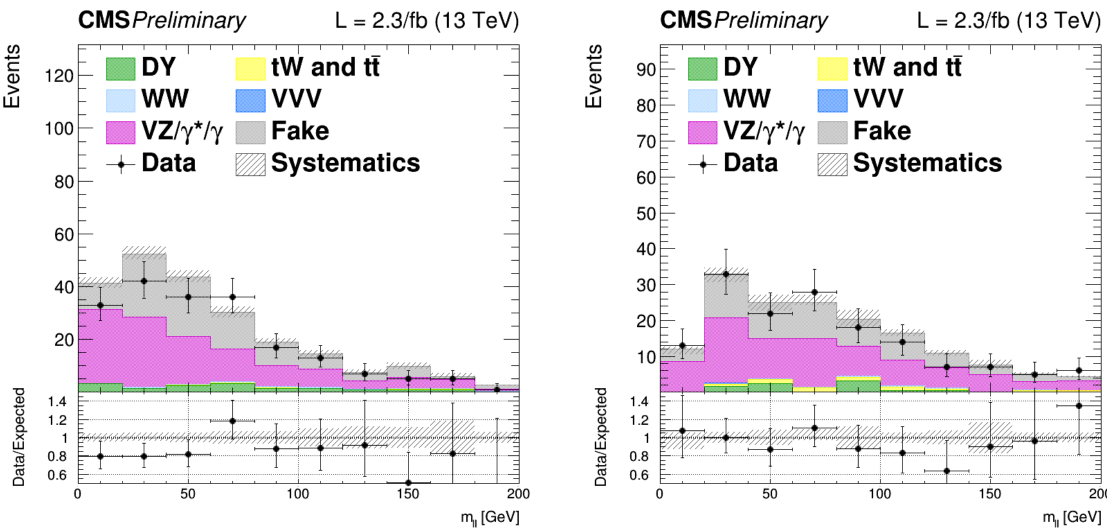

(a) 0 jet (b) 1 jet

Figure 5.12.: Control plots for $m_{\ell\ell}$ in a fakes enriched phase space for events with 0 and 1 jet with $p_T > 30$ GeV, in eμ final state. Fake contribution has been scaled by 0.8 to match data.

5.4.4. DY background

This background contributes to the analysis phase space because of the Z/γ^* decays to a pair of τ leptons, which consequently decays to an eμ pair. This background process is predominant in the low m_T region, which is used as an orthogonal control region to determine the background normalization in the 0 and 1 jet categories separately. In particular this control region is defined by selecting events with $m_\mathrm{T} < 60\,\mathrm{GeV}$ and $30\,\mathrm{GeV} < m_{\ell\ell} < 80\,\mathrm{GeV}$.

The $m_{\ell\ell}$ distributions in these control regions for the 0 and 1 jet categories are shown in Fig. 5.13.

As for the top quark background, the normalization of this background in the 0 and 1 jet categories, is constrained directly in the fit by means of the control regions, which are treated as two additional categories.

The kinematics of this background is taken from simulation, after reweighting the Z boson p_{T} spectrum to match the observed distribution measured in data. In fact, this variable is not well reproduced by the MC generator used for simulating this process, especially in the bulk of the distribution, the discrepancy being ascribed to the missing contribution from resummed calculations.

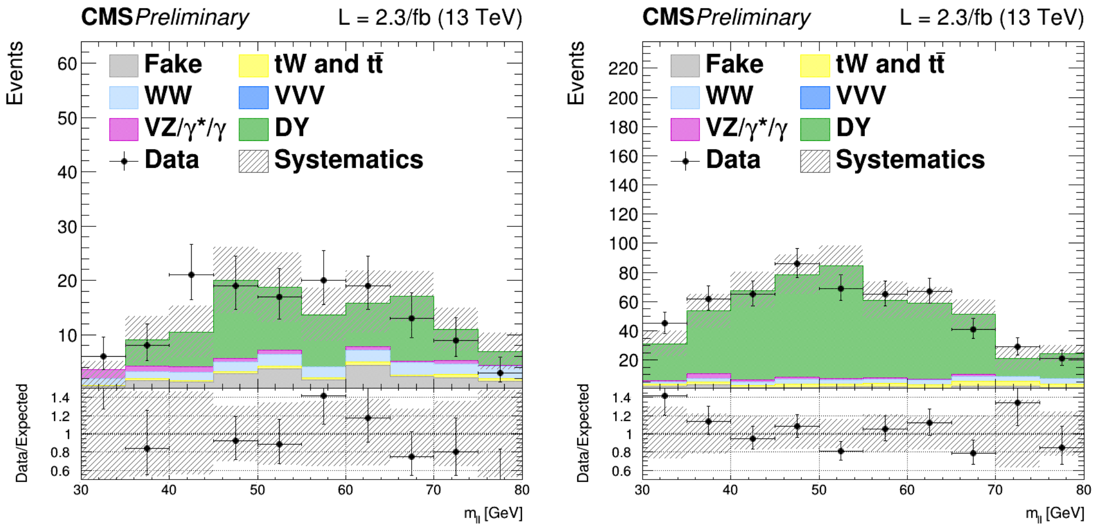

Figure 5.13.: Distributions of $m_{\ell\ell}$ for events with 0 jet (left) and 1 jet (right) in the DY$\rightarrow \tau\tau$ enriched control region. Scale factors estimated from data are applied.

5.4.5. Other backgrounds

The Wγ^* and the WZ electroweak processes can be gathered in the same physical process, although the final state kinematics is rather different. In particular, the invariant mass of the leptons arising from the γ^* decays is generally below 4 GeV, while the leptons from the Z boson decay are characterized by a larger invariant mass. Another background which can be experimentally identical to those is the Wγ production, where a real photon is produced in association with a W boson and consequently undergoes a photon conversion to leptons due to the interaction with the material constituting the first layers of the silicon tracker.

All these backgrounds may contribute to the signal phase space whenever one of the three leptons escape from the detector acceptance or is not identified. The shape and cross section of these backgrounds are taken from simulation. The only exception is the normalization of the Wγ^* background, being this process dominant in the low $m_{\ell\ell}$ region, which is scaled to data defining a proper control region. The control region is defined selecting events with three isolated muons, with $p_{\mathrm{T}} > 10{,}5$ and 3 GeV for the first three leading muons respectively. The selection is further defined by $E_{\mathrm{T}}^{\mathrm{miss}} < 25\,\mathrm{GeV}$ and $E_{\mathrm{T}}^{\mathrm{miss}}$ projected to the leading muon $< 45\,\mathrm{GeV}$. The pair of muons with the smallest invariant mass is taken as coming from the γ^* decay. The k-factor measured in data for this background to be applied in the simulation is 1.98 ± 0.54.

All remaining backgrounds from di-boson and tri-boson production, which are of minor importance in the analysis phase space, are normalized according to their expected theoretical cross sections.

5.5. Systematic uncertainties

The systematic uncertainties affecting this measurement can be divided into three categories: the uncertainties on the background estimation, experimental uncertainties and theoretical uncertainties.

The first category includes the uncertainties related to the background normalization and shape. For the non-resonant WW production the shape is taken from simulation. The input normalization to the fit is set to the expected value from simulation, and an unconstrained nuisance parameter with a flat distribution is associated to this number. This is done separately for the two jet categories.

The top quark background shape is taken from simulation after correcting for the b tagging scale factors. An uncertainty due to these scale factors is included and affects both the normalization and the shape of the top quark background. The uncertainties on the normalization are treated similarly to the WW background case, but constraining the corresponding nuisances by means of the two control regions orthogonal to the signal phase space. A similar procedure is used for the DY background.

Effects due to experimental uncertainties are studied by applying a scaling and smearing of certain variables related to the physics objects, e.g. the p_{T} of the leptons, followed by a subsequent recalculation of all the correlated variables. This is done for simulation, to account for possible systematic mismodeling.

All experimental sources, except luminosity, are treated both as normalization and shape uncertainties, and are correlated among the signal and background processes and all the categories. The following experimental uncertainties are considered:

- the uncertainty determined by the CMS online luminosity monitoring, 2.7% for the first data collected at $\sqrt{s} = 13\,\mathrm{TeV}$;
- the acceptance uncertainty associated with the combination of single and double lepton triggers, which is 2%;
- the lepton reconstruction and identification efficiencies uncertainties, that are in the range 0.5-5% for electrons and 1-7% for muons depending on p_{T} and η;
- the muon momentum and electron energy scale and resolution uncertainties, that amount to 0.01-0.5% for electrons and 0.5-1.5% for muons depending on p_{T} and η;

- the jet energy scale uncertainties, that vary between 1-11% depending on the p_{T} and η of the jet;
- the $E_{\mathrm{T}}^{\mathrm{miss}}$ resolution uncertainty, that is taken into account by propagating the corresponding uncertainties on the leptons and jets;
- the scale factors correcting the b tagging efficiency and mistagging rate, that are varied within their uncertainties. This systematic uncertainty is anticorrelated between the top control regions and the other ones.

The uncertainties in the signal and background production rates due to theoretical uncertainties include several components, which are assumed to be independent: the PDFs and α_s, the underlying event and parton shower model, and the effect of missing higher-order corrections via variations of the renormalization and factorization scales.

The effects of the variation of PDFs, α_s and renormalization/factorization QCD scales, mainly affect the signal processes, being the most important backgrounds estimated using data driven techniques. However, the uncertainties on minor backgrounds that are estimated from simulation are taken into account. These uncertainties are split in the uncertainties on the cross section, which are computed by the LHC cross section working group [114], and on the selection efficiency [115]. The PDFs and α_s signal cross section normalization uncertainties are $^{+7.4\%}_{-7.9\%}$ and $^{+7.1\%}_{-6.0\%}$ for ggH and $\pm 0.7\%$ and $\pm 3.2\%$ for VBF Higgs production mechanism. The PDFs and α_s acceptance uncertainties are less than 1% for gluon- and quark-induced processes. The effect of the QCD scales variation on the selection efficiency is around 1-3% depending on the specific process. To estimate these uncertainties, the events are reweighted according to different QCD scales or different PDF sets and the selection efficiency is recomputed each time. For the QCD scale uncertainty the maximum variation with respect to the nominal value is taken as the uncertainty. For the case of PDF and α_s uncertainties, the distribution of the selection efficiency is built taking into account all the replicas in the NNPDF3.0 set and the uncertainty is estimated as the standard deviation of that distribution.

In addition, the categorization of events based on jet multiplicity introduces additional uncertainties on the ggH production mode related to missing higher order corrections. These uncertainties are evaluated following the prescription described in Sec. [**subsec:stewart-tackman**] and correspond to 5.6% for the 0-jet and 13% for the 1-jet bin categories.

The underlying event uncertainty is estimated by comparing two different PYTHIA 8 tunes, while parton shower modelling uncertainty is estimated by comparing samples interfaced with the PYTHIA 8 and HERWIG++ parton shower programs. The effect on the ggH (VBF) signal expected yield is about 5% (5%) for the PYTHIA 8 tune variation and about 7% (10%) for the parton shower description.

Other specific theoretical uncertainties are associated to some backgrounds. An uncertainty on the ratio of the $\mathrm{t\bar{t}}$ and tW cross sections is included. Indeed, these two processes are characterized by a different number of b-jets in the final state (2 b-jets for $\mathrm{t\bar{t}}$ and 1 for tW) and the b-veto acts differently for the two. A variation of the relative ratio of the cross sections can thus cause a migration of events from the 0 to the 1 jet categories and viceversa. The corresponding uncertainty is of 8%, according to the theoretical cross section calculations [111, 112].

The gg → WW background LO cross section predicted by the MCFM generator is scaled to the NLO calculation, applying a k-factor of 1.4 with an uncertainty of 15% [110]. The interference term between the gg → WW and the ggH signal is also included and simulated with LO accuracy using MCFM. The k-factor to scale the interference term is 1.87, given by the geometrical average of the LO to NNLO gg→H→WW scale factor (2.5) and the LO to NLO gg → WW scale factor (1.4). The uncertainty on this value is estimated as the maximum variation with respect to the two scale factors mentioned above, and is found to be of 25%. Anyway, with the current amount of integrated luminosity, the interference contribution is found to be negligible.

For what the qq → WW background shape is concerned, an uncertainty related to the diboson p_{T} reweighting is evaluated varying the renormalization, factorization and resummation QCD scales.

Finally, the uncertainties due to the limited statistical accuracy of the MC simulations are also taken into account, including an independent uncertainty for each bin of the two-dimensional distribution, and for each category. The uncertainty for a certain bin and process is given by the standard deviation of the Poisson distribution with mean corresponding to the number of MC events in that bin.

5.6. Results

The expected and observed signal significance are shown in Table 5.6 for all the categories separately. Also, the observed signal strengths and the corresponding uncertainties are shown. The best fit signal strength obtained combining all the categories together is found to be $0.3^{+0.5}_{-0.5}$, corresponding to an observed significance of $0.7\,\sigma$, to be compared with the expected significance of $2.0\,\sigma$ for a Higgs boson mass of 125 GeV.

Maybe I should add the nuisances impact plots...

Table 5.6.: Observed and expected significance and signal strength the SM Higgs boson with a mass of 125 GeV for the 0-jet and 1-jet, μe and eμ, categories.

Category	Expected significance	Observed significance	σ/σ_{SM}
0-jet μe	1.1	1.3	$1.13\ ^{+0.9}_{-0.9}$
0-jet eμ	1.3	0.4	$0.33\ ^{+0.7}_{-0.7}$
1-jet μe	0.8	0	$-0.11^{+0.5}_{-1.7}$
1-jet eμ	0.9	0	$-0.54^{+1.4}_{-1.4}$
0-jet	1.6	1.3	$0.71^{+0.6}_{-0.5}$
1-jet	1.2	0	$-0.56^{+1.0}_{-1.0}$
Combination	2.0	0.7	$0.33^{+0.5}_{-0.5}$

Chapter 6.

Search for high mass resonances decaying to a W boson pair with first 13 TeV LHC data

6.1. Introduction

In this chapter, a search for a high mass spin-0 particle (from now on denoted as X) in the X→WW→ $\ell\nu\ell'\nu'$ decay channel is presented, where ℓ and ℓ' refer to an different flavour lepton pair, i.e. eμ. The search is based upon proton-proton collision data samples corresponding to an integrated luminosity of up to $2.3\,\mathrm{fb}^{-1}$ at $\sqrt{s} = 13\,\mathrm{TeV}$, recorded by the CMS experiment at the LHC during 2015. This analysis represents a general extension of the SM Higgs boson search presented in 5 and is performed in a range of heavy scalar masses from $M_{\mathrm{X}} = 200\,\mathrm{GeV}$ up to 1 TeV, extending the range studied in a similar analysis performed using Run 1 LHC data [116], which provided upper limits on the production cross section of new scalar resonances up to 600 GeV.

Despite the discovery of a particle consistent with the SM Higgs boson in 2012, there is a possibility that this particle is only a part of a larger Higgs sector, and hence only partially responsible of the EW symmetry breaking. This can be achieved in different theoretical models that extends the SM, such as the two-Higgs-doublet models [117–119], or models in which the SM Higgs boson mixes with a heavy EW singlet, which predict the existence of an additional resonance at high mass, with couplings similar to those of the SM Higgs boson, as most recently described in [120, 121].

This analysis reports a generic search for a scalar particle with different resonance decay widths hypothesis, produced via the ggH and VBF production mechanisms. The results can then be interpreted in terms of different theoretical models. This analysis is heavily based on the SM Higgs search described in 5, in terms of physics objects, selections and background estimation. The differences and similarities are discussed in this chapter.

6.2. Data and simulated samples

The data sets, triggers, pile up reweighting, lepton identification and isolation used in this analysis are the same as the SM Higgs search and are described in Sec. 5.2.

Also, the same MC simulations are used for the background processes, the only exception being the DY background, for which the MG5_aMC@NLO generator is used with LO QCD accuracy, matching together events with up to four jets in addition to the vector boson with the MLM [122] matching scheme. Given that this analysis aims to probe regions of phase space where the DY contribution is very small, like in the high transverse mass region, the usage of a simulation of the inclusive DY process may lead to large uncertainties due to the limited simulation statistics in the sample. To partially overcome this issue, different DY samples are generated in restricted portions of the phase space defined by the H_T variable, i.e. the scalar sum of all the partons p_T in the event. For $H_\mathrm{T} < 100\,\mathrm{GeV}$ the inclusive simulation is used, while different samples are used for higher values of H_T. The samples are merged using the parton level information, and it has been verified that a smooth transition between different H_T regions is achieved, as shown in Fig. 6.1. The DY LO cross section obtained from the simulation is scaled using the LO to NNLO k-factor of 1.23.

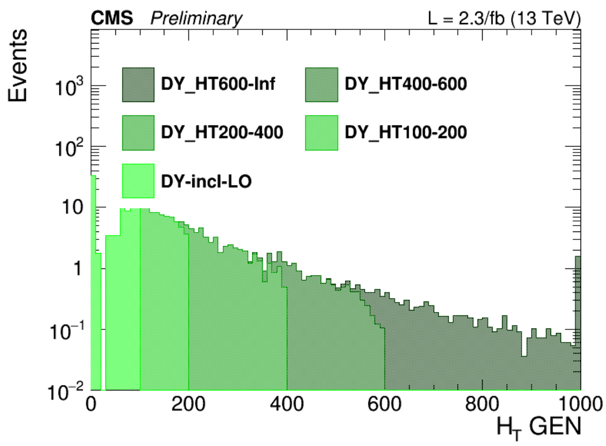

Figure 6.1.: Generator level H_T distribution for the merged DY sample.

In order to perform the resonance search in a large part of the mass spectrum, several signal samples for the gluon-gluon fusion and the vector boson fusion mechanisms have been generated corresponding to different Higgs boson masses in the range between 200 GeV and 1 TeV. The signal width for each mass point corresponds to the one expected for a SM Higgs boson at that mass. The samples are produced with a mass step of 50 GeV from 250 to 800 GeV and of 100 GeV from 800 to 1000 GeV. A finer stepping is used between 200 and 250 GeV. All the signal samples are generated with the Powheg V2 generator, interfaced with the JHUGen v6.2.8 generator, which handles the decay of the Higgs boson to $\mathrm{W^+W^-} \to 2\ell 2\nu$.

The interference effects among gg→X→WW, gg→WW and gg→H→WW are evaluated using the MCFM and JHUGen generators, as implemented in the MELA (Matrix Element Likelihood Approach) framework [97]. Details about the interference effects are given in Sec. 6.3.

6.3. Analysis strategy

The analysis strategy for the first results on the high mass search in the $\mathrm{W^+W^-} \rightarrow 2\ell 2\nu$ decay channel closely follows the strategy presented in the 13 TeV SM Higgs search in the $\mathrm{H} \rightarrow \mathrm{W^+W^-} \rightarrow 2\ell 2\nu$ channel regarding the 0 and 1 jet categories. In addition a dedicated category to the VBF production mechanism is added, given that this production mode is particularly important in the high mass region. Indeed, assuming a SM Higgs boson, the ratio of cross sections $\sigma_{\mathrm{VBF}}/\sigma_{\mathrm{ggH}}$[1] increases with the Higgs boson mass, making the VBF production mechanism more and more important as the mass of the resonance approaches to high values.

This analysis is affected essentially by the same background processes as the SM Higgs boson search, with the difference that in this case the SM Higgs boson processes, including all production modes, are treated as backgrounds.

In addition to requiring the events to pass the single or double lepton triggers, exactly one electron and one muon are required to be reconstructed in the event with opposite charges and a minimum p_{T} of 20 GeV for both the muon and electron. Both leptons are required to be well identified and isolated to reject fake leptons and leptons coming from decays in flight. To suppress background processes with three or more leptons in the final state, such as diboson or triboson production, events with any additional identified and isolated lepton with $p_{\mathrm{T}} > 10\,\mathrm{GeV}$ are rejected. To suppress the contribution of the SM production of the Higgs boson at 125 GeV, $m_{\ell\ell}$ is requested to be higher than 50 GeV. The other event requirements are identical to the 125 GeV Higgs boson search and are described in Sec. 5.3.2.

In addition to the 0 and 1 jet categories, a specific category sensitive to the VBF production mode is defined exploiting the characteristic signature of this process, where two energetic jets are emitted in the forward region of the detector and with large $\Delta\eta$ gap. Events belonging to the VBF-enriched category are selected by requiring at least two jets with $p_{\mathrm{T}} > 30\,\mathrm{GeV}$, an invariant mass $m_{\mathrm{jj}} > 500\,\mathrm{GeV}$ and a gap in pseudorapidity $\Delta\eta_{\mathrm{jj}} > 3.5$.

In addition to the transverse mass variable m_{T}, which is used in the analysis selection to define the DY background control region, an additional variable is defined, that from now on will be labelled as "improved transverse mass" $m_{\mathrm{T}}^{\mathrm{i}}$. This variable is defined as the invariant mass of the four momentum resulting from the sum of the two leptons four momenta $(p_{\ell\ell}, \vec{p}_{\ell\ell})$ and four momentum $\mathbf{E}_{\mathrm{T}}^{\mathrm{miss}} = (E_{\mathrm{T}}^{\mathrm{miss}}, \vec{p}_{\mathrm{T}}^{\mathrm{miss}})$, i.e.:

$$m_{\mathrm{T}}^{\mathrm{i}} = \sqrt{(p_{\ell\ell} + E_{\mathrm{T}}^{\mathrm{miss}})^2 - (\vec{p}_{\ell\ell} + \vec{p}_{\mathrm{T}}^{\mathrm{miss}})^2} \quad . \tag{6.1}$$

This variable allows having a better sensitivity to different resonance mass hypothesis as shown in Fig. 6.2, where the shape of the $m_{\mathrm{T}}^{\mathrm{i}}$ variable is shown for different SM Higgs mass hypothesis and it is compared to the standard m_{T} variable. The usage of this variable

[1]The ggH notation is used for the gluon-gluon fusion production mode, even in the cases where a non-SM Higgs boson is created in the process.

also provide a good discriminating power between signal and background, which depends on the particular signal mass hypothesis.

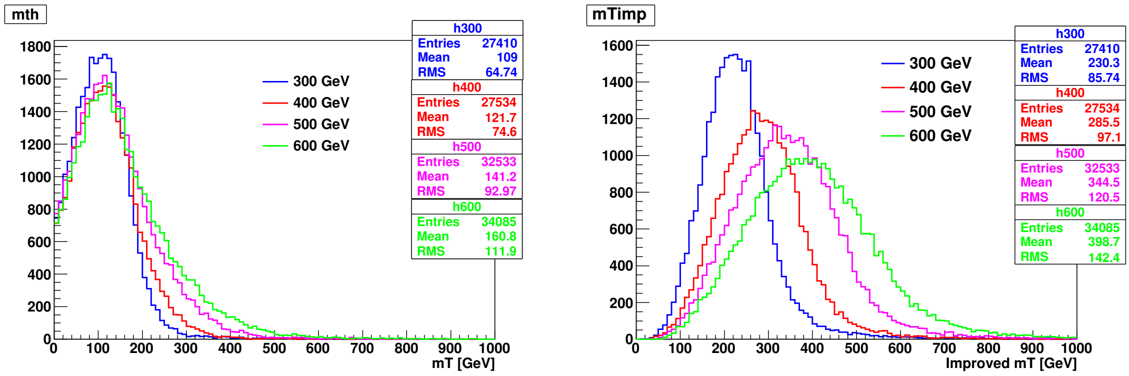

Figure 6.2.: Distribution of the m_{T} and $m_{\mathrm{T}}^{\mathrm{i}}$ variables at generator level for different resonance mass hypothesis.

The signal extraction is based on a binned maximum likelihood fit using the $m_{\mathrm{T}}^{\mathrm{i}}$ distribution for signal and background contributions as templates. The $m_{\mathrm{T}}^{\mathrm{i}}$ template is defined using the following bin boundaries:

- **0/1 jet:** [100,150,200,250,300,350,400,450,500,600,700,1000] ,
- **VBF:** [100,150,200,250,300,350,400,500,700,1000] ,

where the first number represents the lower edge of the first bin while the other numbers represent the upper edges. The last bin is an overflow bin.

In order to test different resonance decay widths hypotheses, the signal samples, which are generated with a decay width corresponding to the expected value for a SM Higgs boson at that mass (Γ_{SM}), are reweighted to obtain the desired width value (Γ'). In particular the following values are used: $\Gamma' = \Gamma_{\mathrm{SM}}$, $\Gamma' = 0.49 \times \Gamma_{\mathrm{SM}}$, $\Gamma' = 0.25 \times \Gamma_{\mathrm{SM}}$ and $\Gamma' = 0.09 \times \Gamma_{\mathrm{SM}}$. The reweighting is performed at generator level by computing the ratio of two relativistic Breit Wigner distributions with different decay widths, $f(E, \Gamma', M_{\mathrm{X}})/f(E, \Gamma_{\mathrm{SM}}, M_{\mathrm{X}})$, where:

$$f(E) \propto \frac{1}{(E^2 - M^2)^2 + M^2\Gamma^2} \quad . \tag{6.2}$$

Here, $f(E, \Gamma_{\mathrm{SM}}, M_{\mathrm{X}})$ represents the distribution used for the simulation of the signal at a mass M_{X}, and $f(E, \Gamma', M_{\mathrm{X}})$ the distribution with the new decay width. Each event is multiplied by this ratio (which depends on the energy E of the event) to obtain the reweighted distribution.

When a resonance with a non negligible width is considered, it is important to take into account the interference effects both with the gg→WW background and the SM Higgs boson off-shell tail. A study of the interference effects for a resonance X produced through the gluon fusion mechanism is performed within the MCFM+JHUGEN framework, and including NNLO corrections for cross section using HNNLO program [123] based on MCFM. The matrix element package MELA supports all of these processes and allows fast MC re-weighting and optimal discriminant calculation. The basic idea of this approach is to compute the matrix elements of the processes under study with the MCFM and JHUGen generators, including the interference terms, and using these matrix elements to compute an event weight used to reweight the simulated samples. Using this approach the simulated events can be reweighted according to different scenarios, for instance including some or all the interference terms, allowing a detailed study of the interference contribution. The effect of the various interference terms for the M_X variable at generator level is shown in Fig. 6.3, after having applied the WW baseline selections. As can be observed the contribution of the interference of the scalar resonance with the gg→WW background and with SM Higgs boson have opposite sign and partially cancel out. This cancellation effect is different for different resonance masses and depends on the event selection. In particular the interference term with the SM Higgs off-shell tail is positive for values below M_X while it turns negative above M_X. The contribution of the interference with the gg→WW background is instead characterized by an opposite sign lineshape, thus leading to a partial cancellation when considering the total interference.

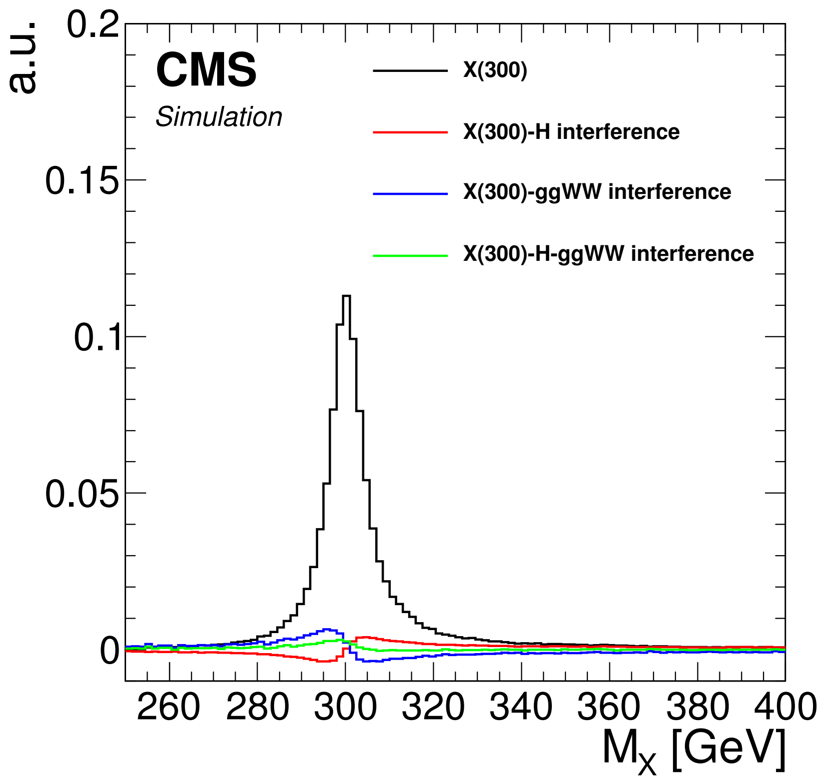

Figure 6.3.: Distribution of the M_X variable for a resonance mass of 300 GeV, showing the various interference terms after the WW baseline selections.

The effect of the resulting interference contribution including all the different terms is shown in Fig. 6.4 for the $m_{\mathrm{T}}^{\mathrm{i}}$ signal templates, in the three categories separately and for different M_{X} hypotheses.

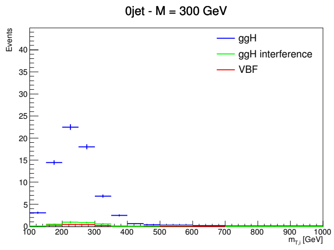

(a) $M_{\mathrm{X}} = 300$ GeV- 0 jets

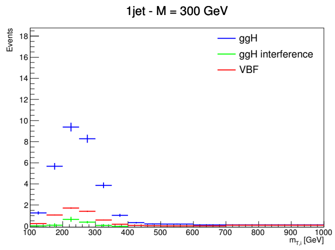

(b) $M_{\mathrm{X}} = 300$ GeV- 1 jet

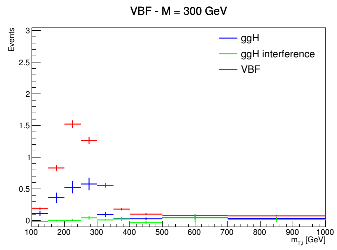

(c) $M_{\mathrm{X}} = 300$ GeV- VBF

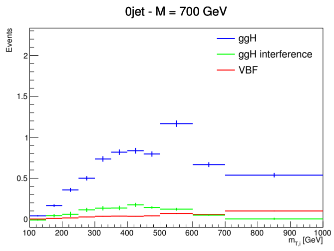

(d) $M_{\mathrm{X}} = 700$ GeV- 0 jets

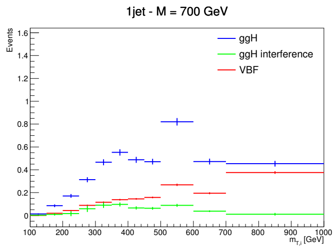

(e) $M_{\mathrm{X}} = 700$ GeV- 1 jet

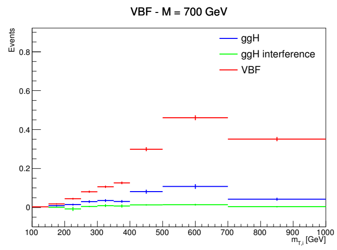

(f) $M_{\mathrm{X}} = 700$ GeV- VBF

Figure 6.4.: Distributions of the $m_{\mathrm{T}}^{\mathrm{i}}$ variable for M_{X} =300 and 700 GeV, showing the signal (both the ggH and VBF processes) and the interference contributions in the three jet categories.

The interference contribution is thus not negligible, especially for large values of M_{X}, and is included in the analysis as part of the signal contribution. More specifically, during the fit procedure the signal yield is scaled by the signal strength parameter μ (which is the parameter of interest of the fit), while the interference yield is scaled by $\sqrt{\mu}$.

6.4. Background estimation

The background processes affecting the analysis phase space are the same as the ones contributing to the SM Higgs search described in Sec. 5.4. The techniques used for the background estimation are the same as well.

The most relevant difference is the addition of the 2 jets category. The WW, top quark and DY background normalizations are estimated in this category using data driven techniques, similarly to the other jet bins.

Given the slightly different WW baseline selection with respect to the SM Higgs search, also the control regions for the top quark and DY backgrounds estimation change, while the WW background normalization is estimated from data in the three signal regions separately, owing to the different $m_{\mathrm{T}}^{\mathrm{i}}$ shapes for signal and background.

For the estimation of the top quark background, three control regions enriched in b-jets are defined by selecting events that pass the WW baseline selections and applying a b tagging requirement which depends on the jet category as follows:

- 0 jets category: at least one b-tagged jet with $20 < p_\mathrm{T} < 30\,\mathrm{GeV}$ is required;
- 1 jet category: exactly one b-tagged jet with p_T above $30\,\mathrm{GeV}$ is required;
- 2 jets category: at least one b-tagged jet with p_T above $30\,\mathrm{GeV}$ is required.

Distributions of the m_T^i variable in the 0 jets, 1 jet and 2 jets top quark enriched control regions after applying the data driven estimation are shown in Fig. 6.5.

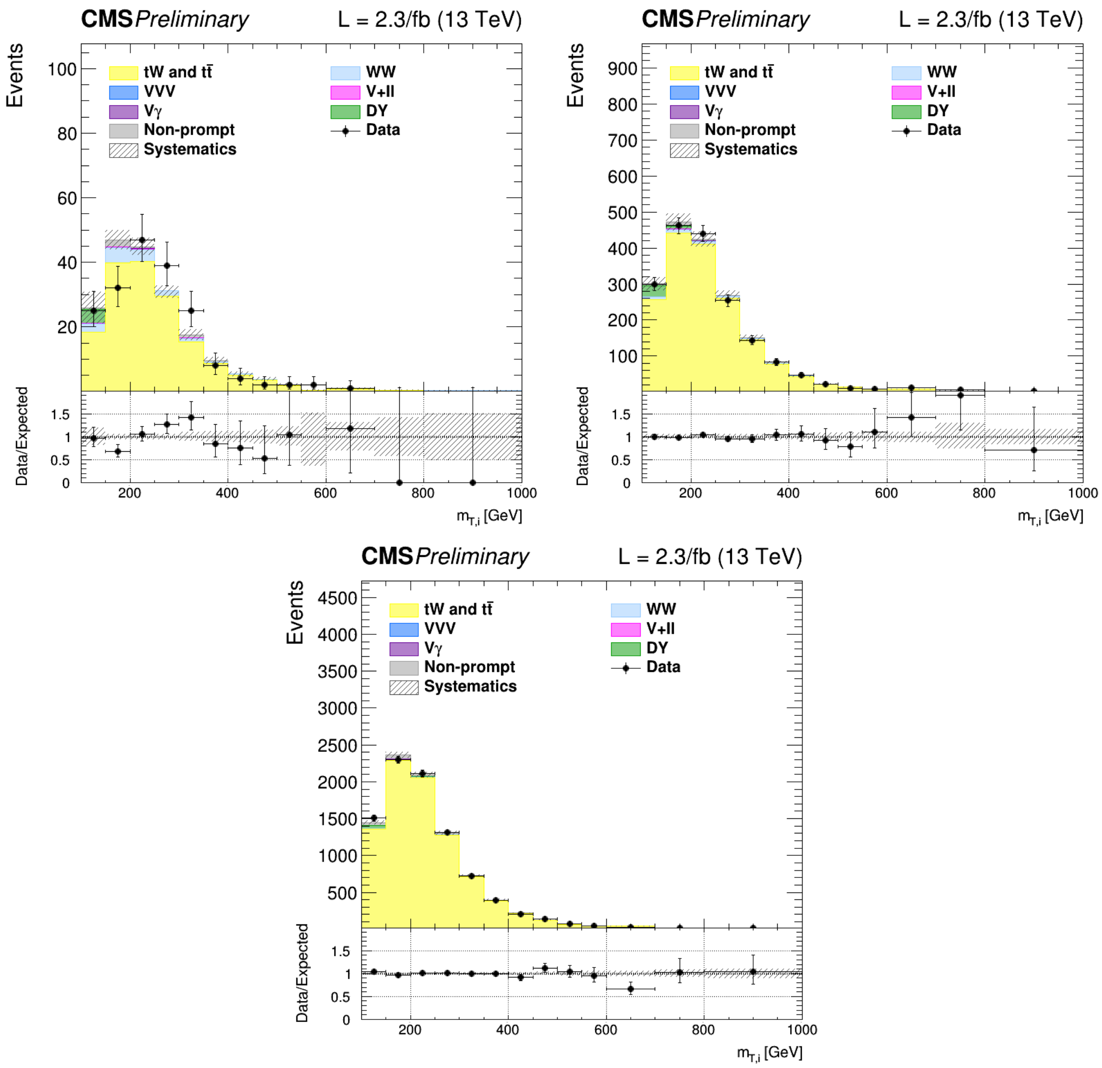

Figure 6.5.: Distributions of m_T^i for events with 0 jet (top left), 1 jet (top right) and 2 jets (bottom) in top enriched control region. Scale factors estimated from data are not applied in the plots.

The jet induced background, also labelled as "non-prompt" background, so as to highlight that these events do not contain prompt leptons, is estimated using the same fake rate method described in 4.4.3. A crosscheck is performed selecting events passing the WW baseline selection but with an eμ pair with same charge. The $m_{\mathrm{T}}^{\mathrm{i}}$ distributions for this phase space are shown in Fig. 6.6 for the three jet categories separately, showing agreement between data and simulation within the uncertainties.

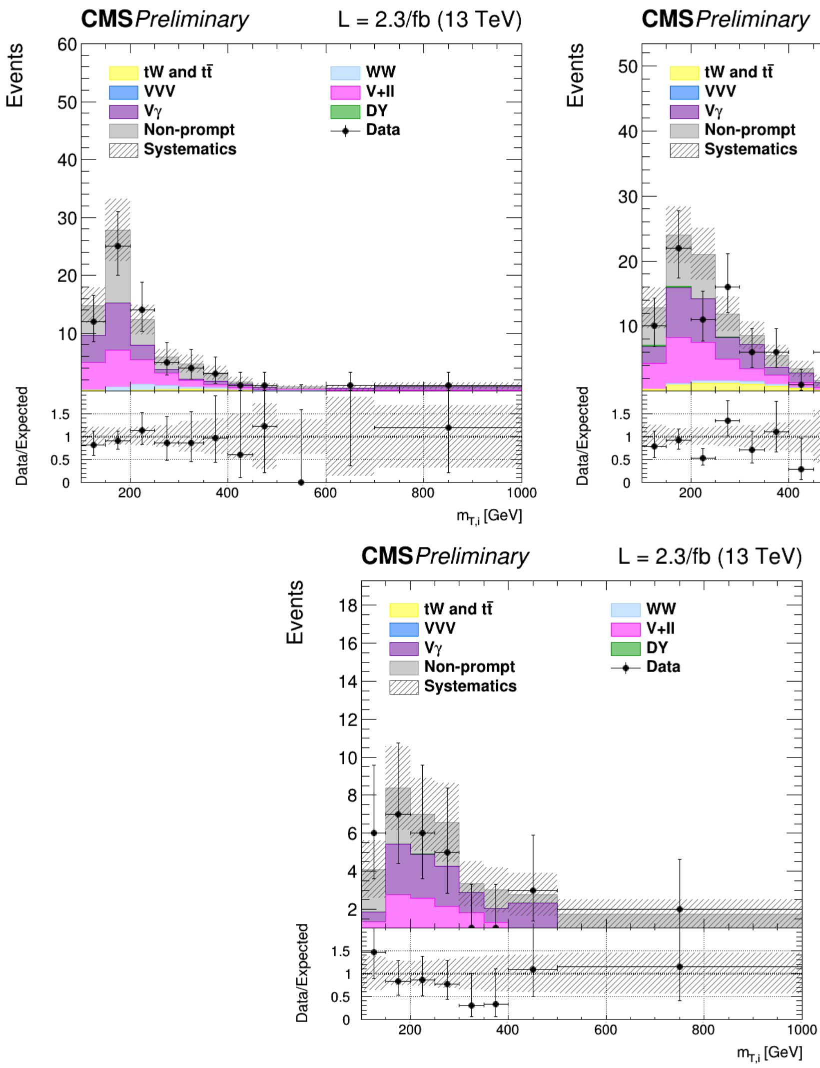

Figure 6.6.: Distributions of $m_{\mathrm{T}}^{\mathrm{i}}$ for events with 0 jet (top left), 1 jet (top right) and 2 jets (bottom) in the same-charge dilepton control region. The last bin of the histograms includes overflows.

Due to the cuts on the leptons p_{T} and on $m_{\ell\ell}$ in the WW baseline requirements, the contribution of the DY background decaying to a pair of τ leptons is very small in the signal regions, especially in the VBF phase space. The normalization of this background is estimated from a control region in data, defined in the same way as explained in 5.4.4, for the 0 and 1 jet categories. In the VBF category, given the very small number of expected events, the normalization of this background is taken from simulation.

Other minor background processes are estimated as described in 5.4.5.

6.5. Systematic uncertainties

The systematic uncertainties affecting this analasys are the same discussed in Sec. 5.5. The differences with respect to the SM Higgs boson search are described below.

The PDF and α_s uncertainties on the signal cross sections are taken from the computations performed by the LHC cross section working group [114], and are included for all the mass points. The value of these uncertainties depends on the resonance mass and vary from 3 and 5% for ggH and from 2 and 3% for VBF production modes. The PDFs and α_s uncertainties on the signal selection are evaluated for every resonance mass and are found to be less than 1% for both ggH and VBF.

The theoretical uncertainties in the signal yields due to the jet categorization are evaluated for all the ggH signals following the prescription described in Sec. 4.5.3.

An additional uncertainty on the modelling of the top pair background is derived from the observed discrepancy between data and Powheg V2 plus Pythia 8.1 simulation on the top quark p_{T} spectrum [124], which is particularly important in the tail of the $m_{\mathrm{T}}^{\mathrm{i}}$ distribution. Another uncertainty affecting the $m_{\mathrm{T}}^{\mathrm{i}}$ tail for the top quark background is the parton shower uncertainty. This is evaluated comparing the generator level $m_{\mathrm{T}}^{\mathrm{i}}$ distributions corresponding to two different simulations of the $\mathrm{t\bar{t}}$ process: one obtained using Pythia 8.1 for the showering and hadronization of the simulated events, and the other using Herwig++. The difference between the two is used to extract a shape uncertainty, which is less than 1% for low $m_{\mathrm{T}}^{\mathrm{i}}$ values and reaches about 6% in the $m_{\mathrm{T}}^{\mathrm{i}}$ tail.

6.6. Signal extraction and limit setting

The signal yield, including both the ggH and VBF production modes, is extracted performing a combined fit of the three categories to the $m_{\mathrm{T}}^{\mathrm{i}}$ simulation templates for backgrounds and signal, and is repeated for each resonance mass hypothesis. Moreover, fixed the mass of the resonance, the fit is performed again for the various hypotheses of the resonance decay width. A single signal strength μ is extracted from the fit, which multiplies both the ggH and VBF contributions. In other words it is assumed that the ratio of the two production mechanism stays the same as the one predicted by the SM[2].

The background yields expected from simulation corresponding to the three jet categories and after the analysis event selection are shown in Table 6.1. The signal yields corresponding to a selection of mass points and assuming $\Gamma' = \Gamma_{\mathrm{SM}}$ are shown in Table 6.2.

[2] This is an approximation which limits the amount of models that can be tested with the provided results. A future development od this analysis will also include the cases for which different ggH and VBF relative contributions are expected.

Table 6.1.: Expected yields estimated from simulation (except for the non-prompt contribution which is estimated using data) for each background process in the three analysis categories, after the analysis event selection. The uncertainties are shown for the processes estimated from simulation.

Background process	0 jets	1 jet	VBF
qq→WW	501.93 ± 0.00 (0%)	198.72 ± 0.00 (0%)	4.54 ± 0.00 (0%)
gg→WW	37.28 ± 5.77 (15%)	19.63 ± 3.04 (15%)	1.05 ± 0.16 (15%)
Top quark	188.75 ± 0.00 (0%)	330.05 ± 0.00 (0%)	25.06 ± 0.00 (0%)
DY	33.24 ± 0.00 (0%)	12.99 ± 0.00 (0%)	0.28 ± 0.00 (0%)
Non-prompt	64.21 ± 19.26 (30%)	31.69 ± 9.51 (30%)	2.10 ± 0.63 (30%)
Vγ	26.62 ± 0.72 (3%)	14.18 ± 0.38 (3%)	0.64 ± 0.02 (3%)
Vγ^*	4.44 ± 1.12 (25%)	3.39 ± 0.85 (25%)	0.14 ± 0.04 (25%)
VZ	13.51 ± 0.76 (6%)	11.67 ± 0.66 (6%)	0.28 ± 0.02 (6%)
VVV	0.01 ± 0.00 (3%)	0.02 ± 0.00 (3%)	0.00 ± 0.00 (3%)
SM H→WW	6.04 ± 0.40 (7%)	3.10 ± 0.11 (5%)	0.34 ± 0.02 (7%)
SM H→ $\tau\tau$	0.50 ± 0.05 (9%)	0.43 ± 0.04 (9%)	0.04 ± 0.00 (9%)
Total background	876.5	625.9	34.5

The strategy for computing the exclusion limits is based on the modified frequentist approach, also referred to as CL$_s$, as described in [113]. The first step is to construct the likelihood function $\mathcal{L}(data|\mu,\theta)$:

$$\mathcal{L}(data|\mu,\theta) = Poisson(data|\mu\cdot s(\theta) + b(\theta))\cdot p(\tilde{\theta}|\theta) \quad , \tag{6.3}$$

where *data* represents the experimental observation, s and b are the expected signal and background yields respectively and θ is the full set of nuisance parameters constrained by the prior distribution functions $p(\tilde{\theta}|\theta)$. The default values for the nuisance parameters are labelled as $\tilde{\theta}$.

For a binned shape analysis, $Poisson(data|\mu\cdot s + b)$ is the product of the Poisson probabilities to observe n_i events in bin i:

$$\prod_i \frac{(\mu\cdot s_i + b_i)^{n_i}}{n_i!} e^{-\mu\cdot s_i - b_i} \quad . \tag{6.4}$$

In order to test the compatibility of the data with the signal plus background (or the background only) hypothesis, the test statistic $\tilde{q}_\mu$ is constructed based on the profile

Table 6.2.: Expected signal yields for the ggH and VBF production modes estimated from simulation after the analysis event selection for different mass hypothesis assuming $\Gamma' = \Gamma_{SM}$ in the three analysis categories. The errors correspond to the theoretical uncertainties in the signal estimation.

Mass (GeV)	0 jets	1 jet	VBF
	ggH signal yields		
200	90.21 ± 6.67 (7%)	37.47 ± 1.81 (5%)	1.25 ± 0.26 (21%)
400	66.35 ± 4.90 (7%)	32.65 ± 1.57 (5%)	2.04 ± 0.42 (21%)
600	13.86 ± 1.05 (8%)	8.56 ± 0.44 (5%)	0.68 ± 0.14 (21%)
800	3.20 ± 0.25 (8%)	2.32 ± 0.13 (6%)	0.22 ± 0.05 (21%)
1000	0.88 ± 0.07 (8%)	0.70 ± 0.04 (6%)	0.07 ± 0.02 (21%)
	VBF signal yields		
200	1.54 ± 0.06 (4%)	6.18 ± 0.25 (4%)	5.05 ± 0.20 (4%)
400	0.91 ± 0.04 (4%)	3.42 ± 0.14 (4%)	3.19 ± 0.13 (4%)
600	0.50 ± 0.02 (4%)	1.95 ± 0.08 (4%)	1.88 ± 0.08 (4%)
800	0.33 ± 0.01 (4%)	1.21 ± 0.05 (4%)	1.16 ± 0.05 (4%)
1000	0.22 ± 0.01 (4%)	0.79 ± 0.03 (4%)	0.69 ± 0.03 (4%)

likelihood reatio:

$$\tilde{q}_\mu = -2\ln\frac{\mathcal{L}(data|\mu,\hat{\theta}_\mu)}{\mathcal{L}(data|\hat{\mu},\hat{\theta})} \quad \text{with} \quad 0 \leq \hat{\mu} \leq \mu \quad , \tag{6.5}$$

where $\hat{\theta}_\mu$ refers to the conditional maximum likelihood estimators of θ, given the signal strength μ. The parameter estimators $\hat{\mu}$ and $\hat{\theta}$ correspond to the global maximum of the likelihood. The $0 \leq \hat{\mu}$ constraint is imposed to have a positive signal yield, e.g. background underfluctuations are forbidden, while $\hat{\mu} \leq \mu$ is imposed to have a one-sided confidence interval. The observed test statistic for the signal strength μ under test is referred to as $\tilde{q}_\mu^{\text{obs}}$. The values of the nuisance parameters obtained maximising the likelihood function are labelled as $\hat{\theta}_0^{\text{obs}}$ and $\hat{\theta}_\mu^{\text{obs}}$ for the background only and signal plus background hypotheses, respectively. The pdf of the test statistic in constructed by generating toy MC pseudo-data for both the background only and signal plus background hypotheses, i.e. $f(\tilde{q}_\mu|\mu,\hat{\theta}_\mu^{\text{obs}})$ and $f(\tilde{q}_\mu|0,\hat{\theta}_0^{\text{obs}})$. These distributions can be used to define two p-values corresponding to the two hypotheses, p_μ and p_b:

$$p_\mu = P(\tilde{q}_\mu \geq \tilde{q}_\mu^{\mathrm{obs}}|\mathrm{signal} + \mathrm{background}) = \int_{\tilde{q}_\mu^{\mathrm{obs}}}^{\infty} f(\tilde{q}_\mu|\mu, \hat{\theta}_\mu^{\mathrm{obs}}) d\tilde{q}_\mu \quad , \tag{6.6}$$

$$1 - p_b = (\tilde{q}_\mu \geq \tilde{q}_\mu^{\mathrm{obs}}|\mathrm{background\ only}) = \int_{\tilde{q}_0^{\mathrm{obs}}}^{\infty} f(\tilde{q}_\mu|0, \hat{\theta}_0^{\mathrm{obs}}) d\tilde{q}_\mu \quad . \tag{6.7}$$

According to these definitions, p_μ and p_b can be identified with $\mathrm{CL_{s+b}}$ and $1 - \mathrm{CL_b}$, respectively. The $\mathrm{CL_s}(\mu)$ is calculated using the following ratio:

$$\mathrm{CL_s}(\mu) = \frac{\mathrm{CL_{s+b}}}{\mathrm{CL_b}} = \frac{p_\mu}{1 - p_b} \quad . \tag{6.8}$$

If, for a given signal strength μ, $\mathrm{CL_s} \leq \alpha$, then the hypothesis is excluded with a $(1 - \alpha)$ confidence level (CL). For instance, if one wants to quote the upper limit on μ with a 95% CL, the signal strength has to be adjusted until $\mathrm{CL_s} = 0.05$.

The expected median upper limit, as well as the $\pm 1\sigma$ (68% CL) and $\pm 2\sigma$ (95% CL) bands, are determined generating a large amount of pseudo-data in the background only hypothesis and calculating $\mathrm{CL_s}$ and the 95% CL upper limit for each of them, as if they were real data. Then the cumulative distribution of the 95% CL upper limits is built and the median expected value is identified as the value at which the cumulative distribution crosses the 50% quantile. The $\pm 1\sigma$ ($\pm 2\sigma$) band is defined by the values at which the cumulative distribution crosses the 16% (2.5%) and 84% (97.5%) quantiles.

In order to assess the sensitivity of the analysis, the expected upper exclusion limits at 95% CL on the signal strength are shown in Fig. 6.7 for the three jet categories separately. For a given mass of the resonance, the limits are derived assuming a signal decay width $\Gamma' = \Gamma_{\mathrm{SM}}$ and a cross section equal to the one expected from a SM Higgs boson at that mass. The other decay width hypothesis have also been tested, showing a very similar expected exclusion limit, suggesting that this analysis is not strongly sensitive to variations of the resonance decay width.

The 0 jets category is the most sensitive especially in the low mass region, while for very large masses of the resonance the 1 jet and VBF categories start being important. This is explained mainly by the fact that the VBF contribution increases, with respect to ggH, as the mass increases. The expected exclusion limit on the signal strength after the combination of the three categories is shown in Fig. 6.8. Comparing the limits in the single categories with the combination of the three it is evident how the higher jet multiplicity categories help in improving the results for large values of M_{X}.

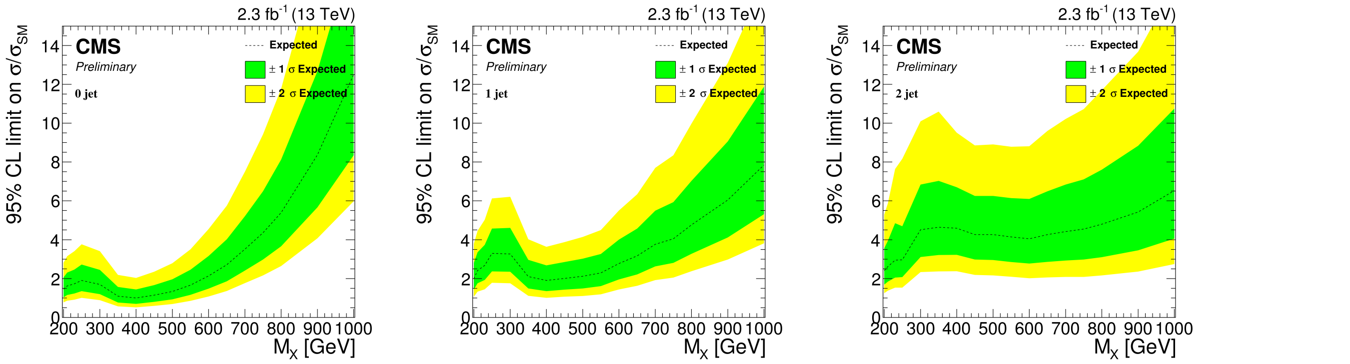

(a) 0 jets (b) 1 jet (c) 2 jets

Figure 6.7.: Expected exclusion upper limits at 95% CL on the signal strength in the three categories, as a function of the resonance mass. The dashed line corresponds to median upper limit, while the green and yellow regions represent the $\pm 1\sigma$ and $\pm 2\sigma$ uncertainty bands, respectively. Limits are derived assuming a SM Higgs boson cross section and decay width for each mass point.

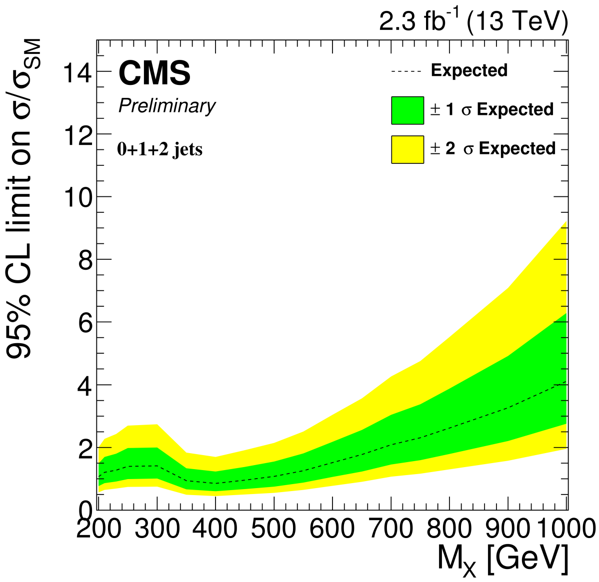

Figure 6.8.: Expected exclusion upper limit at 95% CL on the signal strength for the combination of the three categories, as a function of the resonance mass. The dashed line corresponds to median upper limit, while the green and yellow regions represent the $\pm 1\sigma$ and $\pm 2\sigma$ uncertainty bands, respectively. The limit is derived assuming a SM Higgs boson cross section and decay width for each mass point.

6.7. Results

The $m_{\mathrm{T}}^{\mathrm{i}}$ distributions for the signal region after the full analysis selection are shown in Fig. 6.9 for the three jet categories. Two different signal hypotheses corresponding to $M_\mathrm{X} = 400\,\mathrm{GeV}$ and $M_\mathrm{X} = 800\,\mathrm{GeV}$ are shown superimposed on the background for comparison.

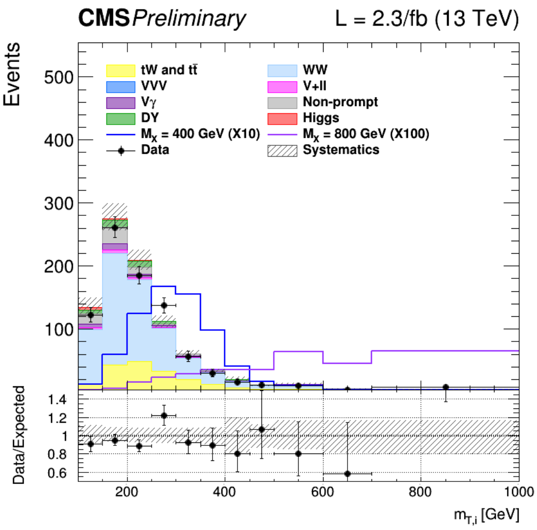

(a) 0 jets

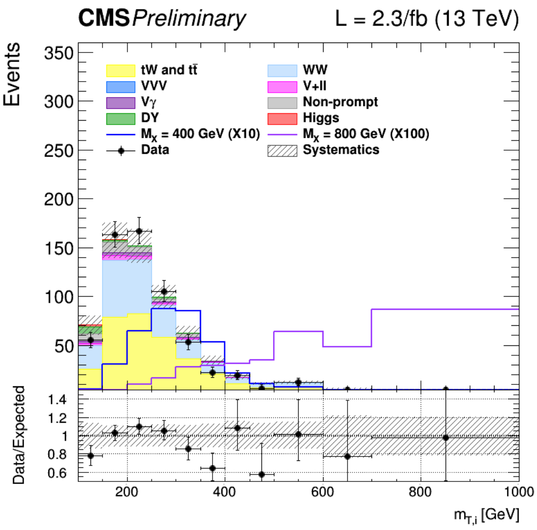

(b) 1 jet

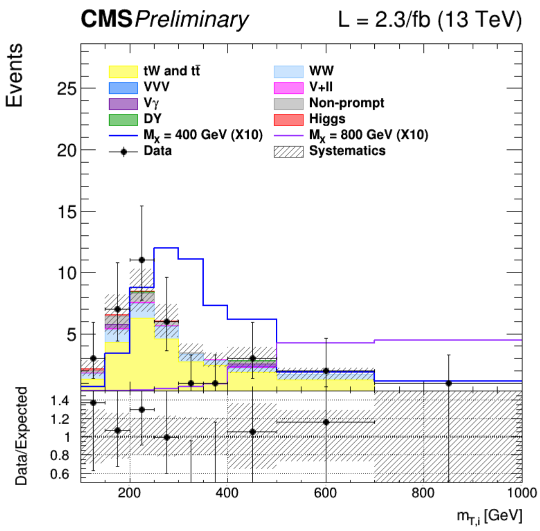

(c) VBF

Figure 6.9.: Distributions of m_T^i in the signal region for the 0 jets, 1 jet and VBF categories. Background normalisations correspond to the pre-fit value. Signal contributions for two mass hypotheses, $M_\mathrm{X} = 400\,\mathrm{GeV}$ and $M_\mathrm{X} = 800\,\mathrm{GeV}$, are shown superimposed on the background and scaled to facilitate the comparison.

For every mass point from 200 GeV up to 1 TeV the observed p-value and the 95% CL upper exclusion limit are calculated for for five hypothesis of the signal width. The observed p-value as a function of the resonance mass for the combination of the three jet categories is shown in Table 6.3.

Table 6.3.: Observed p-value and corresponding significance (set to 0 in case of underfluctuations of the observed number of events) for the combination of the three jet categories for different resonance masses. Different values of the signal width are shown.

Mass [GeV]	$\Gamma = 0.09 \times \Gamma_{SM}$ p-value (signif.)	$\Gamma = 0.25 \times \Gamma_{SM}$ p-value (signif.)	$\Gamma = 0.49 \times \Gamma_{SM}$ p-value (signif.)	$\Gamma = \Gamma_{SM}$ p-value (signif.)
200	0.50 (0)	0.50 (0)	0.50 (0)	0.56 (0)
210	0.58 (0)	0.45 (0.1)	0.35 (0.4)	0.24 (0.7)
230	0.21 (0.8)	0.22 (0.8)	0.23 (0.7)	0.26 (0.6)
250	0.29 (0.5)	0.20 (0.8)	0.15 (1.0)	0.12 (1.2)
300	0.014 (2.2)	0.015 (2.2)	0.016 (2.1)	0.018 (2.1)
350	0.16 (1.0)	0.17 (1.0)	0.18 (0.9)	0.23 (0.7)
400	0.50 (0)	0.49 (0)	0.49 (0)	0.57 (0)
450	0.51 (0)	0.50 (0)	0.50 (0)	0.52 (0)
500	0.50 (0)	0.51 (0)	0.50 (0)	0.52 (0)
550	0.50 (0)	0.51 (0)	0.51 (0)	0.51 (0)
600	0.50 (0)	0.50 (0)	0.51 (0)	0.51 (0)
650	0.50 (0)	0.50 (0)	0.54 (0)	0.50 (0)
700	0.50 (0)	0.50 (0)	0.50 (0)	0.50 (0)
750	0.50 (0)	0.54 (0)	0.50 (0)	0.40 (0.3)
800	0.50 (0)	0.55 (0)	0.39 (0.3)	0.29 (0.6)
900	0.29 (0.6)	0.27 (0.6)	0.24 (0.7)	0.22 (0.8)
1000	0.18 (0.9)	0.18 (0.9)	0.18 (0.9)	0.18 (0.9)

In order to be independent on the particular model assumed for the signal cross section, the results are interpreted as exclusion limits on $\sigma \times \mathcal{B}$, where σ stands for the sum of the ggH and VBF cross sections, and $\mathcal{B}$ represents the X$\rightarrow$WW$\rightarrow$ $2\ell 2\nu$ branching ratio including all lepton flavours. The expected and observed upper exclusion limits on $\sigma \times \mathcal{B}$ for $\Gamma' = \Gamma_{\mathrm{SM}}$ are shown in Fig. 6.10.

A mild excess is observed in the 0 jets category and, more evident, in the 1 jet category around 250-300 GeV. A deficit is instead in the VBF category around 250 GeV, which is mainly due to an underfluctuation of the background. This effect can be understood looking at the VBF shape in Fig. 6.9, where two adjacent data points, corresponding to the fifth

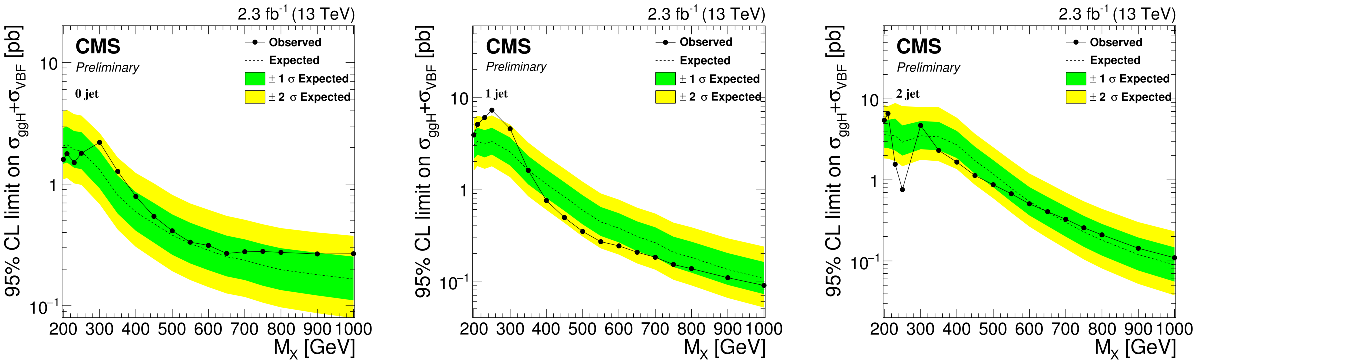

(a) 0 jets (b) 1 jet (c) 2 jets

Figure 6.10.: Expected and observed exclusion upper limits at 95% CL on $\sigma \times \mathcal{B}$ in the three categories, as a function of the resonance mass. The dashed line corresponds to median upper limit, while the green and yellow regions represent the $\pm 1\sigma$ and $\pm 2\sigma$ uncertainty bands, respectively. The dotted line represents the observed limit. Limits are derived assuming $\Gamma' = \Gamma_{\mathrm{SM}}$ for each mass point.

and sixth bins, clearly underfluctuate with respect to the background prediction, causing the dip in the observed limit.

The exclusion limit resulting from the combination of the three categories is shown in Fig. 6.11, for the five Γ' hypotheses discussed before. From the combined exclusion limits no significant evidence of a deviation from the SM prediction is observed. The presence of a scalar resonance with $\sigma \times \mathcal{B}$ higher than the values reported in Fig. 6.11 is thus excluded with a 95% CL for masses ranging from 200 GeV up to 1 TeV.

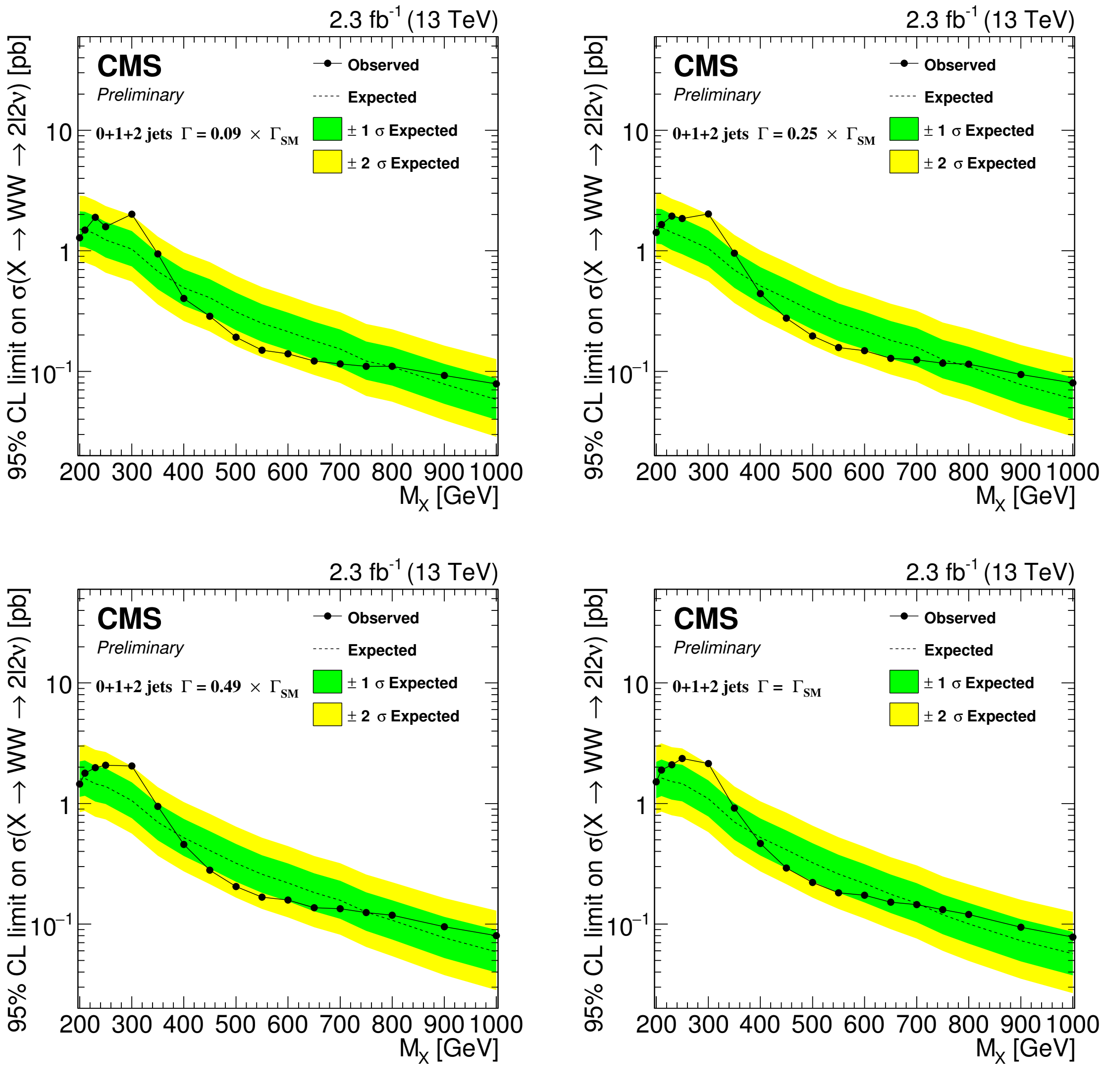

Figure 6.11.: Expected and observed exclusion limits at 95% CL on $\sigma \times \mathcal{B}$ for the combination of the three jet categories as a function of the resonance mass. The black dotted line corresponds to the observed value while the yellow and green bands represent the $\pm 1\sigma$ and $\pm 2\sigma$ uncertainties respectively. Limits are shown for four hypotheses of the resonance decay width.

Chapter 7.

Conclusions

Appendix A.

Fiducial region definition and optimization

The fiducial region must be chosen in such a way to be as close as possible to the selections applied in the analysis, in order to reduce the model dependece in the extrapolation step. That means that for optimizing the fiducial volume definition, the efficiency has to be maximized. Another parameter entering the game is the number of fake events, in other words the number of reconstructed events which do not belong to the fiducial phase space. This parameter should instead be as small as possible. Even if we have to observe the trend of these two quantities as a function of $p_{\mathrm{T}}^{\mathrm{H}}$, we can maximize the ratio between the overall efficiency and the overall fake rate as a proxy for establishing the "goodness" of the fiducial region.

Several different fiducial region definitions were tested and the results show that:

- **of cut:** The fiducial region definition must include only the opposite flavor combination including one electron and one muon. If we include also the combinations involving τ's the efficiency falls down.
- **Lepton cut:** Since the resolution on lepton transverse momentum is good, there is no need to loosen the cuts related these variables, i.e. we can use the same cuts defined in the analysis selection ($p_{\mathrm{T}}^{\ell,1} > 20\,\mathrm{GeV}$, $p_{\mathrm{T}}^{\ell,2} > 10\,\mathrm{GeV}$).
- **Di-lepton $\boldsymbol{p_{\mathrm{T}}}$ cut:** As stated in the previous point, there is no need to loosen this cut, so we kept the same value as the analysis selection, i.e. $p_{\mathrm{T}}^{\ell\ell} > 30\,\mathrm{GeV}$.
- **Di-lepton mass cut:** $m_{\ell\ell} > 12\,\mathrm{GeV}$ as discussed before.
- **neutrino pair $\boldsymbol{p_{\mathrm{T}}}$ cut:** Since the resolution on the measurement of the missing transverse energy is poor, the neutrino pair cut should not be included in the definition of the fiducial region, because it would increase the fake rate without increasing the efficiency, thus resulting in a lower ratio between overall efficiency and fake rate.
- **$\boldsymbol{m_{\mathrm{T}}}$ cut:** Also the m_{T} cut that we have in the analysis selection, i.e. $m_{\mathrm{T}} > 60\,\mathrm{GeV}$, should be loosened or removed because it involves neutrinos and then increase the fake rate. We decided eventually to keep this cut, loosening it to 50 GeV, because in addition to increase the number of fake events, it increases the efficiency as well.

The fake rate and the efficiency as a function of $p_{\mathrm{T}}^{\mathrm{H}}$ after the optimization discussed before are shown in figure A.1. To obtain these plots the fiducial region was modified adding in sequence the various cuts and computing the efficiency and the fake rate each time. In that way we can asses the composition of those distributions.

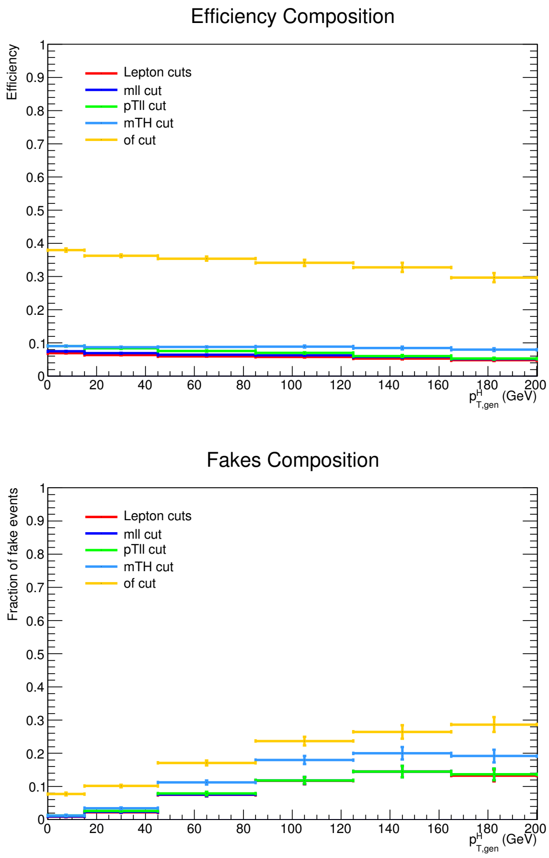

Figure A.1.: Efficiency and fake rate as a function on Higgs transverse momentum. The plots correspond to the optimized fiducial region definition and show the effect of adding each of the mentioned cuts in sequence.

The efficiency and fraction of fake events have been measured also as a function of the $E_{\mathrm{T}}^{\mathrm{miss}}$ and m_{T} cuts in the fiducial region. Since these two variables are correlated, the results are reported as two-dimensional histograms. In Fig. A.2 are reported the efficiency and fraction of fake events for these two variables.

The criterion adopted to define the fiducial region is a tradeoff between having a large efficiency and a small fraction of fake events. Especially when looking at the low resolution variables, such as $E_{\mathrm{T}}^{\mathrm{miss}}$ and m_{T}, a suitable figure of merit has to be chosen for the estimation of the best cuts. Several different figures of merit have been checked, such as ϵ/f, $\epsilon - f$ and $(1-f)/\epsilon$. The results for these three different figures of merit are shown in Fig. A.3 as a function of the $E_{\mathrm{T}}^{\mathrm{miss}}$ and m_{T} cuts in the fiducial region.

Following the same criterion, similar plots as above have been obtained for an alternative model, given by varying up the ggH/VBF ratio within the experimental uncertainties. The

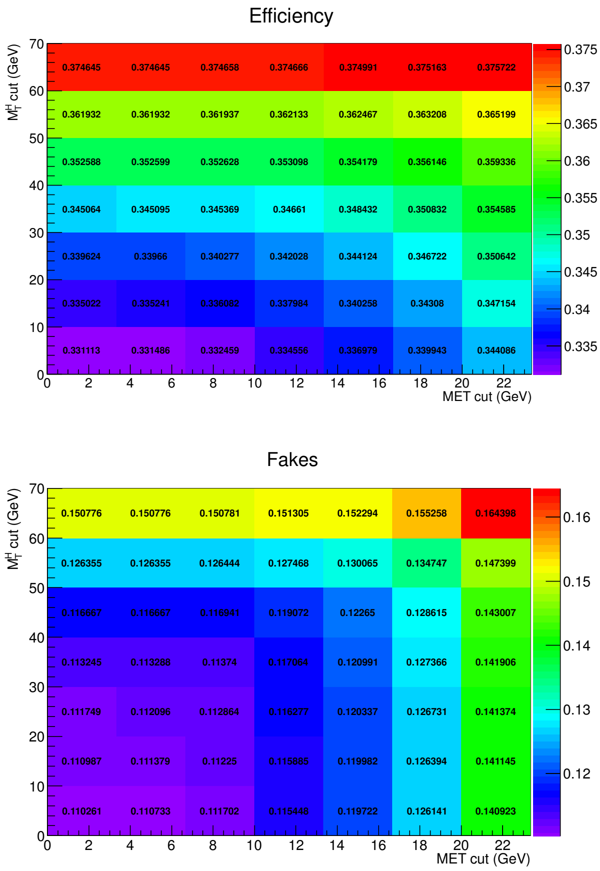

Figure A.2.: Efficiency and fake rate as a function of $E_{\mathrm{T}}^{\mathrm{miss}}$ and m_{T} cuts in the fiducial region.

3107 results, shown in Fig. A.4 and Fig. A.5, show a similar trend with respect to the model
3108 with nominal ggH/VBF ratio.

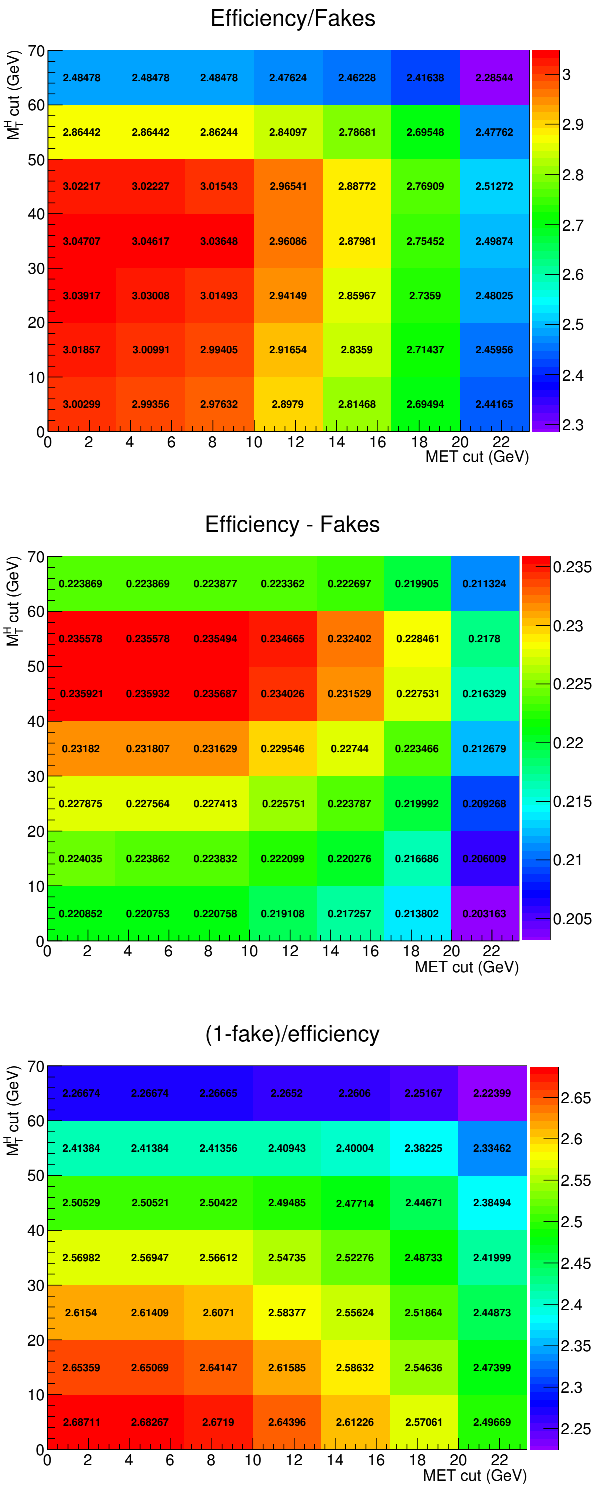

Figure A.3.: Different figures of merit as a function of $E_{\mathrm{T}}^{\mathrm{miss}}$ and m_{T} cuts in the fiducial region.

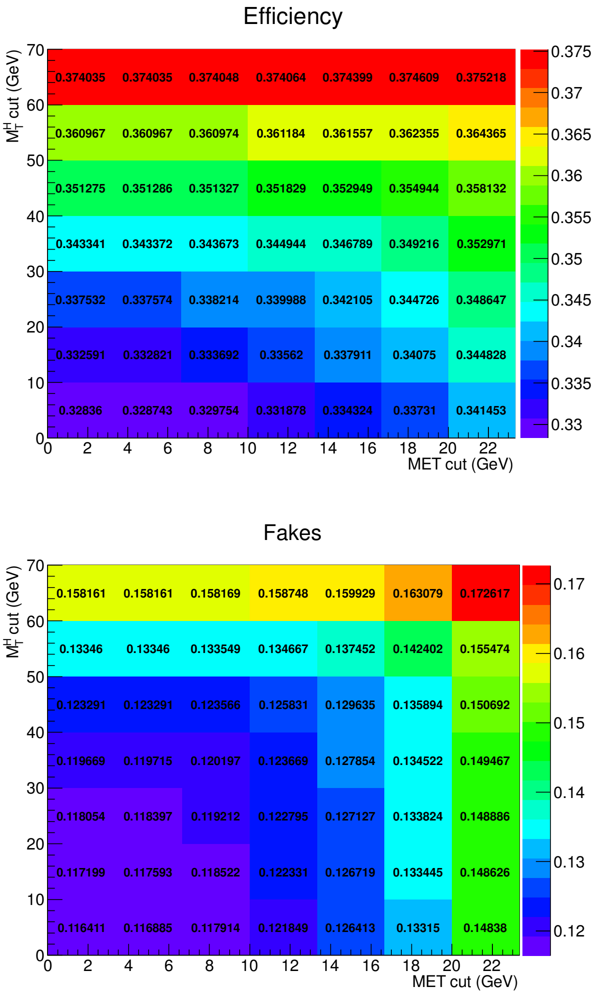

Figure A.4.: Efficiency and fake rate as a function of $E_{\mathrm{T}}^{\mathrm{miss}}$ and m_{T} cuts in the fiducial region, for the alternative model with an up variation of the ggH/VBF ratio.

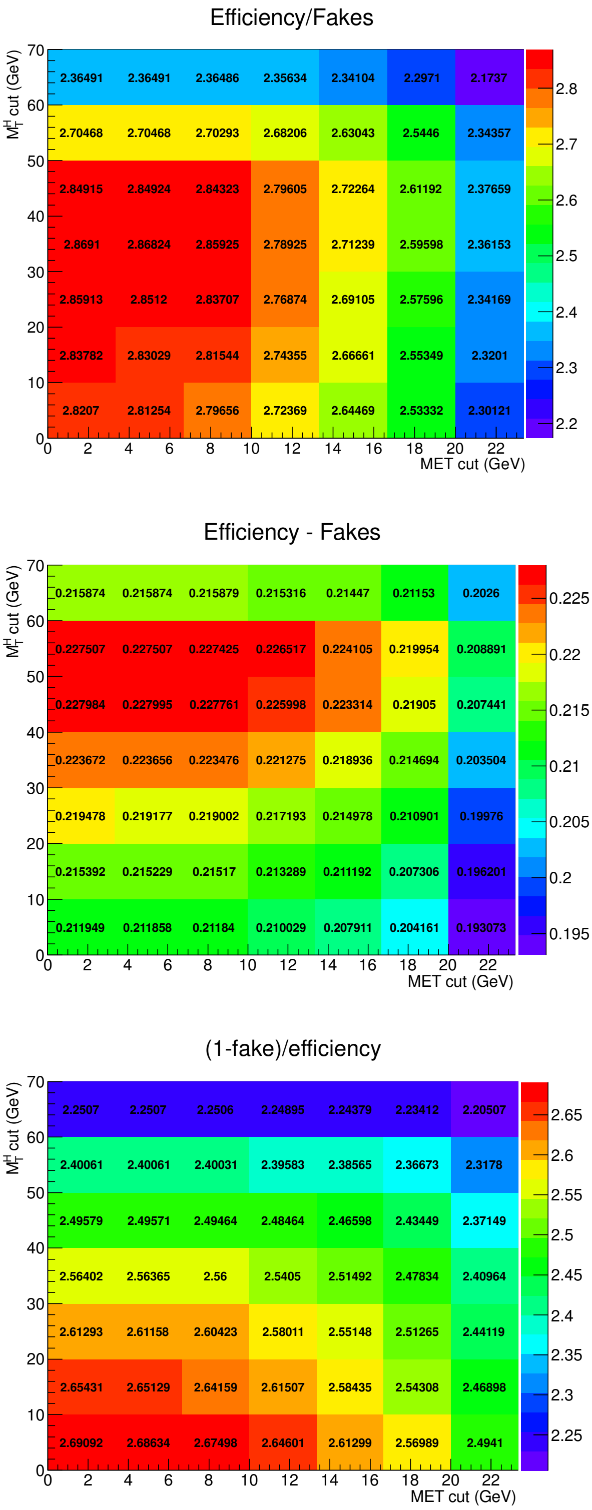

Figure A.5.: Different figures of merit as a function of E_T^{miss} and m_T cuts in the fiducial region, for the alternative model with an up variation of the ggH/VBF ratio.

Bibliography

[1] Thomas Sven Pettersson and P Lefèvre. *The Large Hadron Collider: conceptual design*. Tech. rep. CERN-AC-95-05-LHC. Oct. 1995. URL: http://cds.cern.ch/record/291782.

[2] Oliver Sim Brüning et al. *LHC Design Report*. Geneva: CERN, 2004. URL: http://cds.cern.ch/record/782076.

[3] Oliver Sim Brüning et al. *LHC Design Report*. Geneva: CERN, 2004. URL: http://cds.cern.ch/record/815187.

[4] Michael Benedikt et al. *LHC Design Report*. Geneva: CERN, 2004. URL: http://cds.cern.ch/record/823808.

[5] *LEP design report*. By the LEP Injector Study Group. Geneva: CERN, 1983. URL: http://cds.cern.ch/record/98881.

[6] *LEP design report*. Copies shelved as reports in LEP, PS and SPS libraries. Geneva: CERN, 1984. URL: http://cds.cern.ch/record/102083.

[7] Carlo Wyss. *LEP design report, v.3: LEP2*. Vol. 1-2 publ. in 1983-84. Geneva: CERN, 1996. URL: http://cds.cern.ch/record/314187.

[8] S. Chatrchyan et al. "The CMS experiment at the CERN LHC". In: *JINST* 3 (2008), S08004. DOI: 10.1088/1748-0221/3/08/S08004.

[9] G. Aad et al. "The ATLAS Experiment at the CERN Large Hadron Collider". In: *JINST* 3 (2008), S08003. DOI: 10.1088/1748-0221/3/08/S08003.

[10] A. Augusto Alves Jr. et al. "The LHCb Detector at the LHC". In: *JINST* 3 (2008), S08005. DOI: 10.1088/1748-0221/3/08/S08005.

[11] K. Aamodt et al. "The ALICE experiment at the CERN LHC". In: *JINST* 3 (2008), S08002. DOI: 10.1088/1748-0221/3/08/S08002.

[12] G. Anelli et al. "The TOTEM experiment at the CERN Large Hadron Collider". In: *JINST* 3 (2008), S08007. DOI: 10.1088/1748-0221/3/08/S08007.

[13] O. Adriani et al. "The LHCf detector at the CERN Large Hadron Collider". In: *JINST* 3 (2008), S08006. DOI: 10.1088/1748-0221/3/08/S08006.

[14] *The CMS magnet project: Technical Design Report*. Technical Design Report CMS. Geneva: CERN, 1997. URL: http://cds.cern.ch/record/331056.

[15] *The CMS electromagnetic calorimeter project: Technical Design Report*. Technical Design Report CMS. Geneva: CERN, 1997. URL: http://cds.cern.ch/record/349375.

[16] Philippe Bloch et al. *Changes to CMS ECAL electronics: addendum to the Technical Design Report*. Technical Design Report CMS. Geneva: CERN, 2002. URL: http://cds.cern.ch/record/581342.

[17] *The CMS hadron calorimeter project: Technical Design Report*. Technical Design Report CMS. Geneva: CERN, 1997. URL: http://cds.cern.ch/record/357153.

[18] *The CMS muon project: Technical Design Report*. Technical Design Report CMS. Geneva: CERN, 1997. URL: http://cds.cern.ch/record/343814.

[19] S. Dasu et al. "CMS. The TriDAS project. Technical design report, vol. 1: The trigger systems". In: (2000).

[20] Sergio Cittolin, Attila Rácz, and Paris Sphicas. *CMS The TriDAS Project: Technical Design Report, Volume 2: Data Acquisition and High-Level Trigger. CMS trigger and data-acquisition project*. Technical Design Report CMS. Geneva: CERN, 2002. URL: http://cds.cern.ch/record/578006.

[21] CMS Collaboration. *Particle–Flow Event Reconstruction in CMS and Performance for Jets, Taus, and $E_{\mathrm{T}}^{\mathrm{miss}}$*. CMS Physics Analysis Summary CMS-PAS-PFT-09-001. 2009. URL: http://cdsweb.cern.ch/record/1194487.

[22] Serguei Chatrchyan et al. "Description and performance of track and primary-vertex reconstruction with the CMS tracker". In: *JINST* 9.10 (2014), P10009. DOI: 10.1088/1748-0221/9/10/P10009. arXiv: 1405.6569 [physics.ins-det].

[23] Pierre Billoir and S. Qian. "Simultaneous pattern recognition and track fitting by the Kalman filtering method". In: *Nucl. Instrum. Meth.* A 294 (1990), p. 219. DOI: 10.1016/0168-9002(90)91835-Y.

[24] Wolfgang Adam et al. *Reconstruction of Electrons with the Gaussian-Sum Filter in the CMS Tracker at the LHC*. Tech. rep. CMS-NOTE-2005-001. Geneva: CERN, Jan. 2005. URL: https://cds.cern.ch/record/815410.

[25] Serguei Chatrchyan et al. "Performance of CMS muon reconstruction in pp collision events at $\sqrt{s} = 7$ TeV". In: *JINST* 7 (2012), P10002. DOI: 10.1088/1748-0221/7/10/P10002. arXiv: 1206.4071 [physics.ins-det].

[26] *Electron reconstruction and identification at $\sqrt{s} = 7$ TeV*. Tech. rep. CMS-PAS-EGM-10-004. Geneva: CERN, 2010. URL: http://cds.cern.ch/record/1299116.

[27] Vardan Khachatryan et al. "Performance of Electron Reconstruction and Selection with the CMS Detector in Proton-Proton Collisions at $\sqrt{s} = 8$ TeV". In: *JINST* 10.06 (2015), P06005. DOI: 10.1088/1748-0221/10/06/P06005. arXiv: 1502.02701 [physics.ins-det].

[28] Gavin P. Salam. "Towards Jetography". In: *Eur. Phys. J.* C67 (2010), pp. 637–686. DOI: 10.1140/epjc/s10052-010-1314-6. arXiv: 0906.1833 [hep-ph].

[29] Gerald C. Blazey et al. “Run II jet physics”. In: *QCD and weak boson physics in Run II. Proceedings, Batavia, USA, March 4-6, June 3-4, November 4-6, 1999.* 2000, pp. 47–77. arXiv: `hep-ex/0005012 [hep-ex]`. URL: `http://lss.fnal.gov/cgi-bin/find_paper.pl?conf-00-092`.

[30] Serguei Chatrchyan et al. “Determination of jet energy calibration and transverse momentum resolution in CMS”. In: *JINST* 6 (2011), P11002. DOI: `10.1088/1748-0221/6/11/P11002`. arXiv: `1107.4277 [physics.ins-det]`.

[31] B. Abbott et al. “Determination of the absolute jet energy scale in the D0 calorimeters”. In: *Nucl. Instrum. Meth.* A424 (1999), pp. 352–394. DOI: `10.1016/S0168-9002(98)01368-0`. arXiv: `hep-ex/9805009 [hep-ex]`.

[32] Wolfgang Waltenberger. *Adaptive Vertex Reconstruction*. Tech. rep. CMS-NOTE-2008-033. Geneva: CERN, July 2008. URL: `https://cds.cern.ch/record/1166320`.

[33] *MET performance in 8 TeV data*. Tech. rep. CMS-PAS-JME-12-002. Geneva: CERN, 2013. URL: `http://cds.cern.ch/record/1543527`.

[34] *Performance of missing energy reconstruction in 13 TeV pp collision data using the CMS detector*. Tech. rep. CMS-PAS-JME-16-004. Geneva: CERN, 2016. URL: `http://cds.cern.ch/record/2205284`.

[35] M. Spira et al. “Higgs boson production at the LHC”. In: *Nucl. Phys.* B 453 (1995), pp. 17–82. DOI: `10.1016/0550-3213(95)00379-7`. arXiv: `hep-ph/9504378 [hep-ph]`.

[36] Robert Harlander and Philipp Kant. “Higgs production and decay: Analytic results at next-to-leading order QCD”. In: *JHEP* 12 (2005), p. 015. DOI: `10.1088/1126-6708/2005/12/015`. arXiv: `hep-ph/0509189 [hep-ph]`.

[37] V. Ravindran, J. Smith, and W. L. van Neerven. “NNLO corrections to the total cross-section for Higgs boson production in hadron hadron collisions”. In: *Nucl. Phys.* B 665 (2003), pp. 325–366. DOI: `10.1016/S0550-3213(03)00457-7`. arXiv: `hep-ph/0302135 [hep-ph]`.

[38] Stefano Catani and Massimiliano Grazzini. “An NNLO subtraction formalism in hadron collisions and its application to Higgs boson production at the LHC”. In: *Phys. Rev. Lett.* 98 (2007), p. 222002. DOI: `10.1103/PhysRevLett.98.222002`. arXiv: `hep-ph/0703012 [hep-ph]`.

[39] Charalampos Anastasiou et al. “Higgs Boson Gluon-Fusion Production in QCD at Three Loops”. In: *Phys. Rev. Lett.* 114 (2015), p. 212001. DOI: `10.1103/PhysRevLett.114.212001`. arXiv: `1503.06056 [hep-ph]`.

[40] X. Chen et al. “NNLO QCD corrections to Higgs boson production at large transverse momentum”. In: (2016). arXiv: `1607.08817 [hep-ph]`.

[41] Giuseppe Bozzi et al. “Transverse-momentum resummation and the spectrum of the Higgs boson at the LHC”. In: *Nucl. Phys. B* 737 (2006), p. 73. DOI: `10.1016/j.nuclphysb.2005.12.022`. arXiv: `hep-ph/0508068 [hep-ph]`.

[42] D. de Florian et al. "Higgs boson production at the LHC: transverse momentum resummation effects in the $H \to 2\gamma$, $H \to WW \to l\nu l\nu$ and $H \to ZZ \to 4l$ decay modes". In: *JHEP* 06 (2012), p. 132. DOI: 10.1007/JHEP06(2012)132. arXiv: 1203.6321 [hep-ph].

[43] Massimiliano Grazzini and Hayk Sargsyan. "Heavy-quark mass effects in Higgs boson production at the LHC". In: *JHEP* 09 (2013), p. 129. DOI: 10.1007/JHEP09(2013)129. arXiv: 1306.4581 [hep-ph].

[44] Aleksandr Azatov and Ayan Paul. "Probing Higgs couplings with high p_T Higgs production". In: *JHEP* 01 (2014), p. 014. DOI: 10.1007/JHEP01(2014)014. arXiv: 1309.5273 [hep-ph].

[45] Robert V. Harlander and Tobias Neumann. "Probing the nature of the Higgs-gluon coupling". In: *Phys. Rev. D* 88 (2013), p. 074015. DOI: 10.1103/PhysRevD.88.074015. arXiv: 1308.2225 [hep-ph].

[46] David Marzocca, Marco Serone, and Jing Shu. "General Composite Higgs Models". In: *JHEP* 08 (2012), p. 013. DOI: 10.1007/JHEP08(2012)013. arXiv: 1205.0770 [hep-ph].

[47] Andrea Banfi, Adam Martin, and Veronica Sanz. "Probing top-partners in Higgs+jets". In: *JHEP* 08 (2014), p. 053. DOI: 10.1007/JHEP08(2014)053. arXiv: 1308.4771 [hep-ph].

[48] Georges Aad et al. "Fiducial and differential cross sections of Higgs boson production measured in the four-lepton decay channel in pp collisions at $\sqrt{s} = 8\,\mathrm{TeV}$ with the ATLAS detector". In: *Phys. Lett. B* 738 (2014), p. 234. DOI: 10.1016/j.physletb.2014.09.054. arXiv: 1408.3226 [hep-ex].

[49] Georges Aad et al. "Measurements of fiducial and differential cross sections for Higgs boson production in the diphoton decay channel at $\sqrt{s} = 8\,\mathrm{TeV}$ with ATLAS". In: *JHEP* 09 (2014), p. 112. DOI: 10.1007/JHEP09(2014)112. arXiv: 1407.4222 [hep-ex].

[50] Georges Aad et al. "Measurements of the Total and Differential Higgs Boson Production Cross Sections Combining the $H \to \gamma\gamma$ and $H \to ZZ^* \to 4\ell$ Decay Channels at $\sqrt{s} = 8$ TeV with the ATLAS Detector". In: *Phys. Rev. Lett.* 115 (2015), p. 091801. DOI: 10.1103/PhysRevLett.115.091801. arXiv: 1504.05833 [hep-ex].

[51] Vardan Khachatryan et al. "Measurement of differential cross sections for Higgs boson production in the diphoton decay channel in pp collisions at $\sqrt{s} = 8\,\mathrm{TeV}$". In: *Eur. Phys. J. C* 76 (2016), p. 13. DOI: 10.1140/epjc/s10052-015-3853-3. arXiv: 1508.07819 [hep-ex].

[52] Vardan Khachatryan et al. "Measurement of differential and integrated fiducial cross sections for Higgs boson production in the four-lepton decay channel in pp collisions at $\sqrt{s} = 7$ and 8 TeV". In: *JHEP* 04 (2016), p. 005. DOI: 10.1007/JHEP04(2016)005. arXiv: 1512.08377 [hep-ex].

[53] LHC Higgs Cross Section Working Group. *Handbook of LHC Higgs cross sections: 3. Higgs properties*. CERN Report CERN-2013-004. 2013. DOI: 10.5170/CERN-2013-004. arXiv: 1307.1347 [hep-ph].

[54] Serguei Chatrchyan et al. "Measurement of Higgs boson production and properties in the WW decay channel with leptonic final states". In: *JHEP* 01 (2014), p. 096. DOI: 10.1007/JHEP01(2014)096. arXiv: 1312.1129 [hep-ex].

[55] G. Cowan. "A survey of unfolding methods for particle physics". In: *Conf. Proc.* C0203181 (2002), p. 248.

[56] Michael Krämer, Stephen Mrenna, and Davison E. Soper. "Next-to-leading order QCD jet production with parton showers and hadronization". In: *Phys. Rev. D* 73 (2006), p. 014022. DOI: 10.1103/PhysRevD.73.014022. arXiv: hep-ph/0509127 [hep-ph].

[57] Stefano Frixione, Paolo Nason, and Carlo Oleari. "Matching NLO QCD computations with Parton Shower simulations: the POWHEG method". In: *JHEP* 11 (2007), p. 070. DOI: 10.1088/1126-6708/2007/11/070. arXiv: 0709.2092 [hep-ph].

[58] Nils Lavesson and Leif Lonnblad. "Extending CKKW-merging to one-loop matrix elements". In: *JHEP* 12 (2008), p. 070. DOI: 10.1088/1126-6708/2008/12/070. arXiv: 0811.2912 [hep-ph].

[59] Simone Alioli et al. "NLO Higgs boson production via gluon fusion matched with shower in POWHEG". In: *JHEP* 04 (2009), p. 002. DOI: 10.1088/1126-6708/2009/04/002. arXiv: 0812.0578 [hep-ph].

[60] Paolo Nason and Carlo Oleari. "NLO Higgs boson production via vector-boson fusion matched with shower in POWHEG". In: *JHEP* 02 (2010), p. 037. DOI: 10.1007/JHEP02(2010)037. arXiv: 0911.5299 [hep-ph].

[61] Simone Alioli, Sven-Olaf Moch, and Peter Uwer. "Hadronic top-quark pair-production with one jet and parton showering". In: *JHEP* 01 (2012), p. 137. DOI: 10.1007/JHEP01(2012)137. arXiv: 1110.5251 [hep-ph].

[62] J. Alwall et al. "The automated computation of tree-level and next-to-leading order differential cross sections, and their matching to parton shower simulations". In: *JHEP* 07 (2014), p. 079. DOI: 10.1007/JHEP07(2014)079. arXiv: 1405.0301 [hep-ph].

[63] T. Binoth et al. "Gluon-induced W-boson pair production at the LHC". In: *JHEP* 12 (2006), p. 046. DOI: 10.1088/1126-6708/2006/12/046. arXiv: hep-ph/0611170 [hep-ph].

[64] Marco Bonvini et al. "Signal-background interference effects for $gg \to H \to W^+W^-$ beyond leading order". In: *Phys. Rev. D* 88 (2013), p. 034032. DOI: 10.1103/PhysRevD.88.034032. arXiv: 1304.3053 [hep-ph].

[65] Giampiero Passarino. "Higgs CAT". In: *Eur. Phys. J. C* 74 (2014), p. 2866. DOI: 10.1140/epjc/s10052-014-2866-7. arXiv: 1312.2397 [hep-ph].

[66] Torbjörn Sjöstrand, Stephen Mrenna, and Peter Skands. "PYTHIA 6.4 physics and manual". In: *JHEP* 05 (2006), p. 026. DOI: `10.1088/1126-6708/2006/05/026`. arXiv: `hep-ph/0603175 [hep-ph]`.

[67] Hung-Liang Lai et al. "Uncertainty induced by QCD coupling in the CTEQ global analysis of parton distributions". In: *Phys. Rev. D* 82 (2010), p. 054021. DOI: `10.1103/PhysRevD.82.054021`. arXiv: `1004.4624 [hep-ph]`.

[68] Hung-Liang Lai et al. "New parton distributions for collider physics". In: *Phys. Rev. D* 82 (2010), p. 074024. DOI: `10.1103/PhysRevD.82.074024`. arXiv: `1007.2241 [hep-ph]`.

[69] LHC Higgs Cross Section Working Group. "Handbook of LHC Higgs Cross Sections". In: *arXiv:1101.0593* (2011).

[70] Simone Alioli et al. "A general framework for implementing NLO calculations in shower Monte Carlo programs: the POWHEG BOX". In: *JHEP* 06 (2010), p. 043. DOI: `10.1007/JHEP06(2010)043`. arXiv: `1002.2581 [hep-ph]`.

[71] S. Agostinelli et al. "GEANT4: A simulation toolkit". In: *Nucl. Instrum. Meth. A* 506 (2003), p. 250. DOI: `10.1016/S0168-9002(03)01368-8`.

[72] E. Bagnaschi et al. "Higgs production via gluon fusion in the POWHEG approach in the SM and in the MSSM". In: *JHEP* 02 (2012), p. 088. DOI: `10.1007/JHEP02(2012)088`. arXiv: `1111.2854 [hep-ph]`.

[73] Stefano Actis et al. "NLO Electroweak Corrections to Higgs Boson Production at Hadron Colliders". In: *Phys. Lett. B* 670 (2008), p. 12. DOI: `10.1016/j.physletb.2008.10.018`. arXiv: `0809.1301 [hep-ph]`.

[74] Stefano Catani et al. "Soft gluon resummation for Higgs boson production at hadron colliders". In: *JHEP* 07 (2003), p. 028. DOI: `10.1088/1126-6708/2003/07/028`. arXiv: `hep-ph/0306211 [hep-ph]`.

[75] Yanyan Gao et al. "Spin determination of single-produced resonances at hadron colliders". In: *Phys. Rev. D* 81 (2010), p. 075022. DOI: `10.1103/PhysRevD.81.075022`. arXiv: `1001.3396 [hep-ph]`.

[76] Sara Bolognesi et al. "Spin and parity of a single-produced resonance at the LHC". In: *Phys. Rev. D* 86 (2012), p. 095031. DOI: `10.1103/PhysRevD.86.095031`. arXiv: `1208.4018 [hep-ph]`.

[77] Ian Anderson et al. "Constraining anomalous HVV interactions at proton and lepton colliders". In: *Phys. Rev. D* 89 (2014), p. 035007. DOI: `10.1103/PhysRevD.89.035007`. arXiv: `1309.4819 [hep-ph]`.

[78] Torbjorn Sjöstrand, Stephen Mrenna, and Peter Z. Skands. "A Brief Introduction to PYTHIA 8.1". In: *Comput. Phys. Commun.* 178 (2008), p. 852. DOI: `10.1016/j.cpc.2008.01.036`. arXiv: `0710.3820 [hep-ph]`.

[79] Vardan Khachatryan et al. “Measurement of the $t\bar{t}$ production cross section in the eμ channel in proton-proton collisions at $\sqrt{s} = 7$ and 8 TeV”. In: (2016). arXiv: `1603.02303 [hep-ex]`.

[80] Stanislaw Jadach, Johann H. Kuhn, and Zbigniew Was. “TAUOLA: A Library of Monte Carlo programs to simulate decays of polarized tau leptons”. In: *Comput. Phys. Commun.* 64 (1990), p. 275. DOI: `10.1016/0010-4655(91)90038-M`.

[81] CMS Collaboration. “Standard Model Cross Sections for CMS at 7 TeV”. In: *CMS Generator Group Twiki* (2010).

[82] John M. Campbell, R. Keith Ellis, and Ciaran Williams. “Vector boson pair production at the LHC”. In: *JHEP* 07 (2011), p. 018. DOI: `10.1007/JHEP07(2011)018`. arXiv: `1105.0020 [hep-ph]`.

[83] J. Ohnemus. “Order alpha-s calculations of hadronic W+- gamma and Z gamma production”. In: *Phys. Rev.* D47 (1993), pp. 940–955. DOI: `10.1103/PhysRevD.47.940`.

[84] JetMET group. “Jet energy uncertainties, `https://twiki.cern.ch/twiki/bin/view/CMS/JECUncertaintySources#2012_JEC`”. In: (). URL: `https://twiki.cern.ch/twiki/bin/view/CMS/JECUncertaintySources%5C#2012_JEC`.

[85] Sergey Alekhin et al. “The PDF4LHC Working Group Interim Report”. 2011.

[86] Michiel Botje et al. “The PDF4LHC Working Group Interim Recommendations”. 2011.

[87] Richard D. Ball et al. “Impact of Heavy Quark Masses on Parton Distributions and LHC Phenomenology”. In: *Nucl. Phys. B* 849 (2011), p. 296. DOI: `10.1016/j.nuclphysb.2011.03.021`. arXiv: `1101.1300 [hep-ph]`.

[88] A. D. Martin et al. “Parton distributions for the LHC”. In: *Eur. Phys. J. C* 63 (2009), p. 189. DOI: `10.1140/epjc/s10052-009-1072-5`. arXiv: `0901.0002 [hep-ph]`.

[89] Iain W. Stewart and Frank J. Tackmann. “Theory uncertainties for Higgs and other searches using jet bins”. In: *Phys. Rev. D* 85 (2012), p. 034011. DOI: `10.1103/PhysRevD.85.034011`. arXiv: `1107.2117 [hep-ph]`.

[90] “Procedure for the LHC Higgs boson search combination in summer 2011”. In: (2011).

[91] Glen Cowan et al. “Asymptotic formulae for likelihood-based tests of new physics”. In: *Eur. Phys. J.* C71 (2011). [Erratum: Eur. Phys. J.C73,2501(2013)], p. 1554. DOI: `10.1140/epjc/s10052-011-1554-0,10.1140/epjc/s10052-013-2501-z`. arXiv: `1007.1727 [physics.data-an]`.

[92] Tim Adye. “Unfolding algorithms and tests using RooUnfold”. 2011.

[93] Andreas Hocker and Vakhtang Kartvelishvili. “SVD approach to data unfolding”. In: *Nucl. Instrum. Meth. A* 372 (1996), p. 469. DOI: `10.1016/0168-9002(95)01478-0`. arXiv: `hep-ph/9509307 [hep-ph]`.

[94] G. D'Agostini. "A Multidimensional unfolding method based on Bayes' theorem". In: *Nucl. Instrum. Meth. A* 362 (1995), pp. 487–498. DOI: 10.1016/0168-9002(95)00274-X.

[95] Vardan Khachatryan et al. "Precise determination of the mass of the Higgs boson and tests of compatibility of its couplings with the standard model predictions using proton collisions at 7 and 8 TeV". In: *Eur. Phys. J. C* 75 (2015), p. 212. DOI: 10.1140/epjc/s10052-015-3351-7. arXiv: 1412.8662 [hep-ex].

[96] Paolo Nason. "A New method for combining NLO QCD with shower Monte Carlo algorithms". In: *JHEP* 11 (2004), p. 040. DOI: 10.1088/1126-6708/2004/11/040. arXiv: hep-ph/0409146 [hep-ph].

[97] S. Bolognesi, Y. Gao and A.V. Gritsan *et al.* "JHUGen". In: *URL* http://www.pha.jhu.edu/spin/ (2011).

[98] Gionata Luisoni et al. "$HW^{\pm}$/HZ + 0 and 1 jet at NLO with the POWHEG BOX interfaced to GoSam and their merging within MiNLO". In: *JHEP* 10 (2013), p. 083. DOI: 10.1007/JHEP10(2013)083. arXiv: 1306.2542 [hep-ph].

[99] Tom Melia et al. "W+W-, WZ and ZZ production in the POWHEG BOX". In: *JHEP* 11 (2011), p. 078. DOI: 10.1007/JHEP11(2011)078. arXiv: 1107.5051 [hep-ph].

[100] T. Gehrmann et al. "W^+W^- Production at Hadron Colliders in Next to Next to Leading Order QCD". In: *Phys. Rev. Lett.* 113.21 (2014), p. 212001. DOI: 10.1103/PhysRevLett.113.212001. arXiv: 1408.5243 [hep-ph].

[101] Patrick Meade, Harikrishnan Ramani, and Mao Zeng. "Transverse momentum resummation effects in W^+W^- measurements". In: *Phys. Rev.* D90.11 (2014), p. 114006. DOI: 10.1103/PhysRevD.90.114006. arXiv: 1407.4481 [hep-ph].

[102] Prerit Jaiswal and Takemichi Okui. "Explanation of the WW excess at the LHC by jet-veto resummation". In: *Phys. Rev.* D90.7 (2014), p. 073009. DOI: 10.1103/PhysRevD.90.073009. arXiv: 1407.4537 [hep-ph].

[103] John M. Campbell, R. Keith Ellis, and Ciaran Williams. "Bounding the Higgs width at the LHC: Complementary results from $H \to WW$". In: *Phys. Rev.* D89.5 (2014), p. 053011. DOI: 10.1103/PhysRevD.89.053011. arXiv: 1312.1628 [hep-ph].

[104] Richard D. Ball et al. "Parton distributions with QED corrections". In: *Nucl. Phys.* B877 (2013), pp. 290–320. DOI: 10.1016/j.nuclphysb.2013.10.010. arXiv: 1308.0598 [hep-ph].

[105] Richard D. Ball et al. "Unbiased global determination of parton distributions and their uncertainties at NNLO and at LO". In: *Nucl. Phys.* B855 (2012), pp. 153–221. DOI: 10.1016/j.nuclphysb.2011.09.024. arXiv: 1107.2652 [hep-ph].

[106] Vardan Khachatryan et al. "Event generator tunes obtained from underlying event and multiparton scattering measurements". In: (2015). arXiv: 1512.00815 [hep-ex].

[107] Peter Richardson and Alexandra Wilcock. “Monte Carlo Simulation of Hard Radiation in Decays in Beyond the Standard Model Physics in Herwig++”. In: *Eur. Phys. J.* C74 (2014), p. 2713. DOI: 10.1140/epjc/s10052-014-2713-x. arXiv: 1303.4563 [hep-ph].

[108] J. Bellm et al. “Herwig++ 2.7 Release Note”. In: (2013). arXiv: 1310.6877 [hep-ph].

[109] *SM Higgs production cross sections at $\sqrt{s}$ = 13-14 TeV*. https://twiki.cern.ch/twiki/bin/view/LHCPhysics/CERNYellowReportPageAt1314TeV.

[110] Fabrizio Caola et al. “QCD corrections to W^+W^- production through gluon fusion”. In: *Phys. Lett.* B754 (2016), pp. 275–280. DOI: 10.1016/j.physletb.2016.01.046. arXiv: 1511.08617 [hep-ph].

[111] *NLO single-top channel cross sections*. https://twiki.cern.ch/twiki/bin/view/LHCPhysics/SingleTopRefXsec.

[112] *NNLO+NNLL top-quark-pair cross sections*. https://twiki.cern.ch/twiki/bin/view/LHCPhysics/TtbarNNLO.

[113] *Procedure for the LHC Higgs boson search combination in Summer 2011*. Tech. rep. CMS-NOTE-2011-005. ATL-PHYS-PUB-2011-11. Geneva: CERN, Aug. 2011.

[114] *LHC Higgs Cross Section Working Group*. https://twiki.cern.ch/twiki/bin/view/LHCPhysics/LHCHXSWG.

[115] Jon Butterworth et al. “PDF4LHC recommendations for LHC Run II”. In: *J. Phys.* G43 (2016), p. 023001. DOI: 10.1088/0954-3899/43/2/023001. arXiv: 1510.03865 [hep-ph].

[116] Vardan Khachatryan et al. “Search for a Higgs Boson in the Mass Range from 145 to 1000 GeV Decaying to a Pair of W or Z Bosons”. In: *JHEP* 10 (2015), p. 144. DOI: 10.1007/JHEP10(2015)144. arXiv: 1504.00936 [hep-ex].

[117] G. C. Branco et al. “Theory and phenomenology of two-Higgs-doublet models”. In: *Phys. Rept.* 516 (2012), p. 1. DOI: 10.1016/j.physrep.2012.02.002. arXiv: 1106.0034 [hep-ph].

[118] N. Craig and T. Scott. “Exclusive signals of an extended Higgs sector”. In: *JHEP* 11 (2012), p. 083. DOI: 10.1007/JHEP11(2012)083. arXiv: 1207.4835 [hep-ph].

[119] H. Haber and O. Stal. “New LHC benchmarks for the CP-conserving two-Higgs-doublet model”. In: *Eur. Phys. J. C* 75 (2015), p. 491. DOI: 10.1140/epjc/s10052-015-3697-x. arXiv: 1507.04281 [hep-ph].

[120] Suyong Choi, Sunghoon Jung, and P. Ko. “Implications of LHC data on 125 GeV Higgs-like boson for the Standard Model and its various extensions”. In: *JHEP* 1310 (2013), p. 225. DOI: 10.1007/JHEP10(2013)225. arXiv: 1307.3948.

[121] Tania Robens and Tim Stefaniak. “Status of the Higgs singlet extension of the standard model after LHC run 1”. In: *Eur. Phys. J. C* 75 (2015), p. 105. DOI: 10.1140/epjc/s10052-015-3323-y. arXiv: 1501.02234 [hep-ph].

[122] Johan Alwall et al. “Comparative study of various algorithms for the merging of parton showers and matrix elements in hadronic collisions”. In: *Eur. Phys. J. C* 53 (2008), pp. 473–500. DOI: 10.1140/epjc/s10052-007-0490-5. arXiv: 0706.2569 [hep-ph].

[123] Massimiliano Grazzini. “NNLO predictions for the Higgs boson signal in the $\mathrm{H}\to\mathrm{WW}\to \ell\nu\ell\nu$ and $\mathrm{H}\to\mathrm{ZZ}\to 4\ell$ decay channels”. In: *JHEP* 02 (2008), p. 043. DOI: 10.1088/1126-6708/2008/02/043. arXiv: 0801.3232 [hep-ph].

[124] Vardan Khachatryan et al. “Measurement of the differential cross section for top quark pair production in pp collisions at $\sqrt{s} = 8\,\mathrm{TeV}$”. In: *Eur. Phys. J. C* 75.11 (2015), p. 542. DOI: 10.1140/epjc/s10052-015-3709-x. arXiv: 1505.04480 [hep-ex].